UNIVERSITÉ DE STRASBOURG

ÉCOLE DOCTORAL CHIMIE – PHYSIQUE

Institute de Physique et Chimie des Matériaux de Strasbourg
Laboratoire d'Essais pour la Maîtrise des Accidents Graves, CEA Cadarache

THÈSE présentée par:

Václav TYRPEKL

soutenue le : 26 juin 2012

pour obtenir la grade de: **Docteur de l'Université de Strasbourg**

Discipline/Spécialité : **Chimie des Matériaux**

Effet matériaux lors de l'interaction Corium-Eau: Analyse structurale des débris d'une explosion vapeur et mécanismes de solidification

---

Thèse dirigée par:

Pascal Piluso	Ingénieur de Recherches, CEA Cadarache
Snejana Bakardjieva	Directrice de Recherches, UACH AV CR,v.v.i
Jean-Luc Rehspringer	Directeur de Recherches, Université de Strasbourg
Daniel Nižnanský	Directeur de Recherches, Université Charles de Prague

Rapporteurs:

Vlastimil Matejec	Directeur de'l Institute de la Photonique et l'Electronique, Academie des Sciences, Rep. Tchèque
Gérard Cognet	Conseiller nucléaire auprès de l'Ambassade de France, Budapest, Hongrie, CEA Délégation Regionale

Autres membres du jury:

Miloslav Frumar	Professeur, Université de Pardubice, Rep. Tchèque
Ivan Nemec	Professeur associé, Université Charles de Prague
Rémi Barillon	Professeur, Université de Strasbourg
Nathalie Viart	Professeur, Université de Strasbourg

Vaclav TYRPEKL

Effet matériaux lors de l'interaction Corium-Eau: Analyse structurale des débris d'une explosion vapeur et mécanismes de solidification

Résumé

Ce travail a été réalisé en cotutelle entre l'Université Charles à Prague (République Tchèque) et l'Université de Strasbourg (France). Il a également profité d'une coopération entre l'Institut de Chimie Inorganique de l'Académie des Sciences de République Tchèque et le Commissariat à l'Énergie Atomique et aux Énergies Alternatives (CEA, Cadarache, France). Les résultats des travaux ont contribué au projet OCDE / AEN Serena 2 (Programme portant sur l'étude des effets d'une explosion de vapeur dans un réacteur nucléaire à eau).

La thèse présentée se situe dans le domaine de la sûreté nucléaire et de la science des matériaux. Elle traite de l'Interaction Combustible-Réfrigérant (ICR, ou FCI en anglais pour Fuel-Coolant Interaction) susceptible d'intervenir lors d'un accident grave de réacteur nucléaire et actuellement à l'étude dans les programme de R&D. Au cours d'un accident de fusion d'un coeur de réacteur, les matériaux fondus peuvent interagir avec le liquide de refroidissement (eau légère), aussi appelé réfrigérant. Cette interaction peut se produire à l'intérieur de la cuve ou, en cas de rupture de celle-ci, à l'extérieur. Ces deux scénarios sont couramment appelés Interaction Combustible-Réfrigérant en- et hors- cuve et se distinguent de par les conditions du réacteur lors de l'accident : pression du système, degré de sousrefroidissement de l'eau, etc. L'interaction entre le combustible fondu et le liquide de refroidissement peut évoluer vers une détonation thermique appelée «explosion de vapeur» qui peut endommager le réacteur, voire compromettre l'intégrité du confinement.

Des expériences récentes ont montré que la composition du combustible a un effet majeur sur l'apparition et le rendement d'une telle explosion. En particulier, des comportements différents ont été observés entre un matériau simulant, l'alumine, qui explose très facilement, et diverses compositions de corium prototypique (80 m. % UO_2, 20% m.% ZrO_2). Cet «effet matériau» a suscité un intérêt nouveau pour les analyses post-expériences des débris issus de l'ICR afin de déterminer les mécanismes qui interviennent au cours de ces phénomènes extrêmement rapides.

La thèse est organisée en neuf chapitres. Le chapitre 1 constitue une introduction générale et présente le contexte d'un accident grave d'un réacteur nucléaire. Quelques exemples d'accidents graves (Three Miles Island 1979, Tchernobyl 1986 et Fukushima 2011) sont brièvement abordés. Le chapitre 2 résume les aspects théoriques de l'interaction combustible-réfrigérant. Il est divisé en quatre parties correspondant aux quatre étapes généralement rencontrées lors du mécanisme d'ICR

i) Prémélange - le combustible fondu, versé dans l'eau, se fragmente en gouttelettes grossières qui s'isolent d'un film de vapeur.

ii) Déclenchement – le film de vapeur entourant les gouttes de combustible est déstabilisé, permettant ainsi la fragmentation fine du combustible.

iii) Propagation - la fragmentation du combustible se propage à l'ensemble du prémélange, augmentant ainsi la surface de contact entre le combustible fondu et l'eau. Ceci conduit à une production intense de vapeur à grande échelle.

iv) Expansion (explosion) - l'énergie thermique transférée du combustible à l'eau est transformée en travail mécanique de la vapeur.

Le chapitre 3 résume les recherches menées dans différentes installations qui utilisent des matériaux simulants non-radioactifs ou des matériaux radioactifs prototypiques. Le chapitre 4 présente les résultats de calculs thermodynamiques, dans lesquels les différentes réactions chimiques possibles entre le combustible et l'eau/la vapeur d'eau à haute température ont été modélisées. Une deuxième partie expose les résultats des calculs 1D de transfert de chaleur par rayonnement entre le matériau fondu et l'eau/la vapeur. Le chapitre 5 décrit les analyses de matériaux simulants non radioactifs effectuées sur des débris en provenance du programme de recherche expérimentale MISTEE (KTH, Suède) et des installations PREMIX, ECO (FZK, Allemagne). Les chapitres 6 à 8 décrivent les analyses de matériaux radioactifs prototypiques de débris issus du programme de recherche KROTOS (CEA, France). Le test KROTOS KS2 utilise la composition thermofusible 70 m. % UO_2 et 30 m. % ZrO_2, le test de KS4 80 m. % UO_2 et 20 m. % ZrO_2, et le dernier test KS5 utilise du combustible sous-oxydé 80,1 m. % UO_2 et 11,4 m. % ZrO_2 et 8,5 m. % Zr. Le chapitre 9 conclut le travail et présente les perspectives futures.

Mots-clés

Accident grave d'un réacteur nucléaire, Interaction combustible – refrigerant, Effet des matériaux, Calcul thermodynamique, Analyse de l'état solide

Vaclav TYRPEKL

Effet matériaux lors de l'interaction Corium-Eau: Analyse structurale des débris
d'une explosion vapeur et mécanismes de solidification

Résumé en anglais

This work has been performed under co-tutelle supervision between Charles University in Prague (Czech Republic) and Strasbourg University (France). It also profited from the background and cooperation of Institute of Inorganic Chemistry Academy of Science of the Czech Republic and French Commission for Atomic and Alternative energies (CEA Cadarache). Results of the work contribute to the OECD/NEA project Serena 2 (Program on Steam Explosion Resolution for Nuclear Applications).

Presented thesis can be classed in the scientific field of nuclear safety and material science. It is aimed on the so-called "molten nuclear Fuel – Coolant Interaction" (FCI) that belongs among the recent issues of the nuclear reactor severe accident R&D. During the nuclear reactor melt down accident the melted reactor load can interact with the coolant (light water). This interaction can be located inside the vessel or outside in the case of vessel break-up. These two scenarios are commonly called in- and ex-vessel FCI and they differ in the conditions such as initial pressure of the system, water sub-cooling etc. The Molten fuel – coolant interaction can progress into thermal detonation called "steam explosion" that can challenge the reactor or containment integrity.

Recent experiments have shown that the melt composition has a major effect on the occurrence and yield of such explosion. In particular, different behaviors have been observed between simulant material (alumina), which has important explosion efficiency, and some prototypic corium compositions (80 w. % UO2, 20% w. % ZrO2). This "material effect" has launched a new interest in the post-test analyses of FCI debris in order to estimate the processes occurring during these extremely rapid phenomena.

The thesis is organized in nine chapters. The chapter 1 gives the general introduction and context of the nuclear reactor accident. Major nuclear accidents (Three Miles Island 1979, Chernobyl 1986 and Fukushima 2011) are briefly described. The chapter 2 summarizes the theoretical aspects of the fuel – coolant interaction. It is divided in four thematic fields according to the FCI progression. In general, FCI has four stages:

i)   Premixing – hot melt is poured in water and fragmented in coarse droplets surrounded by steam film

ii)   Triggering – steam film around melt droplets is destabilized allowing fine fragmentation

iii)   Propagation – the fine fragmentation propagate through the premixture increasing the melt – water interface area, which leads to large steam production

iv)   Expansion (explosion) – Thermal energy transferred from the melt to water is changed into mechanical work of the steam.

The chapter 3 summarizes the research conducted in different experimental facilities using nonradioactive simulant or radioactive prototypic materials. The chapter 4 shows the results of thermodynamic calculations, by which the possible chemici reactions between melts and water/steam at high temperatures were modeled. Second part presents the results of 1D calculations of radiation heat transfer from FCI materials to water/steam. The chapter 5 describes the material analyses of non-radioactive simulant debris coming from MISTEE experimental research program (KTH, Sweden) and PREMIX, ECO facilities (FZK, Germany). The chapters 6 to 8 describe the material analyses of radioactive prototypic debris coming from KROTOS research program (CEA, France). The KROTOS KS2 test used melt composition 70 w. % UO2 and 30 w. % ZrO2, the KS4 test 80 w. % UO2 and 20 w. % ZrO2, the last KS5 test used suboxidized melt 80.1 w. % UO2 and 11.4 w. % ZrO2 and 8.5 w. % metallic Zr. The chapter 9 concludes the work and presents future perspectives.

Keywords

Nuclear Reactor Severe Accident, Fuel – Coolant Interaction, Material effect, Thermodynamic modeling, Solid-state characterization

Abbreviation list

A	amplitude, interface area, area
a	thermal diffusivity
ATWS	transients with failure
Bo	Bond number
BWR	boiling water reactor
c	heat capacity, speed of light
CEA	French commission for atomic and alternative energies
d	diameter
D	droplet
DTA	differential thermal analysis
DTG	differential thermal gravimetry
E	energy
EDS	energy dispersive X-ray spectrometry
EPR	European pressurized reactor
f	frequency, function
F	force, dynamic force
fcc	face-centered cubic phase
FCI	fuel - coolant interaction
FZK	Forschung Centrum Karlsruhe, Germany, now KIT
g	gravitational constant
G	Gibbs free energy
h	diameter, Planck constant
H	enthalpy
I	force impulse
IAEA	International Atomic Energy Agency
ICP	Inductively coupled plasma technique
IEA	International Energy Agency
INES	International nuclear event scale
IR	infra-red
k	wave number, Boltzmann constant
KAERI	Korean Atomic Energy Research Institute
KH	Kelvin-Helmholtz instability
KTH	Royal academy Stockholm, Sweden
L	coherent jet length
l	axis
LOCA	loss of coolant accident
LOSP	loss of off-site power
LWR	light water reactor
M	radiation intensity
m	mass
Ma	Marangoni number
MC3D	FCI computer code
MS	mass spectroscopy
n	instability growth rate, molar amount
N	particle number

NEA	Nuclear Energy Agency
NPP	nuclear power plant
OECD	Organization for economic cooperation and development
Oh	Ohnesorge number
OM	optical microscopy
P	pressure, powder, perimeter
POVR	pilot-operated relief valve
PWR	pressurized water reactor
r	radius
R&D	research and development
RBMK	Russian type of carbon moderated reactor
RT	Rayleigh-Taylor instabilities
S	entropy
SE	steam explosion
SEM	scanning electron microscopy
SGTR	steam generator tube rupture
t	time
T	temperature
tet	tetragonal phase
TG	thermogravimetry
TMI	Three mile island power plant
TMLB	transients with scram function
v	velocity
VVER	Russian eastern pressurized water reactor
w	work
We	Weber number
WPPF	Whole pattern profile method, Pawley fit
x	stoichiometry
x_R	Rayleigh number
XRD	X-ray powder diffraction

Greek letters

α	absorption cross-section
γ	surface tension
δ	difference, disturbance
ε	emissivity
η	steam explosion efficiency, viscosity, interface instability
θ	diffraction angle
λ	wavelength
μ	dynamic viscosity
ν	viscosity
ξ	reaction extent
ρ	density
σ	Stefan-Boltzmann constant

Index list

0	initial
j	jet
a	ambient
crit	critical
max	maximal
T	constant temperature
p	constant pressure

Index

List of Figures

List of Tables

Chapter 1. Introduction

1

First chapter provides the general context of presented thesis. At first, a brief description is given describing the nuclear industry position among the world's energy supplies. Following paragraphs are devoted to the safety approach of recent Nuclear Power Plants (NPPs) and general aspects of the nuclear reactor severe accident are discussed as well. Later, the attention is focused on the phenomena of the molten Fuel – Coolant Interaction (FCI) and its progression. Defining the main goals and objectives of this thesis closes the first chapter.

1.1 Nuclear energy of today

Since the late seventies of the last century the production of electricity by nuclear fuel fission has taken a stable position among the economically well-developed countries. *Figure 1.1* shows the evolution of world electricity production being statistically processed by the International Energy Agency (IEA) [1.1]
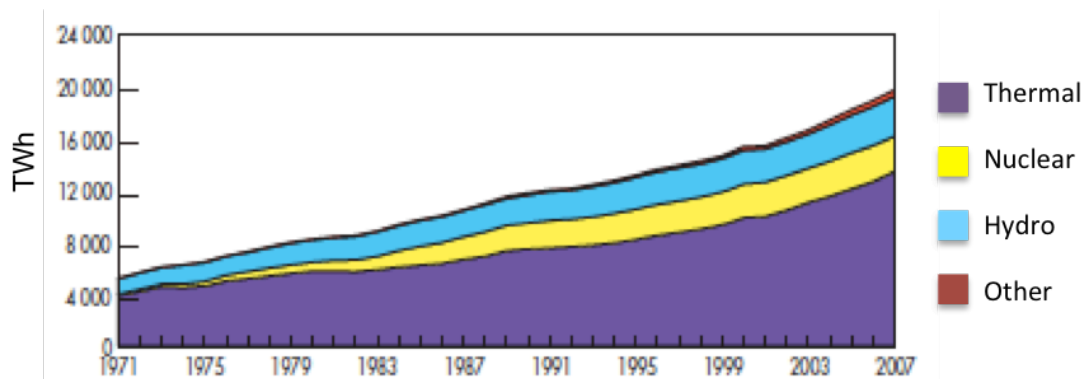
Figure 1.1 Evolution of electricity generation from 1971 to 2007 (by IEA)

For complementary clarification of *Figure 1.1*, the abbreviation "Thermal" represents the fuel-based production by coal, peat, gas and oil, while the abbreviation "Other" represents geothermal, solar, wind, combustible renewables & waste and heat. During past thirty years the nuclear branch has risen to an important worldwide electricity provider, disposing of 370 705 MW of electrical power by 437 reactor units in 2009, delivering 14% of total electricity [1.2] Moreover, 56 reactor units are worldwide in construction, mainly in the countries being recently in important economical growth. For example, twenty new reactor units are being constructed in China and five in India (data from January 2010 by IAEA [1.2])

The most frequent types of commercial nuclear reactor are Pressurized Water Reactor (PWR) and Boiling Water Reactor (BWR), commonly called Light Water Reactors (LWR). PWRs cover 61% and BWRs about 21% of all world reactors. Concerning the reactors in construction, nearly 85% are PWR type (data from January 2011 by IAEA [1.3]).

France and Czech Republic belong to countries that traditionally produce part of their electricity by nuclear power plants. In past decade the number of reactor units in operation in both countries is almost constant. Concretely, France has 59 reactor units of 63 260 MW total electrical power providing 75.2% of all produced electricity, Czech Republic disposes of 6 reactor units in total of 3678 MW(e), which delivered 25.7% of total produced electricity in 2009 [1.2].

Because of the World recently faced a disaster in the Fukushima-Daiichi nuclear power plant, the safety question of nuclear facilities has arisen, like it happened after Three Miles Island and Chernobyl accidents. However, as the technology and science have made progress that the safety standards in the nuclear field have gone forward and the general safety requirements as well. Upon the early first generation of nuclear reactors, being actually the prototypes, mainly OECD (Organization for Economic Cooperation and Development) countries initiated the commercial use of nuclear reactors in early 1970s (Generation II). Nowadays, the reactors being in construction (Generation III and III+) have advanced safety features that have ensued from the past years of research and development (R&D) in this area. For example, a new type of generation III+ reactor, called EPR, can be found among Generation III reactors family proposed by the French company Areva. This reactor of 1650MW(e) equipped with a set of passive and active safety systems is already being built in Olkiluoto (Finland), Flamanville (France) and two units in Taishan (China) [1.4].

Although these large improvement steps in safety of nuclear facilities have been made, still some important issues are under investigation and should be better understood. Large international projects have been launched for these reasons, in order to cluster research institutes, exchange knowledge and finally enhance the safety of plants. One of these, founded by the 7th European Union Framework Program, called SARNET (Severe Accident Research Network of Excellence), assemblies 19 European countries, Canada, United States of America and South Korea [1.5]. Other example is common project of OECD and NEA (Nuclear Energy Agency) named SERENA, which is devoted to the study of steam explosion phenomena during the nuclear reactor severe accident [1.6-7].

This doctoral thesis would like to contribute in both above-mentioned project, as being a part of them, and therefore shift forward the knowledge of several issues linked to the safety of nuclear facilities.

1.2 Safety approach in LWRs

The water-cooled and moderated reactors (BWRs and PWRs) across the world have similar characteristics (given in *Table 1.1.*). Therefore, considering safety questions from the viewpoint of size, power and cooling aspects the ideas could be somehow generalized [1.8].

Table 1.1 Typical characteristics of LWRs

Reactor type	Size [MWt]	System pressure [MPa]	Fluid temperature rise [K]	Power density [kW/kg U]
Eastern PWR (VVER)	1300-4300	12-16	~30	~37
Western PWR	510-4270	~16	30-35	25-40
Western BWR	180-2840	~7	*	20-30

* The inlet and outlet temperatures for BWRs are 470 and 560K, respectively.

There are three main physical barriers that restrain release of the radioactive products, especially the fission products generated by the chain reaction. *Figure 1.2* shows a scheme of typical LWR with labeled above-mentioned barriers: 1) Clad of the fuel, fabricated from the zircalloy (alloy of zirconium, niobium and tin); 2) Reactor vessel and primary circuit; 3) Leak-tight containment, fabricated from concrete and steel.
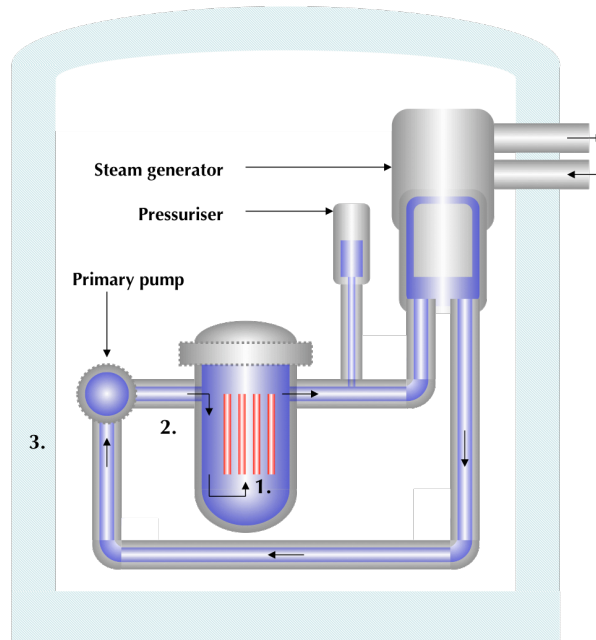
Figure 1.2 Scheme of LWR concept with three safety barriers

All the events that deviate from the routine operation of the NPPs are precisely classified and ranked in order of significance. As a world authority the International Atomic Energy Agency (IAEA), founded in 1957 by impulse of United Nations, established in 1990 the International Nuclear Event Scale (INES). This INES scale splits the events and accidents into eight levels (from zero to seven), calling the first three (1-3) as an incident and the rest (4-7) as an accident (*Figure 1.3*). This classification is done considering three important areas: i) People and the environment, ii) Radiological barriers and control, and iii) Defense-in-depth [1.9].

Figure 1.3 International Nuclear Event scale

In the past, some serious accidents occurred due to the human or technological failure:

- Chernobyl, 1986, Soviet Union – level 7
- Kysthym, 1957, Soviet Union – level 6 (explosion of high activity waste tank)
- Three Mile Island, 1979, USA – level 5
- Windscale Pile, 1957, UK – level 5
- Saint Laurent des Eaux, 1980, France – level 4
- Fukushima, 2011 – level 7

1.3 Severe Accidents in LWRs

The basic goals of safety of nuclear facilities are to prevent the individual and societal health risks, which can be induced by the release of radioactive materials such as fission products and actinides. Another point of view is to prevent plant damage and economic losses.

The case of nuclear reactor melt down accident is at its initiation connected with the loss of sufficient cooling. In the case of LWR the coolant is light water, which also plays a role of neutron moderator. Therefore, if the water is boiled out from the reactor core, the system has a negative answer by decreasing the power and the chain reaction is shut down. Unfortunately, the system temperature, even after termination of the chain reaction, rises up because of the decay heat. There is a threshold temperature about 1200°C, when the exothermic zircalloy oxidation by water vapor causes the clad and later the fuel melting. Consequently, in absence of any cooling, a complex liquid mixture partially formed of nuclear fuel, so called corium, can appear in the reactor core challenging the integrity of the vessel [1.8, 1.10].

The very first study on the plant safety WASH-740 [1.11] came out in the 1950s in USA. This early study estimated the consequences of worst plant accident with high conservativeness. In 1975 the U.S. Nuclear Regulatory Commission released study WASH-1400 [1.12], which deeply elaborated the probabilities, scenarios, release of fission product and land contamination and principal consequences of the melt down accident. In March 1979 a core melt down accident occurred in the Three Mile Island (TMI) nuclear plant near Harrisburg in Pennsylvania, USA. Since that time every other safety study was affected TMI unit-2 accident.

Currently, the safety of NPPs is widely developed and classifies the events into groups according to reactor technology. Here are some examples of possible events for LWRs [1.6]:

- Loss of Off-Site Power (LOSP) or station blackout
- Transients with scram function (TMLB)
- Transients with failure of scram function (ATWS)
- Small break loss of coolant accidents (SB-LOCA)
- Steam generator tube rupture (SGTR)
- Steam generator header cover leakage (only VVER)
- Interfacing loss of coolant accidents or V-Sequence
- Intermediate break loss of coolant accidents
- Large break loss of coolant accidents (LB-LOCA)

1.3.1   Three Mile Island unit-2 accident

For the first time the nuclear reactor core melt down accident occurred in the second unit of the Three Mile Island NPP near Harrisburg in Pennsylvania USA on 28th March 1979.

Loss of feed water to the steam generator initiated primarily the accident, which consequently leaded into the increase of the reactor vessel pressure. In order to decrease the pressure the pilot-operated relief valve (POVR) was opened. After sufficient pressure decrease the valve should be closed, but it failed. The position detector of POVR failed as well and the operating personal believed that POVR was successfully closed. This leaded into a large steam generation in the vessel and temperature increase. Further, the emergency core cooling system injection was no sufficient and finally about 50% of reactor core was melted. Fortunately, the entire melted inventory remained in the vessel and only about ~0.01% of the fission products were released to the environment [1.6].

Several years after, the EG&G Idaho TMI-2 Research Program was started by the U.S. Department of Energy. This research program provided a large and deep study of the TMI-2 reactor core melt down progression and high temperature interaction of core inventory. A big part of this research was summarized in a special edition of Nuclear Technology Journal [1.13].

This accident had a serious impact on the public opinions that were created mostly through media. The investment in nuclear energy was also badly affected. On the contrary, large interest in the nuclear safety research had been formed [1.14].

During this accident, about 62 tons of melted material were formed and about one third was relocated to the lower head of the reactor vessel. A cavity about 9.3 m^3 developed at the top part of the core. Bellow this cavity about 37 tons of melted material covered by a uniform crust were located. Central part of the core contained mainly (U,Zr)O$_2$ with embedded metallic inclusions (Ag, Fe, Ni, In, Sn, Cd, Cr). The top part of the crust (1-3 cm thick) contained Ag, Fe, Ni and In alloy. In contrary, the lower part of the crust (10 cm thick) contained above all Zr, Ag and Fe. About 20 tons of relocated material showed wide distribution of debris diameter, from few to tens of centimeters. The debris bed in the lower head was about 1m high and went through rapid quenching. Global view of the TMI-2 end state is given in the *Figure 1.4* [1.15-17].

Upper grid damage
Cavity
Coating of previously molten material on bypass region interior surfaces
Loose core debris
Crust
Previously molten material
Lower plenum debris
Ablated incore instrument guide
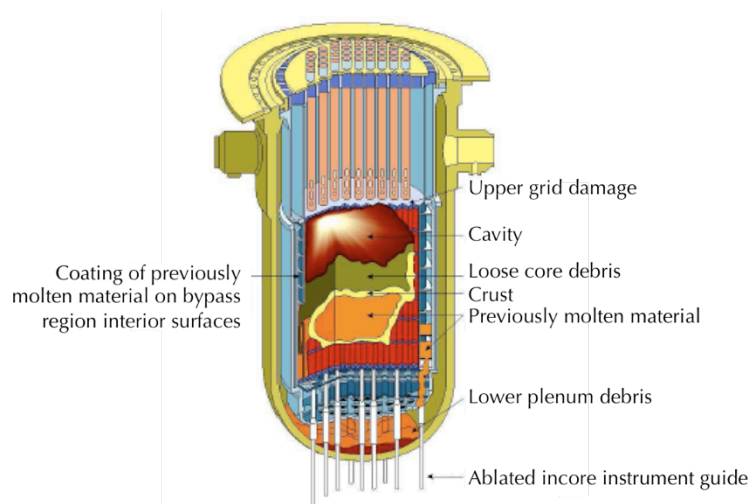
Figure 1.4 TMI unit 2, end state after the accident [1.15]

- The whole accident projected in time line is summarized in several following bullets:
- 0-100 min.: Loss of coolant, temperature increase, emergency cooling system injection
- 100-174 min.: Large steam generation, exothermic zircaloy oxidation, first melting (NiZr eutectic, AgInCd alloy), temperature rise over 1500 K
- 174-180 min.: Continuous melting (zircalloy oxidation could give temperature rise over 2100 K), hydrogen generation
- 180-200 min.: Upper part total dry out, melt pool generation, average temperature about 2700 K
- 200-224 min.: Upper debris quenching after coolant injection
- 224-226 min.: Crust failure and corium relocation (whole movement in one minute)
- 226 min.-15.5 h.: Continuous quenching and cooling

Another interesting point of view is to see the evolution of the materials evolution as a function of the temperature in the reactor core (*Figure 1.5*)

Temperature [K]	
3120	UO_2 melting
2960	ZrO_2 melting
2900	UO_{2+x} melting
2810	$(U,Zr)O_2$ melting
2695	$(U,Zr)O_2/Fe_3O_4$ ceramic mixture melting
2670	α-$Zr(O)$-UO_2 and U-UO_2 monotectic formation
2245	α-$Zr(O)$ eutectic formation
2170	α-$Zr(O)$-UO_2 eutectic formation
2130	Zircalloy (4) melting
1720	Stainless steel melting
1650	Inconel steel (*Ni* rich alloy) melting
1500	Inconel steel and Zircalloy liquefaction
1400	Liquid uranium formation (from Zr/UO_2 redox. reaction)
1200	*Zr-Fe* and *Ni-Fe* eutectic formation
1073	*AgInCd* alloy melting

Figure 1.5 Behavior of materials during the temperature rise up in the TMI-2 reactor core

Very important event occurred 224 minutes after the accident initiation. Large amount of the melt relocated rapidly into the lower plenum, probably due to the failure of upper crust. There are two explanations, why the crust rupture occurred: i) The upper crust did not survived the pressure of above debris, ii) At 220th minute a rapid depressurization took place (down to 0.5 MPa) and this could increase the inner melt pressure. In the lower plenum the melt came in contact with water and was fragmented into small pieces. This event called out a number of questions about the possible

pressure loads during the melt quenching in the water ending into a Fuel – Coolant Interaction (FCI) research area.

1.3.2   Chernobyl unit 4 accident

The World most severe accident happened on 28th April 1984 at Chernobyl NPP unit-4, located in Ukraine (former Soviet Union).

At first, it must be stressed that it exists some fundamental technological differences between RBMK (Chernobyl's) and the other LWR. The RMBK reactor was built solely in the former Soviet Union, it has a channel type structure, low enriched uranium oxide fuel, graphite as a moderator and light water as a coolant. Typically, the physical size is larger than LWRs, because of the large graphite blocks (long slowing length for neutrons). The Chernobyl containment is depicted in the *Figure 1.6* [1.18].
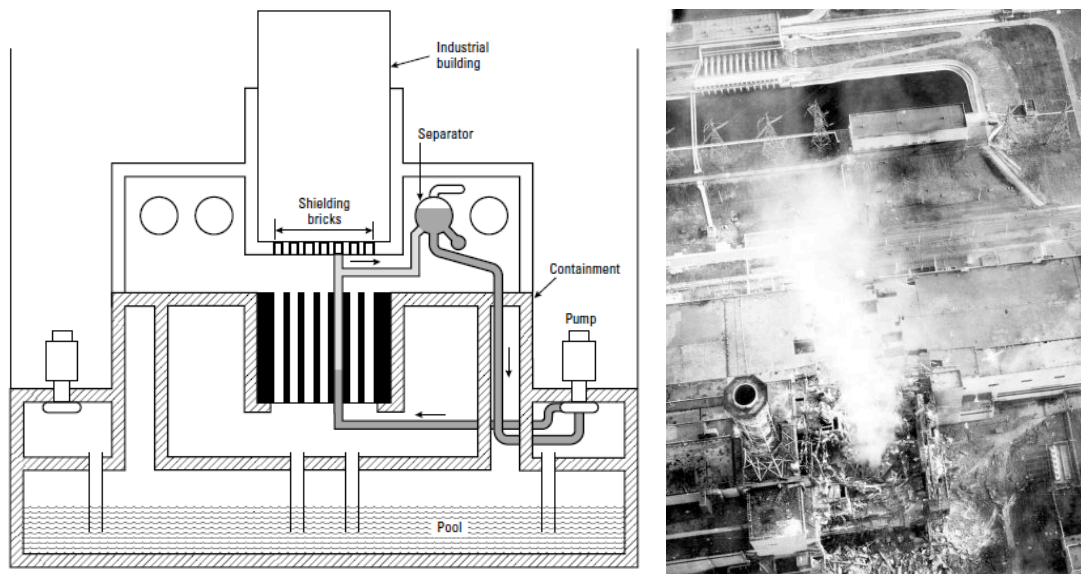
Figure 1.6 RBMK containment (left) and photo of the reactor building from 3rd May 1986 (right)

In contrary to the other LWR, the RBMK reactor has a positive power answer to LOCA due to the graphite moderation. During the accident, several operation principles were violated, for example: there should always be a certain number of control rods (30 for RBMK-1000) in the reactor core and operation of power levels below 20% of full power should be avoided.

The accident was unfortunately a consequence of a test of electrical spinning turbine. The test began on the 25th April with a reduction of the reactor power and all steam was switched to one spinning turbine as planed. The reactor stayed in this state for next 9 hours. At time of the test initiation the power felt down to 1%, this sudden shut down caused the fuel poisoning with xenon (neutron catcher). The operator tried to gain more power, necessary for the test performance. Therefore, all except 6-8 control rods were out from the rector core, breaking the operation guidelines. Moreover, the reactor running was switched to manual and a number of the emergency shutdown signals were disabled. As one of the turbines was disconnected, the water moving more slowly began to boil. After that the power started to rise up rapidly, within four seconds the reactor reached about 10000% of full power, while to shut down the reactor by rods would take six seconds [1.8]. These conditions leaded to a

steam and hydrogen generation, the pressure exceed the limit of the pressure tubes. Most probably, the hydrogen combustion and steam explosion caused ejection of the core from the shaft and lift of the upper cover. Significant release of fission products continued until 6th May due to the graphite burning, see *Figure 1.6* on the left [1.19-20].

The presence of steam explosion phenomena during the Chernobyl accident is an important impulse for study the fuel – coolant phenomena and its possible escalation in the steam explosion.

1.3.3   Fukushima Daiichi Accident

A serious nuclear accident happened in Fukushima province on March 11st, 2011 after a magnitude 9.0 earthquake together with tsunami of 14-15 meters height.

The Fukushima-Daiichi NPP had six BWR units. The units 4-6 were already shut down due to maintenance, however, units 1-3 fully operating were shut down due to the loss of off-site power. The flooding after tsunami disabled five of six emergency diesel generators and some other emergency equipment. Due to the impossibility to cool down the core reactor of unit 1, 2 and 3, the severe accidents have progressed differently according to various scenarios in the following days. Quickly restarted diesel generator cooled units 5 and 6, further, turbine-driven pumps powered by the steam from reactors initially cooled units 2 and 3. The unit 1 was at the beginning cooled by an isolation condenser. However, as the power generated by residual steam decreased, the cooling systems terminated operation. As the analyses show, the water was boiled off quickly in the unit 1, zircalloy has been oxidized by steam and has produced important amount of hydrogen, thereafter the temperature increased enough for the core to melt down. Analyses show the melt relocation to the lower head on March 12 and after a small vessel breakup. Other scenarios occurred for unit 2 and 3. Still today, it is not possible to establish the right scenarios due to the lack of available data from Fukushima Daiichi NPP.

Damages were caused by hydrogen detonation and deflagration phenomena. The hydrogen explosion occurred on March 12 at unit 1, March 14 at unit 3 and March15 unit 2, reactor buildings and spent fuel pools experienced serious impairment. Consequently, the water-cooling helicopters and other specialized fire fighting equipment like concrete pumping trucks minimized further damage and accident escalation [1.21-22]. The overall view of the Fukushima Daiichi NPP after the accident is given in the *Figure 1.7*.

It is to early give certain answer about the accident progression, on the other hand, it can be conclude that the fission product release was about 16% of the Chernobyl accident and no person directly died due to this nuclear accident. As of June 15 2011, eight workers have received a dose over 250 mSv during the accident, which was the highest irradiation exposition [1.21].

Concerning the possible phenomena, which occurred during the severe accidents progression, Tanabe [1.22] reported analyses of core melt and re-melt in Fukushima Daiichi power plant. The measurements during the accident of unit-3 showed a significant rise-up in pressure (~12 MPa) on 21 March at 01:00 a.m. The possible explanation of such behavior can be a large steam generation due to the interaction of molten core with water and citing the author: "***A hypothesis of steam explosion cannot be excluded***".
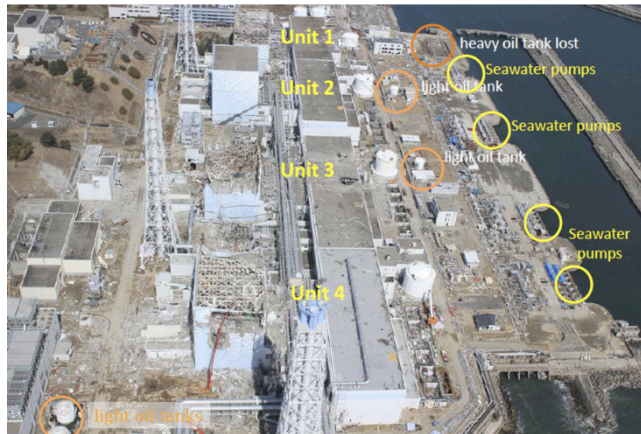
Figure 1.7 Fukushima Daiichi NPP after the accident [1.23]

1.4 Molten fuel – coolant interaction (FCI)

As it has been shown in the previous paragraphs, interaction of the molten material, i.e. corium, and the water coolant, presents important issue during a severe accident. The interaction between a hot fluid and a cool one also exists in other fields like volcanology or steel industry.

In the case of nuclear reactor severe accident, three FCI configurations are taken into account (*Figure 1.8* on the right). The first possible FCI could occur inside the vessel during relocation of the melt pool to the lower head. Another configuration considers the vessel break through and the melt jet ejection into the reactor cavity filled with sub-cooled water. The last configuration presents the cooling of assembled debris bed the bottom of the reactor cavity. This last configuration is said to be of small importance because of small amount of melt available for the mixing.

According to Board et al. [1.24] the fuel – coolant interaction is divided into four main stages (*Figure 1.8* on the left)

- **Premixing** – After the jet penetration in coolant the melt is fragmented by hydrodynamic forces in coarse droplets, which are covered by a steam film that limits the heat transfer from melt to coolant.
- **Triggering** – The protective steam film could be destabilized by a local pressure deviation, for example when the melt reaches the test section wall or the bottom surface. The triggering event can be internal or external by the system itself or by outer source. Disappearing of the vapor film allows a close contact of the coolant and the melt. The melt is broken into fine droplets by thermal fragmentation.
- **Propagation** – Thermal fragmentation process escalates through the premixed volume. The propagation wave could reach supersonic velocities.
- **Expansion (Explosion)** – The thermal energy of the melt is finally transferred to the work of steam in a short time scale (few microseconds) generating consequently high-pressure loads.

Not all the FCI events should end by steam explosion, the progression paths are following:

Premixing > Internal trigger > Propagation > Explosion
Premixing > External Trigger > Propagation > Explosion
Premixing > Quenching
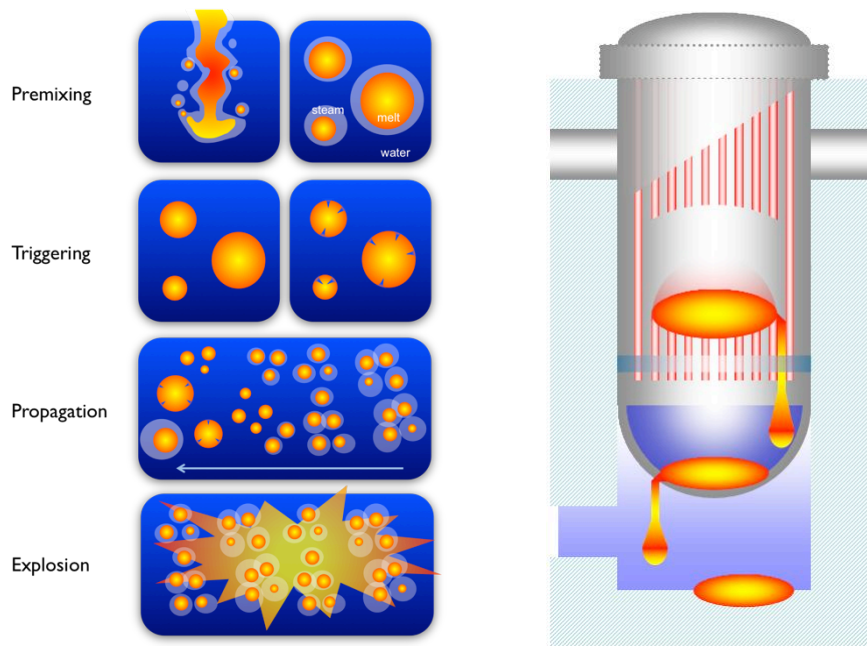
Figure 1.8 Possible FCI configurations during nuclear reactor severe accident (right) and four stages of FCI progression (left)

The authorities in the severe accident research and development assign serious considerations to the topic of fuel – coolant interaction. According to B. R. Sehgal [1.25] the FCI and steam explosion phenomena are of a great importance in the case of severe accident and its termination, however, still lack of deeper knowledge. The European network for the reduction of uncertainties in severe accident safety issues (EURSAFE) listed FCI as an item that needs research to give better prediction mainly in the steam explosion energetics [1.26].

1.5 Objectives and outlines of the thesis

Since the early experiments that had showed a difference in the behavior of chemically different melts during FCI, an important issue concerns the main effects that have the melt composition on the steam explosion energetics (for example KROTOS experiments with molten alumina and UO_2-ZrO_2 mixture [1.27]).

Many materials have been used to simulate corium during the FCI experiments; for example metallic tin, iron, Wood's metal, alumina, zirconium dioxide and CaO-WO_3 mixture as the non-radioactive and UO_2-ZrO_2 solutions as the prototypic corium. Lots of theoretical efforts have been done to answer the questions that have arisen form the experimental results. Especially a difference of behavior in the triggerability and energetics of the steam explosion between simulant materials and prototypical corium has been observed. Up to now, nobody has given any reliable mechanism to explain these differences. It has just been pointed that there was "a material effect" in steam explosion.

For example, *Figure 1.9* shows the approach of Dinh et al. [1.28] explaining the tendencies of melt properties influence on steam explosion occurrence during FCI.

The main goal of presented thesis is to better understand the so-called "material effect" in the fuel – coolant interaction and to propose possible mechanisms to explain

the differences of behavior between the nature of material: simulant or prototypical materials, eutectic or non-eutectic materials. Recent FCI experiments performed in KROTOS facility in the frame of OECD/Serena 2 program allow proposing a new "material effect" approach.
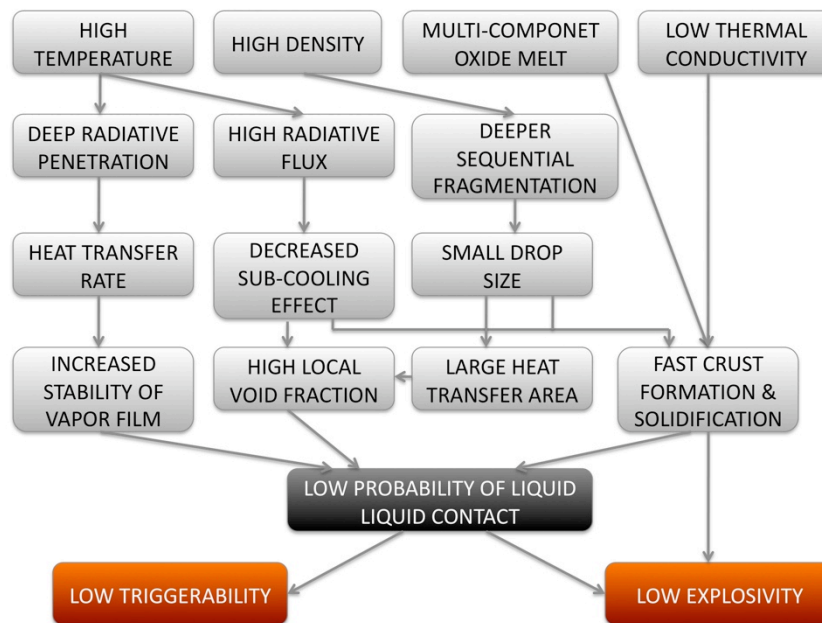
Figure 1.9 The role of melts properties in FCI according to Dinh et al. [1.28]

The thesis is divided into 9 chapters:

- *Chapter 1* is devoted to the general work context and introduction to the nuclear reactor severe accident
- *Chapter 2* presents the state of the art of the fuel – coolant interaction phenomena. It covers the experimental findings about the four FCI stages and recent approach in modeling.
- *Chapter 3* presents the experimental research programs ECO & PREMIX (FZK, Karlsruhe, Germany), MISTEE (KTH Stockholm, Sweden) and KROTOS (CEA Cadarache, France) and gives the first analyses of the material effect in FCI
- *Chapter 4* Contains the modeling of thermodynamically possible chemical reactions in the system melt – water up to 3000 K. Second part of this chapter is devoted to the study physical properties of melts affecting the FCI progression. A set of calculation was developed to quantify the effect of spectral properties on the radiation heat transfer efficiency.
- *Chapter 5* shows the findings obtained during the characterization of non-radioactive simulants
- *Chapter 6* to *8* gives the description and analyses of three KROTOS tests using radioactive prototypic corium materials
- *Chapter 9* concludes the thesis.

1.6 References

1.1   International Energy Agency, Key World Statistics 2009, OECD/IEA 2009

1.2   International Atomic Energy Agency, Nuclear Technology Review 2010, Vienna 2010

1.3   International Atomic Energy Agency, Reference Data Series 2, Nuclear Power Reactors in the World, 2011 Edition, IAEA-RDS-2/31, Vienna 2011

1.4   www.areva.com

1.5   www.sra-net.eu, J. P. Van Dorsselaere et al.: 4th European Review Meeting on Severe Accident Research (ERMSAR-2010), Italy, 2010

1.6   P. Piluso, S. W. Wong: OECD SERENA: A Fuel Coolant Interaction Program (FCI) devoted to reactor case, ISAMM-2009, Villigen, Switzerland, 2009

1.7   http://www.oecd-nea.org/jointproj/serena.html

1.8   B. R. Sehgal, P.Piluso: SARNET Lectures Notes on Nuclear Reactor Severe Accident Phenomenology, CEA Report CEA-R-6194, 2008

1.9   www.iaea.org

1.10   B. R. Sehgal: Nuclear Engineering and Technology 38(8) (2006) 679-732

1.11   U.S. Atomic Energy Commission, Theoretical Possibilities and Consequences of Major Accident in Large Nuclear Power Plants, USAEC Report Wash-740, 1957

1.12   U.S. Nuclear Regulatory Commission, Reactor Safety Study. An assessment of Accident Risks in U.S. Commercial Nuclear Power Plants, USAEC Report, WASH-1400, 1975

1.13   Journal of American Nuclear Technology, Nuclear Technology 87 (1989)

1.14   J. F. Aheame: Nuclear Technology 87 (1989) 23-26

1.15   Research and development with regard to severe accidents in pressurised water reactors: Summary and outlook, Report IRSN-2007/83, Report CEA-2007/351, 2007

1.16   J. M. Broughton et al.: Nuclear Technology 87 (1989) 34-53

1.17   Ch. L. Olsen et al.: Nuclear Technology 87,1989, 57-94

1.18   V. G. Snell and J. Q. Howieson: Chernobyl – A Canadian Perspective, AECL, 1991

1.19   E. I. Grishanin: Physics of Atomic Nuclei 73(14), 2010, 2296-2300

1.20   R. Wakeford: Journal of Radiological Protection 31 (2011) 1-7

1.21   Nuclear Energy Agency, NEA News No. 29.1, 2011

1.22   F. Tanabe: journal of Nuclear Science and Technology 49(1) (2012) 18-36

1.23   Y. Kishimoto: 11/03 East Japan Earthquake and Fukushima Daiichi NPPs, SAGNE IV 3 Meeting, IAEA, Vienna, Austria, April 2011

1.24   S. J. Board, R. E. Hall: Proc. Comm. Saf. Nucl. Install. Sodium-Fuel Interact, Fast Reactor, Tokyo, 1975, 249-293

1.25   B. R. Sehgal: Nuclear Engineering and Design 210 (2001) 79-94

1.26   D. Magallon et al.: Nuclear Engineering and Design 235 (2005) 309-346

1.27   I. Huhtiniemi et al.: Nuclear Engineering and Design 189 (1999) 379 – 389

1.28   T. N. Dinh et al.: An Assessment of Steam Explosion Potential in Molten-Fuel-Coolant Interaction Experiments", Proceedings International Conference on Nuclear Engineering, ICONE-6, San Diego, USA, May 1998

Chapter 2. FCI state of the art

2

This chapter provides the basic physical description of FCI and steam explosion phenomena based on the bibliographic research. The four stages of FCI are discussed in detail referencing on recent theoretical models and experimental observations.

2.1 Understanding of the main physical phenomena

According to Board et al. [2.1] the Fuel- Coolant Interaction is divided into four stages: i) Premixing, ii) Triggering, iii) Propagation, iv) Expansion (Explosion). As a matter of fact, the whole mixing process can escalate to a steam explosion or go just through non-violent melt quenching.

From the thermodynamic point of view the FCI can be treated like a chemical detonation [2.2-3]. The initial system of unreacted material 1 produces a system of reaction products 2 after triggering (pressure shock increase of temperature), both of certain values of density, volume and pressure.
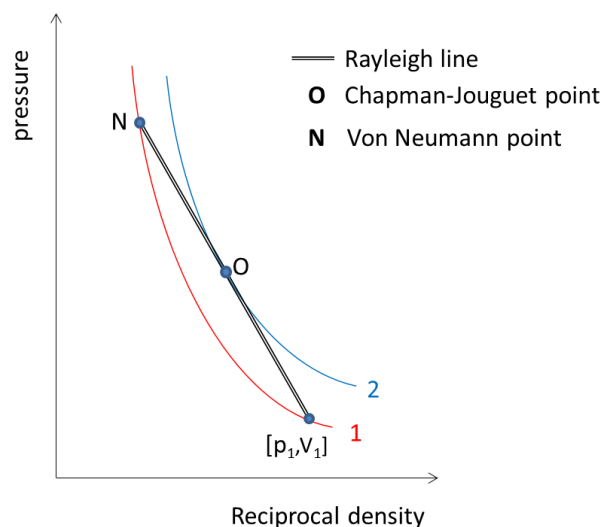
Figure 2.1 Scheme of adiabatic shock chemical detonation, simplified from ref. [2.2]

As illustrated in the *Figure 2.1* the description of steady state chemical detonation is following: shock wave goes through the unreacted material up to the von Neumann point, when the chemical reaction is started and then the pressure falls down to the Chapman-Jouguet point (end of the reaction zone). After that pressure falls based on the far-field conditions [2.2]. The analogy with FCI can be easily seen, Board et al. [2.1] described this analogy: premixed water-melt mixture as a state 1, trigger pressure shock as a shift up to the von Neumann point (destabilizing the water film) and initiating the

fine fragmentation like chemical reaction and lately the energy release and stabilization.

The basic energy evaluation of steam explosion expressed by Hicks and Menzies [2.4-5] as so-called efficiency of SE (η). It is defined as a ratio of work done by the steam Δw and initial melt energy ΔE.

$$\eta = \frac{\Delta w}{\Delta E}$$

Hicks and Menzies proposed a model of the SE efficiency dependence on the volume ratio coolant-fuel. As shown in the *Figure 2.2*, the maximum value of SE efficiency is reached when the ratio is around 2.
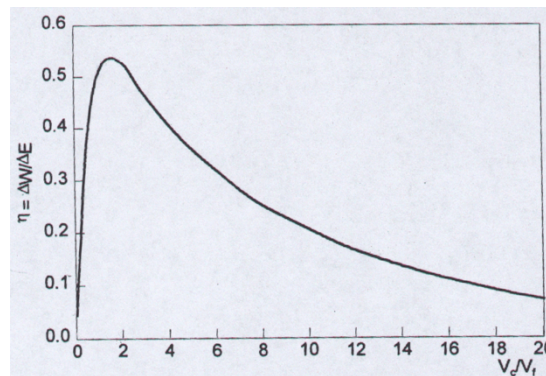
Figure 2.2 Efficiency of the corium – water interaction based on the Hicks & Menzies hypothesis [2.4]

According to this approach, the maximal value of efficiency is 60 % for the corium - water and alumina – water system and 0.3 for the tin – water system [2.5]. In reality this attitude gives values of the SE efficiency much lower, for example, the maximal efficiency of prototypic corium has been established at about 0.2 % for some tests.

Actually, a number of processes may limit energy conversion starting from a given pre-mixture, e.g.:

* Ideal mixing as assumed in thermodynamic models is never encountered in real situations
* Distribution between melt and water is not uniform in pre-mixing
* Fragmentation and heat transfer are incomplete during propagation
* Fragmentation, heat transfer and fuel-coolant equilibration take time leading to energy dissipation
* In real systems, the mechanical energy is always retrieved from and includes the reaction of the surroundings to the SE

"Efficiency" or "conversion ratio" of the explosion is a notion largely used as a measure of the explosivity of a melt-coolant system. This efficiency is considered as being the ratio of the mechanical energy output to the total thermal energy content of the corium mixed with water at the time the explosion occurs. The conversion ratio qualifies the intensity, strength of the explosion for a given melt-water system. Care must be taken with using and extrapolating this notion to other geometries or situations than those used to establish it, especially from one experimental facility to another and

more for the extrapolation to reactor case (PWR or BWR). Explosion strength depends on the real quantity of melt participating to the steam explosion, and lower efficiencies may produce higher damage if sufficient melt is involved. One key point in steam explosion understanding is to established the exact amount of melt participating to steam explosion.

In further paragraphs the FCI progression is described by the means of above-mentioned division in stages.

2.2 Premixing

2.2.1 Basic description of the jet decay

The essential parameters describing the jet decay [2.6-7] (neglecting the ambient atmosphere and concerning only the sinusoidal disturbances) are fluid density ρ, diameter of the unperturbed jet h_0, surface tension γ, dimensionless perturbation amplitude A, initial jet speed v_0, and the driving frequency f. The speed at the nozzle could be defined as

$$v_{nozzle} = v_0 + A\left(\frac{\gamma}{\rho h_0}\right)^{1/2} \sin(2\pi f t)$$
eq. 2.2

Another general parameter that is significant to the jet decay is reduced wave number x:

$$x = 2\pi h_0 / \lambda$$
eq. 2.3

where λ is the wavelength of sinusoidal disturbances, defined by the driving frequency and initial jet speed, $\lambda = v_0/f$. In the resonance, when the disturbances grow most rapidly, the reduced wave number is called Rayleigh wave number x_R. At this wave number the distance between the nozzle and the first drop is the shortest.

Several dimensionless numbers are used for general jet decay description in thermohydraulic considerations [2.7]:

Weber number (We) - is defined as ratio of the kinetic energy, of a drop loosen from the jet, to its surface energy

$$We = \rho h_0 v_0^2 / \gamma$$
eq. 2.4

where notation is the same as for *equation 2.2*.
Ohnesorge number (Oh) – measures the relative importance of the viscosity on the jet decay

$$Oh = v\sqrt{\rho / h_0 \gamma}$$
eq. 2.5

where *v* presents the kinematic viscosity ($v = \mu/\rho$, where μ is the dynamic viscosity).
Bond number (Bo) – is used when the initial jet speed is rather low and, therefore, the gravity governs principally the fragmentation

$$Bo = \rho g h_0^2 / \gamma$$
eq. 2.6

The fragmentation could be given as a ratio of length of coherent (L) jet to its initial diameter (h_0), while neglecting the role of the viscosity, according to Bürger et al. [2.8] it can be written:

$$\frac{L}{h_0} = 1.03 \ln\left(\frac{r}{\delta_0}\right)\sqrt{We}$$

where, r presents jet radius and δ_0 presents the infinitesimal disturbance at the nozzle.

Taking in to account the jet viscosity the L/h_0 ratio can be derived as:

$$\frac{L}{h_0} = \ln\left(\frac{r}{\delta_0}\right) \cdot \left(\sqrt{We} + \frac{3We}{Re}\right)$$

where **Re** is so called **Reynolds number** defined as:

$$Re = \frac{\sqrt{We}}{Oh} = \frac{v_0 h_0}{v}$$

2.2.2   Hydrodynamic description of the jet break-up

The description of the jet – ambient media interface in time and space means to solve the Navier-Stokes equation (*equation 13.* in ref. [2.7]) in the time-dependent fluid domain. This attitude combines:

Kinematic description of the jet boundary in time and space.

Using the Laplace pressure as the most dominant driving force of the jet dynamics and defining the mean curvature of the interface.

Description of the interior forces by the Navier-Stokes equation.

Establishment of the balance of the free boundary pressure and viscous forces with the capillary forces.

The full Navier-Stokes simulation is often hard to solve and, therefore, a large number of numerical methods and helpful simplifications exist [2.7].

2.2.3   Jet decay regimes in the ambient media

The jet formation starts at the nozzle, when the melt is ejected into the considered space. At first, these early conditions start to affect the jet fragmentation. An example of such behavior is the role of the nozzle design [2.9]. The aspect of nozzle length to diameter ratio in the jet fragmentation is shown in the *Figure 2.3*. Simply said, the longer nozzle the more unstable is the jet.

Jet viscosity 11 cP   Jet Ohnesorge no. 0.026
Jet velocity 20 m s⁻¹ (approx.)   Exposure 30 μsec
Nozzle diameter 2.54 mm   Nozzle aspect ratio $AR = L/d = 0, 1, 5, 10$
Jet Reynolds no. 4750
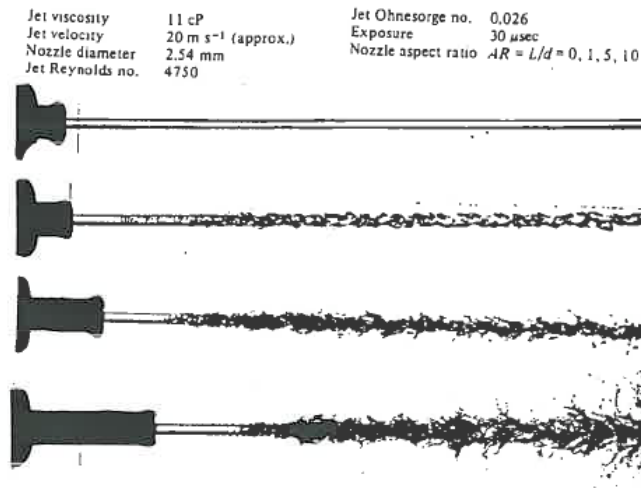
Figure 2.3 Effect of the nozzle design on the jet fragmentation

This effect is attributed to the development of parabolic distribution of the flow velocity by passing the nozzle, which is the source of jet instabilities. External forces in the ambient media have also an important effect on the fragmentation, for example electrostatic, magnetic forces or jet initial rotation [2.7]. However, they are usually neglected in the severe accident studies.

It is generally accepted that the jet fragmentation in ambient media (air, liquid) can be divided into several regimes according to the Weber (or Reynolds) number. The main mechanism of the fragmentation changes as well. As reviewed by Bürger et al. [2.8] the main jet break-up regimes are following:

- **Laminar** – Varicose type break-up, We = (0-0.4)

- **Sinuous** – Sinuous type break-up, We = (0.4-1)

- **Turbulent** – Coarse and stripping break up, We = (1-100)

- **Atomization** – Wave stripping break up, We > 100

Figure 2.4 presents the dependence of the jet break-up length on the Weber number (similar for Re) showing the decay mechanism as well [2.8]. The types of break-up regimes based on ref. [2.8,2.10] are depicted in the *Figure2.5*.

It is widely accepted that the jet fragmentation during the corium – water interaction combines so-called Taylor instabilities, deformation at the jet front and stripping under parallel flow. At the leading edge the jet can be eroded by the Taylor instabilities caused by deceleration force and the side cut off of the material as well. The stripping mechanism is considered to be the most important mechanism of the jet column fragmentation. Coarse break-up mechanism is considered for thin jet or large ones after sufficient thinning up by stripping.
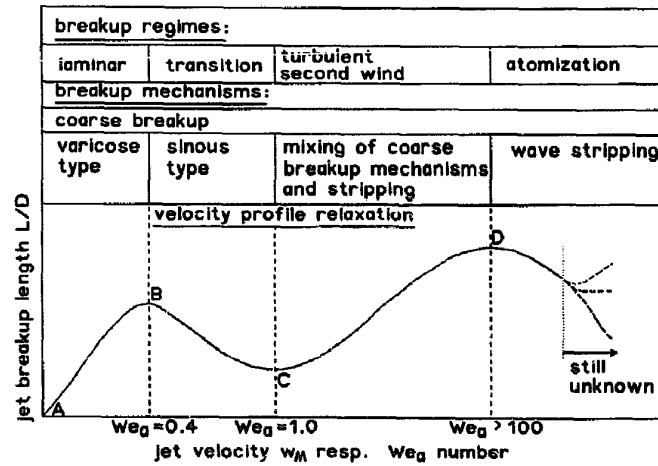
Figure 2.4 Jet break-up length dependence on the Weber number [2.8]
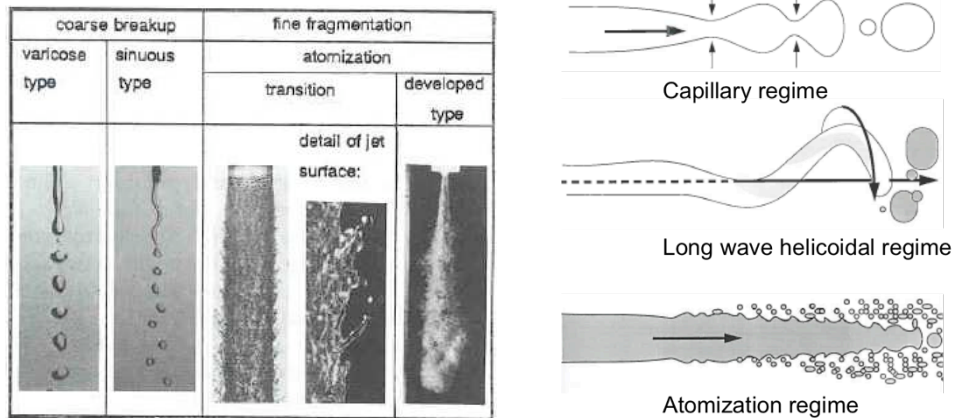
Figure 2.5 Jet decay regimes according to the Weber (Reynolds) number [2.8,2.10]

2.2.4   Hot jet decay in volatile liquid

During FCI very hot melt jet is entering a volatile sub-cooled or saturated volatile liquid that is usually water. Water boils on the jet – steam/water interface and condenses at the steam water interface. There are two main boiling regimes and transition states between them – nucleate and film boiling. Occurrence of both boiling types is well described by the Nikuyama curve [2.11-12]. It shows the dependence of the heat flux on the wall super heat (difference of water and wall temperature). Two visualizations found in the literature are given in the *Figure 2.6*.

Concerning above-mentioned facts, following dependences of the jet break-up were derived by Bürger et al. [2.13-14], for both film and nucleate boiling regimes we can write:

$$\frac{L}{h_0} \sim \frac{|v_j|}{|v_j - v_a|} \cdot \sqrt{\frac{\rho_j}{\rho_a}} \cdot \left(1 + \frac{\rho_a}{\rho_j}\right) \qquad \text{eq. 2.10}$$

Where v_j and ρ_j presents the initial velocity and density of the jet, ρ_a presents the density of the ambient matter.
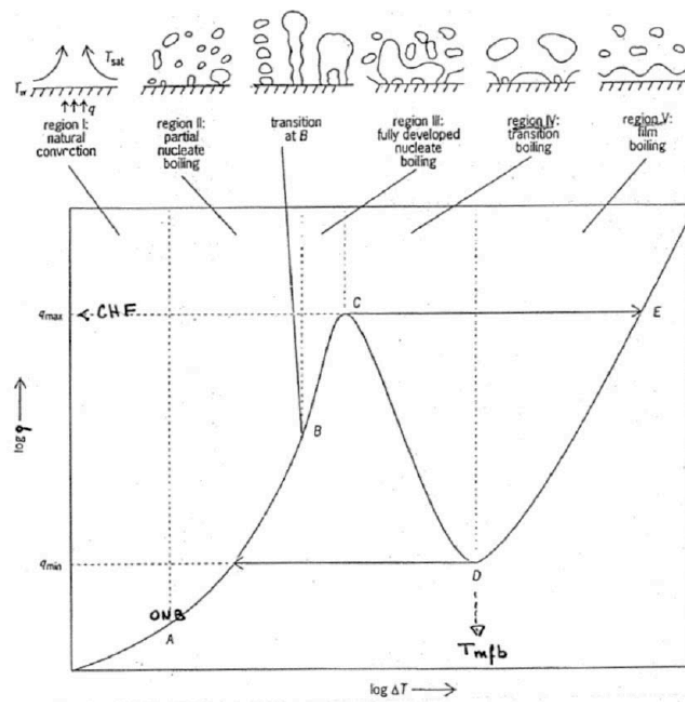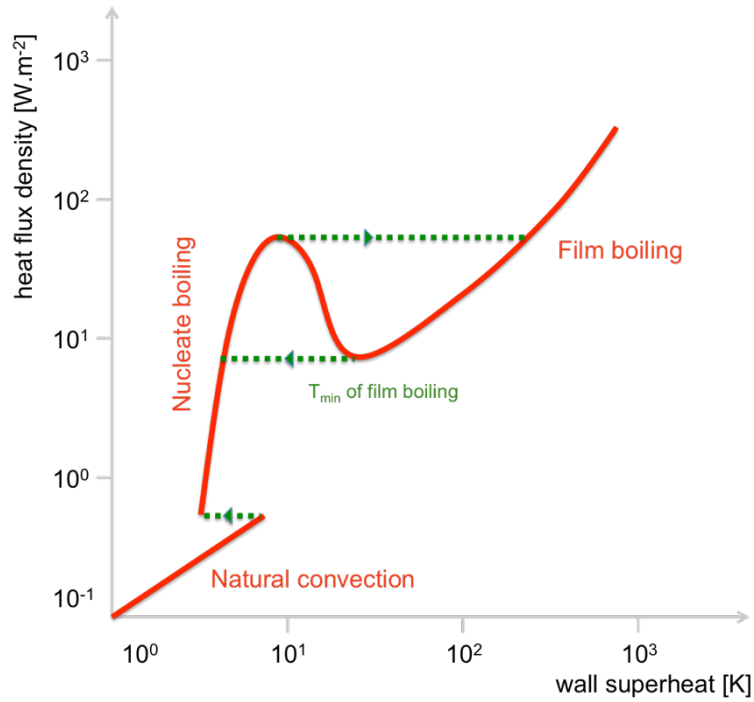
Figure 2.6 Two visualizations of the Nikuyama curve of boiling

In the case without film boiling regime the role of the jet and ambient fluid vanishes and it can be written:

$$\frac{L}{h_0} \sim \sqrt[3]{Fr \cdot \frac{\rho_j}{\rho_a}}$$

eq. 2.11

Where ρ_a presents the density of ambient fluid and **Fr** is so called **Froude number** defined as:

$$Fr = \frac{v_j^2}{gh_0}$$

eq. 2.12

2.2.5   Instabilities relevant in jet fragmentation

As reviewed by Fletcher [2.15], the Kelvin-Helmholtz, Rayleigh-Taylor and capillary (sinuous) instabilities are the most relevant in FCI. It is believed that the leading edge is fragmented due to Rayleigh-Taylor instabilities. The jet body decays mainly due to the Kelvin-Helmholtz instabilities caused by the water/vapor flow. The capillary fragmentation is driven by the surface tension and takes place at the whole jet body.

Rayleigh-Taylor instability
The presence of denser liquid above a lighter one is an unstable situation that tends to relax to stability. So-called Rayleigh-Taylor (RT) instabilities start to grow at the interface (*Figure 2.7*) with certain wavelength and growth speed.
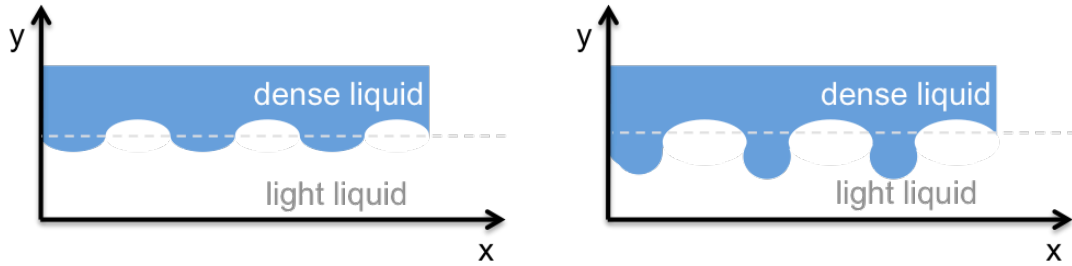
Figure 2.7 Rayleigh-Taylor instabilities, linear phase (left), non-linear phase (right)

At the beginning (linear phase) the instability growth can be described by a wave number $k = 2\pi/\lambda$. The instability interface η can be then described as

$$\eta = \eta_0 \cosh(n \cdot t) \cos kx$$

eq. 2.13

where *n* is the growth rate defined as

$$n = \sqrt{\frac{\rho_j - \rho_a}{\rho_j + \rho_a} gk - \frac{T \cdot k^3}{\rho_j + \rho_a}}$$

eq. 2.14.

The growth rate is defined, when the density of jet is higher than the density of ambient fluid (situation in the *Figure 2.7*) and if

$$k = \frac{2\pi}{\lambda} \le \sqrt{\frac{\rho_j - \rho_a}{T} g}$$

If k is equal to right side of the above equation, critical wavelength λ_{crit} can be derived. Critical wavelength presents a border value for the positive growth rate. Knowing the critical wavelength the maximal wavelength is described by *eq. 2.15*.

$$\lambda_{\max} = \sqrt{3} \cdot \lambda_{crit}$$

eq. 2.15

Certain simplifications are done in this model and other parameters can affect the instability progression. For example, increase of the viscosity shifts the maximum growth rate to higher wavelengths. The two fluids were ideally taken as infinite, so, a certain thickness should be introduced. Moreover, other body forces (not only gravity) should be introduced as well.

During the late time RT growth the non-linear phase should be considered. Bubbles and spikes of liquid mixing take place, as depicted in the *Figure 2.8*. This problem can be solved properly by Navier-Stokes equation mentioned in the paragraph 2.2.2.
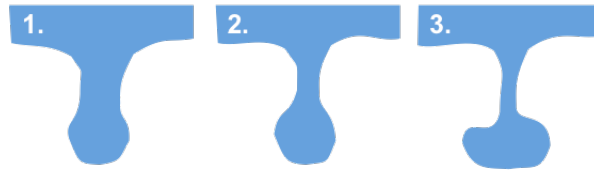
Figure 2.8 Late time growth of Rayleigh-Taylor Instability

Kelvin-Helmhotz instability

The situation is opposite considering the Rayleigh-Taylor instability, the denser fluid lays under the lighter one. The driving force of the instabilities is the tangential slip velocity at the interface. A well-known example of Kelvin-Helmholtz (KH) instability is the creation of waves on the sea by the action of the wind. The model of KH instabilities is shown in the *Figure 2.9*. During the linear phase KH instabilty is described by same means as the RT instabilities (wave number and *equation 2.13*). The difference is in the definition of the instability growth velocity and derived description.

The growth velocity is given by

$$n = \sqrt{\frac{k^2(v_j - v_a)\rho_j\rho_a}{(\rho_j + \rho_a)^2} - \frac{gk(\rho_j - \rho_a)}{\rho_j + \rho_a} - \frac{Tk^3}{\rho_j + \rho_a}}$$

eq. 2.15

where v_j presents the jet speed and v_a is the ambient fluid speed.
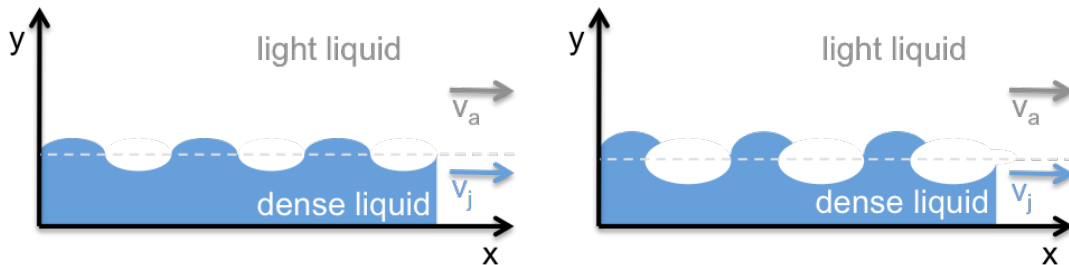
Figure 2.9 Kelvin-Helmholtz instability, linear phase (left), non-linear phase (right)

From the FCI viewpoint more interesting situation is, when the interface is parallel to the gravity vector. Thus, for vertical interface the growth speed is given by

$$n = \sqrt{\frac{\rho_a \rho_j (v_j - v_a)^2 k^2}{(\rho_a + \rho_j)^2} - \frac{k^3 T}{\rho_a + \rho_j}}$$ eq. 2.16

The instability occurs when

$$\lambda(v_j - v_a) > \frac{2\pi T(\rho_j + \rho_a)}{\rho_j \rho_a}$$

The viscosity has a stabilizing effect on the interface. The interfacial tension (surface tension) should be taken into account in real situation.

Capillary instability

This liquid column perturbation is caused by the capillary forces (surface tension). It can be axisymmetric, which is unstable, and non-axisymmetric, which is always stable. Both situations are depicted in the *Figure 2.10*.
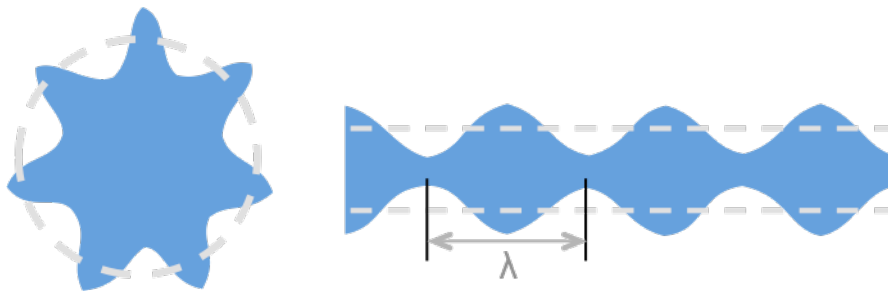
Figure 2.10 Axisymmetric (left) and non-axisymmetric instabilities of a jet column

Spherical particles are produced after the jet break up due to the minimization of the surface area per mass unit. The information about the wavelength, growth speed and particle diameter can be calculated assuming the jet as a circular cylinder (for more details see model in ref. [2.15]).

2.3 Triggering

Triggering is generally described as an event that induce the transition from premixing to propagation. Corradini et al. [2.16] reviewed more than forty possible mechanisms of triggering. Trigger can be spontaneous or external. Steam explosion can be externally triggered by an artificial pressure wave or by cold-water addition. According to Jacobs [2.17], among all proposed mechanisms only two seem important:

• Thermal fragmentation driven by evaporation of small coolant masses
• Fragmentation by purely hydrodynamic effects

The same author continues that very likely the coolant is entrapped inside the melt droplet surface and rapidly overheated.

Explosion is often triggered, when the melt contacts the bottom of the test section. Therefore, Magallon [2.18] mentioned that the reason of this behavior is the change of boiling regime due to the melt impact on the structures (transition form film boiling to transition or nucleate boiling) that can create locale pressure pulses.

Corradini [2.19] reviewed the general trends in triggering based on the experimental results of small-scale tests:

- A "dwell time" is observed between initial fuel-coolant contact and the spontaneously triggered FCI.
- There is an empirically observed region of fuel-coolant temperatures where temperatures are readily triggered.
- If a major portion of the fuel solidifies before vapor film destabilization and collapse no SE occurs, spontaneous or triggered.
- Non-condensable gas within the vapor film impedes the film collapse and precludes a spontaneous interaction.
- As the fuel mass increases for these small tests a single explosive interaction is replaced by multiple cyclic interactions.
- The triggering of the FCI on the coolant chamber base can be strongly affected by the base material.
- The properties of the fuel or coolant directly influence the likelihood of triggered explosion
- Metal can undergo oxidation reaction by water coolant and this can increase the SE efficiency by adding more thermal energy to the melt, if the chemical reaction is highly exothermic.

2.3.1 Triggering suppression

At first one should consider at which conditions the spontaneous internal trigger could take place during FCI. A region of spontaneous triggering, which depends on the coolant temperature and melt overheating, was observed in experiment using tin melt drops [II.20]. *Figure 2.11* proves the tendency that at low coolant sub-cooling and high melt temperature the spontaneous SE triggering is suppressed. By analyzing the single drop experiments using iron oxide it was found that large increase of ambient pressure decrease the ability of steam film to be destabilized [2.21-22]. The region of SE occurrence in experiments using different trigger and test section pressure is shown in the *Figure 2.12*.

Triggering can be suppressed also by painting or filling the chamber base by material with low thermal conductivity like lime or gypsum [2.23]. This fact supports the theory of steam film destabilization by melt impact on the facility base structures.

The coolant viscosity plays other important role. By increasing the water viscosity using cellulose or other chemical the SE occurrence was suppressed. It is believed that the high viscosity enables the water to create micro-jets that can attack the melt drop surface [2.23].
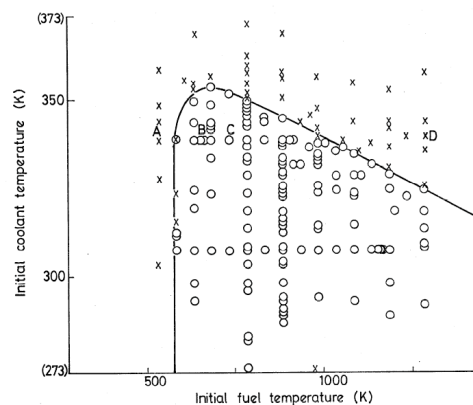
Figure 2.11 Favorable conditions for spontaneous trigger as found in tin single drop experiments [2.20.], o – spontaneous interaction, x – no interaction

2.3.2   Melt drop fragmentation

The breakup of the melt already fragmented during the premixing, so-called fine fragmentation, is the crucial step that makes FCI able to escalate to violent explosion. The heat transfer from hot melt to volatile coolant rises up by increasing the interface area through fine fragmentation. Nowadays it is believed that the secondary breakup combines the hydrodynamic and "thermal" fragmentation [2.18,2.22-23].
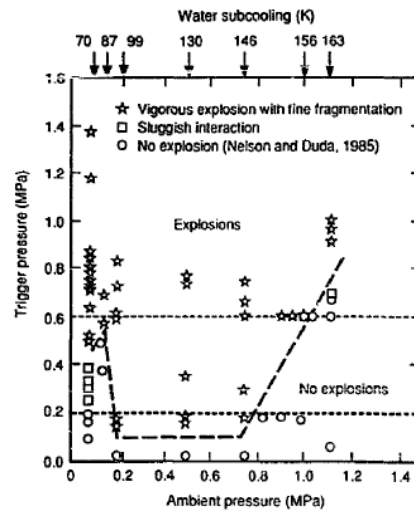
Figure 2.12 Occurrence of SE in experiments using different trigger and test section pressure [2.21]

The hydrodynamic fragmentation is usually described by means of Weber number (see paragraph 2.2.1). On the other hand, thermal fragmentation covers the effects of other than hydrodynamic (interaction morphology, interphase movements). As the number of experimental programs devoted to single droplet fragmentation increased during the past decades, proposed thermal fragmentation mechanisms have become numerous.

2.3.3   Hydrodynamic drop fragmentation

Weber number is commonly used for description of droplet fragmentation: the higher the Weber, the higher tendency for droplets to be broken. Further, there is a critical We that is the lowest value at which the droplet is fragmented into two pieces. *Figure 2.13* shows a plot of We versus number of fragments for molten metals [2.24]. Widely accepted model of fine fragmentation is based on the Weber number was developed by Pilch [2.25-26]. The mechanisms of fragmentation (*Figure2.14*) are ranked as follows:

- We = (0-12)   Vibrational breakup
- We = (12-50)   Bag breakup
- We = (50-100)   Bag and stamen breakup
- We = (100-350)   Sheet stripping
- We > 350   Wave crest stripping and catastrophic breakup

These mechanisms are valid for liquid-liquid and gas-liquid systems. On the other hand, one intensive flow takes place in these considerations, which is not the case in FCI. Similarly, recent work on drop aerobreakup [2.26] has concluded that the main breakup regimes for 10 < We < 100 are the bag and bad and stamen by Rayleigh-Taylor instabilities (multi-wave piercing). Share-induced entrainment dominates for We > 1000.
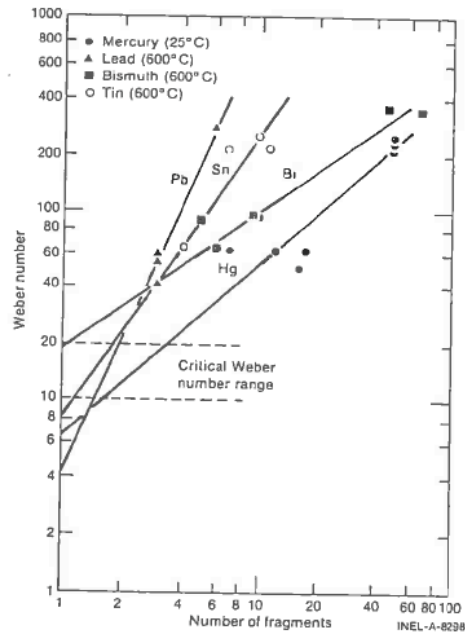
Figure 2.13 Plot of Weber number versus number of fragments for single drop experiments using liquid metals [2.24]
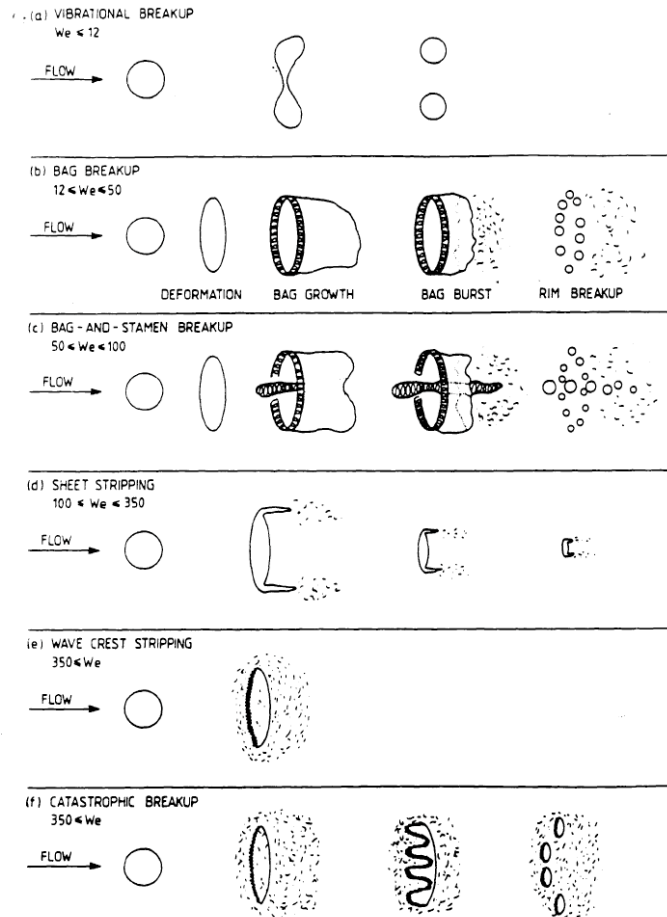
Figure 2.14 Mechanisms of Weber number droplet breakup [2.25]

2.3.4 Thermal fragmentation

As was said earlier the proposed fragmentation mechanisms are numerous and not only based on hydrodynamic forces. The effects covering the droplet breakup by water entrapment, melt micro-jets (fingering) formation, liquid water micro-jets formation or similar are generally called "thermal" fragmentation. The liquid-liquid contact is the step believed to be crucial for occurrence of this type of breakup. Two mechanisms are said to be the most suitable candidates in recent literature [2.27-29].

Ciccarelli & Frost scenario
Following the experimental observations Ciccarelli and Frost proposed a mechanism of thermal fragmentation based on the formation of metal filaments on the drop surface [2.30-32]. Melt mass ejected from the droplet surface in a form of micro-jets is rapidly fragmented (see *Figure 2.15*).

Kim & Corradini scenario
This scenario of thermal fragmentation reposes upon entrapment of liquid water micro-jets (or large amplitude instabilities) inside the melt [2.18,2.33-34]. The water that has penetrated under the melt surface evaporates rapidly breaking the droplet. The mechanism is depicted in the *Figure 2.16*.
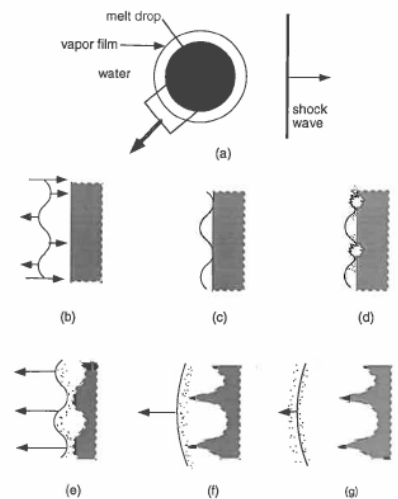
Figure 2.15 Visualization of Ciccarelli & Frost thermal fragmentation mechanism, a) overview, b) to g) time evolution [2.32]
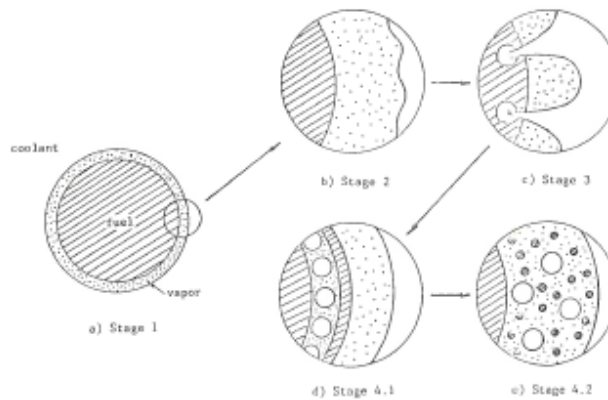
Figure 2.16 Scheme of Kim & Corradini mechanism of thermal fragmentation [2.19]

2.4 Propagation

Propagation stage is characterized by fast movement of the fine fragmentation (trigger) through the premixed volume of fuel and coolant. Jacobs [2.17] described propagation wave as a superposition of one drop triggering induced to its close neighbors. He also pointed out that the timescale of this phenomenon should be very fast, about a few milli-seconds for escalation to a large-scale explosion. In other words, drop fine fragmentation causes a local pressure increase that can trigger fragmentation of nearby droplets. These pressure peak units can accumulate forming a coherent wave that can reach even a supersonic velocity [2.18].

The melt thermal energy is transferred now to the thermal energy of the coolant. The link of FCI with thermal (chemical) detonation mentioned in the beginning of this chapter is often used for the description of propagation. Board and Hall [II.35-36] developed a theoretical model of FCI based on the thermal detonation similar as in one-dimensional jet engines (*Figure 2.17*).
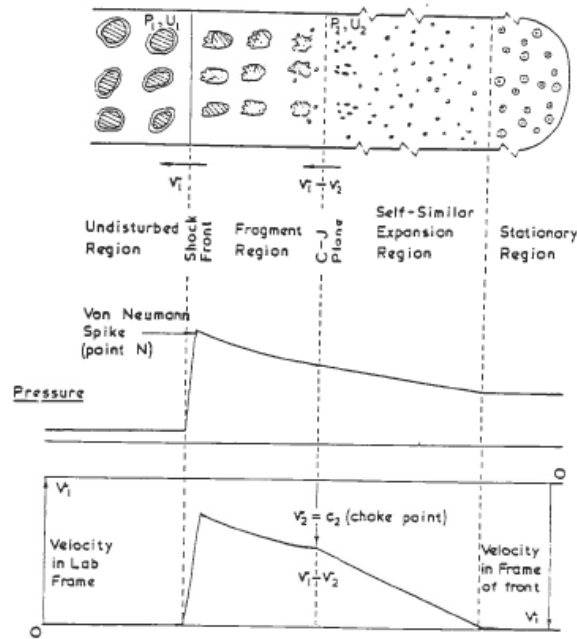
Figure 2.17 Scheme of thermal detonation model [2.16]

Experimentally, the propagation wave velocity can be measured by the time delay of the responses of the dynamic pressure transducers posted at different altitudes in the experimental facilities. Experiments in the KROTOS facility showed propagation wave velocities from 650 to 1000 $m.s^{-1}$ for molten alumina and i.e. 340 $m.s^{-1}$ or higher for molten UO_2-ZrO_2 prototypic mixture [2.37-38].

The confinement of the water pool – the test section for an experiment or the flooded cavity pit for a reactor- is an important factor affecting the propagation of the fine fragmentation wave. Frost et al [2.39] preformed experiments with horizontally arranged tin droplets triggered at one side. The explosion moved through the set of drops, while the propagation velocity depended on the test section confinement. The confined and unconfined geometry of propagation is depicted in the *Figure 2.18*.

Figure 2.18 Steam explosion wave propagation in confined (left) and unconfined (right) geometry [2.39]

The propagation of droplet explosion in both types of geometry is shown in the *Figure 2.19*. Velocity of the wave was estimated to be 50 $m.s^{-1}$ in confined narrow channel and 5-10 $m.s^{-1}$ in unconfined test section [2.39].
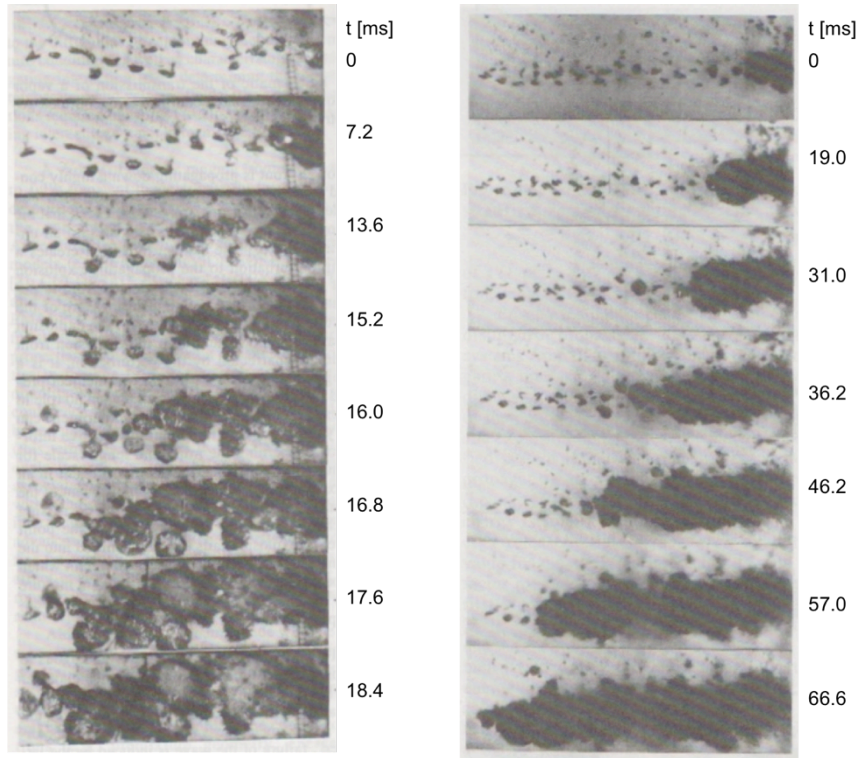
Figure 2.19 Propagation of tin drops SE in confined (left) and unconfined geometry [2.39]

Similarly as in the case of drop fragmentation many mechanisms, theories and limitations of propagation has been proposed. Two important examples are briefly mentioned. Jacobs [2.40] developed a propagation model based on explosive boiling. Fauske [2.41] expressed a spontaneous nucleation temperature criterion according to which large-scale steam explosion can occur only when the interfacial (liquid-liquid contact) temperature exceeds the spontaneous nucleation temperature of the coolant.

2.5 Expansion

Expansion stage of FCI is characterized by conversion of the coolant's thermal energy to expansion work of vapor on the ambient structures. Expansion zone is located behind the propagation wave, where the droplets fine fragmentation ran over.

The basic question of expansion stage is given by the pressure loads (force impulses, *eq. 2.18*) and mechanical properties of the tube and structures. The impulse of force *I* can be calculated by *equation II.18*, while the dynamic force is given by dynamic pressure and test tube surface area S.

$$I = \int_{t_1}^{t_2} F(t)\,dt = \int_{t_1}^{t_2} P(t) \cdot S \, dt \qquad \text{eq. 2.18}$$

Figure 2.20 shows an example of dynamic force measurement during TROI-13 experiment using prototypic UO_2-ZrO_2 mixture [II.42]. If the ambient structures can sustain the pressure loads, the mixture of melt and coolant is usually ejected in the direction of propagation wave. In the case of melt gravity fall and triggering at the bottom of the test section the mixture is ejected vertically out from the test tube. If the

structures are not mechanically immovable, a part of the energy produced by FCI is lost for rupturing and deformation.
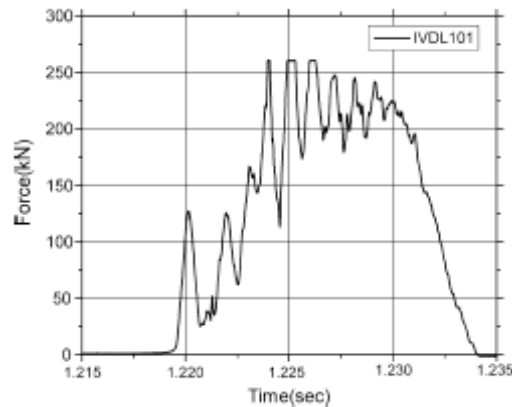
Figure 2.20 Dynamic force during the TROI-13 experiment [2.42]

For application to reactor case, the force impulse is of great importance for in-vessel and ex-vessel scenarios. Mechanical properties of the steel vessel and concrete containment differ significantly as well as the consequences on the structural integrity [2.19].

2.6 FCI and volcanology

The parallel between the fuel-coolant interaction and volcanology is known for several decades. In principle, the violent explosions during the interaction of lava and water or wet sand come through similar phenomena as FCI in the sense of nuclear reactor severe accident [2.43].

Recently, the lava interaction with seawater has been widely studied on the Hawaii islands. Lava flows coming from Kīlauea caldera are able to reach the ocean by simple spreading or by underground channel tubes [2.44-45]. Four general scenarios (types of explosion) can be observed:

- *Tephra jets* – Bench collapse opens a fresh open stream of lava that is subjected to intense wave action. Explosive ejection can be up to 40 m high and fragmented lava is very fine (most of the fragments are bellow 5 mm).
- *Lithic blasts* – Seawater can interact with newly exposed incandescent rock scarp creating an explosion that can rip up previously deposits. Fragments of ripped rock are much bigger, even one meter in diameter.
- *Lava bubble bursts* – These mild explosions can be observed if seawater break into a lava tube at or bellow the sea level. The cone crater after this type of explosion can reach up to 30 m in diameter and 10 m in deep.
- *Littoral lava fountains* – Rare type of explosion caused by abrupt fractioning of a submerged lava tube. As a result a fountains of lava and steam can be formed reaching up to 100 m in height.

Evidently, many experimental research programs have been devoted to study the mechanism of littoral hydrovolcanic explosions as well as the physical and chemical phenomena affecting their energetics. For example, Wohletz [2.46] studied the

interaction of magma and wet sand using thermite melt (Fe and Al_2O_3). Author was focused mainly on the formation of peperite (rock fragments after interaction), however, he mentioned that several percent of melt thermal energy is transferred into work, which result is questionable considering data from FCI experiments (paragraph 2.1.), but stressing again that it will depend on how the efficiency has been calculated.

Shipper et al. [2.47] performed experiments that simulate the interaction of basal melt with "dirty" coolants. "Dirty" means that the composition of the coolant has been changed in order to achieve desired properties mainly viscosity. The coolant composition consisted from pure water up to 30 w. % of bentonite clay, bentonite with pumice or water with sand. It was found that if the concentration of suspended sediment gets over 20 w. % the heat transfer from melt to coolant is significantly inhibited.

Grunewald et al. [2.48] studied the interaction of melt – distilled water and melt – NaCl solution (350 g.l^{-1}). It was observed that the interaction of melt with distilled water escalates to more violent explosions than in case of highly mineralized water.

2.6.1   Nature of volcanic sediments

The geochemical analyses of volcanic sediments are usually of high scientific level. The similarities in morphology of volcanic sediments and FCI debris can be seen. Cross-section micrograph of the Keanakāko'I ash (Kīlauea, Hawaii) is shown in the *Figure 2.21* on the left, for comparison on the right we can see the debris morphology of TROI-51 FCI experiment. Some similarities can be observed: the size of the debris is of the same order as magnitude and the presence of porosity inside the debris.
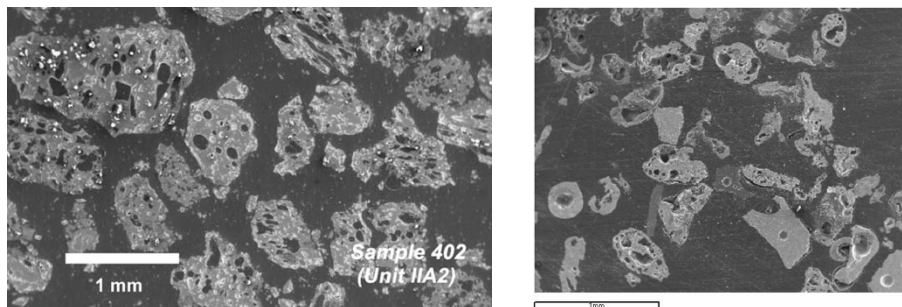
Figure 2.21 Scanning electron micrograph of the powder cross-section, volcanic ash from Kīlauea, Hawaii [2.49] (left) and debris coming from FCI experiment TROI-51 [2.50]

Analytical approach describing morphology of volcanic ash adopted by Pardo et al. [2.51] will be used in further characterization of FCI experimental debris. The list of ash morphotypes is depicted in the *Figure 2.22* together with dominant water-magma interaction.
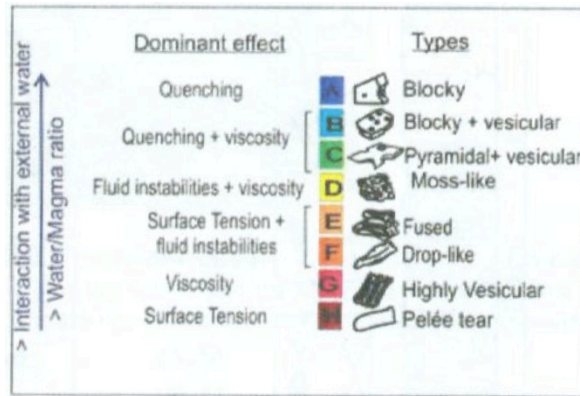
Figure 2.22 Ash morphotypes coming from water-magma interaction connected to physical conditions during its formation [2.51]

The difference of chemical composition should be carefully taken into account. Generally, magma composes of alkaline (Na, K, Ca) silicates, alumino-silicates and other additions (iron oxides, magnesium oxide). The presence of silica is going to modify the rheological properties of the melt so, analogies between FCI and vulcanology have to be taken with care. Mastin et al. [2.49] observed water traces in the volcanic ash using infrared spectroscopy. Moreover, they made a parallel among the content of water (physically or chemically absorbed in the ash), volume of the void bubbles in the melt and ash diameter, the results are shown in the *Figure 2.23*.
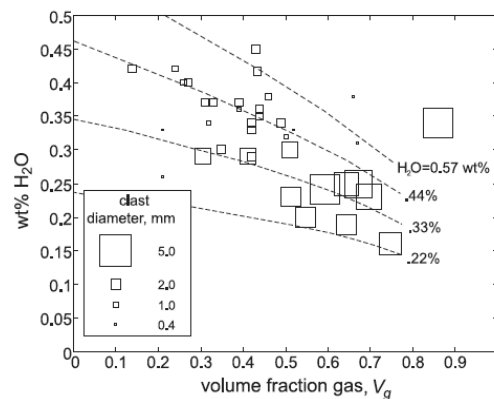
Figure 2.23 Amount of dissolved water versus gas volume fraction, squares are proportional to ash diameter [II.49]

It seems to be natural that smaller magma droplets can dissolve higher amount of water. On the contrary, the amount of water is decreasing with growing of the gas void fraction in the solidified debris. The authors explain that water leaves lava during quenching. The fingerprints of this "degasing effect" are mentioned bubbles (void) in the solidified melt. As a consequence, the magma should be able to dissolve more water in the liquid state that is the structure able to keep during solidification. This behavior was known and experimentally confirmed already in 1980s, Coutures et al. observed the "spitting" (water vapor release during solidification) phenomenon on silica and alumina melts [2.52].

2.7 References

2.1   S. J. Board, R. E. Hall: Proc. Comm. Saf. Nucl. Install. Sodium-Fuel Interact, Fast Reactor, Tokyo, 1975, 249-293

2.2   I. B. Zeldovich, A. S. Kompaneets: Theory of Detonations, London, Academic, 1960

2.3   G. Berthoud: Annual Review of Fluids Mechanics 32 (2000) 573-611

2.4   E. P. Hicks, D. C. Menzies: Proc. Conf. Saf. Fuel Core Des. Large Fast Power React. Argonne National Laboratory (1965) 7120

2.5   B. R. Sehgal, P.Piluso: SARNET Lectures Notes on Nuclear Reactor Severe Accident Phenomenology, CEA Report CEA-R-6194, 2008

2.6   D. Grishchenko et al.: KROTOS KS4 Data Report, CEA Report, No. DEN/DTN/STRI/LMA/2011/006/0, 2011

2.7   J. Eggers, E. Villermaux: Reports on Progress in Physics 71 (2008) 036601

2.8   M. Bürger et al.: Nuclear Engineering and Design 155 (1995) 215-251

2.9   M. J. McCarthy, N. A. Molloy: The Chemical Engineering Journal 7(1) (1974) 1-20

2.10   R. Meigen: Modelisation de la fragmentation d'un jet liquide a tres haute temperature dans un liquid froid volatile, Doctoral Thesis, CEA Grenoble, 1995

2.11   S. Nukiyama: Journal of Japan Society of Mechanical Engineering 37 (1934) 367-381

2.12   S. Nukiyama: International Journal of Heat and Mass Transfer 9 (1966) 1419-1433

2.13   M. Bürger et al.: Proceeding of the International Seminar on The Physics of Vapor Explosions, October 25-29, Tomakomai, Japan, 1993

2.14   E. von Berg et al.: Sixth International Topical Meeting on Reactor Thermal Hydraulics, NURETH 6, October 5-8, Grenoble, France, 1993

2.15   D. F. Fletcher: A Review of Hydrodynamic Instabilities and Their Relevance to Mixing in the Molten Fuel Coolant Interactions, United Kingdon Atomic Energy Authority, AEEW-R1758, United Kingdom, 1984

2.16   M. L. Corradini: Progrress in Nucelar Energy 22(1) (1988) 1-117

2.17   H. Jacobs: Steam Explosions During LWR Melt Down Accidents, Containment of Nuclear Reactors, Los Angeles, USA, 1989

2.18   D. Magallon: Nuclear Engineering and Technology 41(5) (2009) 603-616

2.19   M. L. Corradini: Vapor Explosions, Lecture 18A, Short Course on Modeling and Computation of Multiphase Flows, Zurich, Switzerland, 1999

2.20   T. A. Dullforce, D. J. Buchanan, R. S. Peckover: Journal of Physics D. Applied Physics 9 (1976) 1295-1303

2.21   L. S. Nelson, P. M. Duda: High Temperatures – High Pressures 14 (1982) 259-281

2.22   M. L. Corradini: Nuclear Safety 32 (1991) 337-362

2.23   A. W. Cronenberg, R. Benz: Vapor Explosion Phenomena with Respect to Nuclear Reactor Safety Assessment, NUREG/CR-245, 1978

2.24   R. O. Iivins: Interactions of Fuel, Cladding and Coolant, ANL-7399, 1967

2.25   M. Pilch, C. A. Erdman, A. B. Reynolds: Acceleration induced fragmentation of liquid drops, NUREG/CR-2247, 1981

2.26   M. Pilch, C. A. Erdman: Journal of Multiphase Flow 13(6) (1987) 741-757

II.27   S. Koshizuka et al:Nuclear Engineering and Design 189 (1999) 423–433

2.28   J. Lamome, R. Meignen: Nuclear Engineering and Design 238 (2008) 3445–3456

2.29   R. C. Hansson: An Experimental Study on the Dynamics of a Single Droplet Vapor Explosion, Doctoral Thesis, KTH, Stockholm, Sweden, 2010

2.30   G. Ciccarelli: Investigation of Vapor Explosion with Single Molten Metal Droplets in Water using Flash X-Ray, Doctoral Thesis, McGill University, Canada, 1991

2.31   G. Ciccarelli, D. L. Frost: Fragmentation Mechanisms Based on Single Drop Experiments using Fash X-ray Photography, NURETH 5, Salt Lake City, 21–24 September, USA, 1992

2.32   G. Ciccarelli, D. L. Frost: Nuclear Engineering and Design 146 (1994) 109-132

2.33   B. Kim: Heat Transfer and Fluid Flow Aspects of Small-Scale Single Droplet Fuel-Coolant Interactions, Doctoral Thesis, University of Wisconsin-Madison, 1985

2.34   B. Kim, M. L. Corradini: Nuclear Science and Engineering 98 (1988) 16-28

2.35   S. J. Board, R. W. Hall: Propagation of Thermal Explosions. 1 - Tin/Water Experiments, CEGB Report RD/B/N 2350, 1974

2.36   S. J. Board, R. W. Hall: Propagation of Thermal Explosions. 2 – Theoretical Model, CEGB Report RD/B/N 3249, 1974

2.37   H. Hohmann et al: Nuclear Engineering and Design 155 (1995) 391-403

2.38   I. Huhtiniemi, D. Magallon: Nuclear Engineering and Design 204 (2001) 391–400

2.39.   D. L. Frost et al: The Role of the Confinement in the Propagation of Vapor Explosion, Proceeding of the International Seminar on The Physics of Vapor Explosions, October 25-29, Tomakomai, Japan, 1993

2.40   H. Jacobs: Propagation of Vapor Explosions Due to Explosive Boiling, Proceeding of the International Seminar on The Physics of Vapor Explosions, October 25-29, Tomakomai, Japan, 1993

2.41   H. K. Fauske: Proceeding of the Fast Reactor Safety Meeting, April, Beverly Hills, California, USA, 1974

2.42   J.H. Song et al: Nuclear Engineering and Design 235 (2005) 2055–2069

2.43   S. A. Colgate, T. Sigurgeirsson: Nature 244 (1973) 552–555

2.44   T. N. Mattox, M. T. Mangan: Journal of Volcanology and Geothermal Research 75 (1997) 1-17

2.45   M. Edmonds, T.M. Gerlach: Earth and Planetary Science Letters 244 (2006) 83–96

2.46   K. Wohletz: Journal of Volcanology and Geothermal Research 114 (2002) 19-35

2.47   C. I. Shipper et al: Earth and Planetary Science Letters 303 (2011) 323-336

2.48   U. Grunewald et al: Journal of Volcanology and Geothermal Research 159 (2007) 126-137

2.49   L. G. Mastin et al: Journal of Volcanology and Geothermal Research 137 (2004) 15-31

2.50   J. H. Kim et al: Journal of Mechanical Science and Technology 22 (2008) 2245-2253

2.51   N. Pardo et al: Journal of Volcanology and Geothermal Research 184 (2009) 292-312

2.52   J. P. Coutures et al: Revue Internationale des Hautes Températures et des Refractaires 17 (1980) 351-361

Chapter 3. Experimental simulation of FCI - Material effect

3

In the following paragraphs the FCI experimental research in selected facilities is described and discussed. It is worth mentioning that a large set of FCI tests was launched in 1980 in the SANDIA laboratories [3.1-2]. It provides one of the first systematical studies devoted to FCI phenomena using alumina, iron, iron oxide and prototypic corium melts. More recent experimental programs have been performed recently and the analysis will be focused on these programs.

Experimental approach is divided into two main streams: i) Large scale facilities using prototypic corium material (UO_2-ZrO_2 mixtures), FARO, TROI and KROTOS facilities; ii) Large or small-scale facility using non-radioactive simulant materials (Sn, Al_2O_3-Fe, WO_3-CaO), MISTEE and PREMIX (ECO) facilities. Later the analyses of the material effect in FCI concerning the prototypic and simulant debris are given as well.

3.1 FARO facility

Scope of the FARO program launched in JRC Ispra (Italy) in early 1990s was to understand the quenching behavior of large quantities of prototypic corium melts [3.1]. The experimental setup can be found in the *Appendix A*. as well as the summary of experiments that were published in commonly accessible scientific journals.

Overall twelve experiments L06 to L33 were successfully finished and opened for data analyses. Most of them used 80 w. % UO_2 and 20 w. % ZrO_2 melt material, delivered mass varied from 18 to 177 kg, that interacted with 120 to 719 kg of water. Exception in the melt composition is L11 experiment that used 76.2 w. % UO_2, 19.2 w. % ZrO_2 and 4.6 w. % metallic Zr. Another exception was the last L33 experiment that included an external triggering. Main focus was given to several important parameters affecting the FCI in general [3.3-6]:

- *Melt mass.* The pressurization rate grows usually with the melt mass. A part of the melt (1/6 to 1/3) forms a debris cake at the bottom of the test section, which premises that a significant fraction of the melt arrives at the bottom still liquid.
- *Water depth.* The time of fragmentation at the leading edge depends on the height of the water column. Debris with smaller average size can be obtained by increasing the water depth. On the other hand, no significant effect can be seen on the pressurization before the melt contacts the bottom.
- *System pressure.* System (initial, ambient) pressure doesn't affect the pressurization. However, a rise up in pressurization rate was observed at low pressure (0.5 MPa).

- ***Melt composition.*** As observed in the experiment L11, metallic zirconium in the melt was immediately oxidized affecting the whole quenching process (fragmentation, pressurization and debris size distribution).
- ***Hydrogen production.*** Hydrogen was produced during all experiment. The highest amount was generated during L11 experiment; high amounts were obtained during tests with saturated water as well (*Figure 3.1*).
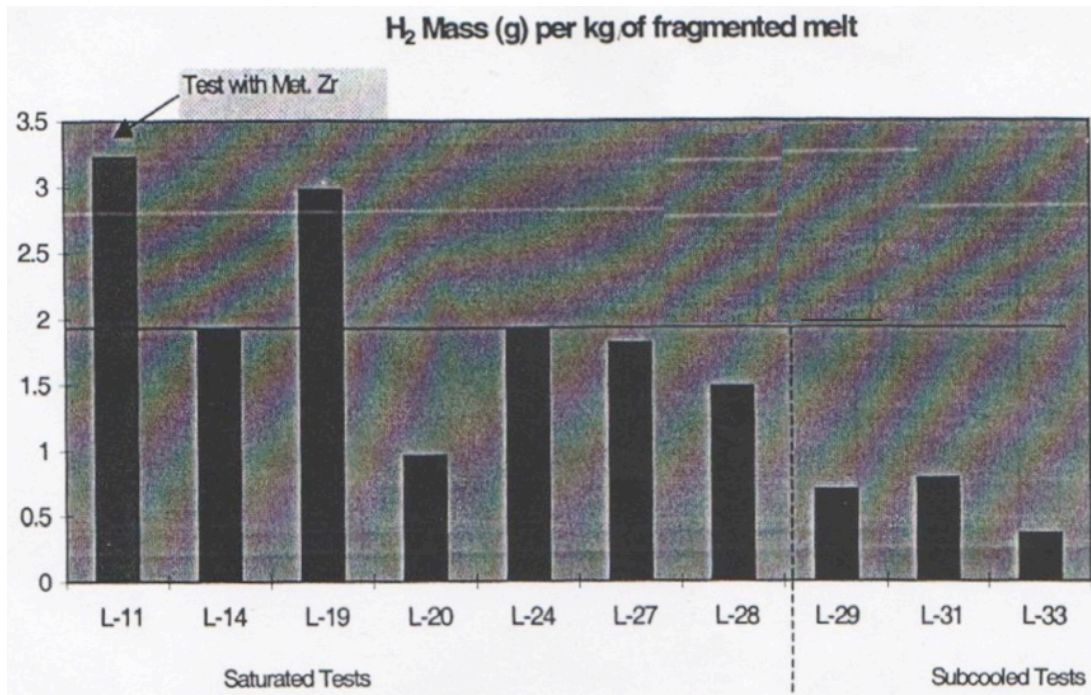
Figure 3.1 Hydrogen production in selected FARO tests [3.7]

3.1.1   Material characterization of FARO debris

In the framework of the FARO program Matzke and Rondinella [3.8] reported material characterization of L19 and L24 specimens. They selected four types of samples:

- Starting material (powder mixture, previously molten material).
- Melt crust not exposed to the water during the experiment.
- Quenched melt exposed to water and then dried in Ar atmosphere at 200°C.
- Powder from the debris catcher (under water) without any treatment.

The debris was found to be chemically homogenous. Differences appeared in the morphology of the melt that was exposed to the water and that located inside the solidified droplets.

Important contrasts were discovered during thermal treatment of four mentioned samples in the Ar/H_2 atmosphere. Debris quenched in the water lost about 0.5 % of its weight. They concluded that the released melt is probably sub-stochiometric and contains metallic uranium inclusions. Simple evaluations of hydrogen production during FCI were done as well.

First powder X-ray diffraction measurements were performed. The cubic cell parameters 5.359, 5.378 and 5.351 Å were obtained for samples no 2. 3. and 4. respectively (L19). Unfortunately, no further investigations were done in this direction.

Samples from FARO L19 and L24 experiments were also examined by oxygen potential measurements. Increase in the oxygen potential was identified between the samples coming from the furnace and those coming from the debris catcher. Authors attributed this behavior to the over and sub-stoichiometry of the powder. However, they compared oxygen potential of FARO debris to values corresponding to pure $UO_{2\pm x}$ neglecting ZrO_2.

Magallon [3.7] reported general considerations about the debris bed characteristics in the FARO program. Typically, there were two types of debris bed. One type composes of large high heap of cake covered by thin layer (~2 cm) of loose debris. The second type presents much smaller cake covered by wide layer (~15 cm) of loose debris. Author attributes the coalesced debris cake to unfragmented jet body. Therefore, the water depth during experiments with significant debris cake was smaller than the jet breakup length. This explanation is supported by a fact that experiments without debris cake have a typical "knee" in the melt front penetration history (experiments L11 and L31), *Figure 3.2*. Surprisingly, no important differences or tendencies were found by the mechanical sieving (granulometry) of collected debris.
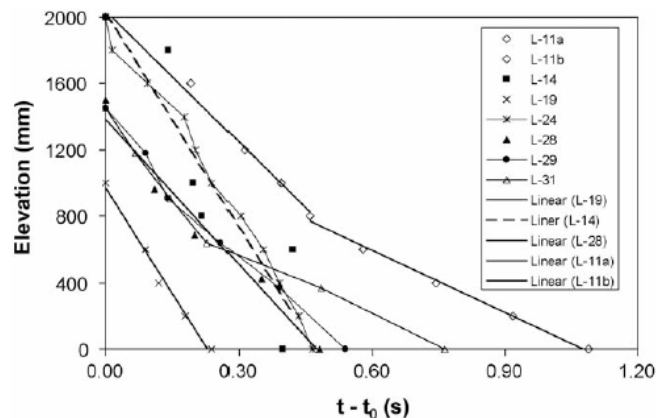
Figure 3.2 Melt front penetration history in the FARO experiments [3.9]

3.2 TROI facility

The TROI facility is located in KAERI (South Korea) and provides information about quenching and steam explosion behavior of prototypic mixtures. Test facility description and tests summary can be found in *Appendix B.*. The TROI facility is said to have a "2D" character due to the broadness of its water pool (60 cm in diameter, 60-130 cm in depth; similar to FARO, but using notably less melt masses). From its beginning the experimental research was partly devoted to the material effect in FCI. Therefore, a variety of melt materials were studied. Following paragraphs summarize findings according the melt material, which, by the way, follows the experimental chronology.

3.2.1   Experiments with ZrO_2

TROI tests marked 1 to 5 were performed using ZrO_2 (99 w. % ZrO_2 and 1 w. % metallic Zr as a starter of induction heating) [3.10]. Any external triggering was reported, however, authors noted steam spike in experiment 1 and steam explosion in experiment 4 and double steam explosion in experiment 5. Obviously, as shown in the dynamic pressure history no self-escalation event took place in all of these experiments. Obtained sharp pressure peaks (up to 2 MPa with duration about 10^{-4} s) can be caused by local droplet explosion close to the pressure transducer.

3.2.2   Experiments with UO_2-ZrO_2 mixture

The TROI team performed around 20 tests using UO_2-ZrO_2 mixture prototypic to reactor composition. They used different amounts of each component (for details see *Appednix B)*. As can be deduced from published literature [3.11-14] the different melt composition (80 w. % UO_2 and 20 w. % ZrO_2 versus 70 w. % UO_2 and 30 w. % ZrO_2) leaded to a different spontaneity of SE or different SE energetics after external triggering.

According to calculated UO_2-ZrO_2 pseudo-binary phase diagram showed in ref. [3.15] authors explained the different behavior according to eutectic (70-30) and non-eutectic (80-20) compositions. In the case of non-eutectic mixture a "mushy" layer on the droplet surface should preclude the fine fragmentation and therefore decrease the conversion ratio. Further, based on the X-ray powder diffraction and thermogravimetry measurements authors conclude that hydrogen formation is not related to oxidation of UO_2 in the melt. Additionally, internal porosity of the solidified droplets was observed, while it was found only in the case of eutectic melt composition. Authors made an assumption that the holes in the particles are a result of tension between solid crust and liquid core. For example, scanning electron micrographs of TROI 23 (78 w. % UO_2 and 22 w. % ZrO_2) and TROI 13 (70 w. % UO_2 and 30 w. % ZrO_2) are shown in the *Figure 3.3*.
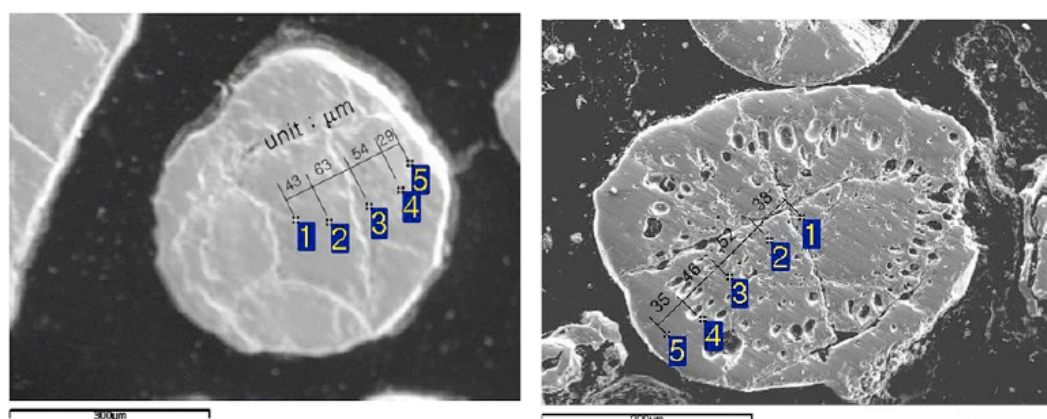
Figure 3.3 SEM crossection photos of TROI 23 (left) and TROI 13 (right) [3.14]

The UO_2-ZrO_2 mixture forms in solid state a solution $U_{1-x}Zr_xO_2$ and one liquid above the liquidus line, as can be seen in the pseudo-binary phase diagram (*Figure 3.4*) provided by Thermodata [3.16]. Two crystallographic phases exist at thermodynamic equilibrium, tetragonal (P42/nmc) for high ZrO_2 contents and face centered cubic (fcc, Fm3m) in the region enriched in UO_2. For description of the solidus and liquidus line

the TROI team provided a phase diagram calculated by MATPRO [3.15,3.16], shown in the *Figure 3.5*. From the first view the shape of the eutectic region differs as well its position and broadness. The eutectic position in the UO_2-ZrO_2 pseudo-binary is 70 w. % UO_2 and 30 w. % ZrO_2 according to the MATPRO data and approximately 57 w. %. UO_2 and 43 w. % ZrO_2 according to Thermodata [3.16]. These facts together with non-systematic explosivity results make the TROI team conclusions about eutectic versus non-eutectic melt tests at least questionable.
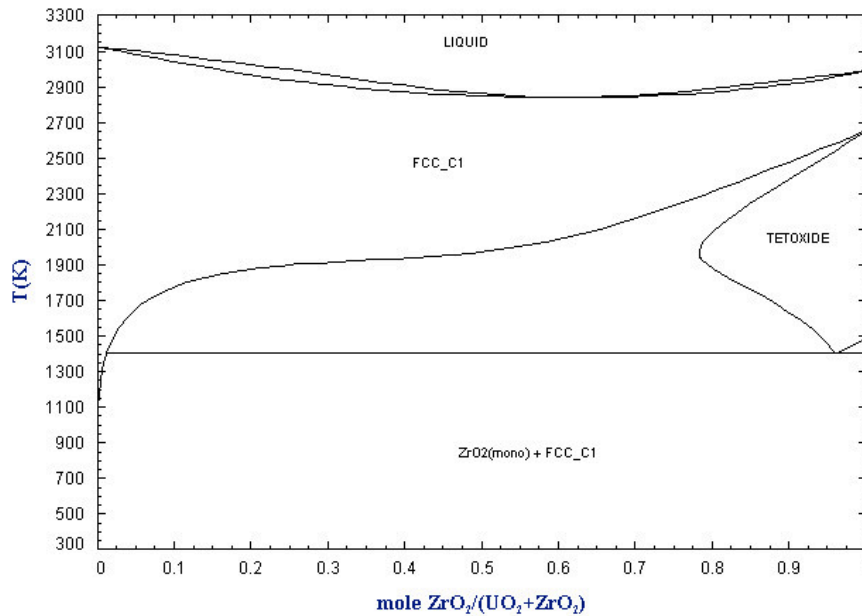
Figure 3.4 Pseudo-binary UO_2-ZrO_2 phase diagram [3.16]
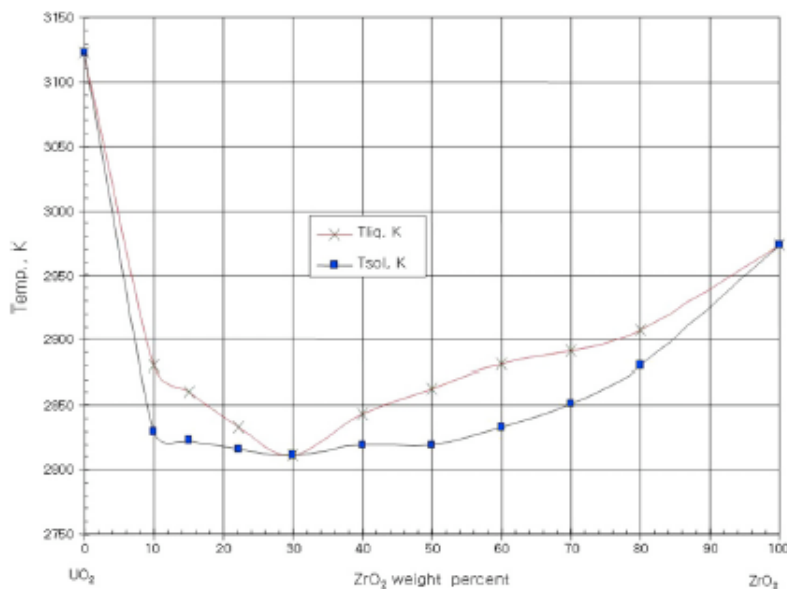
Figure 3.5 Diagram of solidus and liquidus line provided by TROI team [3.15]

3.2.3 Experiments with UO_2-ZrO_2-metal mixture

More recent TROI experiments are focused on the metal added UO_2-ZrO_2 melts [3.18-21]. The TROI 49 melting test (no FCI) showed a miscibility gap phenomenon in mixture of 62.3 w. % UO_2, 15 w. % ZrO_2, 11.7 w. % Zr and 11 w. % Fe. Two immiscible liquids were separated and stratified, while the dense metallic part settled at the bottom of the crucible [3.14-16]. Concerning FCI experiments with metal added corium the reported conclusions scatter. In principal, TROI 51 test (UO_2-ZrO_2/Zr/Fe) went through a steam explosion, while the debris was chemically heterogeneous [3.18]. Authors pointed out the internal porosity of the samples and its probable connection to the explosion strength.

3.3 KROTOS facility

The KROTOS facility has been devoted to investigation of steam explosion phenomena. Originally located in JRC Ispra (Italy) the facility was moved to CEA Cadarache (France) at the turn of second millennium. The facility set-up description and tests summary can be found in *Appendix C*.

Based on published literature the KROTOS program covered two directions, experiments with aluminum oxide and experiments with UO_2-ZrO_2 mixture (80-20 composition) [3.22].

3.3.1 Experiments with Al_2O_3

A set of tests with various conditions (water sub-cooling, fuel/coolant mass ratio, external triggering) were employed to study the steam explosion.

Experiments KROTOS 27 to 30 confirmed the effect of water sub-cooling [3.23]. High water temperature (low sub-cooling: T~90°C) is not favorable for spontaneous steam explosion, however it can be externally triggered. At these conditions debris cake is usually formed, therefore the melt arrives at the bottom of the test section in a liquid state. If the water temperature is rather low (high sub-cooling: T~25°C) the alumina-water system tends to be triggered spontaneously, most often when the melt touches the facility structures. The propagation wave in this case can rise up to 1000 $m.s^{-1}$ and the dynamic pressure peak can reach values more than 100 MPa. Dynamic pressure history (KROTOS 44, externally triggered explosion) and alumina debris morphology (KROTOS 30, spontaneously triggered explosion) are shown as an example in the *Figure 3.6*.
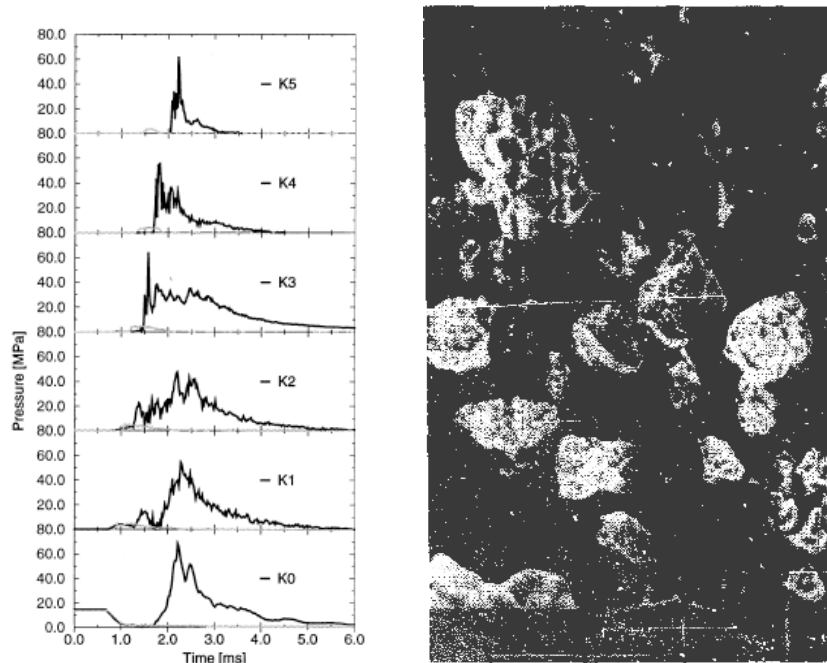
Figure 3.6 On the left, dynamic pressure history in KROTOS 44 (black) with blind external trigger (light gray) [3.22]. On the right, SEM micrographs of alumina debris (KROTOS 30), unfortunately the scale cannot be seen due to the poor picture quality [3.23]

3.3.2   Experiments with UO_2-ZrO_2 mixture

About 13 tests using 80 w. % UO_2 and 20 w. % ZrO_2 melt were conducted in the past [3.24-25]. It was observed that the premixing behavior of alumina and prototypic corium melt differs significantly. The average size of premixed droplets is in the case of corium very small (about a few mm) and droplets fall through the water column in a form of "jet". On contrary, in the case of alumina, the droplets are larger (about a few cm) and fall down in a form of separate globules [3.25]. Average energy conversion of the triggered experiments is around 0.15 %. Important observation is that during all tests (low or high sub-cooling), external or no triggering no energetic interaction took place. By comparison with aluminum oxide tests (*Figure 3.6*) an example of dynamic pressure history (KROTOS 52) and SEM micrograph of corium debris (KROTOS 58) is shown in the *Figure 3.7*. After this series of experimental tests, the alumina behavior characteristics have often been taken as bounding cases for the energetics and for the maximum dynamic pressure in FCI. But finally, no clear understanding of the main mechanisms responsible of the differences in FCI between alumina and prototypical corium has ever been established.
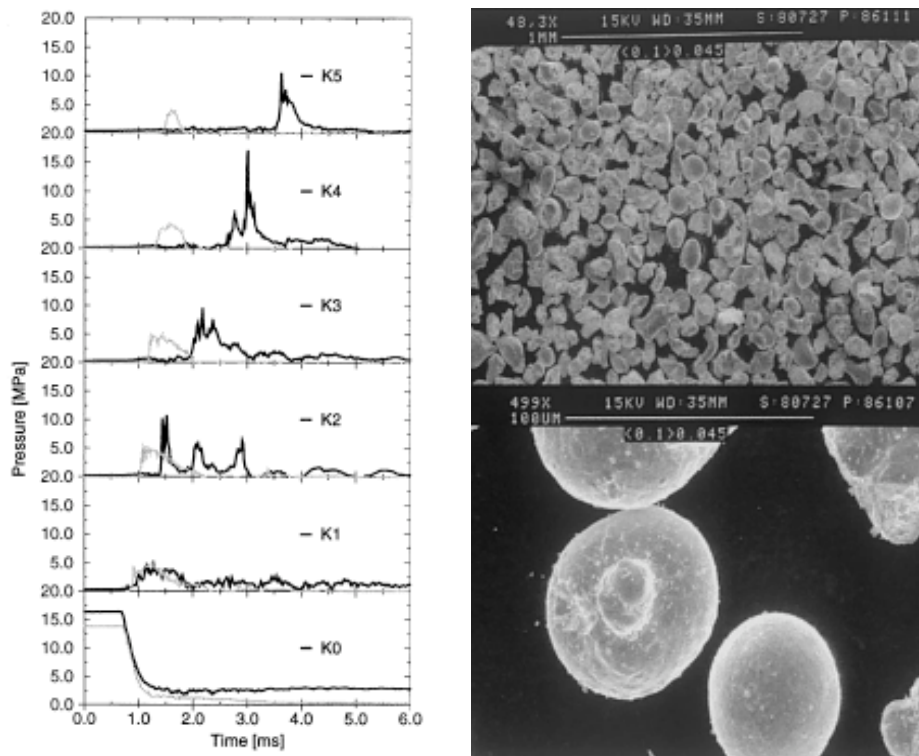
Figure 3.7 On the left, dynamic pressure history in KROTOS 52 (black) with blind external trigger (light gray) [3.22]. On the right, SEM micrographs of corium debris (KROTOS 58) [3.25]

3.4 MISTEE facility

The MISTEE facility has been set up at KTH Stockholm (Sweden) and has been dedicated to the study of a single droplet fragmentation [3.26]. It is equipped by high-speed visualization system combining the visible light and X-ray acquisition [3.27]. The over-all MISTEE program description is given in the *Appendix D*. At first, fragmentation of tin melt drops was studied. Later, experiment with CaO-WO$_3$ and WO$_3$-Bi$_2$O$_3$ were realized with a focus on the melt composition effect (eutectic versus non-eutectic melt).

3.4.1   Molten tin single droplet experiments

Thanks to the video and X-ray acquisition system many observations has been done in the steam bubble dynamics, drop thermal fragmentation and effect of non-condensable gas. The vapor explosion of single droplet can be divided principally in three cycles of bubble growth/collapse, while the fine fragmentation mechanism is rather close to the Kim & Corradini proposal (described in *Chapter 2*). Further, information about the effect of water sub-cooling was enriched by evidence of higher steam film size and symmetry (in other words thickness and distribution) for lower sub-cooling.

It was confirmed that presence of the non-condensable gas in the steam layer around the droplet hinders the liquid-liquid contact and therefore decrease the explosion energetics [3.28]. The conversion ratio versus water temperature (tin/water

experiments) is presented in the *Figure 3.8* with denoted presence of non-condensable gas.
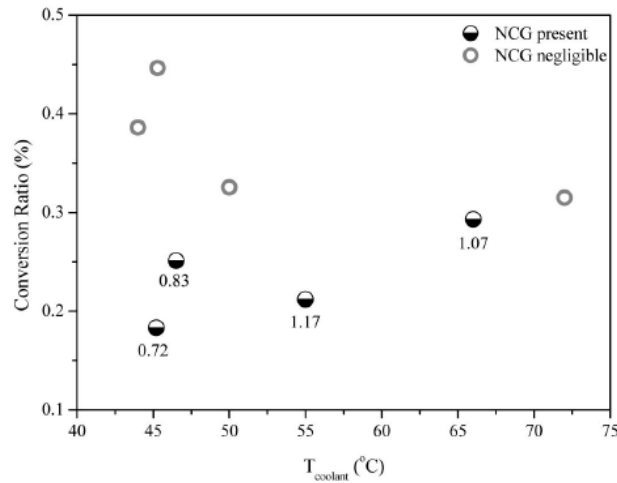
Figure 3.8 Energy conversion ratio in the MISTEE experiments versus water temperature with denoted presence of non-condensable gas [3.28]

3.4.2   Experiments with pseudo-binary WO_3-CaO melts

Inspired by "material effect" found in KROTOS, TROI and other facilities the MISTEE team launched an experimental set using WO_3-CaO melts [3.26]. This pseudo-binary mixture has the eutectic point at 75 mol. % CaO and 25 mol. % WO_3 and temperature 1135°C. Among all performed experiments nine complete and suitable tests were conducted using eutectic melt and three using non-eutectic melt (72 mol. % CaO and 27 mol. % WO_3, $T_{solidus}$ = 1232°C, $T_{liquidus}$ = 1135°C).

No evident difference in the steam bubble dynamics was obtained with eutectic and non-eutectic melts.

3.5 PREMIX and ECO facilities

Both facilities were constructed in FZK Karlsruhe (Germany) in a large pressure vessel called "Fauna" [3.29]. Both experimental programs used thermite generated alumina melt. High amounts of alumina melt can be obtained by a redox reaction of aluminum and iron oxide, so-called "Thermite reaction", (*eq. 3.1*). Further, major part of the liquid iron can be separated thanks to the density difference between iron and alumina.

$$8Al + 3Fe_3O_4 \longrightarrow 4Al_2O_3 + 9Fe + 3.7kJ/g \qquad \text{eq. 3.1}$$
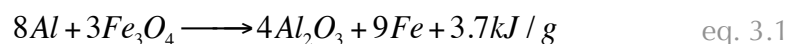
The PREMIX facility research was focused on the premixing phase, while steam explosion phase was studied in the ECO program.

3.5.1   PREMIX experiments

As can be seen in the published experimental documentation [3.29-30] 10 to 50 kg of melt were poured in to sub-cooled or saturated water. It can be generalized that

in the case of melt - saturated water interaction a funnel-shaped interaction zone is developed. This zone extends radially and axially in time. During the interaction at saturated conditions the bulk water seems to be prevented from the contact with melt. No explosion took place even at sub-cooled conditions. Example of the mixing phenomena taken by high-speed camera is given in the *Figure 3.9*.
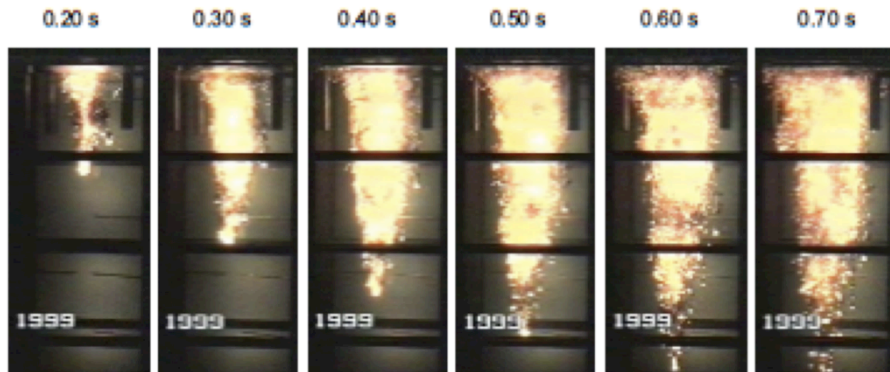
Figure 3.9 Beginning of the melt-water mixing in the PM 18 test [3.26]

3.5.2   ECO experiments

ECO research was devoted to better evaluate the energy conversion ratio during steam explosion [3.31]. Again, the thermite reaction generated molten alumina (eq. 3.1.) was used to simulate the nuclear fuel (load up to 18 kg). Maximally reached conversion ration was 2.39 % and pressure peaks above 100 MPa. Mostly, a triggered SE was obtained independently on the initial water sub-cooling and ambient pressure.

3.6   "Material effect" and Steam Explosion

3.6.1   What is the "material effect" in FCI?

As shown in previous paragraphs the effect of the melt compositions, and the "so-called material effect", on SE energetics was initially point out in the FARO and KROTOS programs and continued later mainly in the TROI program.

It must be stressed that, from experiments performed with simulant materials, many important conclusions on steam explosion energetics have been drawn and extrapolated to nuclear fuels and applied to reactor case.

Another important point for the experimental FCI programs concerns the fact that the differences of behavior between simulant materials and prototypical materials have never been clearly explained, especially for the KROTOS alumina experiments, usually taken as a reference for the high energetics steam explosion. In the next sections, it will be shown that alumina is really a specific material, not representative of FCI phenomena of first importance involved on real nuclear fuel. Finally, the difference of behavior between eutectic and non-eutectic has been considered as being a key-parameter.

In the frame of the SERENA project [3.32] an important analytical work has been done for the identification of the phenomena of first importance in the steam explosion. Four main fields concerning major limiting processes to steam explosions have been identified:

- *melt jet breakup* - determining the mass in mixture and fragment sizes, the limited mass directly and the drop size mainly with respect to void formation and solidification.
- *melt mass and void during premixing phase* - addressing the extension of the mixture and thus local volume parts of melt and their spatial distribution as well as related void formation, all effects of key importance for the possibility of explosions with high efficiencies.
- *melt solidification* - as directly excluding part of the melt from participating in explosions.
- *explosion phase* - involving the inherent limitations to escalation due to void , fine fragmentation and heat transfer.

From this analyse, the following assumptions for the "material effect" have been taken into account as being of first importance for the energetics of steam explosion. Major limitations to steam explosion strength are due to:

- **Limited liquid melt** mass in mixture from scenario (inflow rate into water, water depth) and breakup.
- **High density** material as Corium yields in any realistic scenario of inflow into water relatively **small drops of some mm size**, **independent of material composition**
- **Rather fine breakup of Corium** (compared with alumina in KROTOS and PREMIX) yields a tendency to high void and rapid solidification.
- **Solidification** yields additional significant limitations, especially with sub-cooled water.

According to analytical group [3.33], the "material effect" would be linked to the following properties of the melt:

- *Density* – The higher density the deeper sequential melt fragmentation is observed. Efficient fragmentation is connected with increasing of the surface area and larger heat transfer and consequently higher cooling rate.
- *Liquidus temperature* – The higher melt temperature means a larger temperature difference between melt and water, which tends to higher cooling rate. High temperature melts loose their thermal energy mainly by radiation.
- *Thermal conductivity* – Significant melt thermal conductivity leads to the delay of solid crust growth.
- *Non-eutectic melt composition* – A mushy layer can be formed on the melt drop surface and prevent the further fragmentation
- *Oxidation* – Hydrogen (non-condensable gas) can be produce. Exothermic oxidation reaction can increase the melt thermal energy.

Other authors of above-mentioned article [3.28] built up a similar diagram of material effect phenomena (*Figure 3.10*) as was done by Dinh [3.34] (see *chapter 1 Figure 1.9*)
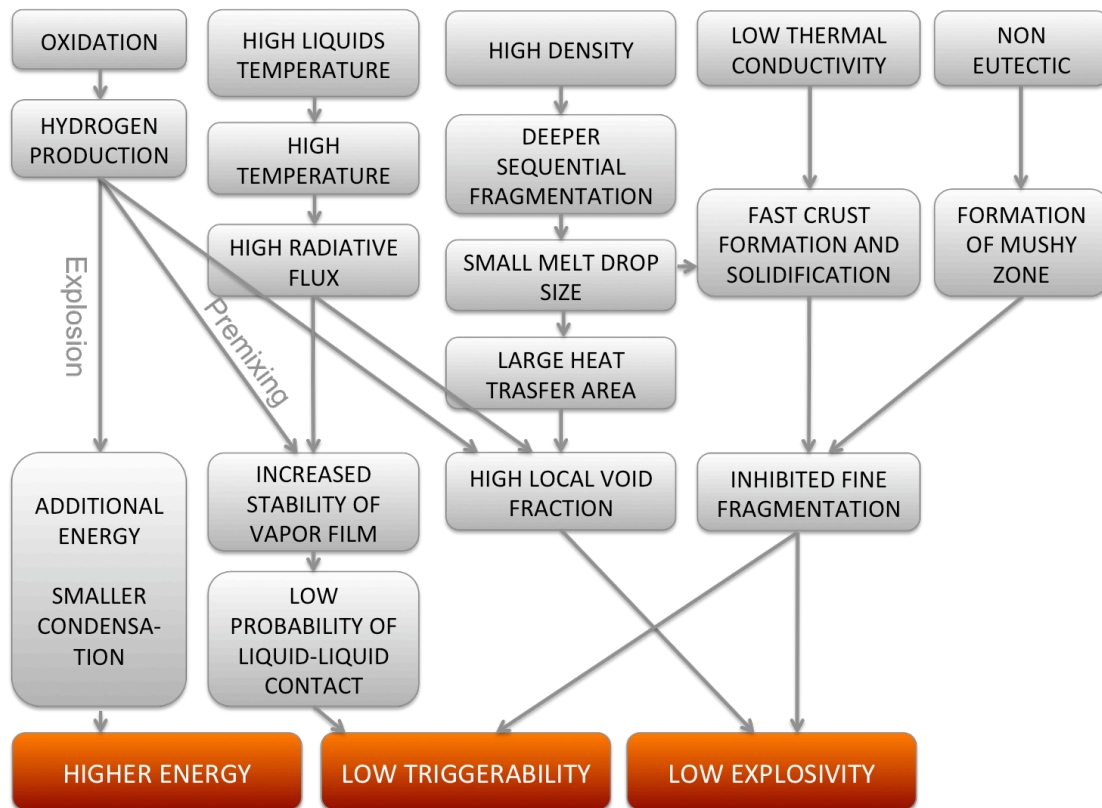
Figure 3.10 Diagram of material effect phenomena [3.33]

3.6.2 State of the art for "material effect"

In following paragraphs the main findings about the "material effect" in FCI are summarized and critically analyzed.

3.6.3 Solidification Modeling

Being a topic of material effect the solidification affects the explosion efficiency simply by cutting off the amount of melt participating to fine fragmentation (steam explosion). Recently, efforts have been done to rigorously describe the solidification of melt droplets during premixing phase in FCI computer codes. M. Ursic et al. [3.35-36].

A model of temperature profile in the droplet was combined with modified Weber number approach. The droplet temperature profile is divided in to three zones (*Figure 3.11*). These different zones grow or shrink according to the heat dissipation according to conduction and radiation in the modelling.

The fine fragmentation is later affected by solid crust preventing the drop. Therefore a modified Weber number **We*** was proposed including crust mechanical properties (*equation 3.2*)

$$We* = \frac{\rho v_0^2 D^3}{E \delta_s^3}(1 - \mu^2)$$

<div align="right">eq. 3.2</div>

where ρ presents melt density, v_0 relative velocity, D drop diameter, δ_s is the crust thickness, E is the Young's modulus and μ is the Poisson's ratio.

This model present one general approach how to describe the droplet solidification in FCI, but without taking into account any structural, chemical or other specific information. Further more, the Young's modulus E and the Poisson's ratio of prototypical solid crust on droplets is not known, so meaning strong assumptions on the approach. At least, the influence on steam explosion is not clearly demonstrated.
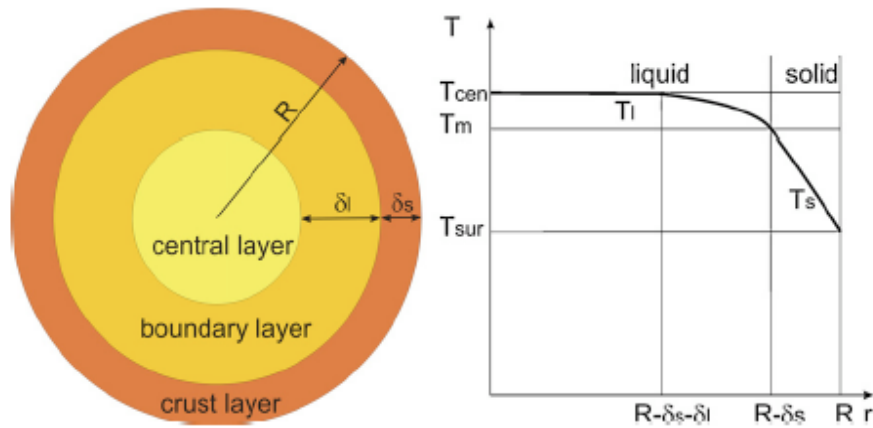
Figure 3.11 Model of drop temperature profile used in [3.35-36]

3.6.4 Material effect and simulant materials

Aluminum oxide

Piluso et al. [3.37] reported crystallographic characterization of debris coming from KROTOS alumina tests. It was found that during steam explosion alumina melt solidifies mainly to γ (defective spinel) phase and during FCI without steam explosion to α (rhombohedral) phase. The *Table 3.1* summarizes the known crystallographic phases of aluminum oxide. The rapid melt cooling during FCI is analogous to plasma spraying experiments, where feedstock powder is melted and carried by plasma gas. Melted powder drifts to a target and solidifies. Specific conditions, mainly cooling rate, can be adjusted according to parameters (temperature) and thermophysical properties (thermal conductivity). Behavior of aluminum oxide during these rapid quenching experiments was partially understood.

Table 3.1 Main crystallographic phases of aluminum oxide

Phase	Crystallographic system	Occurrence	
		Equilibrium	Out of equilibrium
Alpha (α)	Rhombohedral	✔	
Beta (β)	Hexagonal	✔	
Gamma (γ)	Defective spinel		✔
Delta (δ)	Deformed tetragonal		✔
Epsilon (ε)	Hexagonal		✔
Theta (θ)	Monoclinic		✔

Piluso et al. [3.37] further implies that the melt solidification into gamma phase occurs at lower temperature (~2010 K) than equilibrium melting point (2330 K) due to

lower nucleation energy and very well known meta-stable conditions promoting supercooling effect. It was noted that gamma-phase chemical formula is generally $Al_2[]_{0.4}O_{2.8}(OH)_{0.4}$, where [] represents vacancy, and it might correspond to the alumina coming from KROTOS experiments. This formula became deep-seated due to the world most common fabrication of γ–Al_2O_3 (*Equation 3.3*) that is the decomposition of $Al(OH)_3$ (gibbsite) [3.38].

$$Al(OH)_3 \xrightarrow{\sim 300^{\circ}C} \gamma - AlOOH \xrightarrow{\sim 500^{\circ}C} \gamma - Al_2O_3 \qquad \text{eq. 3.3}$$
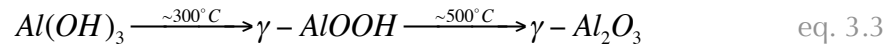
More arguments imply that γ–Al_2O_3 is formed due to the high cooling rate and the chemical formula cannot be represented as mentioned above. However, the presence of OH groups should be considered due to the possible reaction with water vapor during FCI. During plasma spraying experiments it was found that higher cooling rate leads to higher amount of gamma-phase in the solidified melt on the target [3.39-40]. The cooling rates necessary to obtain gamma-phase are i.e. 10^6 $K.s^{-1}$, while in water non-violent quenching the cooling rates i.e. 10^4 $K.s^{-1}$ leads to δ-phase [3.41]. Even lower quenching rates result in equilibrium α-phase. These results are supported by fact that during plasma spraying smaller particles contain gamma-phase in majority, while larger particles contain mainly alpha-phase [3.41]. Interesting fact is that the density of gamma-phase is only 4 % lower than in the liquid state, while alpha phase shrinks by 19 % (ρ_{gamma} = 3.43 $g.cm^{-3}$, ρ_{alpha} = 3.95 $g.cm^{-3}$). During such rapid cooling the melt structure has no time to be reconfigured and closely packed. If the melt already contains solid nuclei of alpha-alumina, the solidification is induced into alpha-phase even at high quenching rates [3.42-43].

Aluminum oxide reacts with water vapor at high temperature producing volatile compounds (hydroxides, oxo-hydroxides) that are carried away by the vapor flow. Volatilization rate dependence on temperature measured by Opila et al. [3.44] is shown in the *Figure 3.12*. These rates for both Al_2O_3 and UO_2 could be extrapolated to higher temperature, but one should take care about the reaction mechanism that changes above the melting point.

The ability of alumina reaction with water vapor is related to the ability to dissolve water vapor. The amount of dissolved water vapor rises up with $\sim \sqrt{p_{H_2O}}$ and significantly decreases the melt viscosity [3.45].
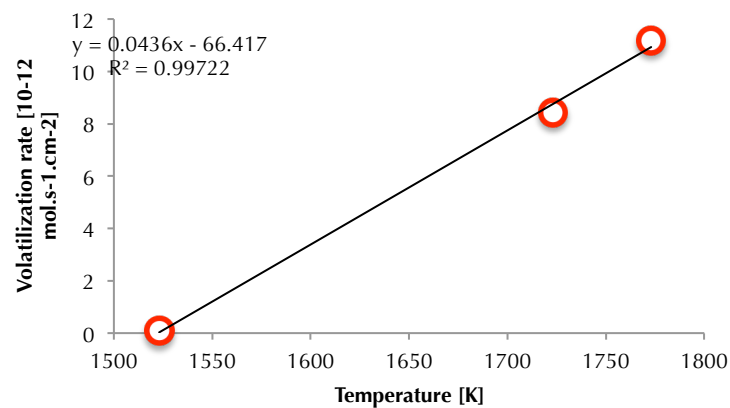
Figure 3.12 Volatilization rate of aluminum oxide versus temperature (50 % H_2O and 50 % O_2, flow rate 4.4 $cm.s^1$) [3.44]

Metals

Less information has been published about metallic melt and post-test analyses. Experiments were performed for example using steel [3.46], gallium [3.47], tin [3.26], Zr/stainless steel and Zr/ZrO$_2$ [3.48-49] or aluminum [3.50]. Most of the questions in this case arise from the metal ability to be oxidized by water/water vapor. Experiments using molten aluminum showed that 30-40 % was oxidized in the explosion timescale [3.50]. ZREX experimental program using Zr/stainless steel or Zr/ZrO$_2$ mixtures concluded that 70-100% of zirconium was oxidized during triggered tests [3.49]. The pressure peak size versus amount of produced hydrogen in the ZREX experiments is given in the *Figure 3.13*. As was already mentioned the oxidation reaction is connected with hydrogen and energy production. Very important reaction in severe accident studies – zirconium oxidation by water vapor is highly exothermic:

$$Zr + 2H_2O \longrightarrow ZrO_2 + 2H_2 \quad \Delta H \approx -64 MJ / kg \qquad \text{eq. 3.4}$$

Up to now still unanswered question is asked, if the high-pressure peaks are caused by the increased melt thermal energy due to the oxidation or expansion of high-temperature hydrogen created during fine fragmentation. But, it was mentioned that hydrogen has a negative effect on the explosion energetics as a non-condensable gas during premixing. We can assume that elevated melt thermal energy cannot assure the effective thermal transfer to the water and consequent pressure rise. This was confirmed in FARO L11 test using metallic zirconium addition.

The kinetics of the oxidation process has not been deeply reviewed or experimentally described. The various metals oxidation mechanism and kinetics in solid state are known being a part of whole research area – corrosion science. However, data for high temperatures or liquid state are hard or even impossible to find especially in microsecond timescale necessary for FCI analyses. According to the experimental results a very rough comparison can be done, the oxidation speed decreases according to the following range zirconium > aluminum > iron > tin.
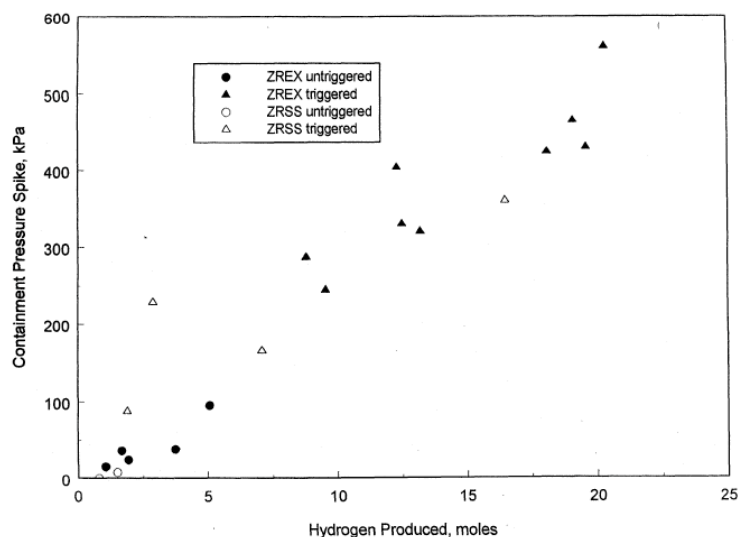
Figure 3.13 Experimental pressure peaks versus amount of produced hydrogen in ZREX tests [3.49]

3.6.5   Material effect and prototypic corium (UO_2-ZrO_2) mixtures

Very few studies have taken into account the specificities of uranium in the real case of prototypical corium to explain the differences of behavior with alumina.
The main points that have been stressed for prototypical materials are:

- Difference of densities (Alumina/Corium) to explain smaller droplets during premixing/fragmentation phase.
- Higher melting point of corium (2600-2750°C) and lower over heating (+150°C) in comparison with alumina (2020°C) and higher overheating (+300°c) promoting higher energetics for alumina.
- Difference between "eutectic" and "non-eutectic" composition like alumina or azeotrop, like 70 w. % UO_2-30 w. % ZrO_2 having a single "melting point" and a material having a solidification interval with a liquidus and solidus temperature like 80 w. % UO_2- 20 w. % ZrO_2. This last category would promote lowest steam explosion because of possible mushy zone.

A deeper study on prototypical materials can be added according to the following points for prototypical materials.
The crystallographic characteristics depend on the composition (U/Zr ratio). The size of the fcc elementary cell was described by means of Wegard's law (*eq. 3.5*) by Cohen et al. [3.51]. Later, this law was applied to severe accident studies by Piluso et al. [3.52]. For the solid solution $U_{1-x}Zr_xO_2$ we can write:

$$a = 5.468 - 0.3296x \qquad \text{eq. 3.5}$$

where a is the fcc lattice parameter in Å. Recently the crystallographic studies has been enriched by extension to ternary system and taking to account the possible oxygen stoichiometry $U_{1-x}Zr_xO_{2+y}$ [3.53]. If we consider the basic cell as UO_2, by addition of ZrO_2 the cubic cell shrinks and by increase of oxygen stoichiometry the situation is similar. For the a (Å) parameter of the fcc solid solution $U_{1-x}Zr_xO_{2+y}$ we can write:

$$a = 5.4704 - 0.30x - 0.21y \qquad \text{eq. 3.6}$$

If we consider UO_2-ZrO_2 solution in the liquid state, Stolyarova at al. [3.54] observed higher activity of UO_2 in the gas above the UO_2-ZrO_2 than should be in the ideal case. Therefore, uranium rich aerosols are mainly formed during the melting experiments.

Another interesting fact concerning over(hyper)-stoichiometric UO_{2+x} should be mentioned. Manara et al. [3.55-56] showed that UO_2 passes from single point melting to ($T_{solidus}$-$T_{liquidus}$) solidification interval with oxygen over-stoichiometry (*Figure 3.14*). This fact confirms that UO_2-ZrO_2 in pseudo-binary eutectic composition or pure UO_2 should not be used as eutectic or single point melting in oxidative atmosphere. Further, the high temperature reaction of UO_2-ZrO_2 with water vapor has not been found in accessible literature. However, Hashizume et al. [3.57] studied the high temperature interaction of pure UO_2 and water vapor. It was found that UO_2 is oxidized by steam to UO_3 and much less to $UO_2(OH)_2$. The volatilization rate dependence on temperature is shown in the *Figure 3.15*. It decreases with presence of hydrogen in the atmosphere.
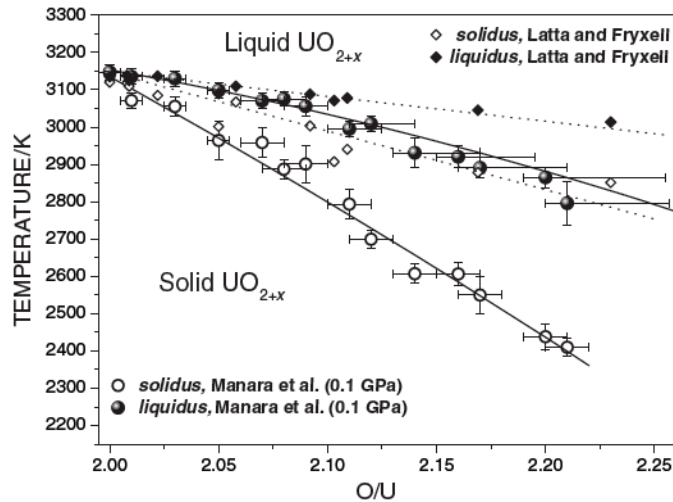
Figure 3.14 Solidus and liquidus line for over(hyper)-stoichiometric UO_{2+x} [3.55]

$$y = 3E\text{-}10e^{0.0128x}$$
$$R^2 = 0.99629$$
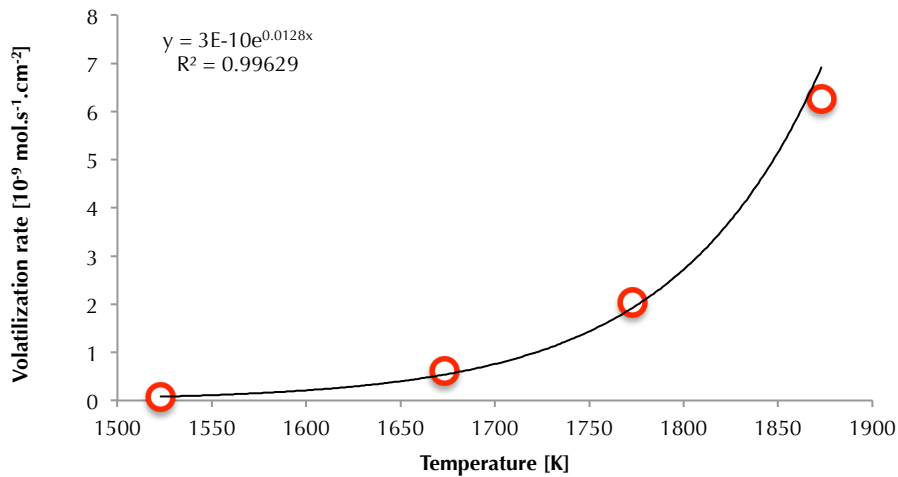
Figure 3.15 Volatilization rate of UO_2 under steam flow (0.8 $cm^3.s^{-1}$) [3.57]

The ability of pure ZrO_2 to be eroded and volatilized by water vapor at high temperature was not described. However, footmarks of zirconia stability were observed by Ueno et al. [3.58]. Zircon ($ZrSiO_4$) surface was irritated by water vapor, SiO_2 was volatilized and carried out by the steam flow, while pure monoclinic zirconia left entire.

3.6.6   Material effect and debris morphology

One main point has never been significantly highlighted in FCI experiment analyses. The debris morphology mentioned in chapter 2 (volcanic ahs sediments) gives important information about the process history, mechanism and provides data for further analyses. For example, *Figure 3.16* presents a SEM cross-section of TROI TS4 debris [3.59].
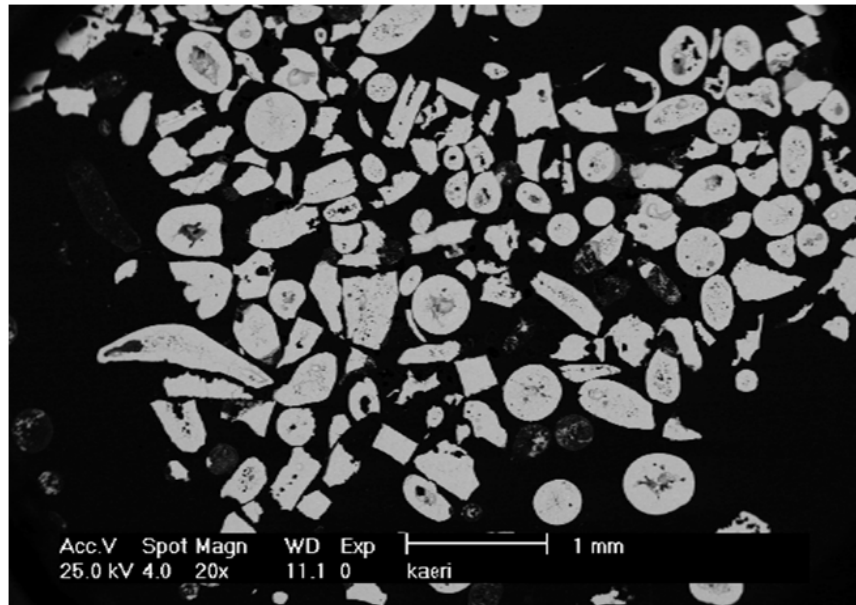
Figure 3.16 SEM micrograph of TROI TS-4 debris (<0.450 mm) [3.59]

Based on a statistics (153 particles), it can be seen that 69 % of the debris has angular shape like piece of rock, the remaining 31 % are rounded. Concerning the internal void inside the debris, we can see that 65 % has some kind of internal porosity, one large or several smaller cavities, and 35 % are full. The overall characteristic is shown in the *Figure 3.17*. Similar situation is concerning KROTOS debris (shown in the *Figure 3.7* top left) (240 particles) 90 % is angular and only 10 % has rounded shape. Rounded (elongated or circular) pieces can be attributed to fragmentation of the liquid jet, while angular particles (with sharp edges) can be attributed to fragmentation of solid. Angular morphology is not possible to be obtained during break up of liquid, but during destruction of initially rounded solid droplets. The reason, why the solid droplets can be crushed, lies in the mechanical properties of UO_2-ZrO_2 mixture that can be assimilated to brittle materials like ceramics with low toughness. Totally different behavior accompanies metallic melts, since metals have significant elastic/plastic deformation domain and creep at solid state especially at elevated temperatures. Solid break up is probably caused by pressure and temperature gradients during FCI and internal stress in the droplets as well. Also, other droplets can be crushed during handling after the experiment.

Why do we give to the droplet fragmentation so much attention? The experimentally measured drop size distribution is one of the most important input data for modeling the fragmentation in the computer codes. Especially, the mean Sauter diameter of the droplet is taken as being as one of the key parameter for the modeling of fragmentation/steam explosion: below a certain value for the mean Sauter diameter, it is considered that all the droplets below this value have participated to steam explosion, above the droplets have not participated. This value will determine the amount of corium participating to steam explosion on a subjective consideration: namely, there is no criterion to define how this value has been chosen.
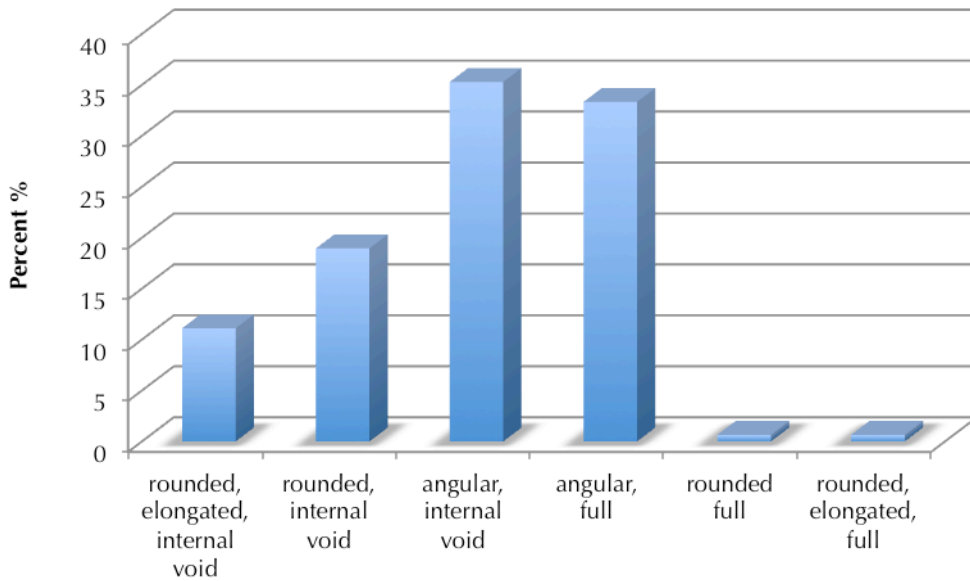
Figure 3.17 Statistical information about the debris morphology for TS 4 debris in the Figure 3.16

If we consider the liquid melt fragmentation during premixing or after explosion, we obtain round droplets with a distribution in diameter (situation is depicted in the *Figure 3.18* on the left). If the fragmentation of solidified droplets is taken into account, the solid drops pertaining to certain size fraction are crushed into several pieces and they move into size fraction below even several levels lower. Experiments performed in the DEFOR facility [3.60] using binary oxide ceramic mixture showed above-mentioned phenomena. Kudinov et al. [3.61] pointed out the effect of water sub-cooling, at sub-cooling less than 50°C most of the particles are spherical, while at sub-cooling more than 80°C particles are mostly rock-like. It is usual that mechanical sieving is done after each experiment. This method fractionize the debris according the size hiding above-mentioned problem. This data further used in computer codes or other analyses provide misrepresented view about the situation after coarse of fine fragmentation linked to FCI.

Another interesting fact concerning TROI material analyses is that a significant phase segregation was observed for TS4 experiment using 80 w. % UO_2 and 20 w. % ZrO_2. Two phases, one enriched in uranium and other in zirconium, are formed during the solidification process (*Figure 3.19*). Cause of this behavior can attributed to the low solidification rate, when the two chemical species have time locally to segregate by diffusion.
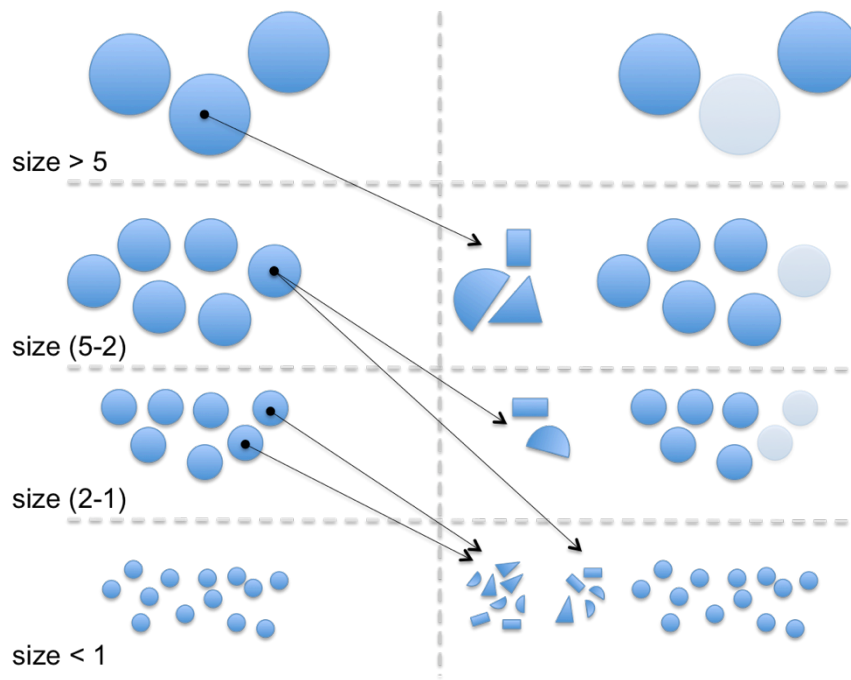
Figure 3.18 Scheme of melt fragmentation into droplets (left). Fragmentation taking into account breakage of solid drops (right)

TROI team explained the porosity inside the melt as a result of volume shrinkage during solidification. However, if we take a close look on the porosity, it is located always in the uranium rich phase (light). The porosity caused by volume shrinkage has usually different morphologies (for example linear cracks), which is not the case for this experiment.
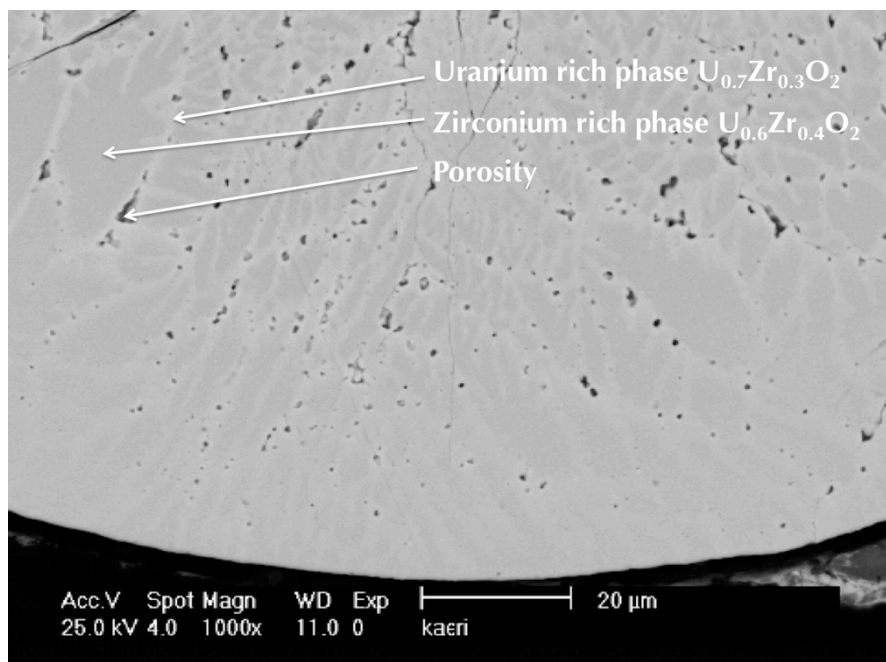
Figure 3.19 Cross-section of solidified droplet from TROI TS 4 experiment showing phase segregation and porosity

3.6.7 Methodology applied to "the material effect" in the steam explosion

In the previous paragraphs, we have seen that the approach to explain the "material effect" in steam explosion seems to be incomplete.

From our understanding, the following points have to be taken into account because of first importance on steam explosion energetics:

The thermodynamic properties of the melt (liquidus, solidus, solidification interval, composition) and the thermo-physical properties must be distinguished as having different consequences on Steam explosion.

The thermodynamic properties of the melt (liquidus, solidus, solidification interval, composition) will give an order of magnitude for the solidification process. Nevertheless, in any case, the solidification processes during premixing and steam explosion phases are at thermodynamic equilibrium. The cooling must be assimilated to quenching process (cooling rates between 10^4 and 10^{10} °C/s) with phenomena out of equilibrium: formation of meta-stable phases, super-cooling phenomena (decrease of the "real" solidification temperature below the thermodynamic solidification temperature).

The composition of the melt can change if there are possible reactions with the water and/or evaporation of part of the melt. In this case the thermodynamic properties will change as shown in chapter 4.

Some important thermo-physical properties of the melt are missing in these analyses of "material effect": surface tension, viscosity, emissivity and mechanical strength of the crust during the solidification process.

According to this analyze, we propose a new approach and to explain the so-called "material effect" on steam explosion (*Figure 3.20*):

| Initial composition of melt before FCI |
| - oxide, sub-oxide, over-oxide, metallic |

Thermodynamic properties

Liquidus temperature, solidus temperature, solidification interval, composition, reaction of the melt with water, vaporisation of the melt

Thermophysical properties

Density, viscosity, surface tension, emissivity, thermo mechanical properties of the crust

See chapter 4

Premixing phase: jet break-up, coarse fragmentation

Size, distribution, shape, surface area of droplets ?

Void fraction ?

See chapters 5-8

Explosion phase: propagation, Fine fragmentation

Hydodynamic fragmentation ?

Thermal fragmentation ?

High or Low energetics ?

Figure 3.20 Material effect and steam explosion

A first series of objectives will be to establish by calculation the impact of the thermo-physical and thermodynamic properties on steam explosion according to the nature of the materials (simulant or prototypical) (chapter 4).

A second series of objectives will be devoted to the studies of the post-test debris of FCI experiments using simulant materials (MISTEE) chapter 5, and prototypical materials (KROTOS) (see chapter 6 to 8) . Thanks to these post-test analyses, it will be shown how it will be possible to identify the main mechanisms responsible of fine fragmentation, the solidification path of the materials steam or non steam exploded, the amount of melt droplet having participated to steam explosion.

3.7 References

3.1   G. Berthoud: L'interaction CORIUM-EAU : Synthèse et analyse des résultats expérimentaux , CEA report STT/LPML/87/28/C, 1987
3.2   G. Berthoud: L'interaction CORIUM-EAU : Synthèse et analyse des résultats expérimentaux, CEA report SMTH/LDTA 2002-016, 2002
3.3   D. Magallon, H. Hohmann: Nuclear Engineering and Design 155 (1995) 253-270
3.4   Magallon, H. Homann: Nuclear Engineering and Design 177 (1997) 321-337
3.5   D. Magallon, I. Huhtiniemi: Nuclear Engineering and Design 204 (2001) 369-376
3.6   G. Magallon et al: Nucelar Engineering and Design 189 (1999) 223-238
3.7   A. Annunziato et al: FARO Test L-33 Quick Look Report, Technical Note No. I.00.111, JRC Ispra, Italy 2000
3.8   H. Matzke, V. Rondinella: Investigation of specimens from the FARO tests L-19 and L-24, JRC ITE Karlsruhe, Germany, Report KA 10/97, 1998
3.9   D. Magallon: Nuclear Engineering and Design 236 (2006) 1998-2009
3.10   J. H. Song et al: Nuclear Engineering and Design 213, 2002, 97-110
3.11   I. K. Park et al: An investigation on the material effect on the results of fuel coolant interactions in the TROI experiments, Paper 8123, International Congress on Advances in Nuclear Power Plants, Anaheim, USA, 2008
3.12   J. H. Song et al: Nuclear Engineering and Design 222 (2003) 1-15
3.13   J. H. Song et al: Annals of Nuclear Energy 22 (2006) 1437-1451
3.14   J. H. Kim et al: Nuclear Technology 158 (2007) 378-395
3.15   B. T. Min et al: Journal of Nuclear Materials 358 (2006) 243-254
3.16   B. Cheynet et al: NUCLEA Nuclear Thermodynamic Database, Thermodata, Sain Martin d'Heres, France
3.17   MATHPRO: A Library of Materials Properties for Light Water Reactor Accident Analysis, NUREG/CR-5273, EGG-2555, vol. 4, 1990
3.18   J. H. Song et al: Nuclear Technology 160 (2007) 279-293
3.19   J. H. Song et al: Heat Transfer Engineering 29(8) (2008) 740-747
3.20   B. T. Min et al: Journal of Nuclear Materials 377 (2008) 458-466
3.21   J. H. Kim et al: Heat Transfer Engineering 29(8) (2008) 748-756
3.22   I. Huhtiniemi et al: Nuclear Engineering and Design 189 (1999) 379-389
3.23   H. Hohmann et al: Nuclear Engineering and Design 155 (1995) 391-405
3.24   I. Huhtiniemi et al: Nuclear Engineering and Design 177 (1997) 339-349
3.25   I. Huhtiniemi et al: Nuclear Engineering and Design 204 (2001) 391-400

3.26   R. C. Hansson: An Experimental Study on the Dynamics of a Single Droplet Vapor Explosion, Doctoral thesis, KTH Stockholm, Sweden, 2010

3.27   H. S. Park et al: Continuous High-Speed X-ray Radiography to Visualize Dynamic Fragmentation of Molten Liquid Droplet in Liquid Coolant, 4th Pacific Symposium on Flow Visualization and Image Processing, F4090, Chamonix, France, 2003

3.28   R. C. Hansson: Nuclear Engineering and Technology 41(9) (2009) 1215-1222

3.29   F. Huber et al: PREMIX, Documentation of the Results of Experiments PM01 to PM06, Wissenschaftliche Berichte, FZKA 5756, FZK Karlsruhe, Germany, 1996

3.30   A. Keiser et al: PREMIX Experiments PM12-PM18 to Investigate the Mixing of a Hot Melt with Water, Wissenschaftliche Berichte, FZKA 6380, FZK Karlsruhe, Germany, 2001

3.31   W. Cherdron et al: ECO Steam Explosion Experiments – Documentation and Evaluation of Experimental Data, Wissenschaftliche Berichte, FZKA 7011, FZK Karlsruhe, 2005

3.32   D. Magallon: FCI phenomena Uncertainties Impacting Predictability of Dynamic Loading of Reactor Structures. PSA-2 Workshop, Aix en Provence, France, November 7-9, 2005

3.33   M Leskovar et al: Material Influence on Steam Explosion Efficiency: State of Understanding and Modelling Capabilities, The 2nd European Review Meeting on Severe Accident Research (ERMSAR), FZK Karlsruhe, Germany, 2007

3.34   T. N. Dinh et al: An Assessment of Steam Explosion Potential in Molten-Fuel-Coolant Interaction Experiments", Proceedings International Conference on Nuclear Engineering, ICONE-6, San Diego, USA, 1998

3.35   M. Ursic: Modelling of Solidification Effects in Fuel Coolant Interactions, Doctoral Thesis, Univeristy of Ljubljana, Slovenia, 2011

3.36   M. Ursic et al: Journal of Nuclear Engineering and Design 241 (2011) 1206-1216

3.37   P. Piluso et al: International Journal of Thermophysics 26(4) (2005) 1095-1114

3.38   K. Wefers: Oxides and Hydroxides of Aluminium, Alcoa Technical Paper 19, Alcoa Lab., 1987

3.39   P. Chraska et al: Journal of Thermal Spray Technology 6(3) (1997) 320-326

3.40   C. X. Ding et al: Thin Solid Films 118 (1984) 467-475

3.41   J. Dubsky et al: The Influence of Cooling Rate on Phase Transformations in Al_2O_3, Proceeding of 7th Metallographic Symposium, Part 1, Vysoke Tatry, Czechoslovakia, 168- 171, 1989

3.42   R. McPherson: Journal of Material Science 15 (1980) 3141-3149

3.43   R. McPherson: Journal of Material Science 8 (1973) 859-862

3.44   E. J. Opila et al: Journal of the American Ceramic Society 87 (2004) 1701-1705

3.45   J. P. Coutures et al: Revue Internationale des Hautes Températures et des Réfractaires 17 (1980) 351-361

3.46   X. Chen et al: Nuclear Engineering and Design 189 (1999) 163–178

3.47   X. Chen et al: Nuclear Engineering and Design 177 (1997) 303–319

3.48   D. H. Cho et al: Experiments on Interaction Between Zirconium-Containing Melt and Water (ZREX): Hydrogen Generation and Chemical Augmentation of Energetics, Argon National Laboratory, ANL/ASO/CP-92443

3.49   D. H. Cho et al: Experiments on Explosive Interactions Between Zirconium-Containing Melt and Water (ZREX), 6th International Conference on Nuclear Engineering, San Diego, USA, 1998

3.50   M. J. Rightley et al: NPR/FCI EXO-FITS Experiments Series Report, Sandia National Laboratories,S AND.91-1544, NPRW-SA 91-3, 1993

3.51   I. Cohen, B. E. Schaner – Journal of Nuclear Materials 9 (1963) 18-52

3.52   P. Piluso et al: Journal of Nuclear Materials 344 (2005) 259–264

3.53   N. K. Kulkarni et al: Journal of Nuclear Materials 384 (2009) 81–86

3.54   V. Stolyarova et al: Journal of Nuclear Materials 247 (1997) 41-45

3.55   D. Manara et al: Journal of Nuclear Materials 342 (2005) 148-163

3.56   D. Manara et al: Journal of Nuclear Materials 362 (2007) 14–18

3.57   K. Hashizume et al: Journal of Nuclear Materials 275 (1999) 277-286

3.58   S. Ueno et al: Corrosion Science 49 (2007) 1162–1171

3.59   S. W. Hong et al: TROI TS-4 data report, OECD/SERENA-2010-TR07, 2010

3.60   A. Karbojian et al: Nuclear Engineering and Design 239 (2008) 1653-1659

3.61   P. Kudinov et al: Molten Oxidic Particle Fracture during Quenching in Water, 7th International Conference on Multiphase Flow, Tampa, USA, 2010

Chapter 4. Theoretical analyses of phenomena involved in "Material effect in FCI"

4

   Chapter 4 describes the results coming from approach assuming chemical thermodynamics for the material effect in FCI. It covers two main parts. First paragraphs are devoted to the specification of the possible chemical reactions at thermodynamic equilibrium between the melt and water/steam for most common materials used in FCI experiments. Second section is focused on the radiation heat transfer again with emphasis on the material effect. Radiation heat transfer, being the most dominant type of heat transfer at high temperature, was not given much attention in the past. The spectral properties of the different melt materials (emitter) and water/steam (absorber) are connected in a 1D calculation in order to see the differences in the heat transfer.

4.1 Thermodynamic modelling of chemical reactions

   Except the melt oxidation by steam other possible chemical reactions have been very few taken into account in FCI. The aim of this study is to list and describe the thermodynamically possible chemical reactions between melt and water/steam at high temperatures.

   Generally the thermodynamic modeling requires accurate values and temperature dependencies of fundamental thermodynamic properties like standard enthalpy of formation ΔH°_{298}, standard entropy S°_{298}, heat capacity c_p and transition enthalpies L_{tr}. All these parameters should be attributed to all chemical substances in desired system. Knowing above-mentioned characteristics the Gibbs energy (free enthalpy at constant pressure) can be calculated. In simple words, the system reaches equilibrium at constant pressure and temperature, when the Gibbs energy of each reaction reaches minimum versus extent of reaction ξ:

$$\left(\frac{dG}{d\xi}\right)_{p,T} = 0 \qquad \text{eq. 4.1}$$

   Thermodynamic modeling then combines the database values of fundamental properties of chemical substances and Gibbs energy minimization to obtain prediction of the system behavior at certain temperature and pressure.

   Various software packages exist in the scientific communities, for example FactSage [4.1], Claphad [4.2] and Thermosuite [4.3].

The last mentioned Thermosuite was developed by Thermodata [4.4] and provides a wide database focused on nuclear materials TD Nuclea (annually updated) and Gibbs energy minimizer Gemini2. It was used to describe four main melt compositions in reaction with steam:

- $Al_2O_3 - H_2O$
- $ZrO_2 - H_2O$
- $UO_2\text{-}ZrO_2 - H_2O$
- $Fe - H_2O$

The following paragraphs summarize the condition of performed calculations. Results and discussion is sectioned according to the melt initial composition.

4.1.1 Calculations input and conditions

The single equilibrium points (temperature, pressure and composition) were calculated as a closed system. The input composition was 1 mol of melt and 1 mol of water for all the cases. Temperature interval was chosen from 600 to 3000 K in order to cover the melt existence, solidification interval and solid phase transformation.

Results are given mainly in a form of temperature dependency of phase or substance existence/content, oxide phase stoichiometry and water vapor content. The system properties are selected according to the principal needs of FCI material effect investigation.

The phase/substance amounts were plotted as received. Oxygen over/sub-stoichiometry of general oxide $A_JB_KO_{L+x}$ (A, B are oxide generating elements like uranium and zirconium; O represents oxygen; J, K, L are stoichiometric parameters; x present deviation from ideal stoichiometry) was calculated using following equation:

$$x = n_O - (n_A \cdot L / J + n_B \cdot L / K)$$

<div align="right">eq. 4.2</div>

where n_A and n_B are molar amounts of elements A and B, n_O presents molar amount of oxygen.

The Gemini 2 software uses typical phase description and notation (for example FCC1, FCC2, TET) according to the crystal structure and compostion. We tried to change the phase notation to be best understandable. However, if for example two face-centered cubic phases were present in the same system we kept the notation " Face-centered cubic phase 1" or "FCC1" and "Face-centered cubic phase 2" or "FCC2". Other example can be, if two liquid phases are present, we kept the notation " Liquid phase 1" and Liquid phase 2".

4.1.2 $Al_2O_3 - H_2O$ system

As shown in the *Figure 4.1* on the top the melting point of alumina in the presence of steam doesn't differ from the value known for inert atmosphere. Calculations at thermodynamic equilibrium assume only the existence of alpha-alumina and one liquid phase. Its oxygen over-stoichiometry, originating from alumina oxidation by steam, is depicted in the *Figure 4.1* (bottom chart). The deviation of oxygen from ideal stoichiometry is negligible reaching about 2.10^{-4} at 3000 K,

therefore, the melt – steam reaction doesn't pass over significantly. Careful look on the gas phase composition (*Figure 4.2*) brings out presence of non-oxidative reaction of alumina and steam producing aluminum hydroxides or oxo-hydroxides. Amounts of these compounds approach units of percent reaching 3000 K. The amount of generated hydrogen shows steady increase as typical for water thermolysis without presence of oxidative reaction producing hydrogen as mentioned above.
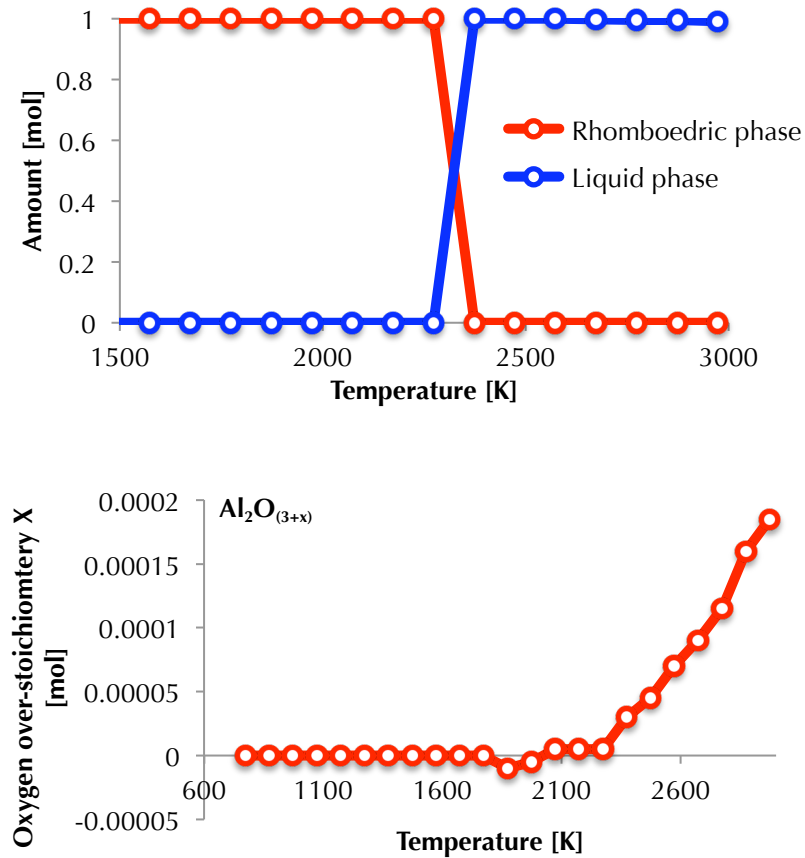
Figure 4.1 Phase evolution in the Al_2O_3 – H_2O system (top) and the oxygen over-stoichiometry of alumina solid and melt versus temperature (bottom)
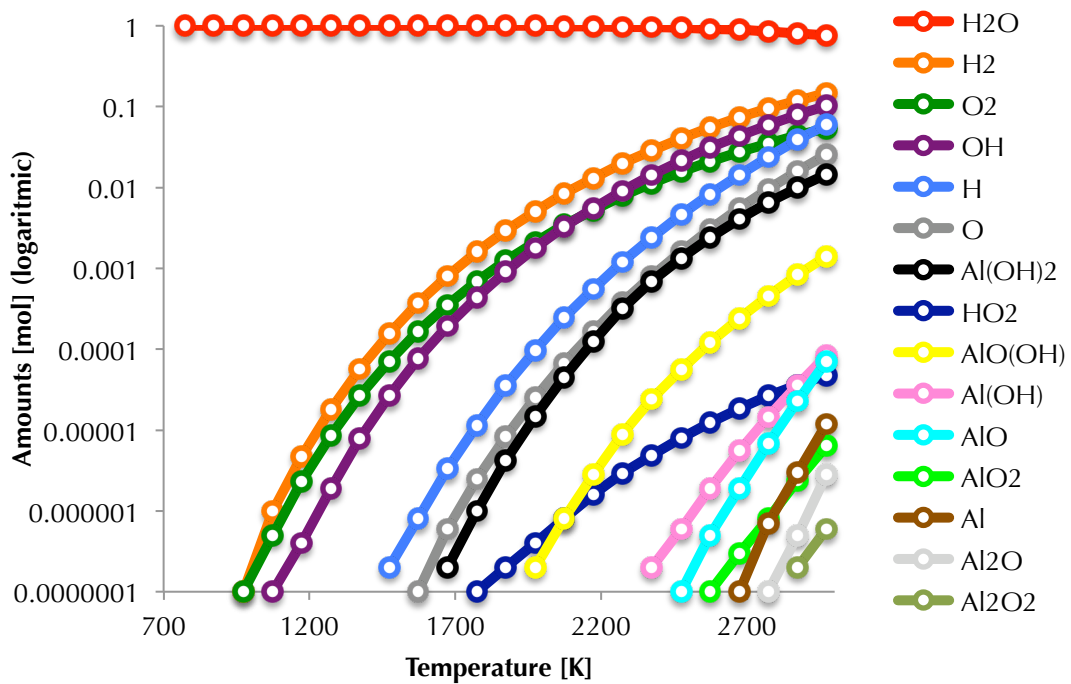
Figure 4.2 The gas phase composition versus temperature for the $Al_2O_3 - H_2O$ system

The numerous reaction products in the gas phase point to a variety of possible reaction routes for alumina a steam resulting mostly in volatile compounds.

4.1.3 $ZrO_2 - H_2O$ system

Results of the thermodynamic calculations well correspond to the known behavior of zirconium dioxide. The monoclinic phase transforms into the tetragonal phase about 1450 K and into the face centered cubic phase about 2550 K (*Figure 4.3*).
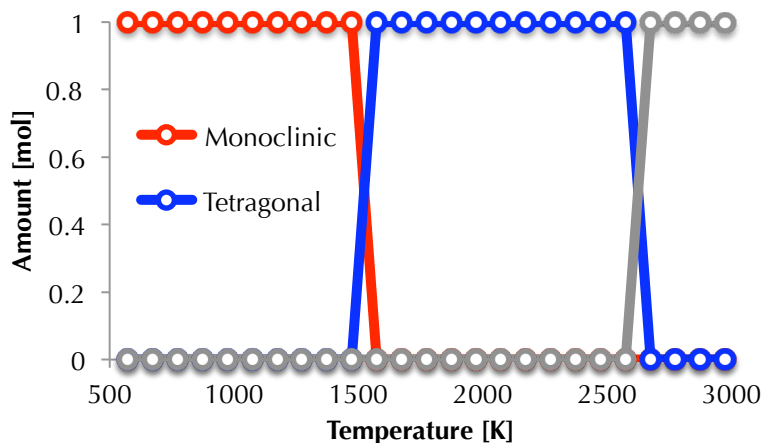
Figure 4.3 Phases evolution in the ZrO_2 -H_2O system

The oxygen over-stoichiometry versus temperature is given in the *Figure 4.4*. The model assumes that low over-stoichiometry is possible after transformation into fcc

phase. But, again as in the case of aluminum oxide the values are about 10^{-3} and therefor negligible.
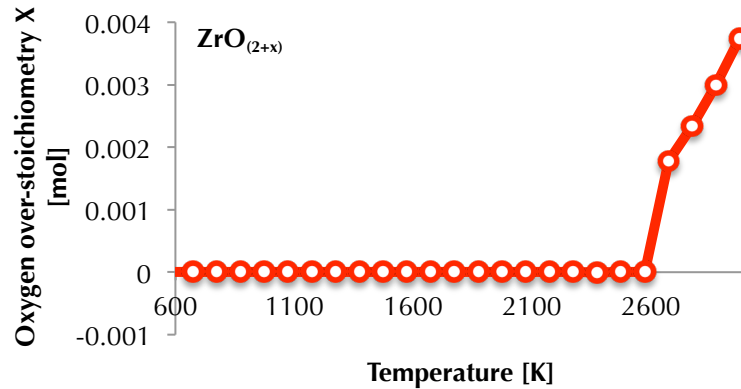
Figure 4.4 The zirconia oxygen over-stoichiometry versus temperature

Composition of the gas phase represents the *Figure 4.5*. The variety of compounds in the gas phase is notably lower than in the case of alumina-steam reaction. The melt products of melt evaporation (ZrO_2 and ZrO) can be observed. Other compounds can be attributed to the water decomposition. These results indicate high zirconia resistance and stability against high water attack (oxidative reaction or production of volatile hydroxides).
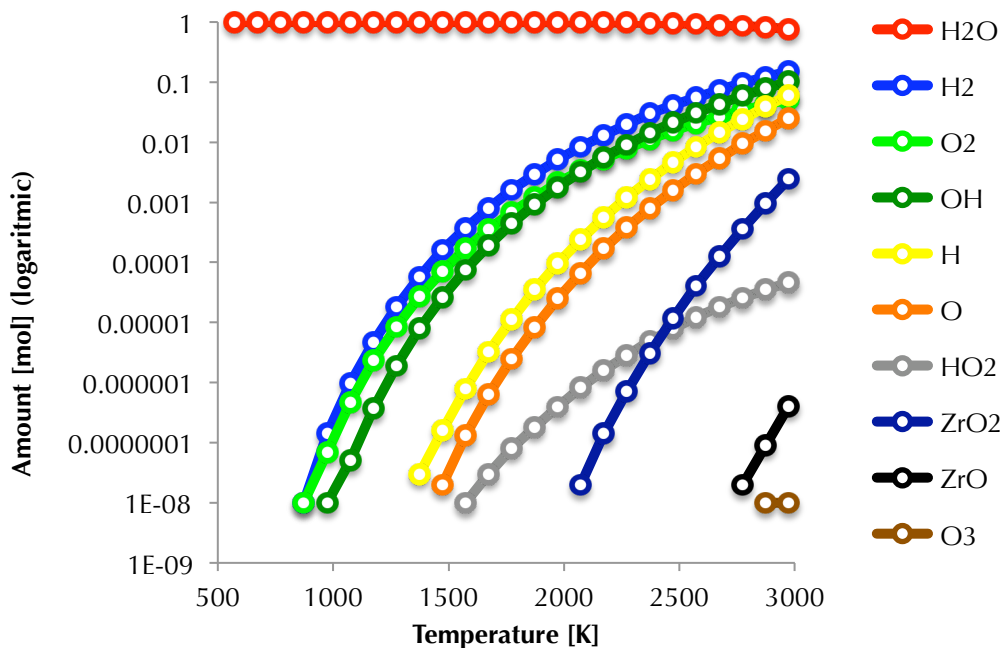
Figure 4.5 Gas phase composition versus temperature for the ZrO_2 - H_2O system

4.1.4 UO_2-ZrO_2 – H_2O system

The UO_2-ZrO_2 mixture, being a prototypic mixture of melted reactor core, is the most important. To model the interaction water/steam we used $U_{0.65}Zr_{0.35}O_2$

composition that corresponds approximately to 80 w. % of UO_2 and 20 w. % ZrO_2 widely used in KROTOS, FARO and TROI experiments. The overall phase evolution with temperature is depicted in *Figure 4.6*.
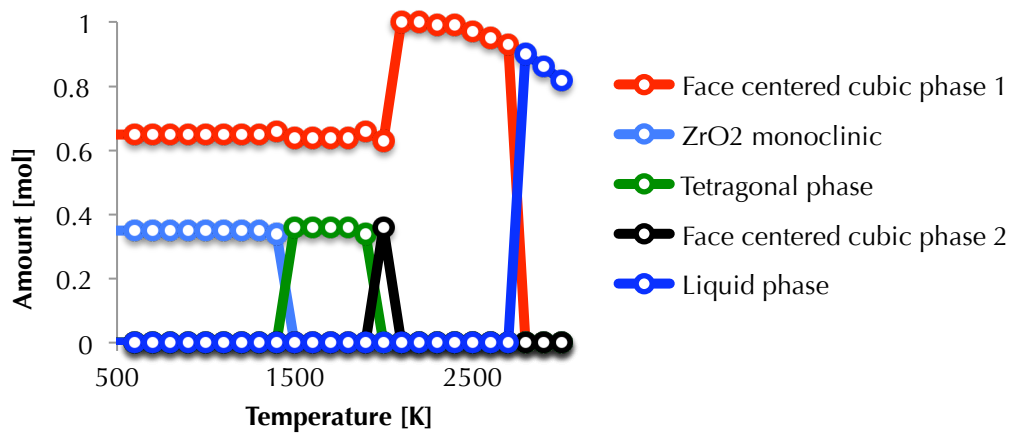
Figure 4.6 Evolution of the phases versus temperature in the $U_{0.65}Zr_{0.35}O_2$ - H_2O system

The results follow main known behavior of this system – melt solidification in face-centered cubic crystal lattice. However, several deviations can be observed. First of all, the solidus and liquidus lines are significantly shifted to lower temperature ($T_{solidus}$ = 2720 K for steam atmosphere and $T_{solidus}$ = 2880 K for inter atmosphere). Further, the amounts of fcc and liquid phases decrease at high temperature. The reason of such behavior lies in the oxidation of the melt by steam (mainly UO_2) into UO_3 and its transfer into the gas phase. Another important phenomenon connected to the melt oxidation by steam is the formation of oxygen over-stoichiometric phases (*Figure 4.7*). In contrast to zirconium dioxide and alumina the deviation from ideal oxygen stoichiometry reaches units of percent and becomes more important especially for the liquid state. The production of an over-stoichiometric compound is allowed by the ability of uranium to easily increase the oxidation state from +IV to +VI, while Al (+III) and Zr (+IV) are the highest stable states.
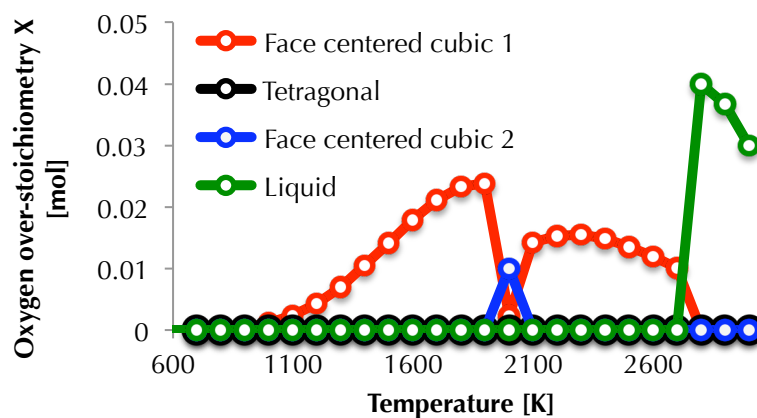
Figure 4.7 Oxygen over-stoichiometry of phases in the $U_{0.65}Zr_{0.35}O_2$ - H_2O system

Increase of the oxygen content in the condensed phases is connected to the hydrogen generation. The composition of the gas phase is shown in the *Figure 4.8*.

80
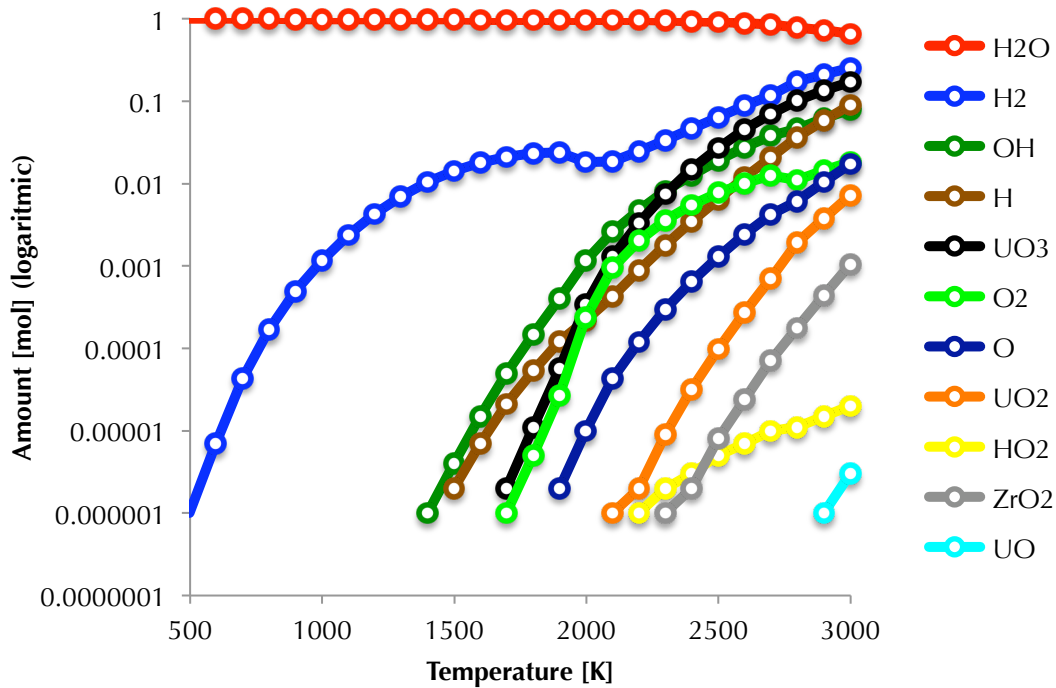
Figure 4.8 Gas phase composition in the $U_{0.65}Zr_{0.35}O_2$ - H_2O system

At the first view one can see the unusual evolution of hydrogen compared to previous systems. Secondly, above 2300K UO_3 is the most frequent compound in the gas phase after steam and hydrogen. The UO_2-ZrO_2 oxidation by steam to over-stoichiometric phases and UO_3 is, therefore, the key phenomenon in this system.

4.1.5 UO_2-ZrO_2 solidus and liquidus lines in oxidizing atmosphere

According to above-mentioned findings the effect of the oxidative properties of the atmosphere on the liquidus and solidus points is developed more in depth. Calculations describing $U_{0.65}Zr_{0.35}O_2$ in inert, steam and oxygen atmosphere were performed. *Figure 4.9* presents its melting/solidification behavior.
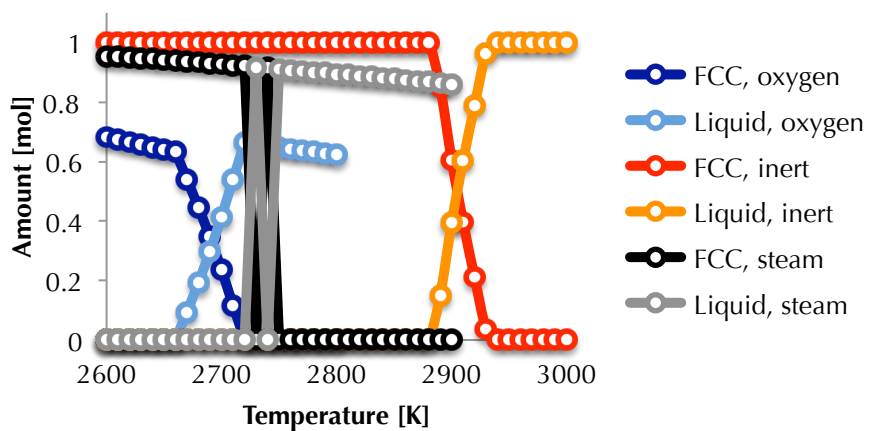
Figure 4.9 Equilibrium solidification interval of $U_{0.65}Zr_{0.35}O_2$ in inert, steam and oxygen atmosphere

The shift of the solidus and liquidus points is obvious (*Table 4.1*). The oxidation capability of the atmosphere rise in the direction inert < steam < oxygen. $T_{solidus}$ and $T_{liquidus}$ decrease in the same way. The differences are caused by oxygen over-stoichiometry of the solid and liquid phases (*Figure 4.10*) as for pure UO_2 discussed in *chapter 3*. As results from the nature of inter atmosphere, in this case the mixture has ideal stoichiometry. For steam atmosphere the melt oxygen stoichiometry is increased to i.e. 2.05 and in the case of oxygen atmosphere to 2.1 at the liquidus point.

Table 4.1 Solidus and liquidus points for $U_{0.65}Zr_{0.35}O_2$ in different atmosphere

Atmosphere	Temperature [K]	
Inert	Solidus	2880
	Liquidus	2940
Oxygen	Solidus	2640
	Liquidus	2720
Steam	Solidus	2720
	Liquidus	2750

In order to confirm above-mentioned observations calculations again using $U_{0.65}Zr_{0.35}O_2$ were performed this time in oxygen atmosphere, but with different initial pressure (0 to 4 atm). Shift of solidus and liquidus points to lower temperature displays a clear tendency with increasing oxygen over-stoichiometry adjusted by initial oxygen (system) pressure. The differences between the values for inert and oxidative atmosphere can be up to i.e. 500 K.
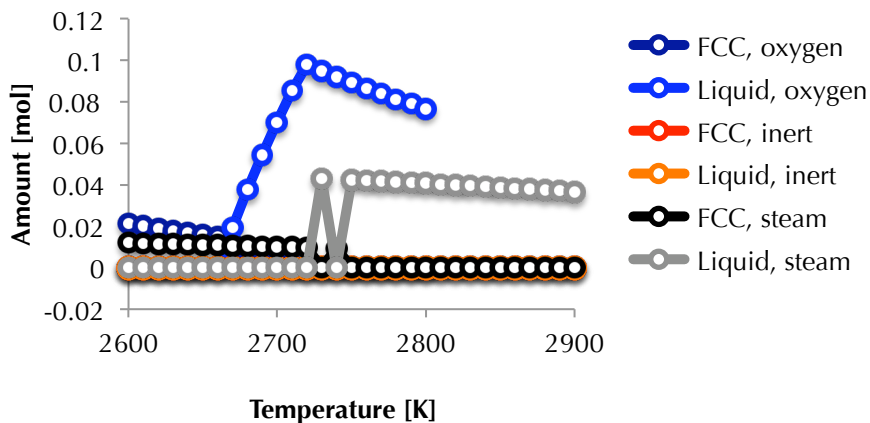
Figure 4.10 Oxygen over-stoichiometry of melt and fcc (face-centered cubic) phase in different atmospheres
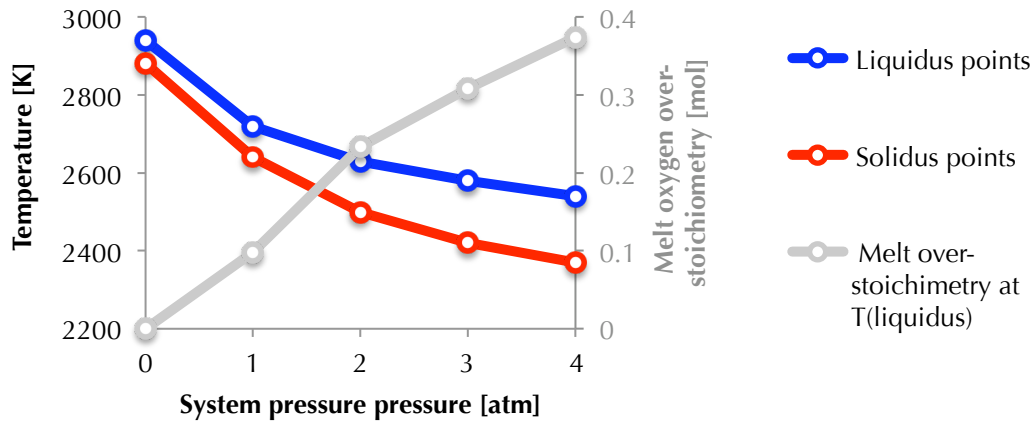
Figure 4.11 Solidus and liquidus points of $U_{0.65}Zr_{0.35}O_2$ as function of oxygen system pressure and melt oxygen over-stoichiometry at liquidus point

4.1.6 Hydrogen generation in UO_2-ZrO_2 – H_2O system

Melt – steam oxidative reaction gains its importance also due to the hydrogen generation - possible source of non-condensable gas in FCI. A series of calculations was carried out using a set of UO_2-ZrO_2 compositions (*Table 4.2*). The calculation input conditions are - pressure 1 to 4 atm, molar ratio material/water is 1, temperature 2600, 2800 and 2900 K.

The results are given in the *Figure 4.12* for all compositions and temperatures.

Table 4.2 Compositions of UO_2-ZrO_2 mixture used as data input

Notification	UO_2 w.%	ZrO_2 w.%	Chemical formula
100-0	100	0	UO_2
80-20	80	20	$U_{0.65}Zr_{0.35}O_2$
70-30	70	30	$U_{0.52}Zr_{0.48}O_2$
50-50	50	50	$U_{0.34}Zr_{0.66}O_2$
20-80	20	80	$U_{0.11}Zr_{0.89}O_2$
0-100	0	100	ZrO_2

2600 K

2800 K
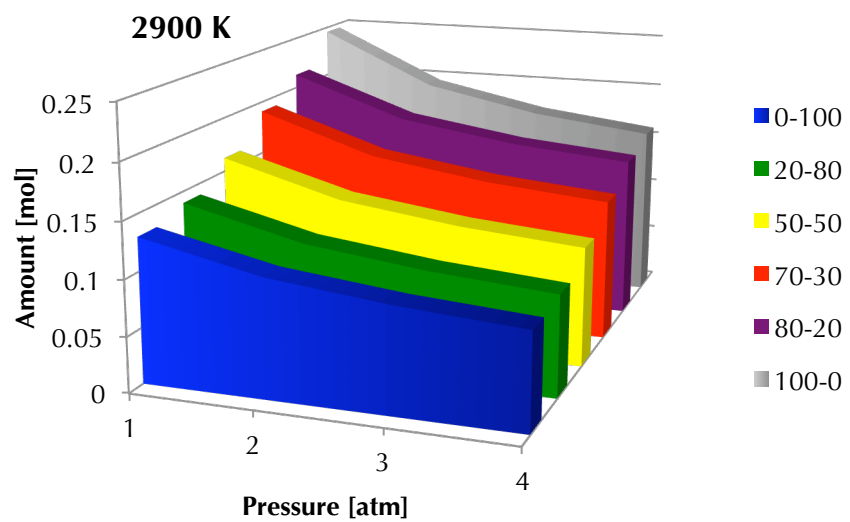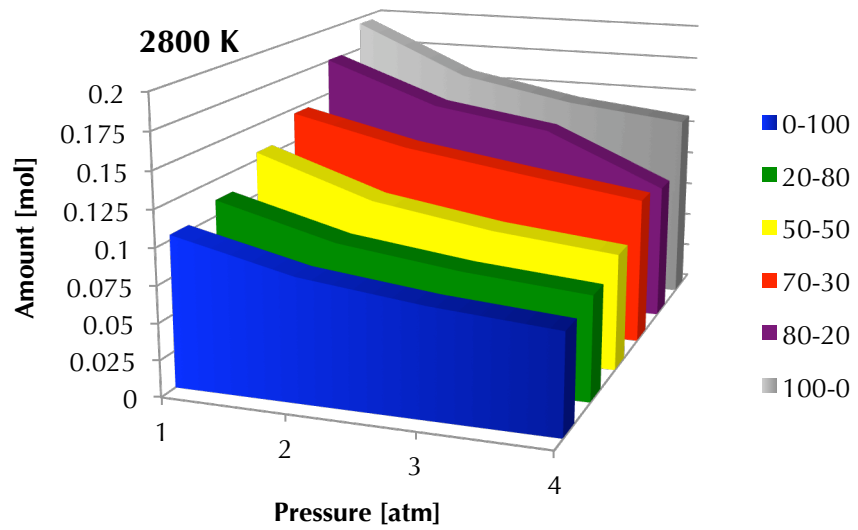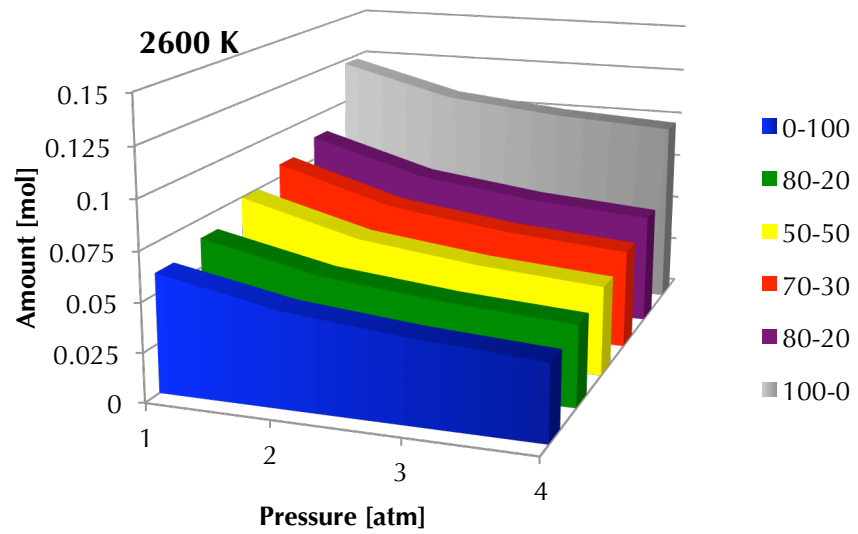
2900 K

Figure 4.12 Amounts of generated hydrogen in a set of UO_2-ZrO_2 - H_2O systems at 2600, 2800 and 2900 K. Notation of the composition is given in the Table 4.2

Two main tendencies can be observed: i) the amount of hydrogen increases with the content of UO_2 in the mixture; ii) the amount of hydrogen decrease with the system pressure. These results confirm the responsibility of UO_2 for hydrogen production by chemical reaction and stability of zirconia, in which case all the hydrogen is formed mainly by water thermolysis. The amount of produced hydrogen combining both effects (chemical reaction and water thermolysis) is considerably high and approaching the reaction extent of 25 % (0.25 mol of produced H_2 from initial 1 mol of H_2O) at 2900 K for pure UO_2.

4.1.7 Fe – H_2O system

First of all it is worth mentioning that this is a classical system pertaining to the classical corrosion science. However, the conditions during FCI are usually marked by higher temperatures and initial liquid state.

Evolution of the phases can be found in the *Figure 4.13*. The chart seems rather complicated at the view. It is caused by the computer software that assign different names to phases with very close composition and crystalline cell. With closer look the phase composition corresponds to face-centered cubic (fcc) phase (magnetite) and body-centered cubic (bcc) phase (slightly oxidized metallic iron). With higher temperature the phase composition gets settled on fcc FeO (wüstite like) and bcc metallic iron. The situation is clearer, when the Fe/O molar ratio of all the phases is put up versus temperature (*Figure 4.14*). Above 1000 K two liquids are observed, one based on FeO and the other on Fe, adverting to the miscibility gap phenomenon.

Due to the oxidation of metallic iron the gas phase composition differs significantly from the previous systems (*Figure 4.14*). The amount of hydrogen is slightly higher than or almost equal above 1000 K. It should be repeated that these values correspond to the thermodynamic equilibrium, in reality the amount of hydrogen depend on the oxidation kinetics. Similarly to the aluminum oxide iron forms volatile hydroxide. On the other hand, the evaporation of metallic iron becomes strong at high temperature (more than 1% of Fe in the gas at 2400K).
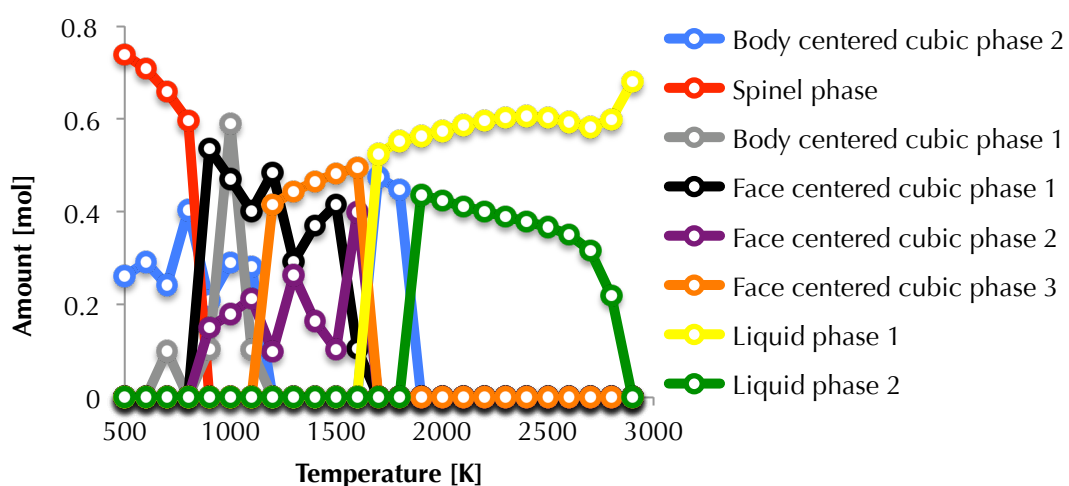
Figure 4.13 Phase evolution in the Fe – H_2O system

85
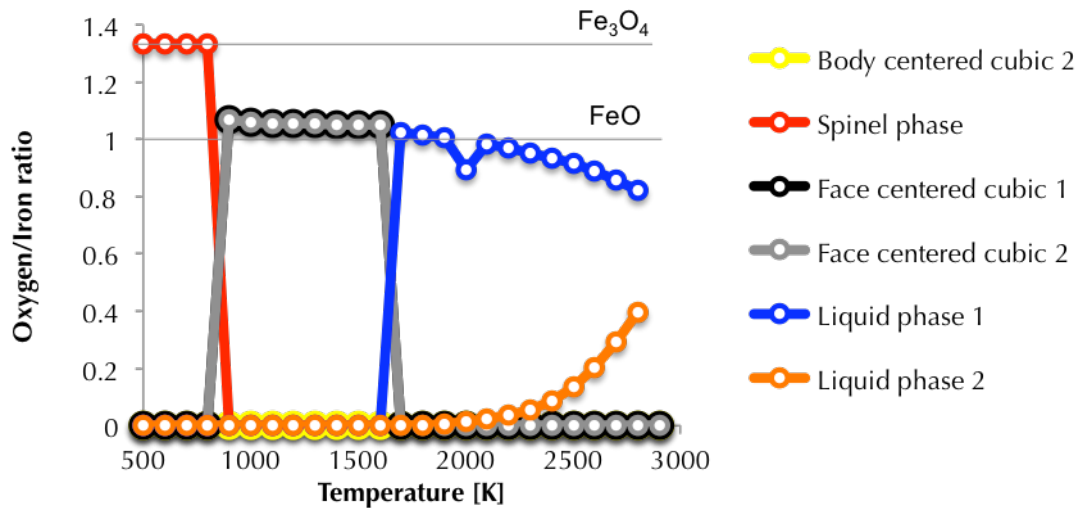
Figure 4.14 Oxygen to iron molar ratio with temperature
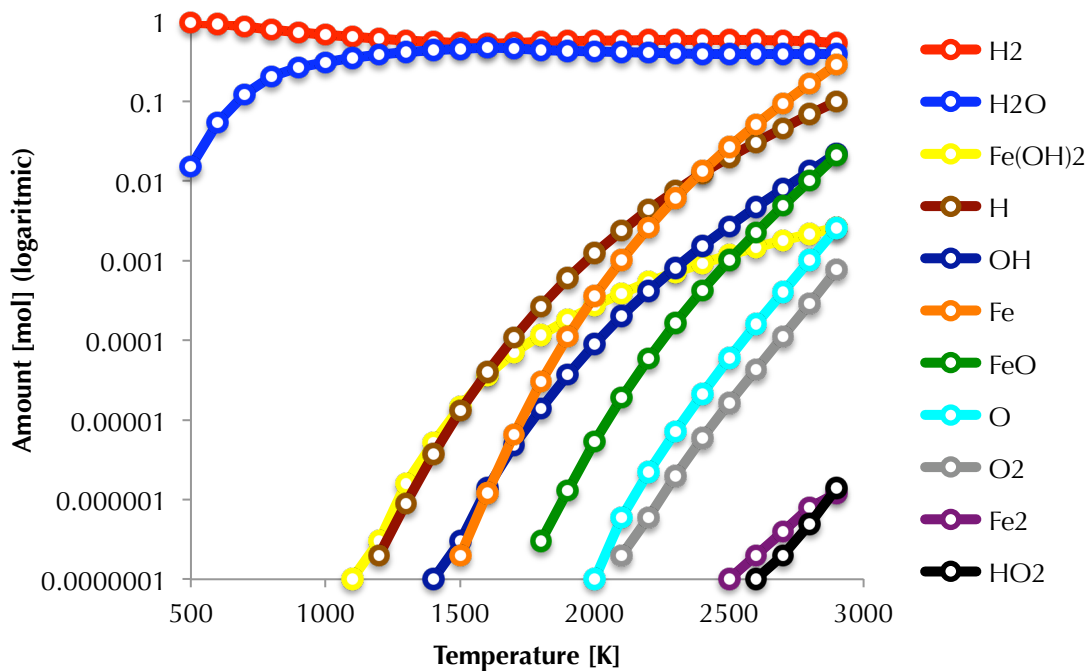
Figure 4.15 Gas phase composition in the Fe –H$_2$O system

4.1.8 Summary and comparison

The oxygen over-stoichiometry for all systems except iron is given in the *Figure 4.16*. The iron – steam system was skipped due to its complexness. The considerable ability to produce oxygen over-stoichiometric phase is confirmed for $U_{0.65}Zr_{0.35}O_2$. This phenomenon is linked to the hydrogen generation, the comparison is given in the *Figure 4.17*. A significant deviation for the $U_{0.65}Zr_{0.35}O_2$ – H$_2$O system can be seen considering the oxide systems. The iron – steam system should be treated in another way due to the metal ability to be easily oxidized. Of course, the amounts of hydrogen in this case are notably high.
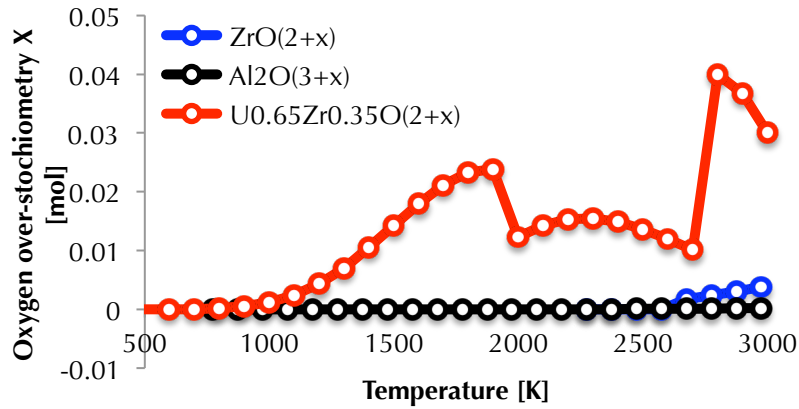
Figure 4.16 Comparison of oxygen over-stoichiometry for $U_{0.65}Zr_{0.35}O_2$, Al_2O_3 and ZrO_2 in steam atmosphere
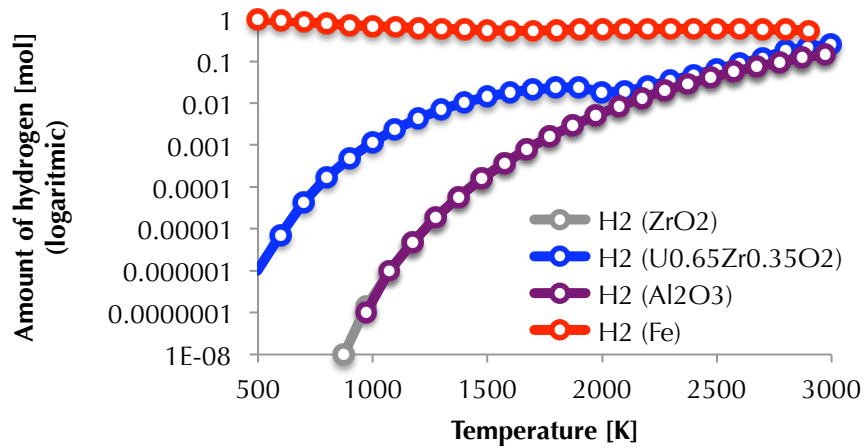
Figure 4.17 Comparison of hydrogen production for $U_{0.65}Zr_{0.35}O_2$, Al_2O_3, ZrO_2 and iron in steam atmosphere

The sum of all gaseous species for all systems versus temperature is plotted in the *Figure 4.17*. Although the amount of hydrogen is extremely high for iron – steam system compared to other systems, considering the sum of all gaseous species the difference is not so evident. From i.e. 2000 to 2500 K the total amount is even higher for UO_2-ZrO_2 mixture. It should be mentioned that alumina and zirconia have very similar behavior considering the hydrogen generation and amount of all gaseous species.

In conclusion, the UO_2-ZrO_2 mixture deviates from the threesome of studied oxide systems. It produce high amount of gaseous species including considerable amount of hydrogen. The oxidative reaction increases its oxygen stoichiometry and consequently affects the solidus and liquidus points.

Aluminum and iron can produce by non-oxidative reaction with water volatile hydroxides and oxo-hydroxides with way different thermo-physical properties than the original material.

Zirconium oxide seems to be very stable and resistant to any kind of chemical irritation by steam.
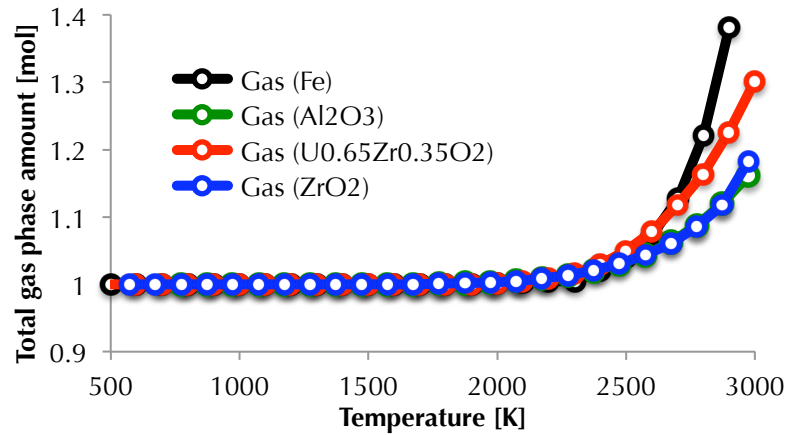
Figure 4.18 Sum of all the species in the gas phase for all the systems

Iron as a representative of metal goes through remarkable oxidation by steam. This effect can be observed for all metals except noble. The question then lies in the kinetics of this reaction and its application to FCI.

4.1.9 Conclusion

It can be seen that the material are not similar during reaction with steam at high temperature. The most chemical reactions in studied systems can be summarized as:

$$U_{0.65}Zr_{0.35}O_2 + xH_2O \longrightarrow U_{0.65}Zr_{0.35}O_{2+x} + xH_2$$
$$U_{0.65}Zr_{0.35}O_2 + xH_2O \longrightarrow U_{0.65-x}Zr_{0.35}O_2 + xUO_3 + xH_2$$

$$Al_2O_3 + 3H_2O \longrightarrow 2Al(OH)_3$$
$$Al_2O_3 + H_2O \longrightarrow 2AlO(OH)$$

$$ZrO_2 + H_2O \longrightarrow \quad \times$$

$$Metal + xH_2O \longrightarrow MO_x + xH_2 ; MO_a(OH)_b$$
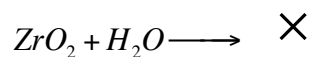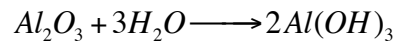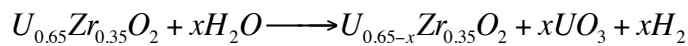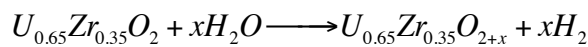
where a and b are general stoichiometric numbers pertaining to certain metal oxidation preference. According to the results the reaction extent can reach maximally 0.04 for $U_{0.65}Zr_{0.35}O_2$ reaction with water producing hydrogen at thermodynamic equilibrium.

4.2 Thermo-physical approach

The melt thermo-physical properties are believed to play important role in the SE efficiency. In following paragraphs a summary of the thermo-physical properties of main FCI materials will be given. A deeper extension will be done for the radiation properties and energy transfer by radiation.

4.2.1 Thermo-physical properties

A summary of thermo-physical properties of materials important for FCI studies is reported in the Table 4.3. Such values are used in the general FCI considerations.

Table 4.3 Thermo-physical properties of selected materials for FCI studies [4.5]

	Fe	UO$_2$	Al$_2$O$_3$	ZrO$_2$	Sn
Density [kg/m^3]*	7028	8860	2926	~ 5990	6990
Melting point [K]	1808	3120	2327	2983	505
Viscosity [mPa.s]*	0.1639	~4.3	0.0086	-	1.9 (500 K)
Surface tension [mN.m^{-1}]*	1888	5130	~650	-	~540 (500K)

* Approximate values at the melting point

Since the above-mentioned classical thermo-physical properties were already analyzed by numerous authors or FCI projects. Main focus of presented work will be given to the less investigated area – radiation properties of melts at high temperature and water. It can be noted that some important differences exist between nuclear fuel and similar materials, especially for the surface tension, the viscosity and the density. These differences on thermo-physical properties will have huge impact on FCI phenomena, especially during the premixing/fragmentation phases (Weber and Ohnesorge numbers).

4.2.2 Material effect in the radiation heat transfer

Radiation heat transfer is the fastest among three know mechanisms of heat transfer (conduction, convection, radiation) At high temperature radiation becomes predominant. In the past, certain attention has been given the role of the radiation heat transfer in FCI. Dombrovsky [4.6-7] worked out a model combining conduction and radiation heat transfer in droplet solidification. The model is based on the spectral properties of melt material, mainly on emission and reabsorption of radiation in near-infrared region. This property has a significant effect on the droplet solidification, when material is tarnsparent, semi-transparent or opaque. Alumina was found to be semi-transparent, while corium mixture is opaque. Reabsorption, in the case of opaque materials, makes the solidification slower, however, in the case of corium, having low thermal conductivity, a solid crust is formed rapidly. Semi-transparent material solidifies much more rapidly due to the large heat losses even from the central droplet region.

In following paragraph a simple radiation heat transfer model is presented. Instead of being focused on solidification like above-mentioned model, main focus is given to the real material high temperature emission and radiation absorption in water.

4.2.3 Spectral properties of black body and real materials

Most of the FCI computer codes calculate the radiation heat transfer at certain temperature according to the Stefan-Boltzmann law (*eq. 4.3*) regarding the melt as a gray body.

$$M_T = A\varepsilon\sigma T^4$$

<div align="right">eq. 4.3</div>

where A represents interfacial area, ε total emissivity of the material, σ Stefan-Boltzmann constant ($5.67.10^{-8}$ W m^{-2} K^{-4}) and T is thermodynamic temperature. The Stefan-Boltzmann law was derived from the integration of Planck law describing the spectral radiation of black body (*eq. 4.4*)

$$M_T = \int_0^\infty M_{\lambda,T}\, d\lambda = \int_0^\infty \frac{2\pi c^2 h \lambda^{-5}}{e^{\frac{ch}{k\lambda T}} - 1} d\lambda = \frac{2\pi^5 k^4}{15 c^2 h^3} T^4 = \sigma T^4$$

<div align="right">eq. 4.4</div>

where λ corresponds to the wavelength, c to the speed of light in vacuum, h presents the Planck constant ($6.626.10^{-34}$ J.s), k is the Boltzmann constant ($1.38054.10^{-23}$ J.K^{-1}. $M_{\lambda,T}$ is called spectral radiance at certain temperature. Comparing $M_{\lambda,T}$ of ideal black body and real material the spectral emissivity of real material can be defined (*eq. 4.5*).

$$\varepsilon_{\lambda,T} = \frac{M_{\lambda,T,real}}{M_{\lambda,T,black}}$$

<div align="right">eq. 4.5</div>

The total radiance of the real material at certain temperature can be then integrated as shown in *eq. 4.6*.

$$M_T = \int_0^\infty \varepsilon_{\lambda,T} M_{\lambda,T,black}\, d\lambda$$

<div align="right">eq. 4.6</div>

The spectral emissivities are usually experimentally measured values. The near-infrared region (1 to 10 μm) is important for radiation heat transfer. One should also note that the energy transferred by 1 mol of photons of 1 μm wavelength is significantly higher than by photons having 10 μm due to the Plank's law E=h.c/λ.

Spectral data for UO_2 was provided by Bober et al [4.8-9]. The spectral emissivity lies constantly between 0.8 and 0.9 independent on temperature and wavelength. Above 3500 K the spectral emissivity at higher wavelengths begins to decrease. This situation is depicted for 0.63 and 10.6 μm in the *Figure 4.19*. Unfortunately, no experimental measurements were performed on the UO_2-ZrO_2 mixture. The optical properties are usually taken as for pure UO_2 being its dominant component.
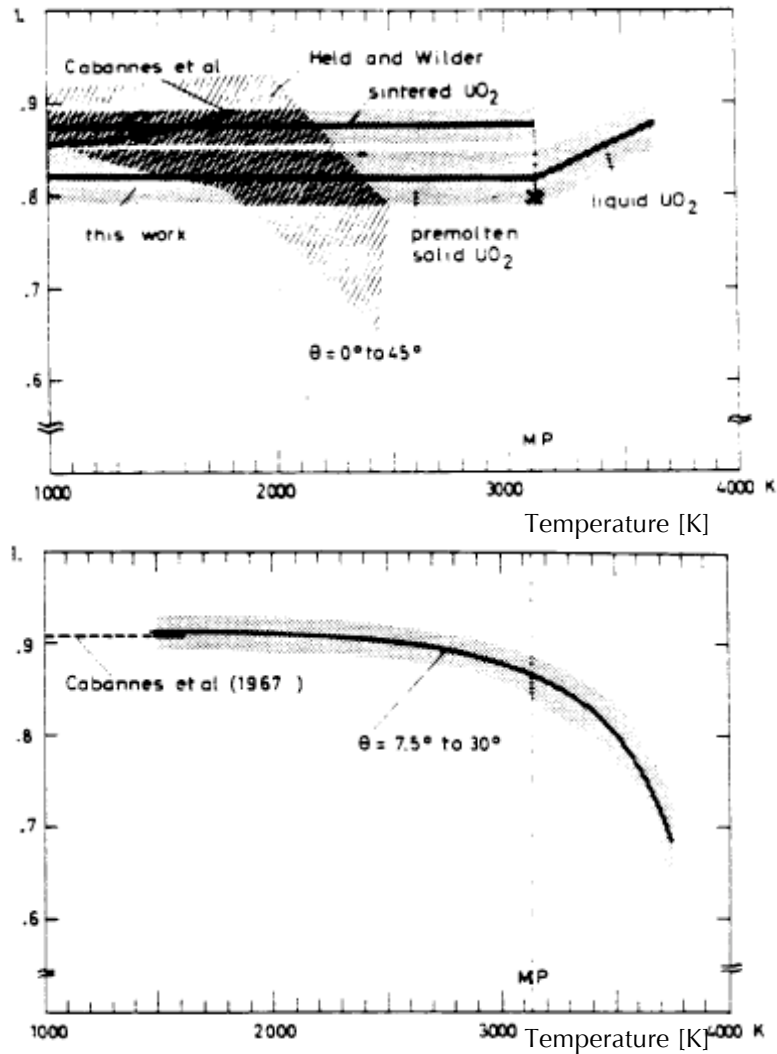
Figure 4.19 Spectral emissivity of UO$_2$ at 0.63 (top) and 10.6 µm (bottom) versus temperature [4.8]

Generally, the databases of spectral properties are not systematic in the sense of temperature or wavelengths. Therefore, the complete view is rather made from crops. However, the global tendency of spectral emissivity of aluminum oxide versus temperature is obvious. Low emissivity takes place in the region from 1 to 4 µm at low temperature. This valley disappears with increasing the temperature (*Figure 4.20*). These results prompt that aluminum oxide cannot be simply modeled as the black or gray body.

Similar situation arises concerning metallic and other materials. Example of spectral emissivities of steel, oxidized steel, silica and zirconia at certain temperatures are given in the *Figure 4.21*. Metals have generally low emissivity in the near-infrared region. On the other had, if the metal surface is oxidized, the emissivity increases dramatically.
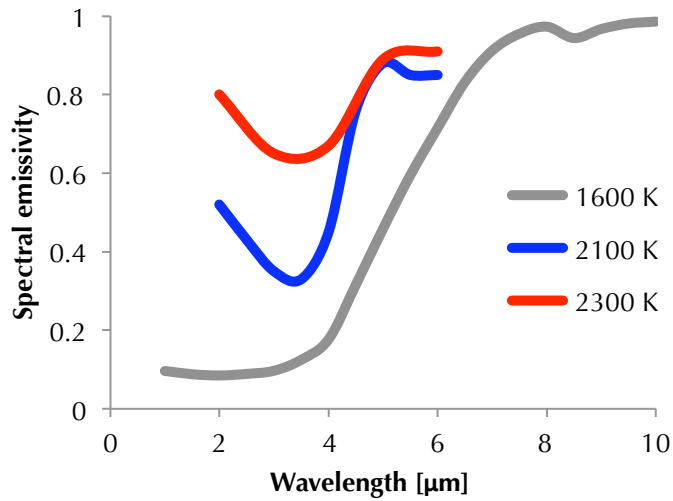
Figure 4.20 Spectral emissivity of Al_2O_3 in the near-infrared region at 1600, 2100 and 2300 K [4.10-11]
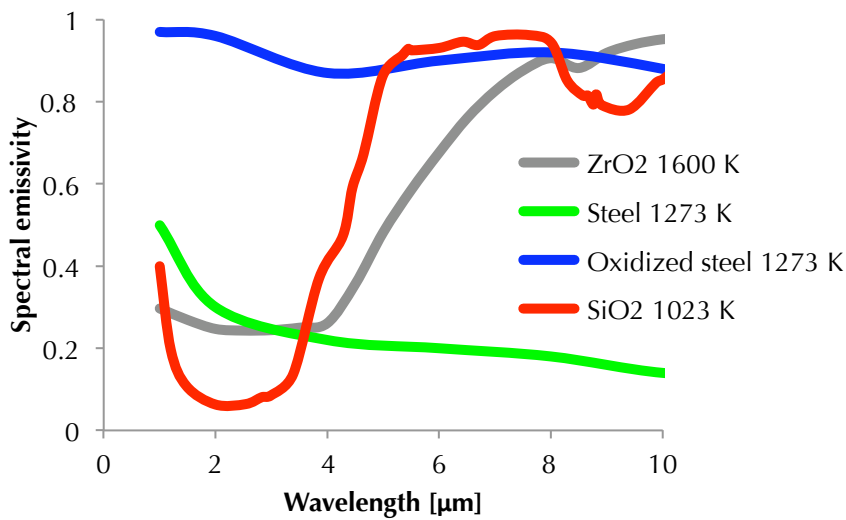
Figure 4.21 Example of spectral emissivity of steel, silica and zirconia at certain temperatures [4.10,4.12]

4.2.4   Absorption of thermal radiation and water spectral properties

The absorption of thermal radiation follows general Lambert-Beer's law written in the *Equation 4.7* and in integral form in *Equation 4.8*.

$$\frac{dM}{M} = -\alpha N_V dl$$

eq. 4.7

$$\frac{M}{M_0} = e^{-\alpha N_v l}$$

eq. 4.8

where M_0 means the initial radiation intensity, N_v presents the density per volume unit, l the distance and α represents the cross-section of absorption (absorption coefficient).

Water is the center of our interest as absorber of the radiation emitted from the melt drops during FCI. In the near-infrared spectral region water has three absorption bands explained by the combination of stretching (symmetric and asymmetric) and bending molecular vibrations. These bands are located around 3, 4.6 and 6.1 μm (*Figure 4.22*)
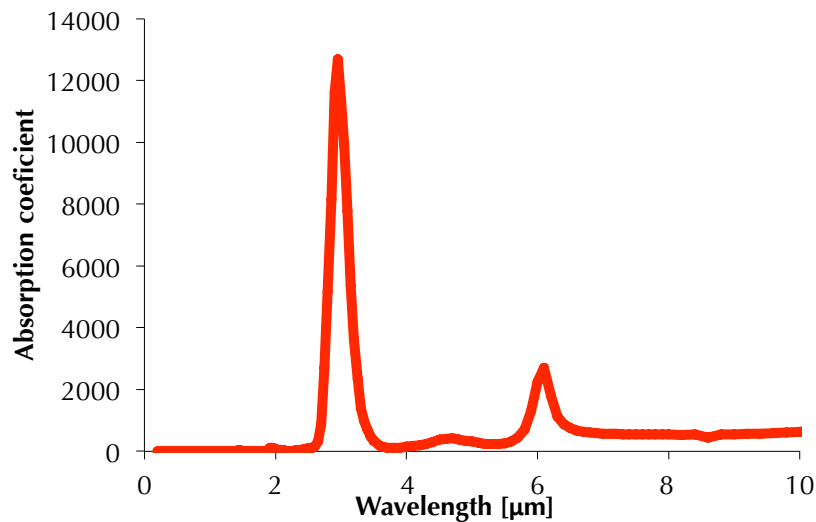
Figure 4.22 Absorption spectrum of water in the near-infrared region [4.13]

The main absorption peak lies at 3 μm and strongly exceeds the size of the other two peaks. The shape of the spectrum doesn't change significantly while changing the state. Only in solid-state two bands (vibration and translation) arrive due to the crystal cell vibrations at lower frequencies (higher wavelengths).

4.2.5   Radiation heat transfer model

A difference can be found in the spectral emissivity of UO_2 (constantly i.e. 0.85 versus wavelength or temperature) and aluminum oxide (*Figure 4.23*). In the case of Al_2O_3 a cut-down of emissivity bellow 4 μm can be seen with decreasing temperature. In this interval, on the other side, the most important absorption band of water is located. The situation is depicted in the *Figure 4.23* and demarked by yellow fill.

In order to evaluate consequences of such situation, a 1D steady state model has been developped using *Equations 4.4* to *4.8* and above-mentioned spectral properties of Al_2O_3, UO_2 and water. A chart describing the model is given in the *Figure 4.24*. Radiation comes from the emitter through a steam layer 1 mm wide (500 K, 1 atm) having properties of ideal gas to liquid water (room temperature density). The model is focused just on thermal radiation, effects like phase transitions, other types of heat exchange, droplet shape or reflectivity are neglected.

Detail description of the model is provided in the *Appendix E*. It was written in MATLAB® programing code [4.14].
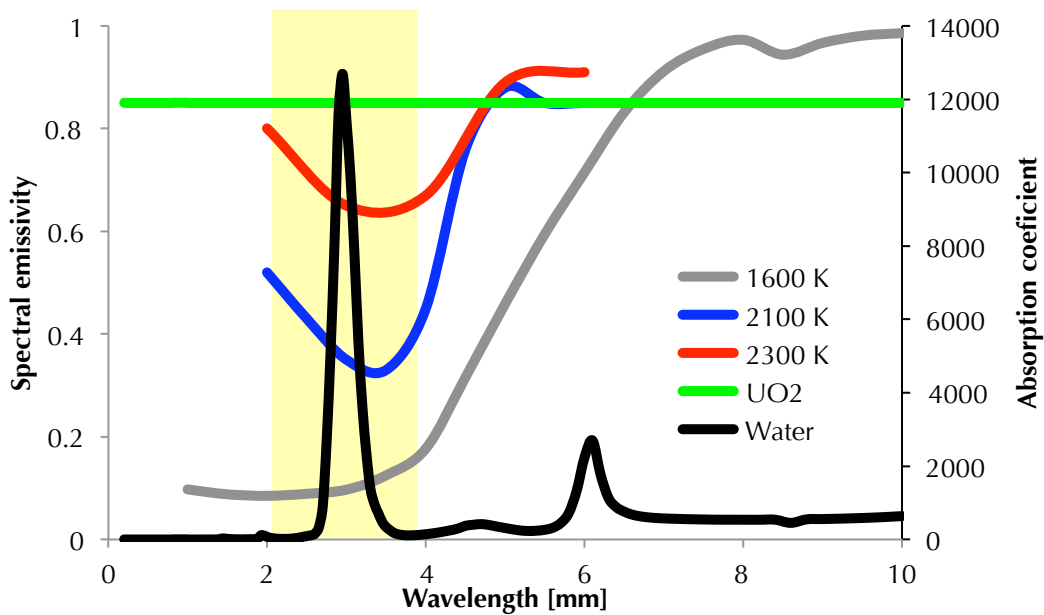
Figure 4.23 Overlay of the UO$_2$ and Al$_2$O$_3$ emission and water absorption in the near-infrared region
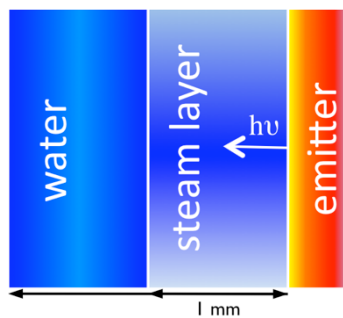
Figure 4.24 Description of 1D steady state model of radiation heat transfer

4.2.6   Results of the radiation heat transfer calculations

Information obtained by the model can be expressed as relation of the total radiation intensity (integrated over all the wavelengths) on the distance from the water/steam interface in the liquid water. Similarly, one can use the spectral radiation intensity (distribution) versus distance from the interface.

The *Figure 4.25* shows the spectral intensity distribution for UO$_2$ calculation on the water/steam interface just before entering the liquid water using the material spectral properties for 1600, 2100 and 2800 K. Ideal match can be found between the intensive UO$_2$ emission and water absorption that is indicated on the spectral distribution on the water/steam interface. This "resonance" is even stronger going from 2800 to 1600K. Therefore, during the melt/solid cooling the emission power is controlled by temperature and the efficiency of radiation absorption in water/steam remains very high.

The same information for Al$_2$O$_3$ is given in the *Figure 4.26*, but this time at 1600, 2100 and 2300 K relevant for alumina solidification. There is a significantly
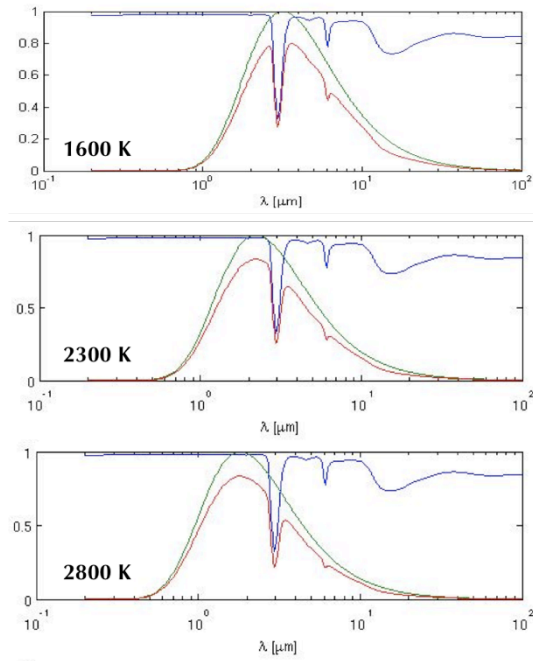
Figure 4.25 Overview of the radiation spectral distribution for UO_2; ideal black body – green; water/stem interface (real radiation) – red and for comparison water transmittance – dark blue

lower intensity of radiation at 1600 and 2100 K compared to ideal black body emission. The spectral properties play important role and mainly control the emission intensity. This effect becomes smaller with higher temperature. The efficiency of the radiation heat transfer to water should be lower than in the case of UO_2.
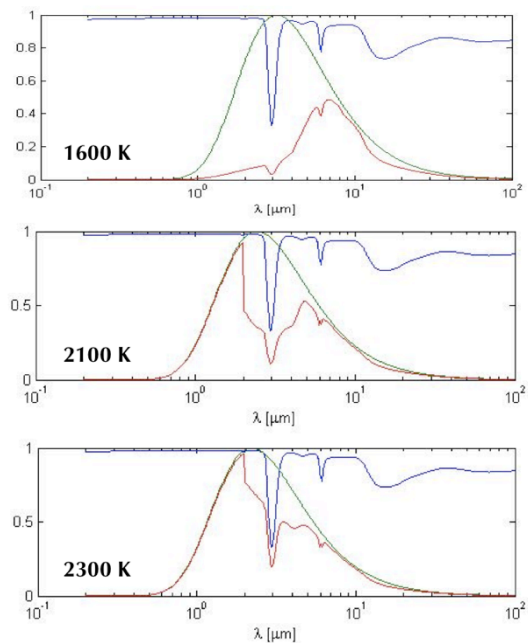
Figure 4.26 Radiation spectral distribution for Al_2O_3 at different temperatures, ideal black body – green, water/stem interface (real radiation) – red and for comparison water transmittance – dark blue

Finally, the integral radiation intensity versus distance from water/steam interface is shown in the Figure *4.27*. UO_2 is powerful radiation body at 2800 K compared to Al_2O_3 at 2300 K both around its solidification temperature. At 2100 K, the profile of energy absorption is almost copying line for UO_2 at 1600 K, thus 500 K cooler. For comparison, data for bright and oxidized steel at 1273 K were introduced.

One can argue that most of these considerations are for solid state and not for liquid state more important in FCI. First, this work was done from the viewpoint of void (steam) fraction built up that continues after the melt solidification as well. Secondly, the past work of Piluso et al. [4.15], proved that alumina melt can be during FCI highly sub-cooled (down to 1900 K).
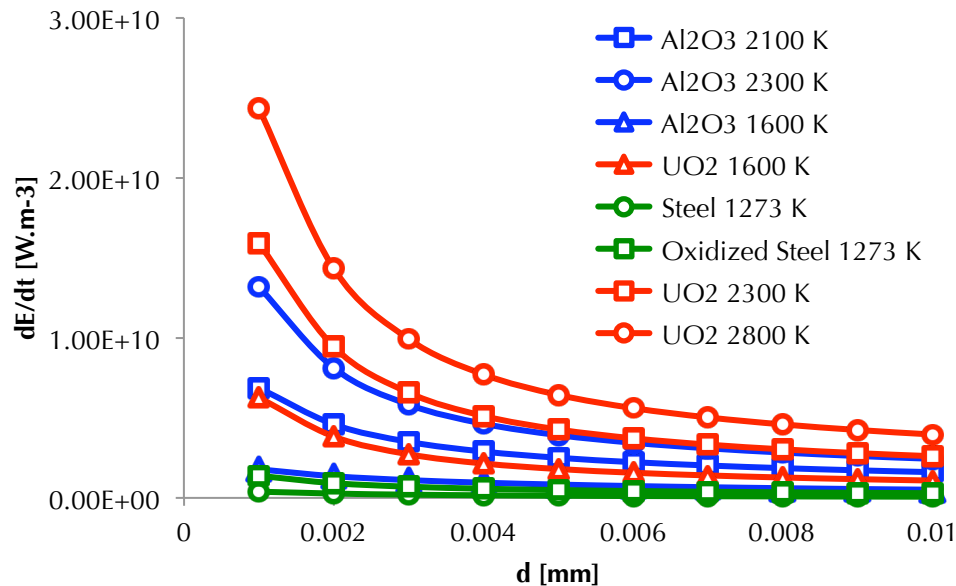
Figure 4.27 Integrated radiation intensity in distance from the water/steam interface for various materials and temperature

4.2.7 Role of emissivity by MC3D calculations

MC3D is a severe accident code used for FCI modeling of experiences and reactor case. For further information, see re. [4.16].

According to above-mentioned results a simple set of calculations was done using MC3D computer code in order to see the role of emissivity. We searched the possible variations in void fraction build up, droplet surface temperature.

Calculations were done with two emissivity values (0.2 and 0.8). The 0.2 total emissivity was chosen to low power radiation and the value 0.8 to represent the usual number taken for FCI calculations. The scheme representing the calculations set up is given in the *Figure 4.28*. Eight meshes ($1\times1\times8*10^{-3}$ m) system was chosen, while the first mesh was filled with alumina spheres (5 mm in diameters) occupying 20 vol. %.
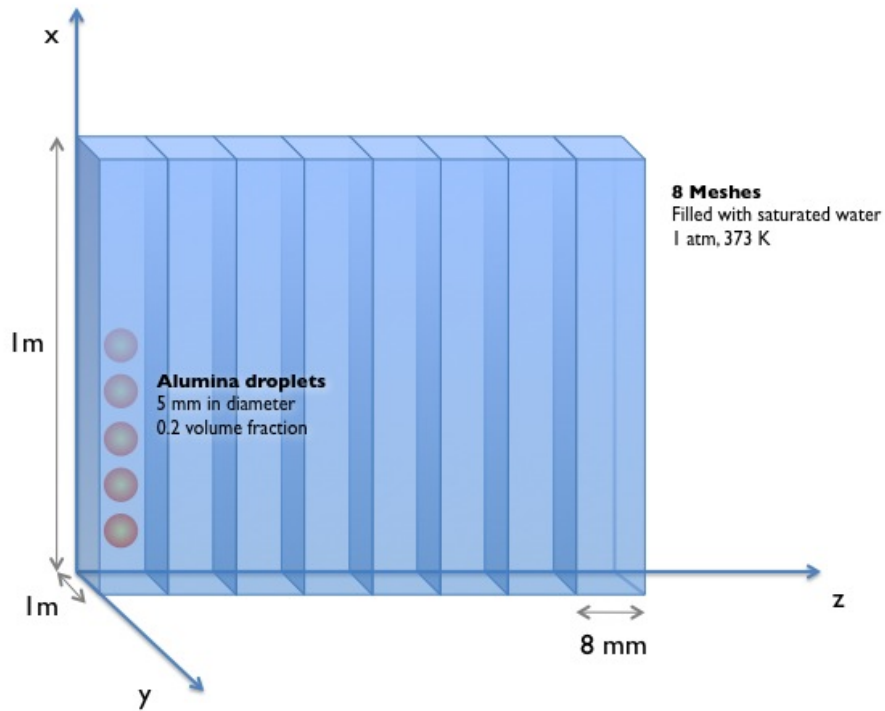
Figure 4.28 Scheme of model for MC3D calculations

Three initial droplet temperatures were chosen – 2700, 2300 and 1900 K to partially represent the difference in the temperature of the droplets of the fragmented jet. The water in all meshes is saturated at 1 atmosphere.

Following *Figures 4.29* a to c show the void fraction build-up in the first mesh containing alumina spheres for three mentioned droplet initial temperatures and having emissivity 0.2 and 0.8. The typical progress of steam generation has two parts; at first a plateau is reached rapidly, after certain time the steam fraction rises up gradually. An interesting fact was observed in all three cases with different initial temperature: the volumes of steam fraction are similar for both emissivity values, but the void fraction rise-up in time is delayed using lower emissivity. The time for the rise up after the first plateau is almost double for 0,2 than 0,8 emissivity.

The evolutions of the droplet surface temperature are shown in the *Figure 4.29* a to c. It was observed that the droplet with lower emissivity reaches lower temperature during the first void formation and after that the temperature decrease more slowly, in the case of 1900 K and 0.2 emissivity the temperature almost constant after 0.3 s.

In summary two main points were found:
i) The steam (void) generation is delayed in time with low emissivity droplet
ii) The droplet temperature after steam film generation decrease significantly slower in the case of low emissivity.
These two points have a direct impact for propagation and steam explosion.
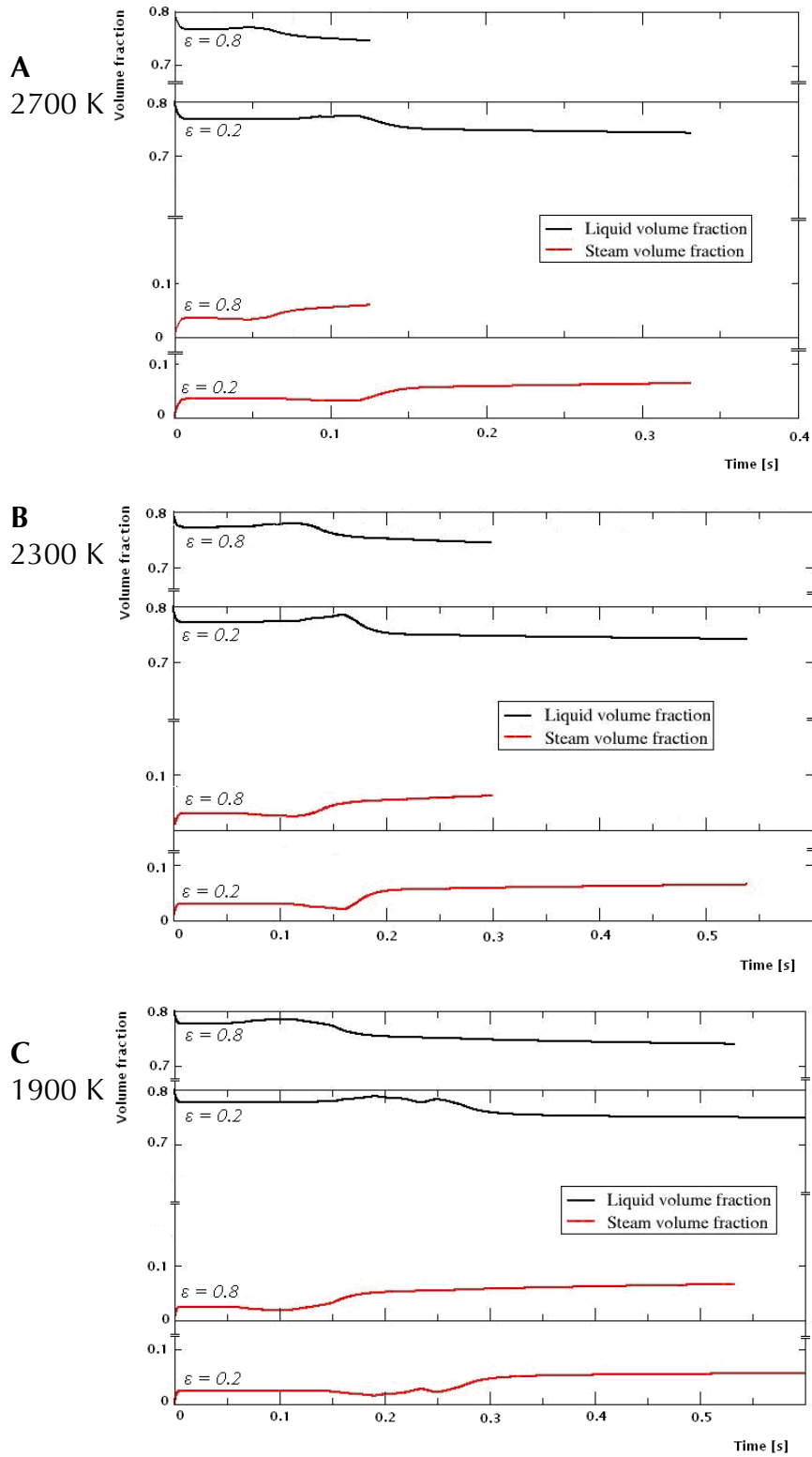
Figure 4.29 **Steam fraction generation for droplets initial temperatures: at A) 2700, B) 2300 and C) 1900 K.**

A
2700 K
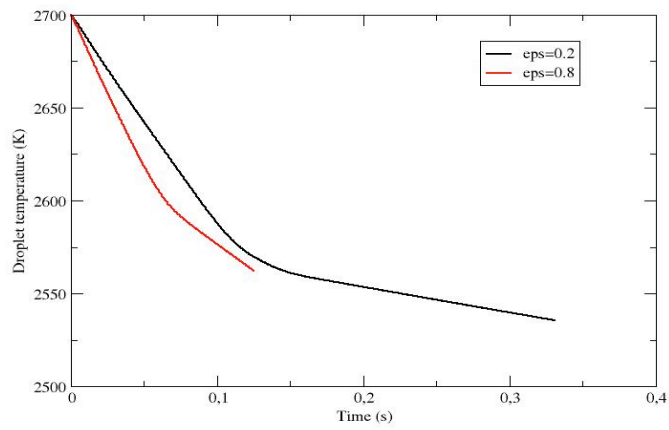
B
2300 K
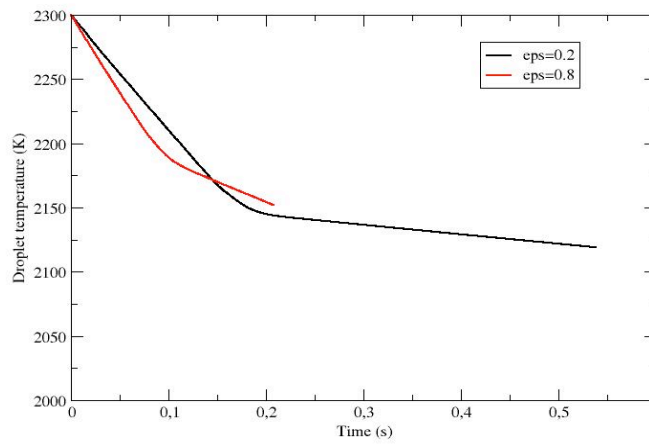
C
1900 K
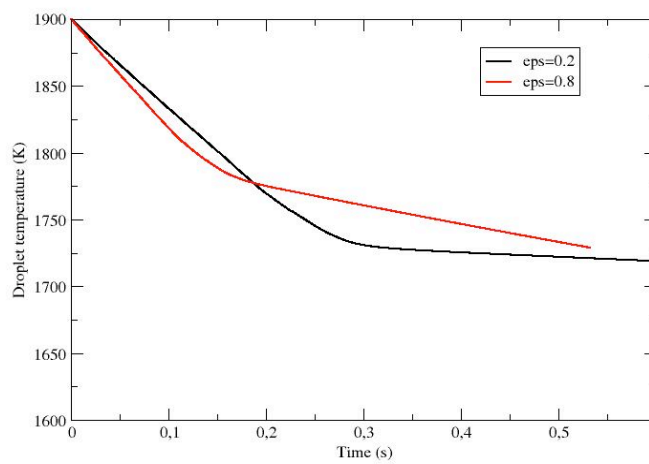
Figure 27 Surface temperatures of the droplets with the initial temperature

A) 2700, B) 2300 and C) 1900

4.2.8   Conclusion

It must be pointed that corium is a powerful radiator compared to alumina and non-oxidized metals.

If we compare the absorbed radiation energy in water just after 1 mm of steam layer, we can say that for UO_2 at 2800 K the absorbed energy is almost four times higher than for Al_sO_3 at 2100K having impact in void fraction generation.

Low emissivity can have impact on the delay of steam generation and slow decrease of the droplet temperature.

These facts show the importance of emissivity for steam explosion.

4.3 References

4.1   C. W. Bale et al: Calphad 26(2) (2002) 189-228

4.2   CALPHAD, www.calphad.org

4.3   B. Cheynet et al: Calphad 26(2) (2002) 167-174

4.4.   Themodata, 6 Rue du Tour de l'Eau, 38400 Saint Martin d'Heres, France, www.thermodata.online.fr

4.5   Development of a Database for Thermo-physical Properties of Corium, ISTC 3078, 207

4.6.   L. A. Dombrovsky, T. N. Dinh: Nuclear Engineering and Design 238 (2008) 1421-1429

4.7.   L. Dombrovsky: International Journal of Heat and Mass Transfer 43 (200) 2405-2414

4.8   M. Bober: High Temperatures High Pressures 12 (1980) 297-306

4.9   M. Bober, H. U. Karow: Revue Internationale des Hautes Températures et des Réfractaires 16 (1979) 51-56

4.10   Y. S. Toloukian, D. P. Dewitt: Thermal Radiative Properties: Non-metallic solids, New York, IFI/Plenum, 1972

4.11   V. Sarou-Kanian et al: Interantional Journal of Thermophysics 26 (2005) 1263-1275

4.12   W. Bauer et al: Spectral Emissivities of Metal Surfaces, 8th Symposium on Temperature and Thermal Measurement in Industry and Science, Berlin, Germany, 2001

4.13   G. M. Hale, M. R. Querry: Applied Optics 12 (1973) 555-563

4.14   MATLAB®, 1994-2012 The MathWorks, Inc.

4.15   P. Piluso et al: International Journal of Thermophysics 28(4) (2005) 1095-1114

4.16   http://www.irsn.fr/EN/Research/Scientific-tools/Computer-codes/Pages/MC3D-code-3830.aspx

Chapter 5. MISTEE, ECO and PREMIX debris

5

This chapter summarizes the experimental work performed on the MISTEE, PREMIX and ECO debris. These three programs use non-radioactive materials to simulate corium. Hereafter, the details about the experimental techniques are summarized in the *Appendix F*.

5.1 MISTEE debris

A set of MISTEE debris was selected for analyses. Information about the debris nature and experimental conditions are shown in the *Table 5.1*. R. C. Hansson, responsible for MISTEE facility at KTH Stockholm, provided us all the samples for analysis. The facility is focused on the single melt drop experiments.

Table 5.1 Description of the tests and debris coming from the MISSTE facility

Sample	Mass [mg]	T_{tin} [°C]	T_{water} [°C]	Steam explosion	Coarse debris (pieces)	Fine powder
16	692,0	1050	45	partial	3	yes
22	699,6	800	41,7	total	-	yes
25	701,4	800	52,6	no	2	no
26	703,3	1050	52,6	partial	2	yes

The tin debris after steam explosion was usually in a form of fine powder < 1 mm (test 22). If the melt went through non-violent quenching, the debris kept shape of a large droplet (test 25). A combination of larger droplets and powder was observed in experiments 16 and 26, which exhibited "partial" steam explosion. Closer look on the morphology obtained by optical microscopy is shown in the *Figure 5.1*. Hereafter, the powder samples are marked by "P" and large drops by "D".

In case of steam explosion, partial or total, the shape of the powder droplets is for all cases rather similar and doesn't change,. Round and elongated droplets, wires, hollow spheres or irregular octopus-like shapes can be found. Large coarse droplets have analogous morphology in the first view as well.
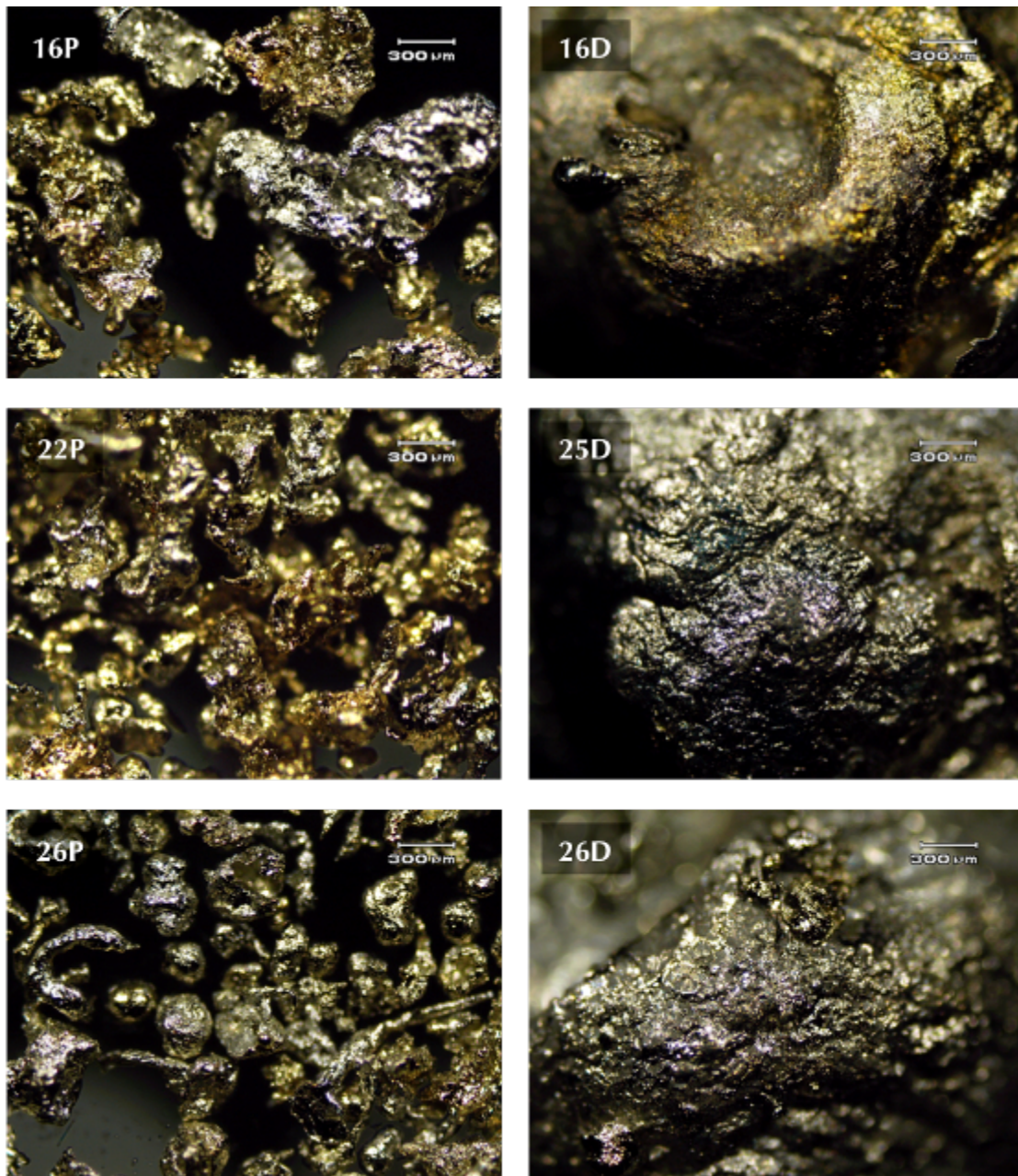
Figure 5.1 Optical microscopy of MISTEE debris, tests 16, 22, 25 and 26 (P – powder, D – large droplet)

5.1.1   MISTEE debris by SEM/EDS

All the debris were characterized by Scanning Electron Microscopy (SEM) coupled with Energy Dispersive X-ray Spectrometry (EDS) in its nature form. The important features found in the case of sample 16P are shown in the *Figure 5.2* a to d. The debris contain a mixture of shapes (spheres, wires, irregular). However, it is worth showing a detail of typical irregular particle (*Figure 5.2b*). This shape could be attributed to thermal fragmentation in the case of metallic melt. A brief example of fragmentation types implied by different shapes is given in the following *Figure 5.3*. Very well defined flat oxide micro-crystals grow sporadically on the debris surface during the interaction (*Figure 5.2d*). The SnO and SnO_2 crystallize in tetragonal phases,

showing an oxidation process of the metallic melt. Thus, the square shape of the crystals can be explained by the presence of (001) lattice plane parallel to the debris surface. Further, the (100) and (010) lattice planes confine the crystals perpendicularly to the surface (*Figure 5.2 d*).
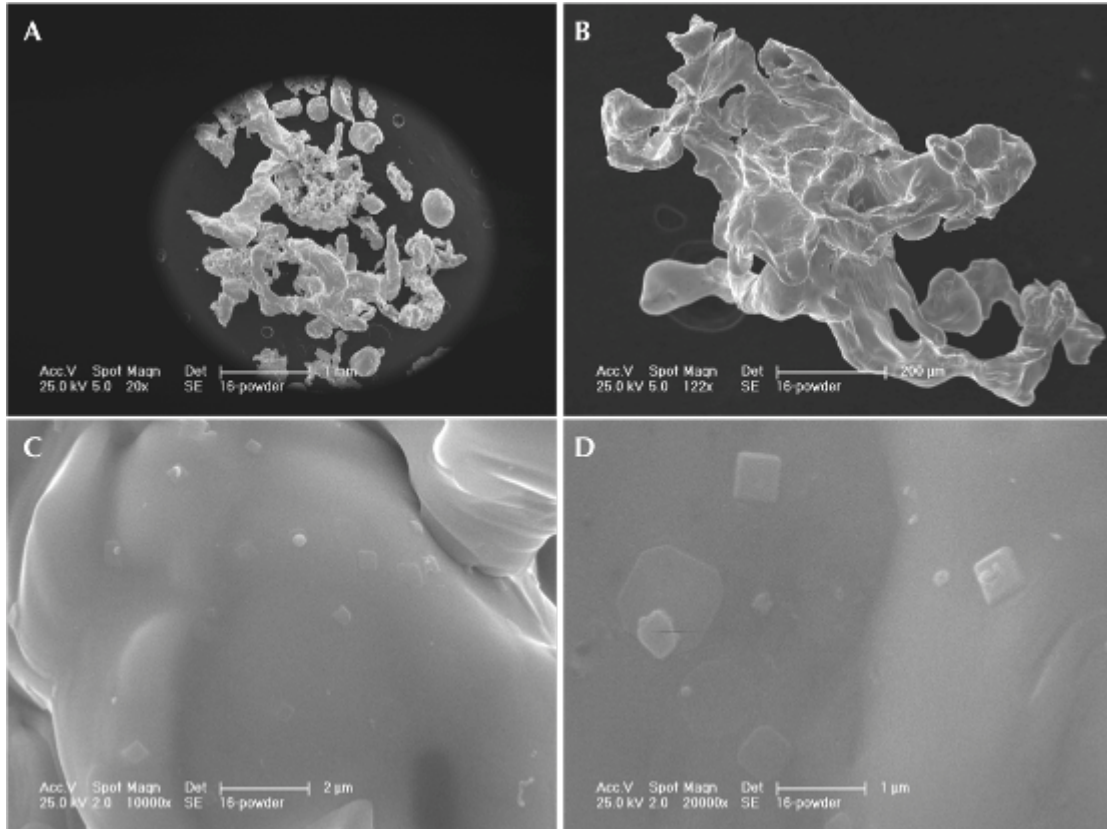
Figure 5.2 SEM/EDS studies of the sample 16P
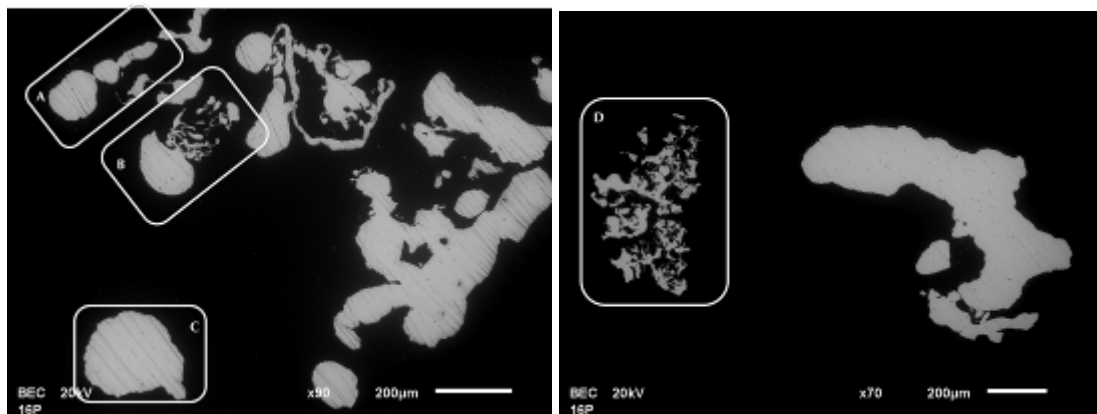
Figure 5.3 Cross-sections of 16P debris in SEM/EDS with demarked morphologies assigned to different type of fragmentation: a) sinusoidal fragmentation; b) fragmentation due to the non-symmetrical distribution of type water boiling; c) hydrodynamic fragmentation; d) thermal fragmentation

Examination of the large droplet (16D) surface is shown in the *Figure 5.4 a* to *d*. Drop surface is irregular and contains holes probably by erosion due to detaching of smaller melt pieces. The fact that there are two oxide phases, Sn and SnO_2, shows an

oxidation gradient: a protective oxide layer is formed at the surface and stops the oxidation process (*Figure 5.4 c,d*).
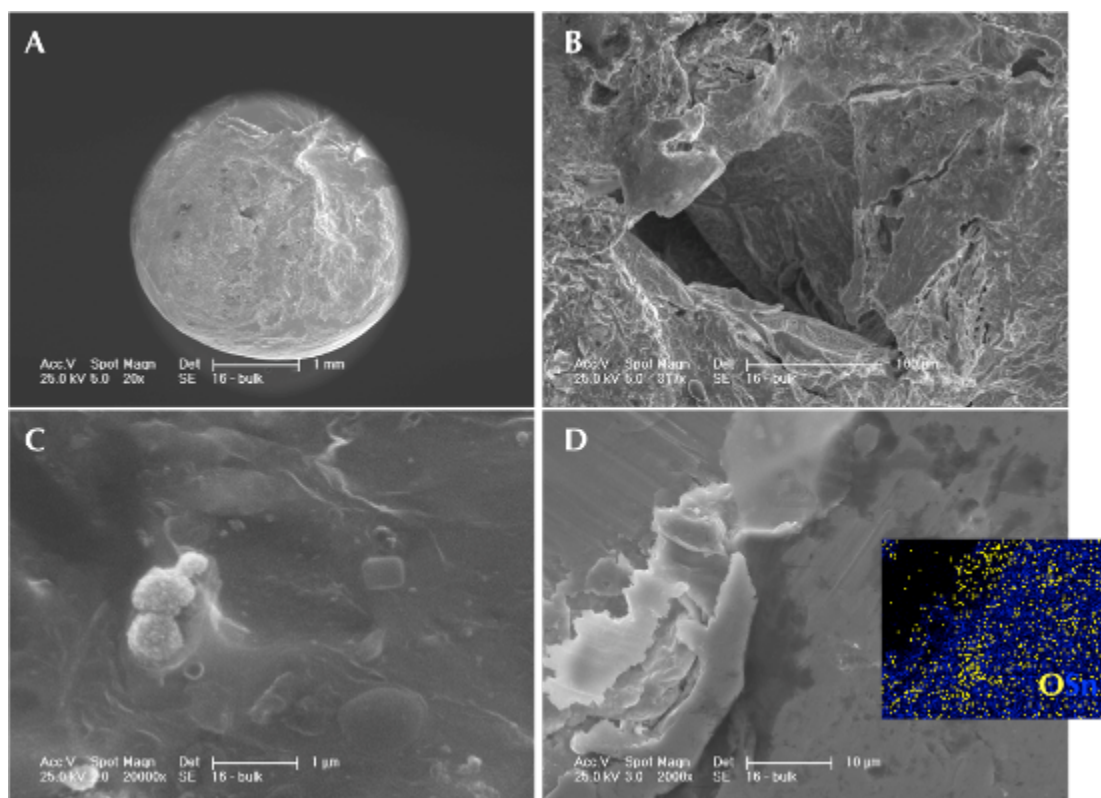
Figure 5.4 SEM/EDS studies of the sample 16D. Elemental mapping is shown in the picture D (oxygen – yellow, tin – blue)

Similar morphology as in the case of sample 16P can be found for test 22 (*Figure 5.5 a to d*), for melt with total steam explosion. Main difference is in the nature of surface oxidation. The tin oxide is not in the form of isolated square crystals, like for partial steam explosion, but rather as a continuous fine layer (*Figure 5.5 c,f*). Particles participating to the steam explosion have significantly high surface curvature, which can be clearly seen comparing *Figure 5.5 e* and *d*.

Test 25 didn't progress into the steam explosion and only coarse droplets were obtained (*Figure 5.6*). The surface is poorly oxidized, which can be attributed to low melt initial temperature. Fine oxide assemblies are randomly distributed in clumps (*Figure 5.6 d*) on the droplet surface.

26P debris shows morphology of above-mentioned powders (*Figure 5.7 a,b*). Surface oxidation looks like in the case of sample 16P. However, not only square tin oxide crystals were observed. More often star like crystals are found and transition between star and square as well (*Figure 5.7 c,d*). The micro-crystals of such morphology can be obtained by principal growth of the nuclei in orthogonal directions (110) and ($\bar{1}11$).

The surface oxidation is mostly developed in the case of sample 26D. The debris is covered by islands created by assemblies of micro-crystals (*Figure 5.8 a to d*). These micro-crystals seem to be well crystallized and are of a leaf like shape. High initial melt and water temperatures are therefore favorable for tin – water chemical reaction.

A confrontation of oxide surface content for all tests is given in the *Table 5.2*. Even if from morphological point of view the differences are explicit, the average

values obtained by EDS are close to each other. The only sure exception is sample 25D with smooth surface and low oxidation. In this case the melt quenching should have been very fast stopping the tin - water reaction progression.
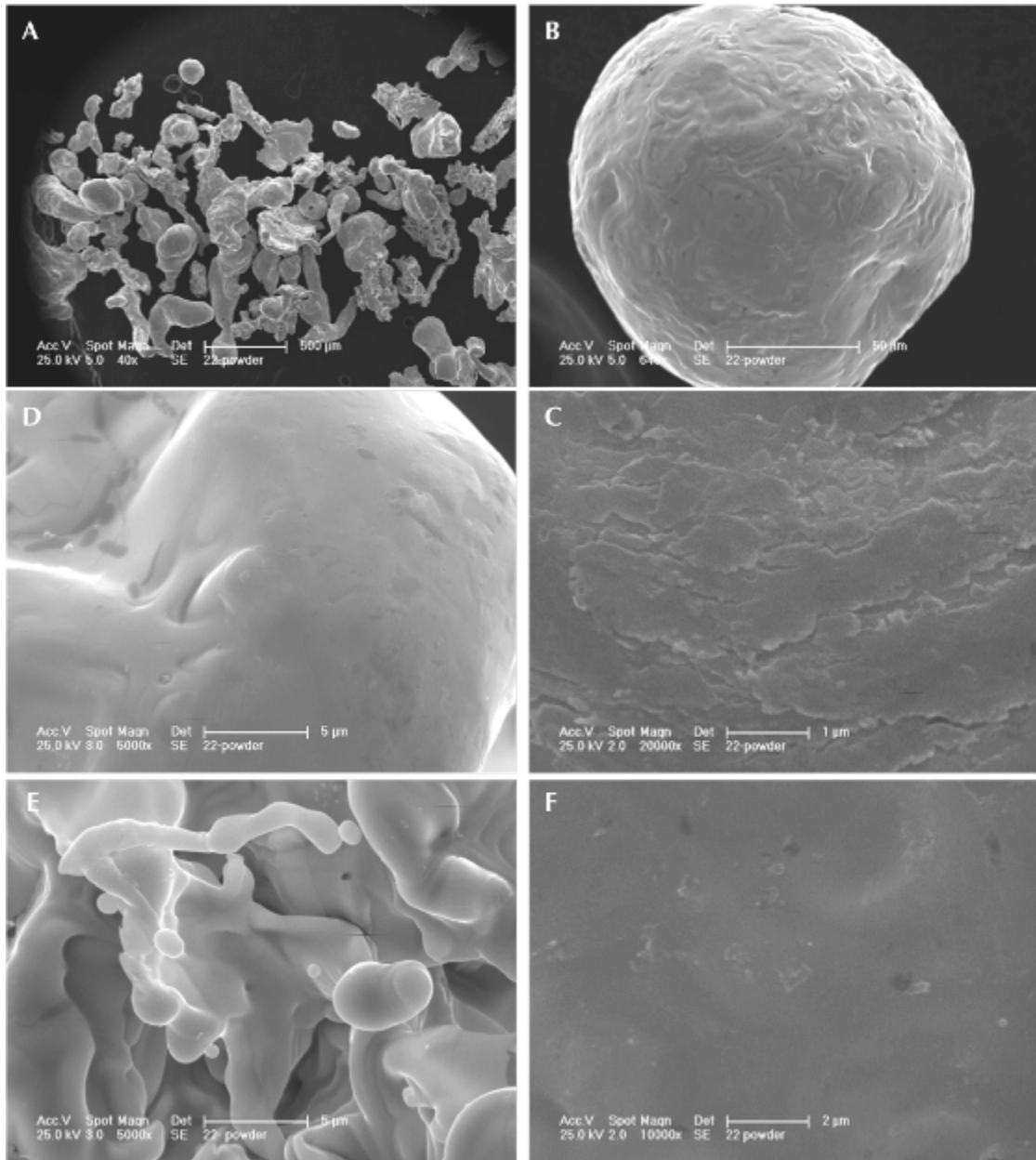
Figure 5.5 SEM/EDS micrographs of the 22P debris
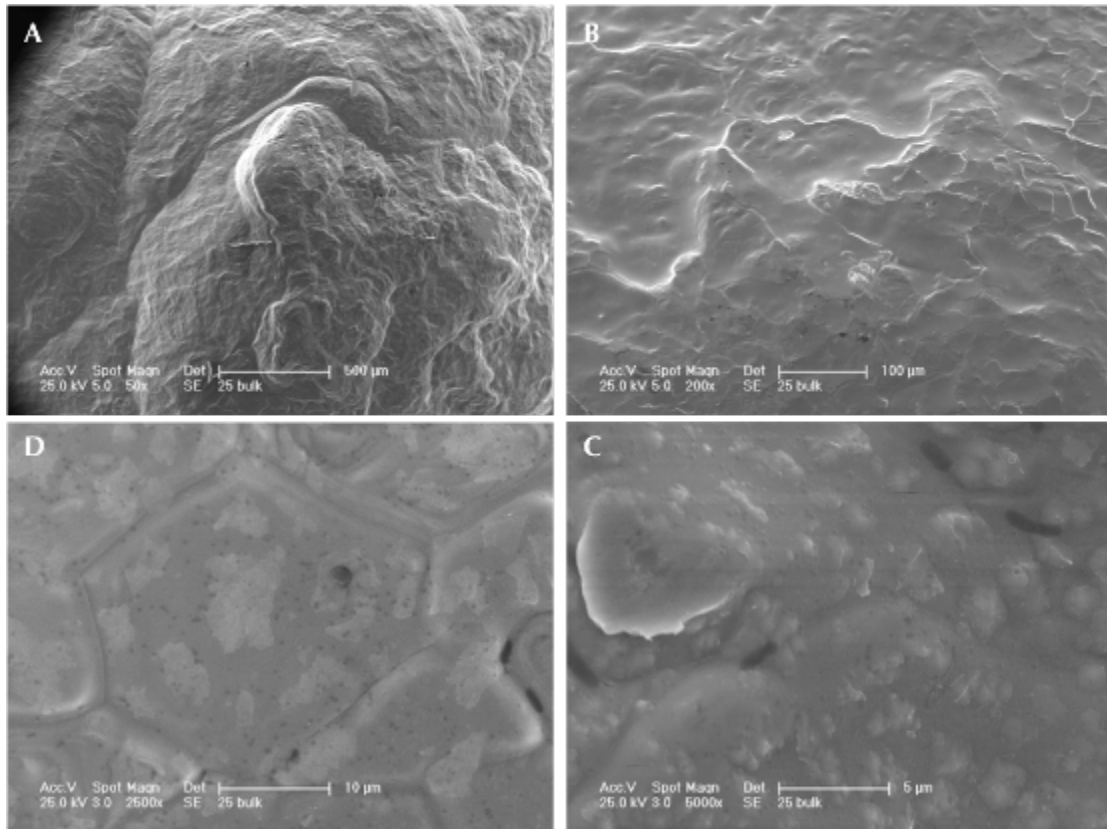
Figure 5.6 Sample 25D surface examination by SEM/EDS
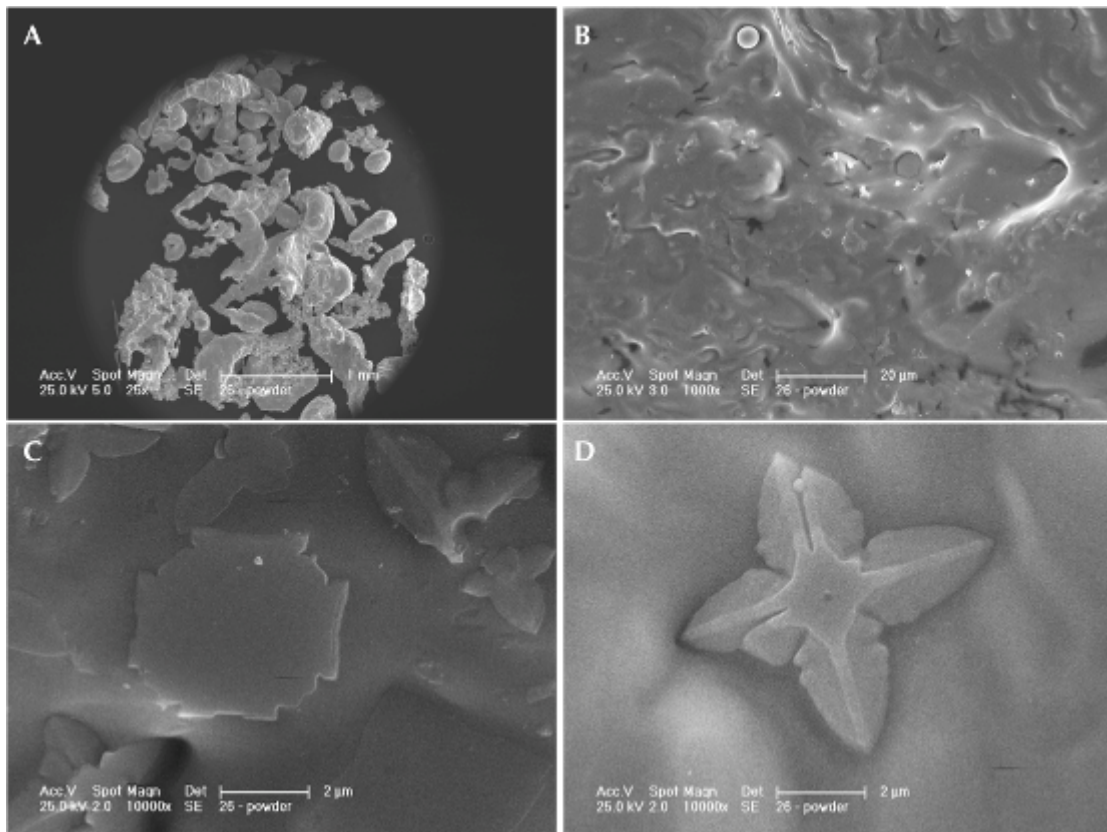
Figure 5.7 SEM/EDS micrographs of the sample 16P
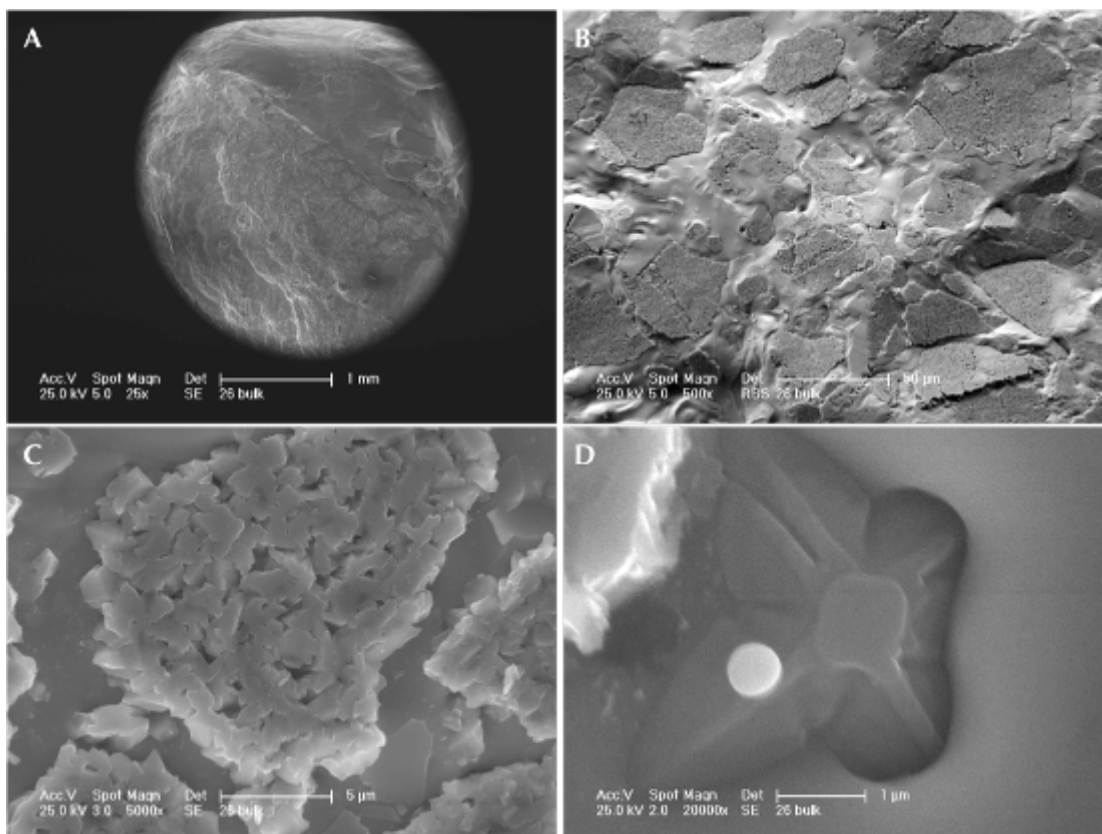
Figure 5.8 SEM/EDS investigation of sample 26D

Table 5.2 Average composition of the debris surface

Sample	O [mol. %]	Sn [mol. %]
16P	27	73
16D	10	90
22P	17	83
25D	7	93
26P	15	85
26D	15	85

Infrared spectroscopy of powder samples

Infrared spectroscopy (IR) measurements were performed on samples (16P, 22P and 26P). The *Figure 5.9* represents the IR absorption spectrum of powder samples and empty KBr pellet. It's obvious that besides Sn, the samples contain small amount of SnO_2. The bands around 3400 cm^{-1} (stretching vibrations) and 1630 cm^{-1} (bending vibrations) correspond to adsorbed water. The SnO_2 stretching vibration is present at 777,6 cm^{-1} [5.1-3]. Further, the peaks at 1100 cm^{-1} correspond to the bending vibration of OH group [5.4-5].

IR absorption spectra of as-received sample 22 and sample 22 annealed to 900°C is reported on the *Figure 5.10*. Sample annealed to such temperature is free of adsorbed water and OH groups and contains larger amount of tin dioxide. Changes in the intensitiy of OH bending vibration of normal and annealed sample are evident. Presence of small amount of dampness in all measurements is due to the hygroscopicity of KBr pellet.

The powder samples don't differ significantly in the composition or OH groups content. It was not possible for the coarse debris samples to measure in the transmission mode in KBr pellet.
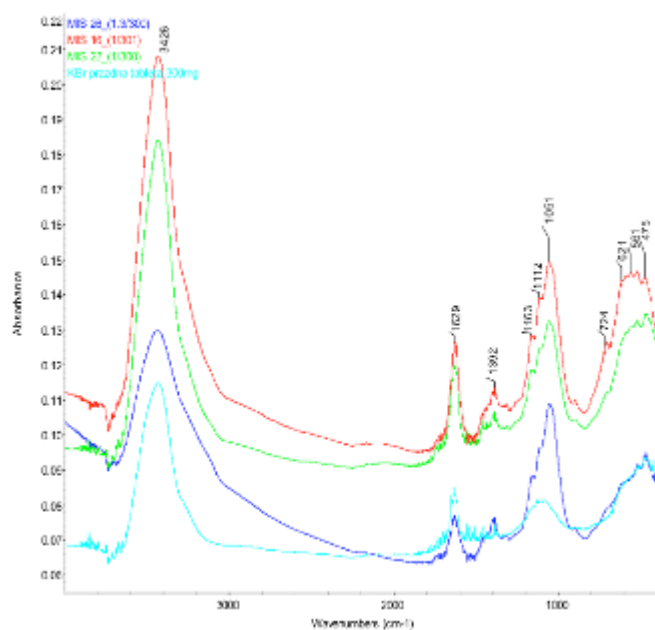
Figure 5.9 Infrared absorption spectra of MISTEE debris (16P – red, 22P green, 26P-dark blue, empty KBr tablet – cyan)
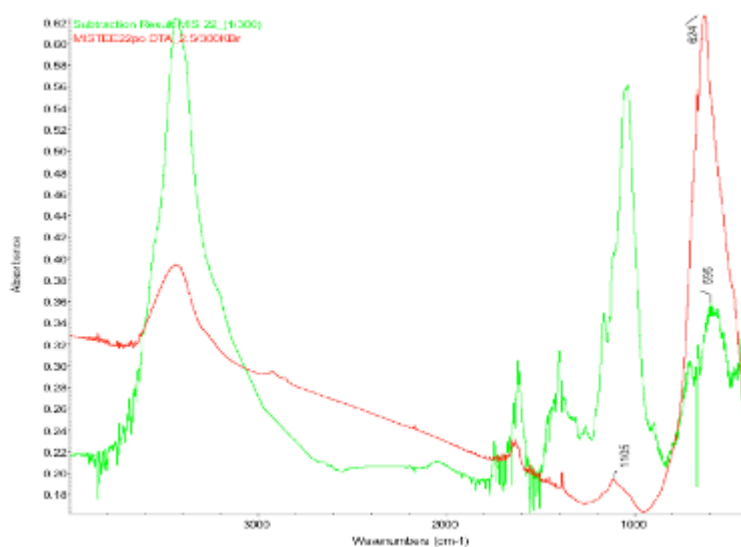
Figure 5.10 IR absorption spectra of sample 22P as received (green) and annealed to 900 °C (red)

5.1.2   Thermogravimetric studies of MISTEE debris

Classical thermogravimetric techniques (TG, DTA, DTG; 10°C/min, air atmosphere) were used to study the thermal behavior, especially the water release. The device was coupled with the mass spectroscopy to track in situ the out-coming gas

composition. The 22P debris was chosen due to its total participation to SE, the interaction with water should be the most intensive. At i.e. 122°C the first maximum of water release takes place. These water molecules are physically adsorbed on the surface by weak inter-molecular bonds. Weight decrease up to 200°C is 0,4 w. %. A second maximum is around 309°C. This weight decrease is insignificant, nevertheless, it proves chemically bonded OH groups to tin or more probably tin oxide. The start point of oxidation in air is around 550°C and strongly continues in two maxima at 605 and 813°C.
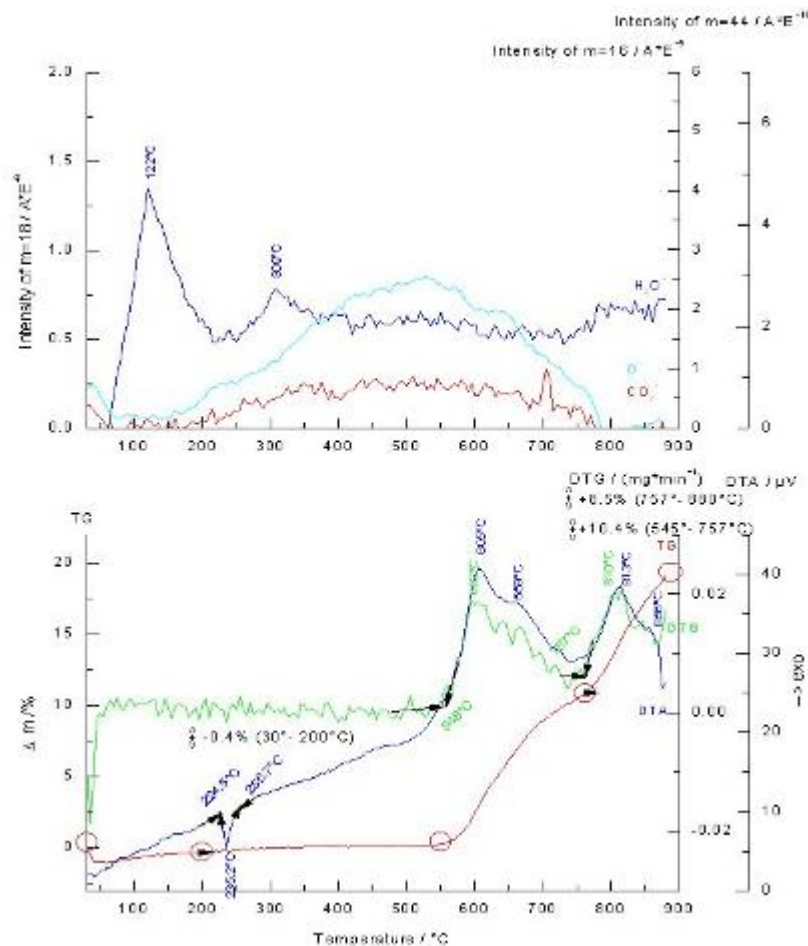
Figure 5.11 Thermogravimetric analyses of MISTEE 22P debris (bottom), in situ mass spectroscopy of released gases

5.1.3   Debris phase composition

The crystallographic composition of all the debris is very similar (*Figure 5.12*). The main component corresponds to tetragonal tin (a = b = 5.831 Å, c = 3.182 Å). The diffraction line positions and intensities are slightly scattered due to the fast melt quenching. Therefore, effects like preferential crystallographic orientation or cell deformation should be considered. The background noise can hide the possible minor components like SnO or SnO_2 (both tetragonal), the three most intensive diffraction lines are denoted in the *Figure 5.12*. Because the diffraction lines of tin oxides are not fully developed, it can be assumed that the content is very low: less than a few percents.

The diffractograms of the debris are shown in the *Figure 5.13*. Tin oxides can be identifies thanks to three most intensive diffraction peaks of SnO and SnO_2.
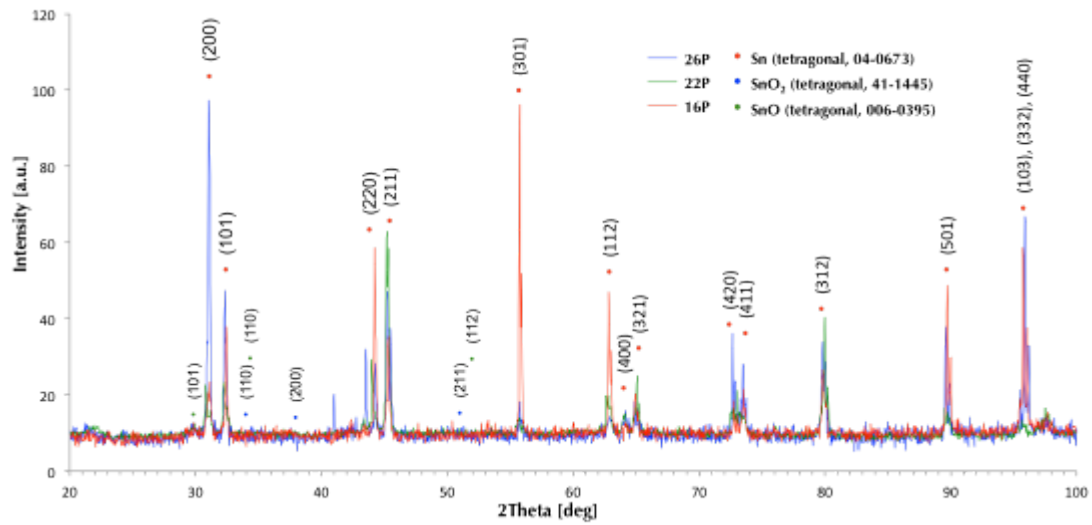
Figure 5.12 Powder X-ray diffraction patterns of the samples 16P, 22P and 26P; diffraction positions are marked for Sn and for the three most intensive peaks SnO and SnO_2
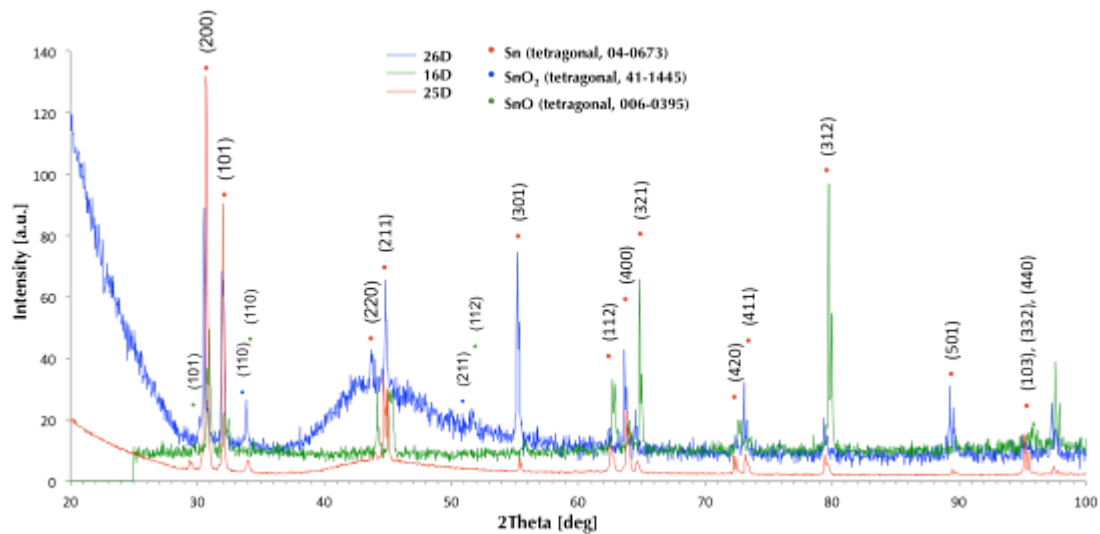
Figure 5.13 Powder X-ray diffraction patterns of the samples 16D, 22D and 26D; all diffraction positions are marked for Sn and for the three most intensive peaks of SnO and SnO_2

5.1.4   Debris image analyses

Image analyses was applied to the melt that has high degree of fragmentation. As mentioned above, particles, which participated to the fine fragmentation of the melt droplet, have irregular crumbled shape. Void fraction, i.e.porosity of such particles was calculated from the micrographs of debris cross-section. Example of such evaluation is given in the *Figure 5.14* for sample 16P and *Figure 5.15* for sample 26P. Image analyses were performed using ImageJ open-source software [5.5].
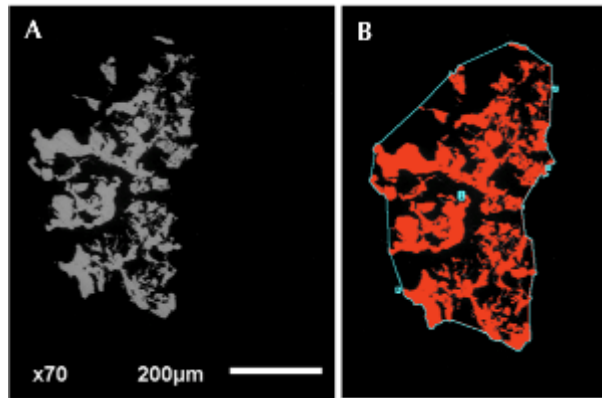
Figure 5.14 Selected particle of MISTEE 16P debris (a) and contours of particle during image analyses
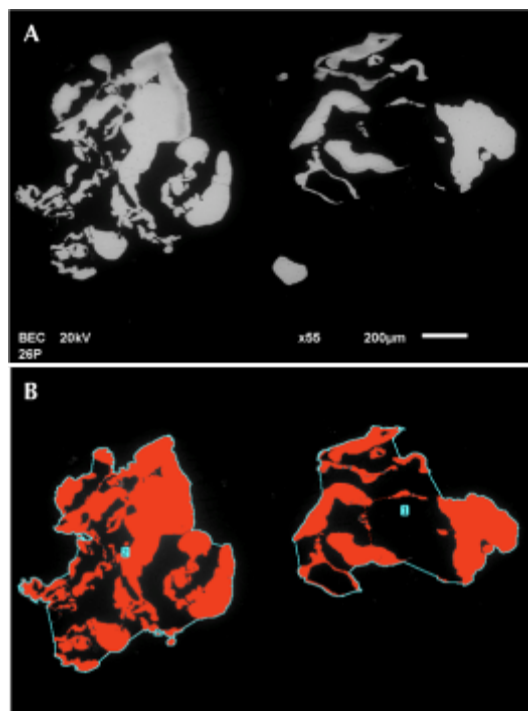
Figure 5.15 MISTEE 26P debris – SEM micrograph of a cross-section (a), contours of particles (b)

This figure allows us to give an order of magnitude for the final porosity: it can be estimated at 52%. If we consider that the initial melt is full and dense, it increases the volume approximately twice during the thermal fragmentation. Furthermore, the melt-water interface becomes notably larger. According to the above-published micrographs of powder samples the void inside the particles seems to be formed mainly by open porosities, which can be attributed to the water micro-jets perpetrating the drop surface as was described as Kim-Corradini's thermal fragmentation mechanism in the *paragraph 2.3.4*.

5.1.5   Conclusion

For this kind of metallic simulant melt, it has been shown the strongest the explosion, the highest the oxidation. This fact means that the oxidation processes are of first iomportance in this case.

Concerning the morphology, irregular shapes debris ("octopus" like) have been observed: this family of debris can be identified as participating to steam explosion. Tin reacts during FCI with water/steam, while this reaction proceeds mainly of the droplet surface and doesn't progress to the whole melt volume. Evidences of the SnO and SnO_2 presence were confirmed by SEM/EDS and powder X-ray diffraction.

The high value of void fraction inside the droplet means a possible mechanism in which water would be entrapped. At least, the final morphology could be in favour of possible thermal fine fragmentation processes (see Chapter 3). Neither hydrate nor water adsorption have been observed.

5.2 PREMIX and ECO debris

Debris coming from PREMIX 18 and ECO 07 experiments was provided by FZK Karlsruhe (Germany). The initial melt was generated using alumina thermite reaction (*paragraph 3.5*). The melt consisted of mixed aluminum oxide and metallic iron,approximately 90 w. % alumina and 10 w. % iron.

The PM 18 test was focused on the premixing behavior in low sub-cooled water (initial system pressure 0.22 MPa, water temperature 362-370 K). The debris bed composed of 5.68 kg of debris cake, 5.48 kg of loose particles on the top of the cake and 3.44 kg of loose particles in the bottom of the facility. The debris size distribution can be found in the *Figure 5.16* [5.5].

The ECO 07 experiment used external triggering, however, no violent escalation was observed. The initial system pressure was 0.23 MPa and water temperature 331-347 K. 15.2 Kg of the melt was transferred into the water pool, while no debris cake was formed. The debris size distribution is given in the *Figure 5.17* [5.6].
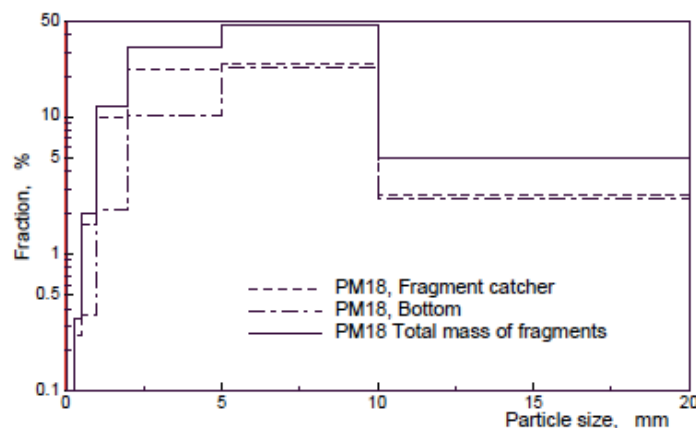
Figure 5.16 Debris size distribution of the PREMIXM 18 test [5.5]
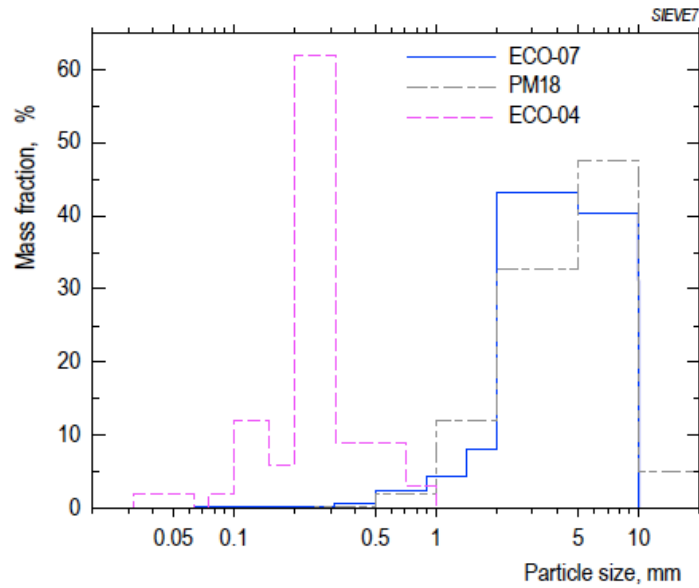
Figure 5.17 Debris size distribution of the ECO 07 test, compared with PM 18 and ECO 04 (violent SE) [5.6]

5.2.1 PREMIX 18 debris

General view of the debris as received is shown in the *Figure 5.18* for large size fractions and in the *Figure 5.19* for small size fractions. Large particles seem to be homogenous, while the color doesn't correspond to pure alumina (white) due to the presence of amounts of iron in the initial melt. Smaller debris (< 1 mm) contains two main types of debris – dark gray as observed for large debris and light (orange) solidified droplets corresponding to aluminum oxide with low iron pollution.

First important remark is that large particles (> 5 mm) present very often assemblies of several pasted droplets. Smaller droplets (<1 mm) are mostly rock like pieces of destroyed spheres. The sieving distribution, therefore, doesn't correspond to the real situation during premixing. Further, the heterogeneity in composition of small debris affects its morphology – round droplets correspond to alumina and rock like debris belongs to the dark (Al, Fe, O) phase.
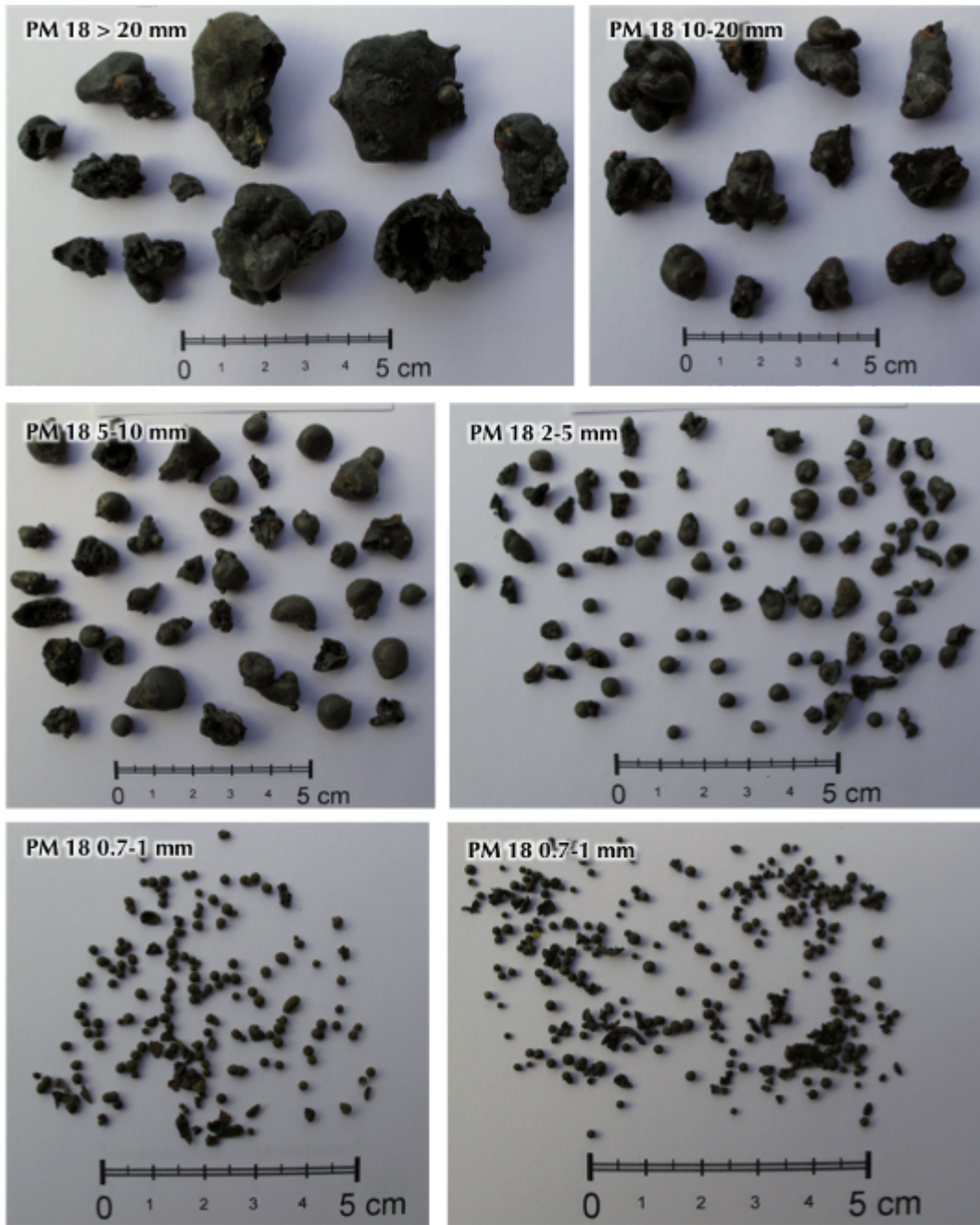
Figure 5.18 Photographs of the debris from PREMIX 18 test - large sieving fractions

Figure 5.19 Optical micrographs of the debris from PREMIX 18 experiment - small sieving fractions

5.2.2 PM 18 debris by SEM/EDS

An example of droplet fresh fracture (PM 18 > 20 mm) is shown in the *Figure 5.20* on the right. Drop shape channels perpendicular to the surface and spherical porosity can be observed. A possible explanation could be that water droplets or jets had penetrated the surface. The morphology of internal primary crystals is depicted in Figure 5.20 on the left. Well-developed prismatic (cubic) crystals of aluminum-iron oxide can be seen.
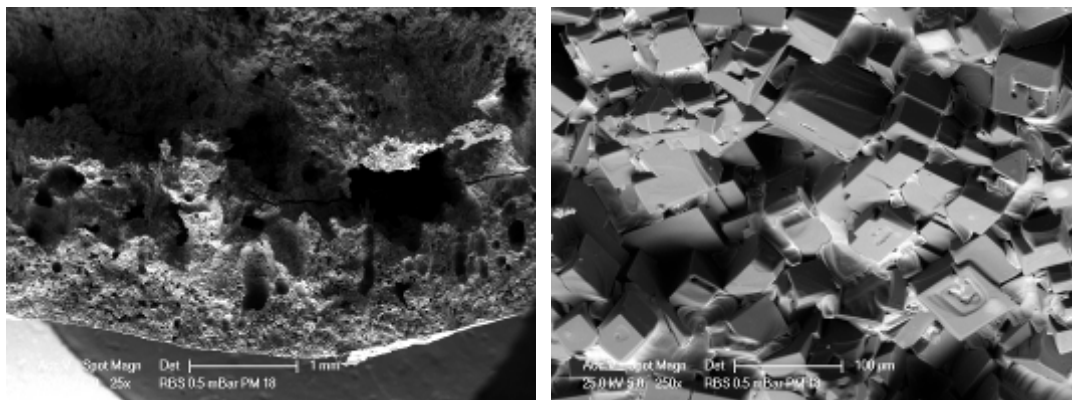
Figure 5.20 Fresh fracture of PREMIX 18 > 20 mm debris (SEM/EDS)

Composed cross-section of the PM 18 5-10 mm particle is given in the *Figure 5.21a*. Similar channel structure and porosity can be found even for less porous droplets (*Figure 5.21b*).
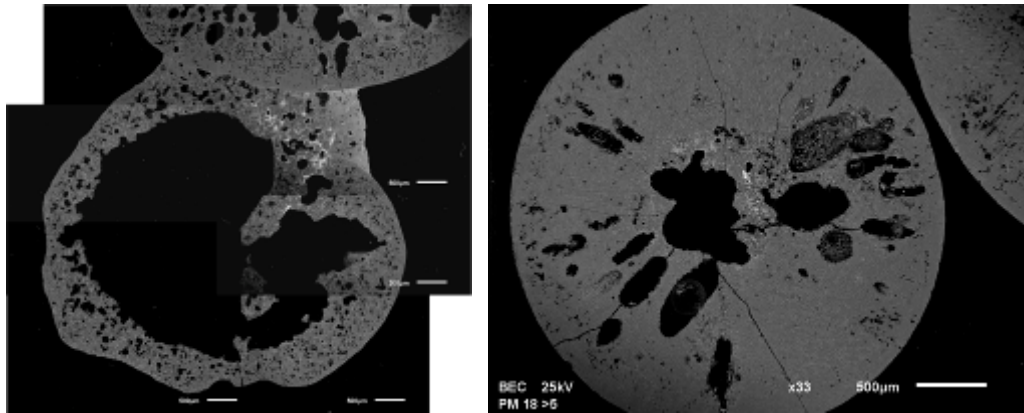
Figure 5.21 Cross-section of PM 18 debris 5-10 mm by SEM/EDS

The morphology of debris coming from the smaller size fractions is shown in the *Figure 5.22* for size fraction 0.25-0.5 mm and in the *Figure 5.23* for fraction 0.125-0.25 mm. In general, all the sieving fractions contain spherical and angular particles. Typical composition of the spherical droplet is shown in the *Figure 5.24* using EDS element mapping. The main component of the spherical debris is aluminum oxide with low iron content, which is located mainly on the surface. Explanation of the surface contamination could be also due to inter-particle friction and adhesion of small iron oxide impurities.
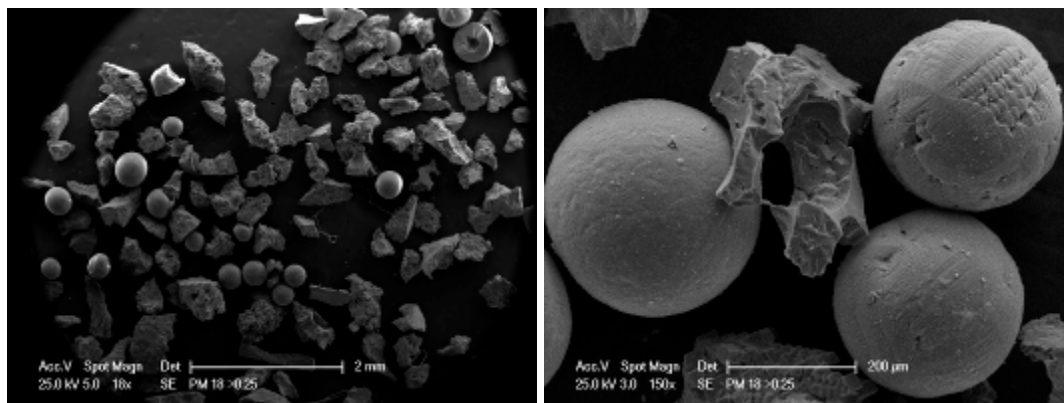
Figure 5.22 Morphology of the PREMIX 18 0.25-0.5 mm by SEM/EDS

116
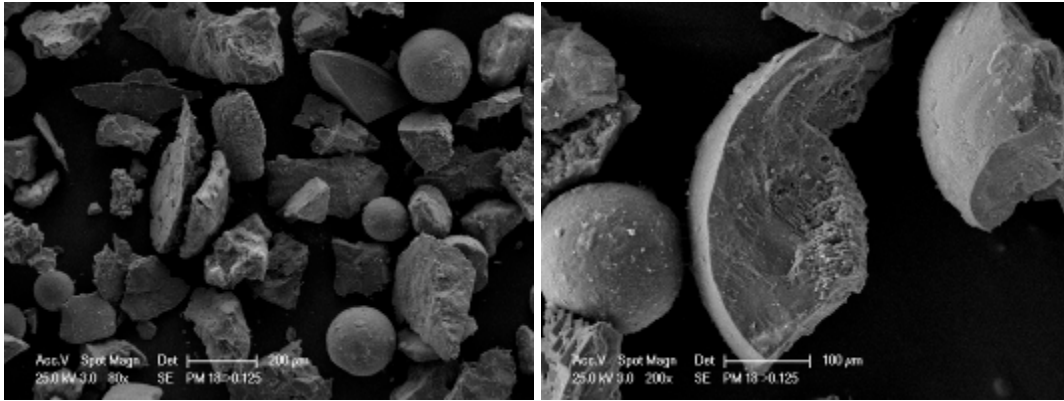
Figure 5.23 SEM/EDS investigation of the sample PREMIX 18 0.125-0.25 mm

Analysis of typical angular debris is shown in *Figure 5.25* in similar way. It is a mixture of aluminum oxide and binary aluminum-iron oxide. Moreover, contamination by calcium was observed.
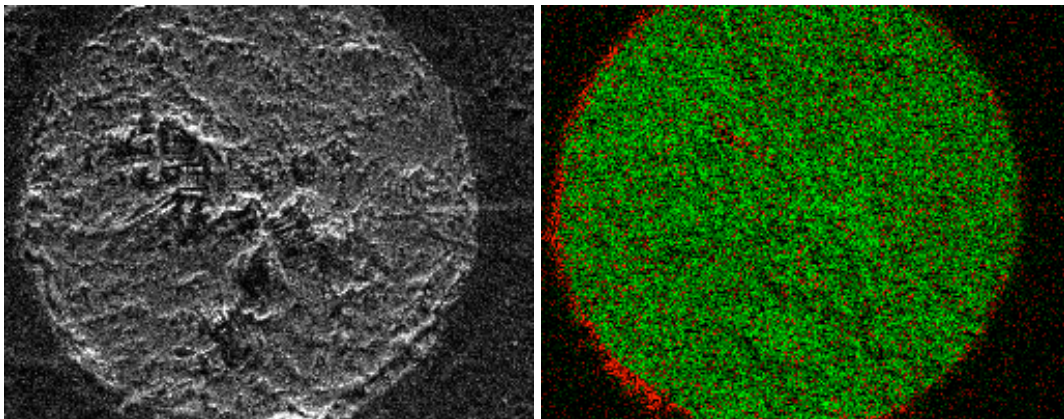
Figure 5.24 Cross-section of PM 18 0.125-0.25 droplet (right), elemental mapping (right, Al - green, Fe - red)
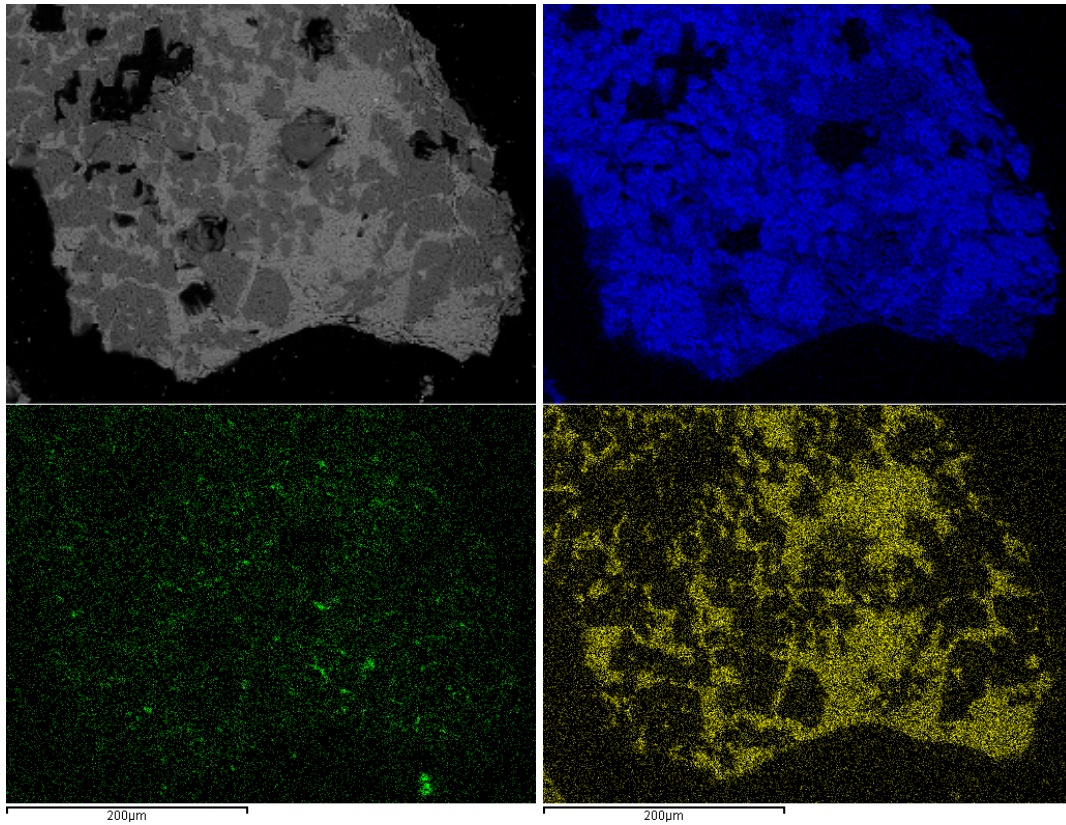
Figure 5.25 SEM/EDS mapping of angula PM 18 fracton 0.25-0.5 mm debris (Al - blue, Ca - green, Fe - yellow)

Well-developed dendrite structures were found inside some particles. This implies that there can be a difference in the cooling rate between the surface and the center of the droplet (*Figure 5.26*).
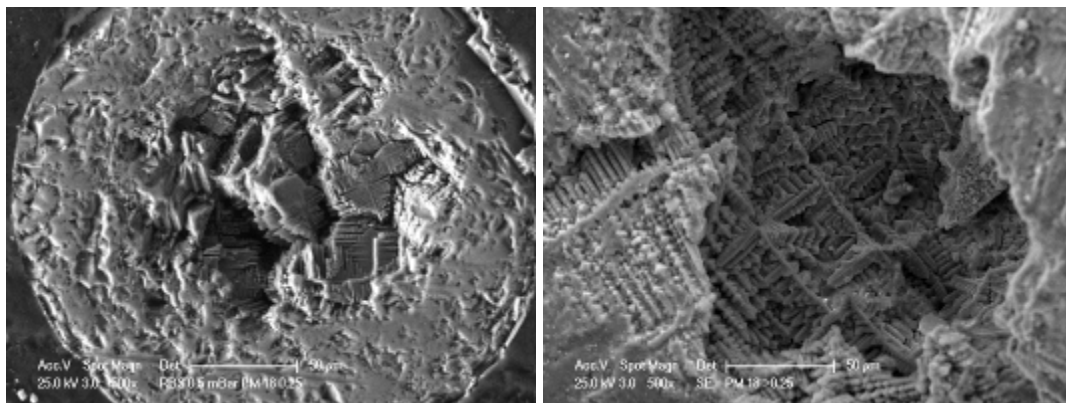
Figure 5.26 Dendrite structures observed inside the PM 18 debris

5.2.3   X-ray powder diffraction of PREMIX 18 debris

Whatever the debris sieving fractions, the diffractograms are the same for the quantity and the nature of the crystalline phases. To illustrate this point, an example is given in the *Figure 5.27*.
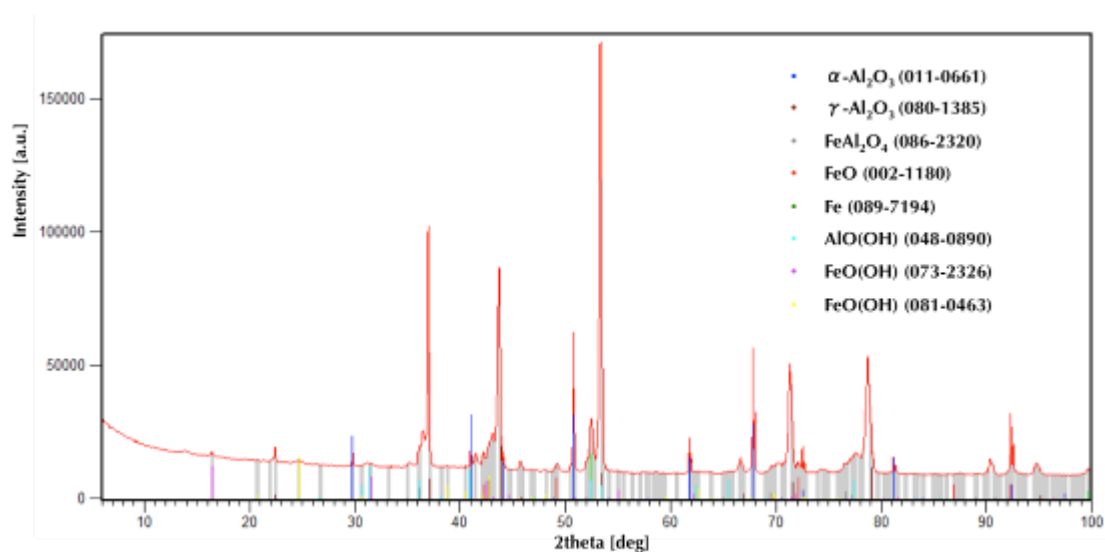
Figure 5.27 X-ray powder diffractogram of the PREMIX 18 0.5-0.7 debris

Main components of the debris are hercynite ($FeAl_2O_4$ spinel), rhombohedral aluminum oxide, cubic aluminum oxide, wüstite (FeO cubic), aluminum and iron oxo-hydroxides. We cannot exclude presence of metallic iron and other iron oxides (Fe_2O_3, Fe_3O_4). Main differences are in the amounts of each phase according to the size distributions, but no evident tendencies were estimated. A solution of $FeAl_2O_4$ and γ-Al_2O_3 presents the main component. The presence of gamma alumina is surprising, because it was observed only in experiments with SE in the KROTOS facility: the presence of gamma alumina is representative of metastable conditions: very rapid quenching or nucleation-germination-growth phenomena out of equilibrium. Alpha phase was observed during experiments without SE. The iron ions probably stabilize the cubic structure of alumina even at low concentration.

5.2.4   Thermogravimetric studies of PREMIX 18 debris

The first three size fractions (bellow 0.5 mm) were characterized by the thermogravimetry coupled with mass spectroscopy. Typical result is given in the *Figure 5.28.*, while the results are summarized in the Table 5.3. The debris contains up to 4 w. % of absorbed water (could be in various forms – as H_2O or OH groups). This can be taken as a proof of the melt – water non-oxidative reaction. The first water release can be attributed to the decomposition of iron oxo-hydroxides (pure FeO(OH) decomposes around 200 °C), while the second peak belongs to the aluminum oxo-hydroxides decomposition (pure AlO(OH) decomposes around 500 °C).
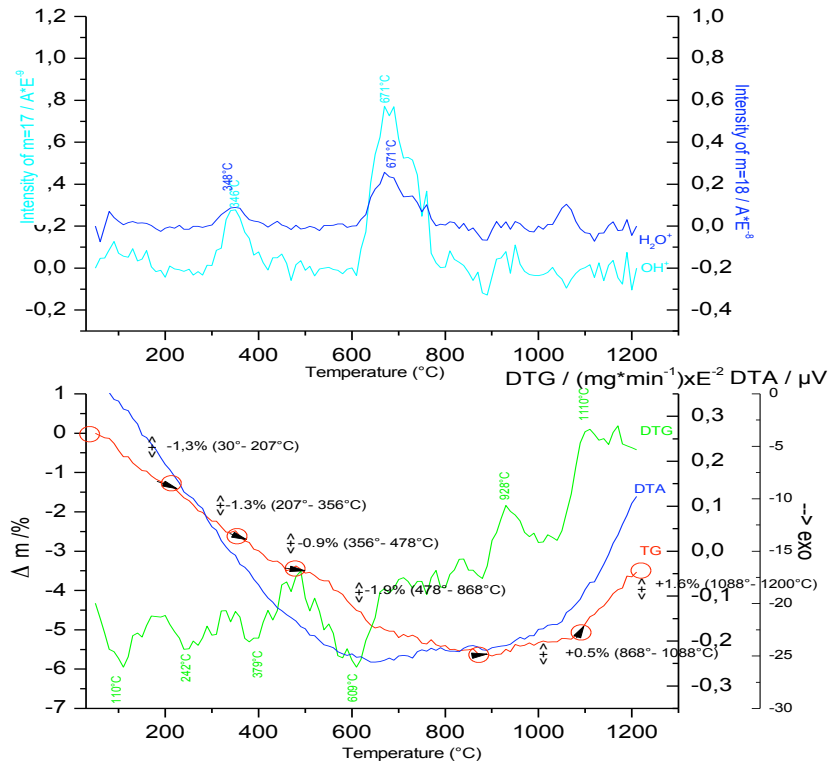
Figure 5.28 TGA/ MS investigation of the sample PREMIX 18 0.125-0.25

Table 5.3 TGA/MS analyses of PREMIX 18 debris

Sample	First peak		Second peak	
	Temperature [°C]	Weight decrease [w. %]	Temperature [°C]	Weight decrease [w. %]
PM 18 >0.5	282	1.2	630	1.2
PM 18 >0.25	431	0.4	673	0.9
PM 18 >0.125	348	2.2	671	1.9

5.2.5   ECO 07 debris

Even if the size distribution of the PREMIX 18 and ECO 07 are similar, the ECO 07 debris occupied also size fraction bellow 0.125 mm (see *Figure 5.29 and Figure 5.30*).

Large debris (> 2mm) presents again assemblies of several pasted droplets. The composition looks homogeneous. This is not the case for smaller debris that are heterogeneous. The situation is slightly different from PREMIX 18, most of the particles of ECO debris are spherical, even if it is composed mainly of hercynite, which were broken (angular) in the case of PREMIX 18.

An important difference between PREMIX and ECO debris is that for the size of the debris bellow 0.125 mm, the morphology appears to be angular.
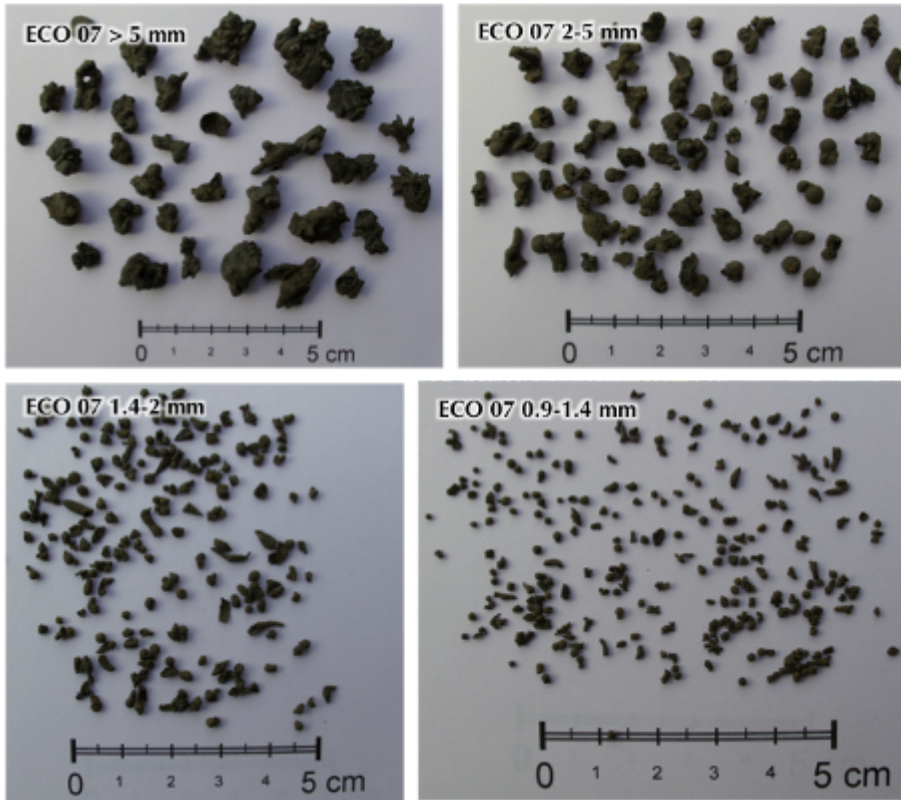
Figure 5.29 Photography of the ECO 07 debris, large size fractions
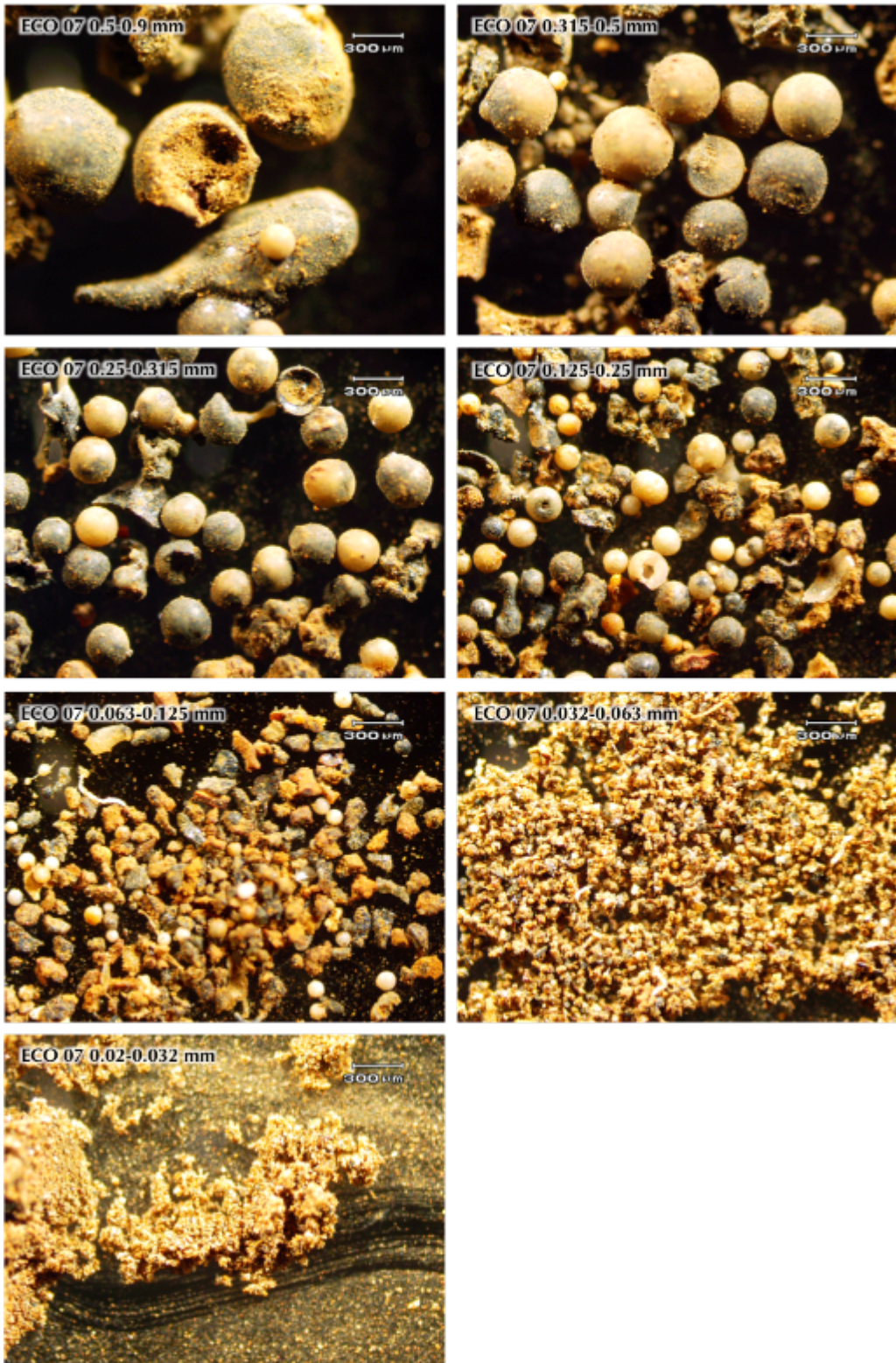
Figure 5.30 Smaller size fractions of the ECO 07 debris by optical microscopy

5.2.6   SEM/EDS studies of ECO 07 debris

SEM micrographs of the larger, spherical (0.25-0.315 mm) and fine powder (0.02-0.032 mm) debris are given in the *Figure 5.31*.

Above-mentioned small debris contains also higher amount of iron and calcium. Comparison of EDS spectra for debris 0.5-0.9 mm and 0.02-0.032 mm are shown in the *Figure 5.32*. Due to its different composition and mechanical properties it probably was more fractionize in the solid state and formed fine powder.

Similar phenomena as for PREMIX 18 can be observed for cross-section of ECO 07 droplets (*Figure 5.33*). The pollution by iron oxide can be found on the surface probably caused by inter-particle friction. Likewise, the angular (fine powder) debris is chemically inhomogeneous as can be seen from the EDS elemental mapping shown in the *Figure 5.34*.
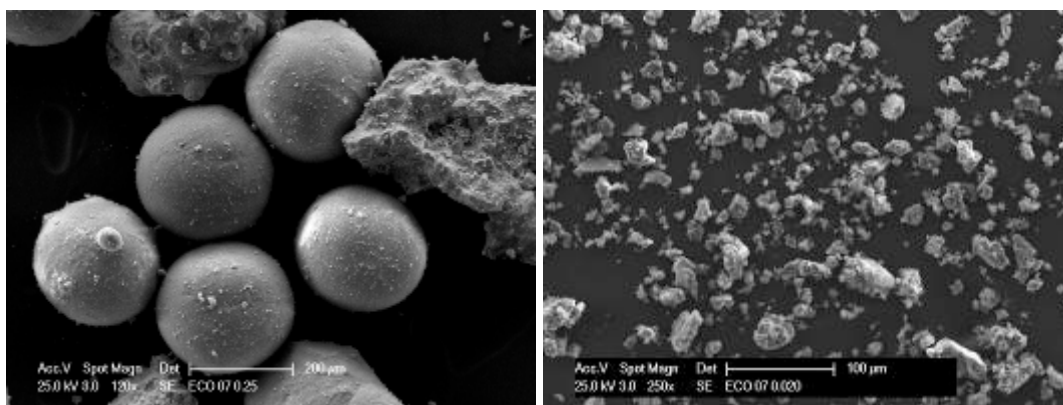
Figure 5.31 SEM micrographs of the ECO 07 debris, 0.25-0.315 mm - right, 0.02-0.032 mm – left
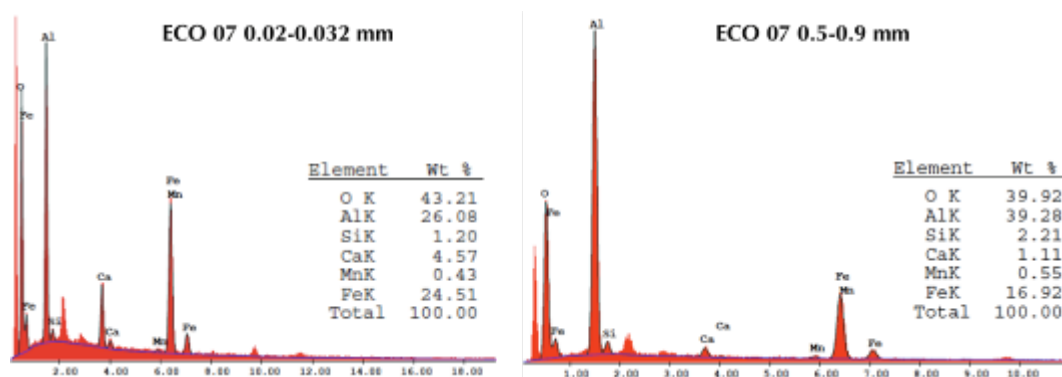
Figure 5.32 EDS elemental analyses of ECO 07 debris
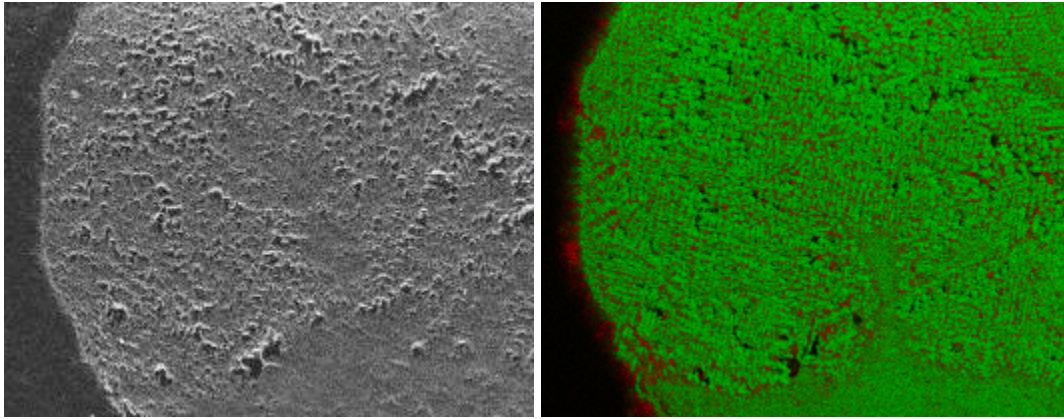
Figure 5.33 Cross-section of ECO 07 (0.5-0.9 mm) droplet with elemental mapping (Fe - red, Al - green)
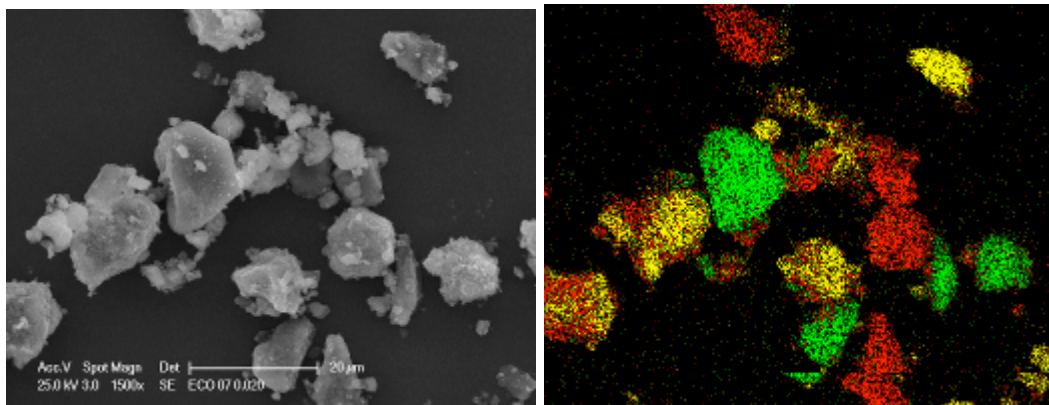
Figure 5.34 EDS elemental mapping of ECO 07 (0.02-0.032) debris (Fe - red, Al - green, Ca - yellow)

5.2.7   X-ray powder diffraction of ECO 07 debris

Heterogeneous composition can be found thanks to the results of X-ray powder diffraction. Large debris that could be attributed to non-steam explosion is composed mainly of alpha and gamma alumina and iron-aluminum oxide. Fine powder (debris under 0.125 mm) contains new phases coming from reaction with water (oxo-hydroxides, hydroxides). The results are depicted for ECO 07 0.5-0.9 mm in the *Figure 5.35* and for ECO 07 0.032-0.063 mm in the *Figure 5.36*.

5.2.8   Thermal analyses of ECO 07 debris

The thermogravimetry coupled with mass spectroscopy was also employed to study the ECO 07 debris. Debris size fractions below 0.5 mm were annealed in air atmosphere with the step 10 °C per minute. The results are summarized in the *Table 5.4* and an example of such measurement is given in the *Figure 5.37*. Water is released firstly at 300°C and secondly at 700°C.
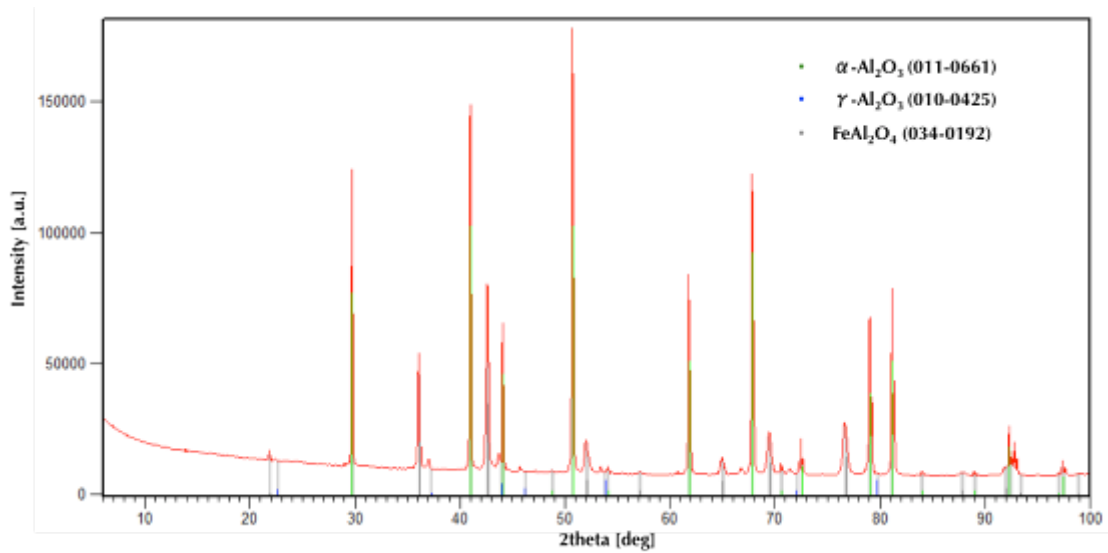
Figure 5.35 X-ray powder diffraction results for ECO 07 0.5-0.9 mm
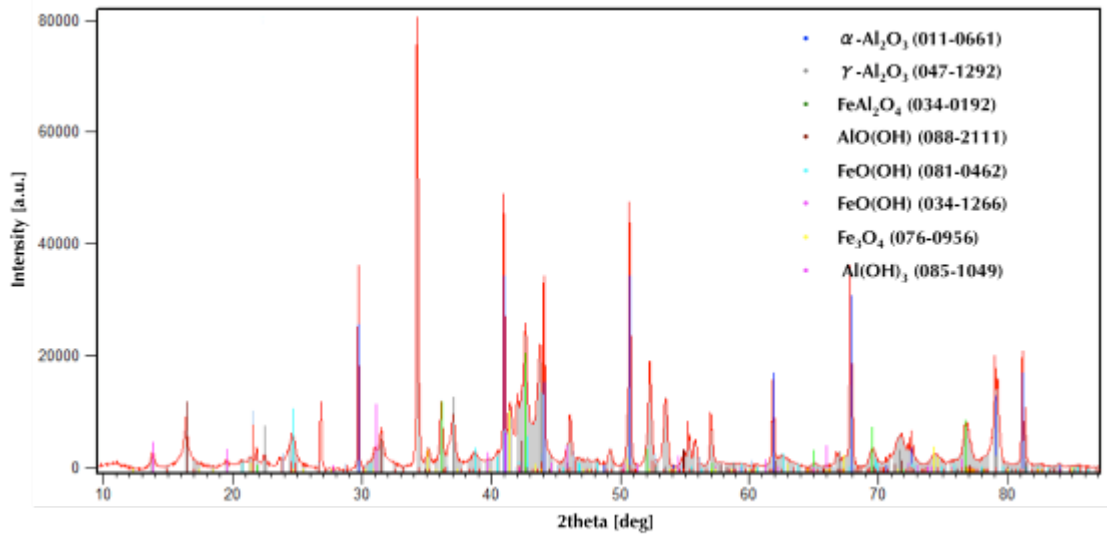
Figure 5.36 X-ray powder diffraction results for ECO 07 0.032-0.063 mm

Table 5.4 TGA/MS results for ECO 07 debris bellow 0.5 mm

Sample	First peak		Second peak	
	Temperature [°C]	Weight decrease [w.%]	Temperature [°C]	Weight decrease [w.%]
ECO 07 >0.02	269	4.7	671	3.9
ECO 07 >0.032	269	7.4	707	4
ECO 07 >0.063	259	4	650	2.3
ECO 07 >0.125	268	1.6	670	2.2
ECO07 >0.25	271	3.5	660	0.9
ECO 07 >0.315	282	1.5	691	0.9
ECO 07 >0.5	339	1	659	1

ECO 07 0.032
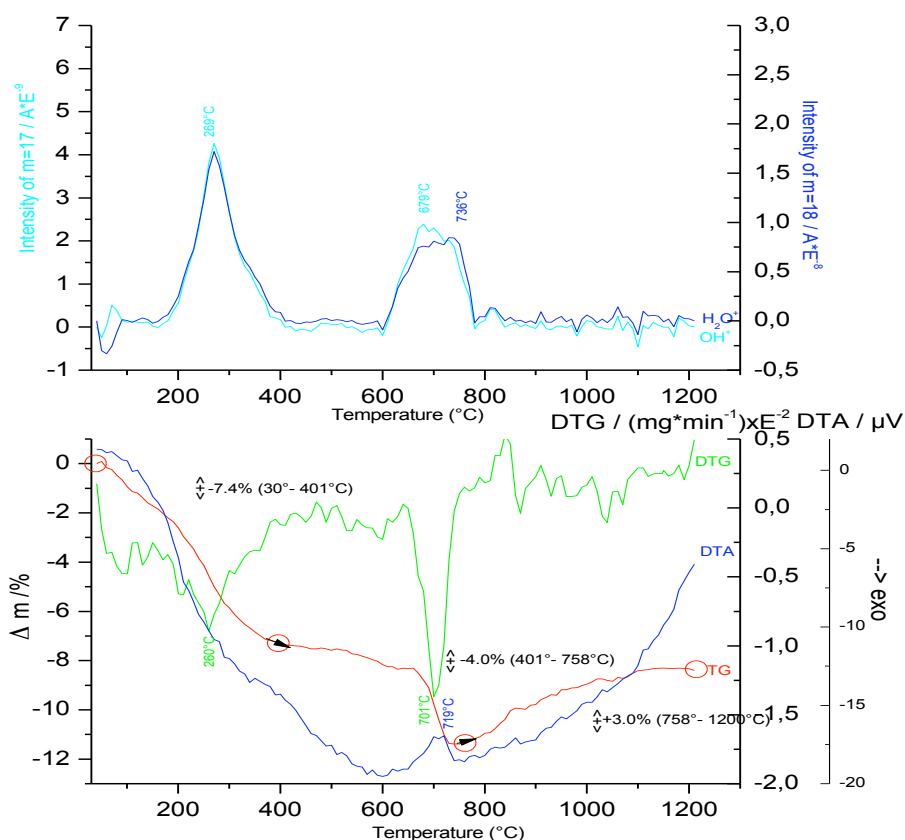
Figure 5.37 DTA/MS investigation of the ECO 07 0.032-0.053 mm debris

Figure 5.38 presents the sum of the weight decreases versus medial value of the size fraction. The amount of water (or OH groups) increases with decreasing size of the debris. This tendency is in a good agreement with increase of the surface area going down to smaller debris. The surface is the only interface for possible reaction water/steam and melt.

$$y = 1.8255x^{-0.483}$$
$$R^2 = 0.84508$$
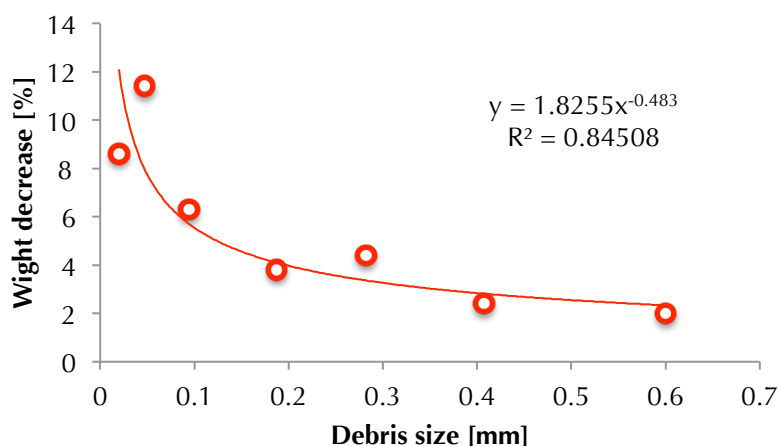
Figure 5.38 Total weight decrease versus size of the ECO 07 debris

5.2.9   Conclusion

PREMIX and ECO debris characterization have shown that the melt composition differs significantly from the initial state. The melt released from the furnace contained approximately 90 w. % of Al_2O_3 and 10 w. % of metallic iron. Most of the metallic iron was oxidized to Fe^{2+} cations that formed $FeAl_2O_4$ mixed oxide. Therefore, these experiments can be misleading during being used for computer code validation "against" thermo-physical properties of aluminum oxide, simply because the solidification and chemical reactions in the system are much more complex and far from pure alumina.

Two phenomena have been observed: paste of droplets into larger pieces and droplet break up at solid state. Both effects play significant role in the size distribution by mechanical sieving and influence the results reliability. Further, a material effect in the solid droplet break up was found in the PREMIX debris, where the Fe-Al mixture oxide debris has higher tendency to be broken in angular pieces.

The presence of aluminum oxide gamma phase means metastable conditions for solidification even in the case of no steam explosion experiments. Presence of this phase can be attributed to the stabilizing effect of the Fe^{2+} ions on the cubic alumina the structure.

High amounts of water can be chemically absorbed in the debris. The ECO 07 small powder debris contained up to 10 w. % of water. This water can be in the form of hydrated oxides or in the form of hydroxides and oxo-hydroxides..

The post-test analyses of FCI experiments using simulant materials have shown the importance of the following phenomena in premixing/fragmentation/steam explosion stages:

- Oxidation mechanism
- Reaction between water and melt
- Final size and morphology of the debris

5.3 References

5.1   I. Beattie et al: Oxide phonon spectra, Journal of Chemical Society A (1969) 2322-2327
5.2   V.C.:Farmer: The Infrared Spectra of Minerals, London 1974
5.3   S.D. Ross: Inorganic Infrared and Raman Spectra, London 1972
5.4   A. Beran, J. Zemann: Measurement of Infrared pleochroism minerals XI. Pleochroism of the hydroxyl-stretching frequency in rutile, anatas, brookite and cassiterite, Tschermaks. Mineral. Petrogr. Mitt. 15 (1971) 71-80
5.5   http://rsbweb.nih.gov/ij/
5.6   A. Keiser et al: PREMIX Experiments PM12-PM18 to Investigate the Mixing of a Hot Melt with Water, Wissenschaftliche Berichte, FZKA 6380, FZK Karlsruhe, Germany, 2001
5.7   W. Cherdron et al: ECO Steam Explosion Experiments – Documentation and Evaluation of Experimental Data, Wissenschaftliche Berichte, FZKA 7011, FZK Karlsruhe, 2005

Chapter 6. KROTOS KS2 experiment

6

    Four tests were performed within this thesis in the KROTOS facility. Experimental conditions (triggering, water and melt temperature) were maintained similar, while the initial melt compositions were:

- KS2 – 70 w. % UO_2 and 30 w. % ZrO_2
- KS4 – 80 w. % UO_2 and 20 w. % ZrO_2
- KS5 – 80.1 w. % UO_2, 11.4 w. % ZrO_2 and 8.5 w. % Zr

The KS3 experiment should have served as a reproducibility test using KS2 melt composition. However, the test failed during the melt release phase.

6.1   SERENA 2 project

    This Ph.D. thesis has been worked out in the frame of OECD/NEA SERENA 2 project (running from October 2007 till March 2012). It is a continuation of OECD/NEA Serena 1 project, which was focused on the code predictions of in-vessel and ex-vessel dynamic loads in the reactor case. In other words, the scope of SERENA 1 was to find the areas of discrepancies in calculations by different FCI codes and to identify the phenomena of first importance of steam explosion [3.28-29]. The SERENA 2 objectives were:

- Provide experimental data to clarify the explosion behavior of prototypic corium melts.
- Provide innovative experimental data for validation of explosion models for prototypic materials, including spatial distribution of fuel and void during the premixing and at the time of explosion, and explosion dynamics.
- Provide experimental data for the steam explosion in more reactor-like situations to verify the geometrical extrapolation capabilities of the codes.

6.1.1   SERENA 2 experimental grid

    In the frame of SERENA 2 project a set of experiments in the TROI and KROTOS facilities was launched. Initial melt material and experimental objectives are listed in the *Table 6.1*.

Table 6.1 SERENA 2 experimental grid

Experiment	Composition [w. %]	Objective
1	70 % UO_2, 3O % ZrO_2	TROI and KROTOS geometry comparison
2	70 % UO_2, 3O % ZrO_2	Material effect
3	70 % UO_2, 3O % ZrO_2	Reproducibility test
4	80 % UO_2, 2O % ZrO_2	Material effect
5	80.1 % UO_2, 11.4 % ZrO_2 and 8.5 % Zr	Material effect - Oxidation
6	73 & UO_2, 20.4 % ZrO_2, 4.1 % Fe_2O_3, 1.3 % Cr_2O_3, 0.3 % BaO, 0.8 % LaO and 0.2% SrO	Material effect - Large solidification interval

6.2 KROTOS facility description

The KROTOS facility consists of three parts – furnace, release channel and test sections. Tungsten crucible filled with prototypical corium powders is heated up and released through a channel in the lower part of the facility. A puncher perforates the bottom of the crucible and the melt flows out. Further, the melt falls through a gas gap in the water pool and interacts with the water.

6.2.1 Furnace

The furnace is confined with stainless steel housing. It contains heating elements and eight concentric tungsten, molybdenum and steel thermal shielding blocks. In the center tungsten crucible hangs on a pneumatically controlled hook. The furnace works under noble gas (He, Ar) atmosphere up to 4.0 MPa.

The tungsten crucible is 200 mm high and it has 84 mm outer diameter and 80 mm inner diameter. It can hold maximally about 0.5 liter of melt. The bottom of the crucible is electro-eroded to 0.25 mm in thickness to be easily perforated by the puncher.

Overall scheme of the furnace is given in the *Figure 6.1*.
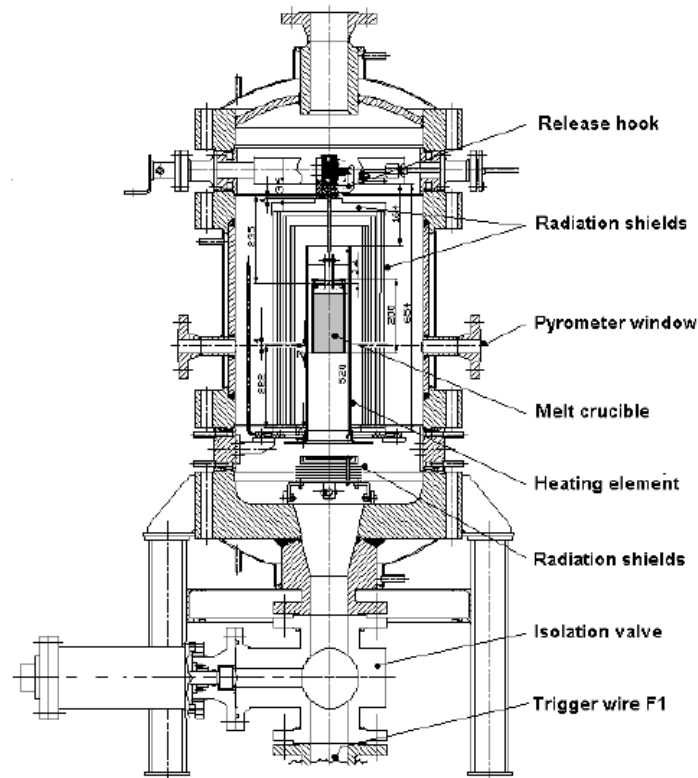
Figure 6.1 KROTOS furnace description

6.2.2 Release channel

When the operator starts the release action, the crucible with melt load falls by gravity through ~4 m long tube to the puncher. After passing of the crucible a valve closes the furnace and isolates it from the FCI. During its fall, the crucible cuts two wires defining the zero time for data acquisition and activating the countdown of external trigger. Finally, the crucible impacts on the puncher that perforates the bottom and allows the melt to flow out to a conical release nozzle defining the melt jet diameter. The nozzle characteristics are given on following paragraph.

6.2.3 Test section

The water pool itself is located inside a tubular test section placed in a pressure vessel. The vessel is made from aluminum alloy (7075) and designed to sustain 2.5 MPa at 493 K. At the bottom it provides a support for the water pool. Further it contains a number of feedthroughs for gas, water and instrumentation inlets and connections.

The water pool section (aluminum alloy 7075) has diameter of 200 mm and thickness 24 mm. The water slope can be up to 1.20 m high. Pressure transducers and thermocouples are mounted at certain elevations to follow the melt front history and pressure wave movement. The trigger device is mounted at the bottom of the test section. It consists of a 30 ml capsule that can be charged by argon up to 15 MPa and closed by steel membrane. The test section contains also a force measuring system, level and void fraction measuring device and high-speed camera.

General description is given in the *Figure 6.2*.
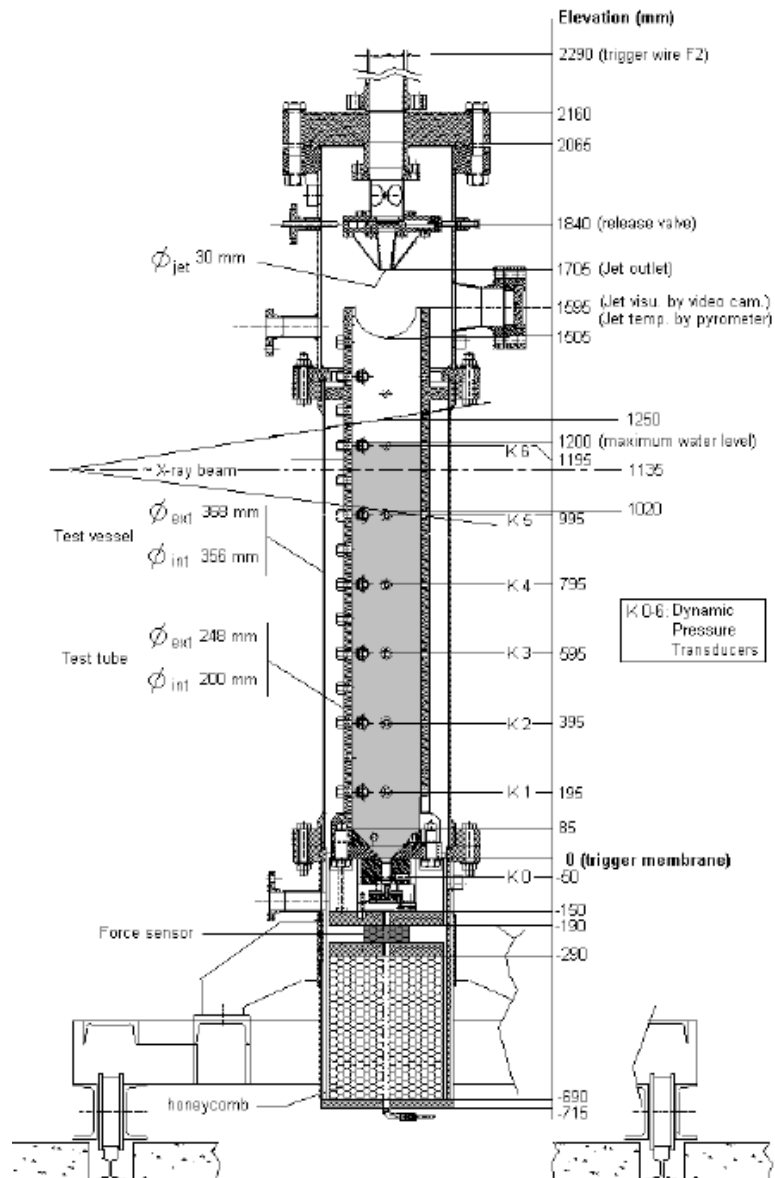
Figure 6.2 KROTOS facility test section

A modification of the release nozzle was done for KS4 experiment. The nozzle shown in the *Figure 6.3* corresponds to the KS2 situation.. For KS2 a tin membrane was placed just before the end of the nozzle (1767 mm) from the same reason. In the KS4 modification a tin membrane was placed just 1.3 cm bellow the puncher (1900 mm), see the *Figure 6.3*.

6.2.4   KROTOS facility instrumentation

The melt temperature is controlled by two bi-chromatic pyrometers. First is focused on the down side of the crucible, while the melt temperature is considered to be the same as crucible temperature. Second pyrometer is mounted bellow the release nozzle to capture the temperature of melt jet.

131
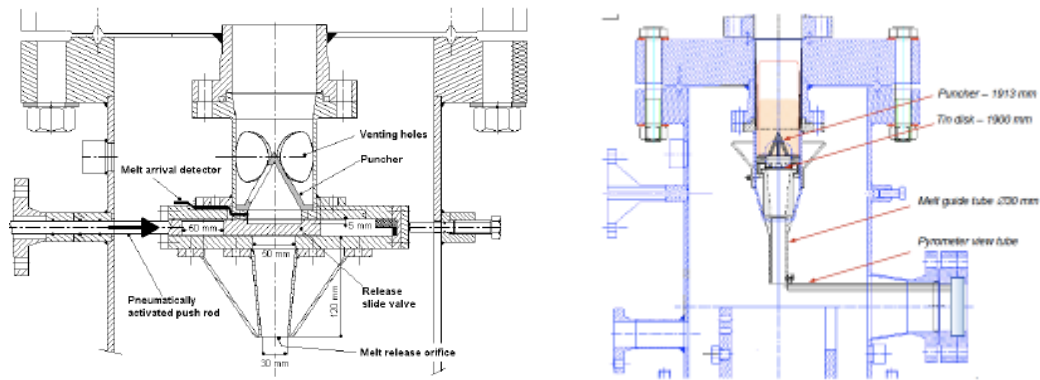
Figure 6.3 Release nozzle in the KS2 experiment (left; in the KS4 and KS5 experiments (right)

The dynamic pressure in the water column is measured by seven pressure transducers (KISTLER, denoted K0, K1, … to K6) with measuring range 0 to 100 MPa and frequency 140 kHz. First detector K0 measures the trigger pressure, the rest six K1 to K6 are mounted on the test section at different elevations.

Test vessel pressure is recorded by three piezzo-resistive pressure transducers (KELLER, denoted C1, C2, C3) at different positions. The measuring range is 0 to 4 MPa with frequency 5 kHz.

The force impulse is measured by force transducer (KISTLER, denoted as CF) with range 0 to 1.2 MN. It is located in the holding structures of the test section.

K-type thermocouples are used for temperature measurements of the gas (TT high, middle and low) in the vessel and water in the test tube (TT0, TT1, …TT5). Ten sacrificial K-type thermocouples are mounted in the corium melt path at different elevations in order to measure the jet front position during the release and mixing with water. They are denoted ZT0, ZT1, …ZT10.

The water level is measured by TDR-type device based on the reflectometry. It has fast time respond 1 kHz and is able to measure liquid surface even with high void fraction.

Generated gases, mainly hydrogen from the test section and gases from the furnace, are detected and quantified by mass spectrometer connected to the test section by preheated capillary tube. A cold trap is mounted before the measuring device in order to condense steam.

Desired data is received and saved on two NI boards on PCs. The mass spectrometer has its own PC.

The summary of the KROTOS facility instrumentation is given in the *Table 6.2* and visualized in the *Figure 6.4*.

Additional notes for *Table 6.2* are:
r – radius [mm], to the test tube centerline, z – elevation [mm], θ – azimuthal position [°]

Table 6.2 KROTOS facility instrumentation (KS4status)

Transducer name	Position (r, z, θ)	Measured quantity	Transducer type	Range	Sampling time/Acquisition duration	Comments
K0	015, -0050, 330	Explosion pressure	Dynamic pressure transducer KISTLER 6005	0 – 20 MPa	0.02 ms/10 s	K0 is in trigger chamber.
K1	100, 0195, 330			0 – 100 MPa		K1 - K6 installed flushed to the inner wall of the test tube.
K2	100, 0395, 330					
K3	100, 0595, 330					
K4	100, 0795, 330					
K5	100, 0995, 330					
K6	100, 1195, 330					
C1	340, -20, 225	Vessel pressure	Pressure transducer KELLER EI 71/2	0 – 4 MPa	1 ms/10s and 0.1s/20min	
C2	340, 1560, 270					
C3	340, 1985, 315					
Pc	340,1560,270		Pressure transducer WIKA		1 ms/10s and 2 s/∞	
ZT1*	0, 0195, 150	Melt front detection	Thermocouple K-Type 0.5 mm	1250°C	1 ms/10s	Below water level
ZT15	0, 295, 150					
ZT2	0, 0395, 150					
ZT2'	0, 0395, 180		Thermocouple K-Type 0.5 mm	1250°C	1 ms/10s	
ZT3	0, 0595, 150					
ZT35	0, 695, 150					
ZT4	0, 0795, 150					
ZT5	0, 0995, 150					
ZT6	0, 1195, 150					Above water level
ZT7	0, 1543, 150					
ZT8	0, 1642, 150					
ZT9	0, 1896, 150					Below tin membrane
ZT10	0,1904,150					Above tin membrane
TTV	50,2020, 150					Melt detection in the pre-catcher
TT0	50, 0080, 180	Water temp.	Thermocouple K-Type 0.5 mm	1250°C	1 ms/10s and 0.1s/20min	
TT1	95, 0195, 180					
TT3	95, 0595, 180					
TT5	95, 0995, 180					
TT low	170, -70, 225	Vessel temp.	Thermocouple K-Type 1.5 mm	1250°C	1 ms/10s and 0.1s/20min	
TT middle	180, 1510, 270					
TT high	180, 1935, 315					
SN	80, from 500 to 1500, 180	Water level	Transducer: Ispra Electronics: METRAWARE	1 m	1 ms/10 s	
Video camera	2000, 1595, 0	Jet visualization	Video camera NAC		250 fps during 7s	View window ⌀10 cm
X-ray radioscopy	878, 895, -90	Premixing visualization	LINAC		55 fps during 20s	X-ray source position is given
PyJ	400, 1595, 0	Jet temperature	Pyrometer IMPAC ISQ-LO 3 873 330	1250 – 3300°C	10 ms/10s	Jet under release cone
PyF	Furnace	Initial melt temperature	Pyrometer IMPAC ISQ-LO 3 873 330	1250 – 3300°C	2 s / heating duration	Temperature of crucible wall 23 mm from bottom
CF	0, -230, 0	Force	Force sensor KISTLER 9091A	0 - 1200 kN	0.02 ms/10 s	
F1	Transfer tube-, 3800, -	Rupture	W/Re wire 0.2 mm	9 – 2 V	0.02 ms/10 s	Starts fast acquisition
F2	-, 2316, -					Starts backup timer for the trigger delay

*ZT1 malfunctioned during the test

The inner processes of the test section are surveyed using radioscopy system. The X-ray beam is generated by LINATRON (VARIANT, 6-11 MeV, 0.3 Gy/s), after going through the test section and visible picture is generated on a scintillation screen and recorded by high sensitivity CCD camera (HAMAMATSU 8000). The radioscopy system covers a window 200x300 mm, thus, it is not possible to cover all the test section during the experiment. The X-ray window center position was settled to be 695 mm for KS2 and 845 for KS4 and KS5 according to the vertical facility notation.
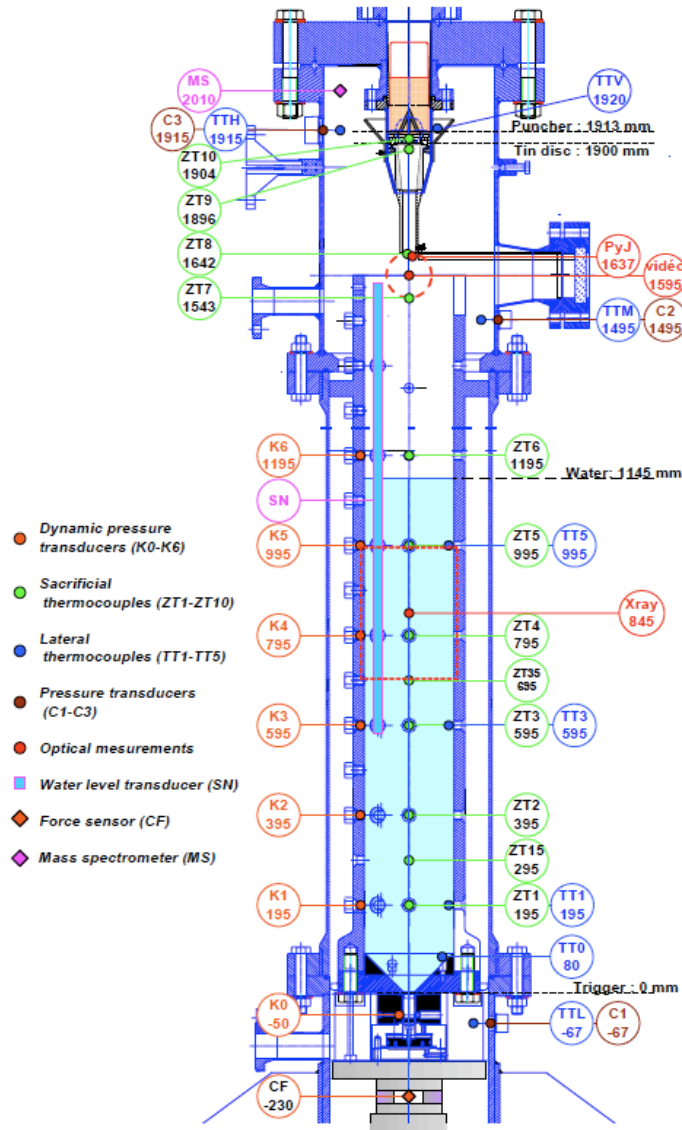
Figure 6.4 KROTOS facility instrumentation (KS4 and KS5 test status)

No differences are in the adjustment of the facility or instrumentation for different tests. The only exceptions are positions of the radioscopy system and modification of the release nozzle.

6.2.5   Trigger wave evolution

A blind experiment was performed in order to study the pressure evolution during triggering. The water temperature was set to 60 °C, while no melt was poured in the test section.

The pressure history measured by transducers at different elevation in the water pool is shown in the *Figure 6.5*. The K0 transducer gives the information about the pressure inside the gas capsule. After opening the steel membrane immediate trigger propagation was observed by other transducers (K1, K2, …, K6). The calculated propagation speed reached 1333 m.s^{-1}, which is close to the speed of sound in pure water (1551 m.s^{-1} at 60 °C).
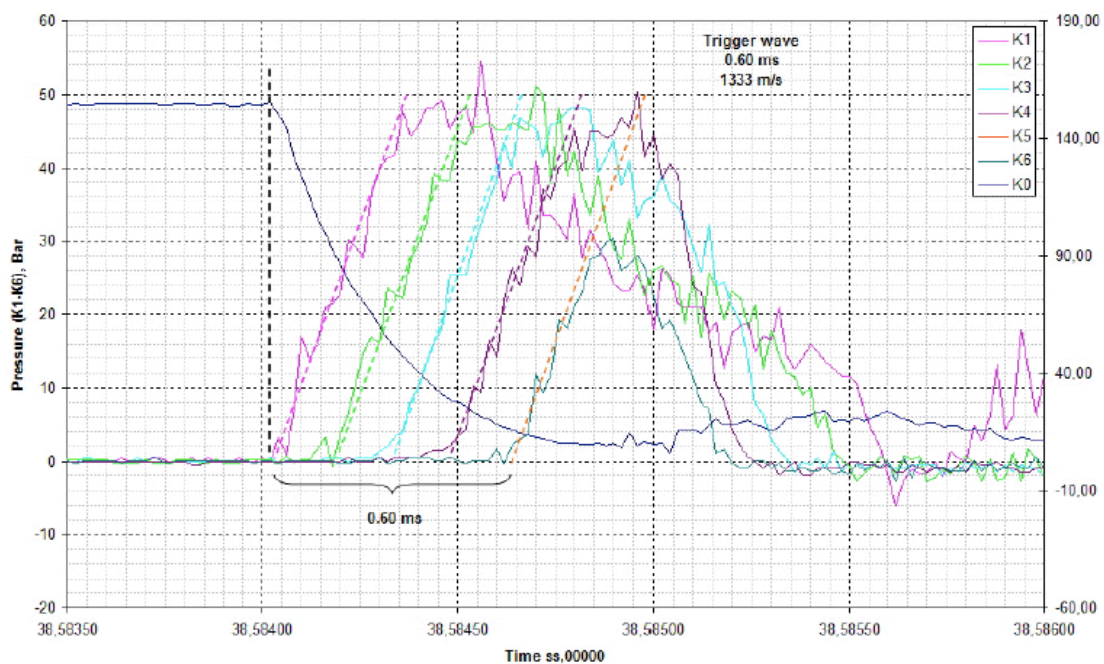
Figure 6.5 Trigger wave propagation in pure water

6.3 KROTOS tests: Overview

Information about the three KROTOS tests is summarized in the *Table 6.3*.

The KS2 and KS4 tests were performed successfully and they provide full data for post-test treatment. Because one of the data recording PCs during the KS5 failed, not all the data are at disposal.

The KS3 experiment should be a reproducibility test of KS2. Therefore, the set-up and experimental conditions should have been kept. However, it failed, because the crucible remained wedged in the release channel.

Table 6.3 Summary of the KS2, KS4 and KS5 experiments

Component	Property	KS2	KS4	KS5
Melt	Composition [weight ratio $UO_2:ZrO_2:Zr$]	70:30:00	80:20:00	80.1:11.4:8.5
	Transferred mass [kg]	4.12	3.211	2.331
	Release temperature [C]	2776	2690	2587
	Free fall in gas [m]	0.56	0.492	0.492
	Jet release diameter [mm]	30	30	30
Water	Temperature [C]	60	59	53.5
	Depth [m]	1.145	1.145	1.145
	Diameter [m]	0.2	0.2	0.2
	Volume [dm^3]	-	35.4	35.9
Gas	Composition	He	He	He
	Pressure [Mpa]	0.2	0.21	0.21
	Volume [m^3]	0.203	0.203	0.203
Radioscopy	Position [mm]	695	845	845
Trigger	Gas volume [cm^3]	29.5	29.5	29.5
	Pressure [Mpa]	15	15	15
	Activation	F2	ZT2	F2
	Time delay after signal [ms]	177	233	294
SE	SE efficiency	~ 0.08	~ 0.182	-

6.4 KROTOS KS2 experiment

The experiment started by heating up the loaded crucible by step increase of the power. The heating power and crucible temperature history is depicted in the *Figure 6.6*. Last temperature value before the crucible release was 2776 °C (3049 K). The crucible was then released from the hook and felt by gravity on the puncher. It was calculated that the melt after entering the test section from the nozzle had initial speed 20 m.s^{-1}. Therefore, the tin membrane failed to stop the melt providing coherent jet without axial disorders. Just above the water level the melt jet speed was 20.3 m.s^{-1}. During the FCI the melt jet front history has a typical knee of complete jet break up. The speed of melt fragments decreased in water to 2.29 m.s^{-1} just before explosion.

The interaction went through triggered steam explosion. The detailed numbers about dynamic pressure and melt jet front history are unfortunately confident due to restrictions of the OECD projet.

The pressure inside the vessel increased significantly after the melt release due to the ambient gas heat up and steam generation.
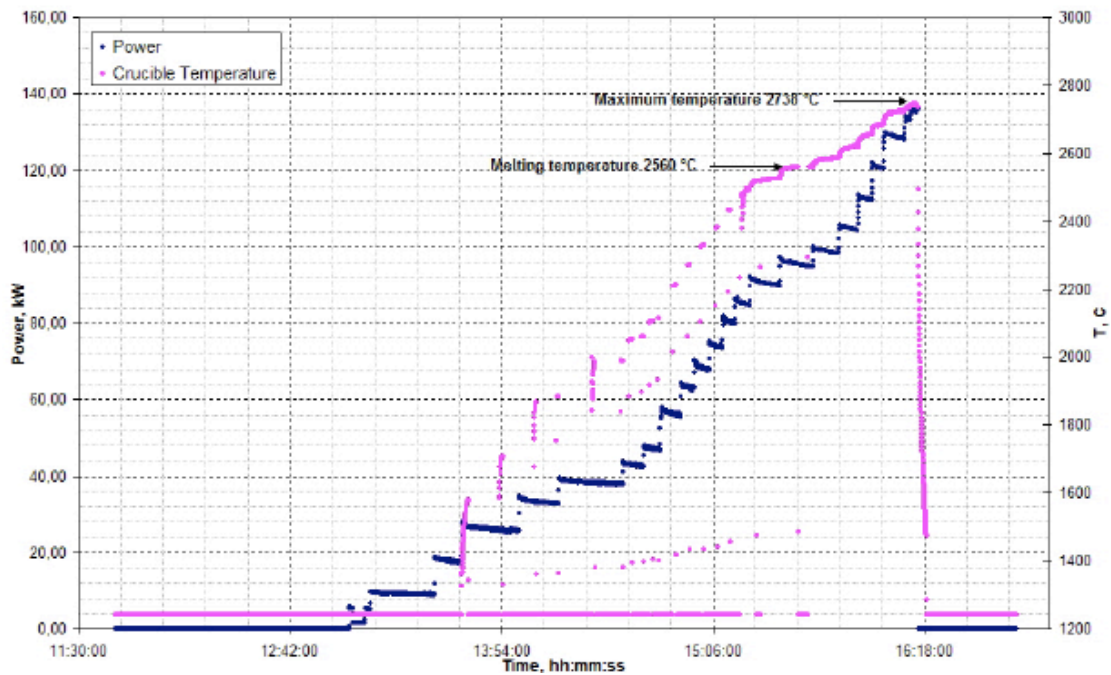
Figure 6.6 Heating power and crucible temperature history

The steam explosion efficiency was calculated according to the *equation 2.1* (*chapter 2*):

$$\eta = \frac{\left(\int F\,dt\right)^2 / 2m_{water}}{m_{melt}(c_p \Delta T + H_f)} = \frac{E_{kinetic,explosion}}{E_{melt,thermal}}$$

$$\eta = \frac{(742.5)^2 / (2 \cdot 40.5)}{4.1 \cdot (630 \cdot 2500 + 422.10^3)}$$

$$\eta = \frac{6.806.10^3}{8.227.10^6} = \underline{\underline{0.0827\%}}$$

where F presents dynamic force, m_{water} mass of water, m_{melt} mass of melt assumed as having participated, c_p is heat capacity, ΔT is the difference of melt and water initial temperatures and H_f enthalpy of fusion.

6.4.1 KS2 debris size distribution

After the experiment the facility was dismantled, the debris was collected and dried for 8 hours at 150 °C. Mechanical sieve (Fisher Scientific, Test Sieve) was used for the debris separation according to the size (*Figure 6.7*).

The size distribution and cumulative size distribution for KS2 test are depicted in the *Figure 6.8* and summarized in the *Table 6.4*. Interesting observation is that the debris size distribution has two maxima (0.2-0.5 and 0.05-0.1 mm) and therefore doesn't follow classical size distributions functions (log-normal, Weibull or log-hyperbolic).

137

Figure 6.7 Debris mechanical sieve
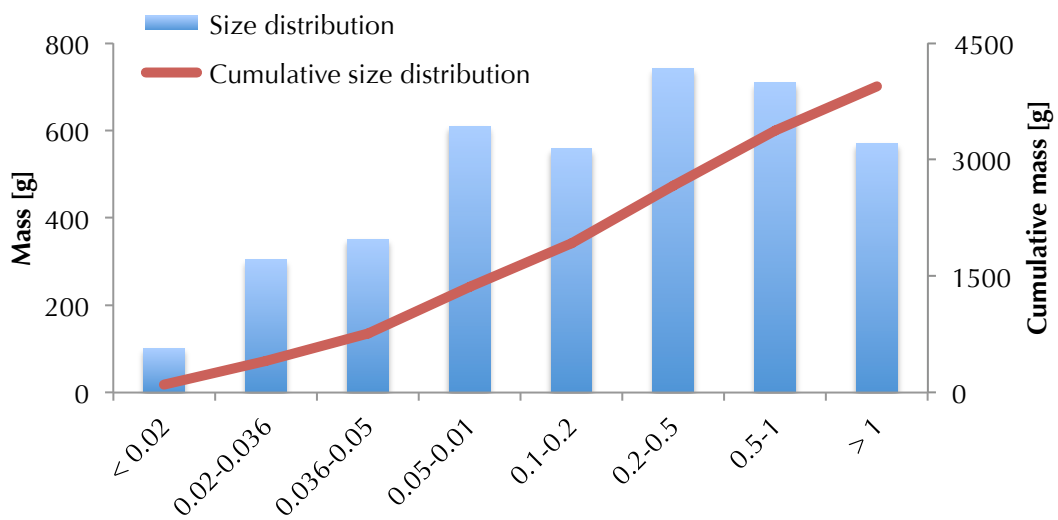
Figure 6.8 Size distribution of the KROTOS KS2 debris [mm]

Table 6.4 Summary of the size distribution of KROTOS KS2 debris

KS2 debris [mm]	Mass [g]	Cumulative mass [g]
< 0.02	101.9	101.9
0.02-0.036	304.7	406.6
0.036-0.05	351.6	758.2
0.05-0.01	608.8	1367
0.1-0.2	558.2	1925.2
0.2-0.5	741.9	2667.1
0.5-1	709.1	3376.2
> 1	570.6	3946.8

6.4.2   SEM/EDS analyses of KS2 debris

Figure 6.9 a-d presents the SEM micrographs of 0.5-1 mm debris as an example of large debris. It contains angular particles, relicts of broken drops. Another type of debris is of spherical shape and has well-conserved surface evidently exposed to water/steam (*Figure 6.9 c,d*). Periodical structure of squamous or jut like objects can be seen on the particle surface. Size of the cells varies between 10 and 100 µm.
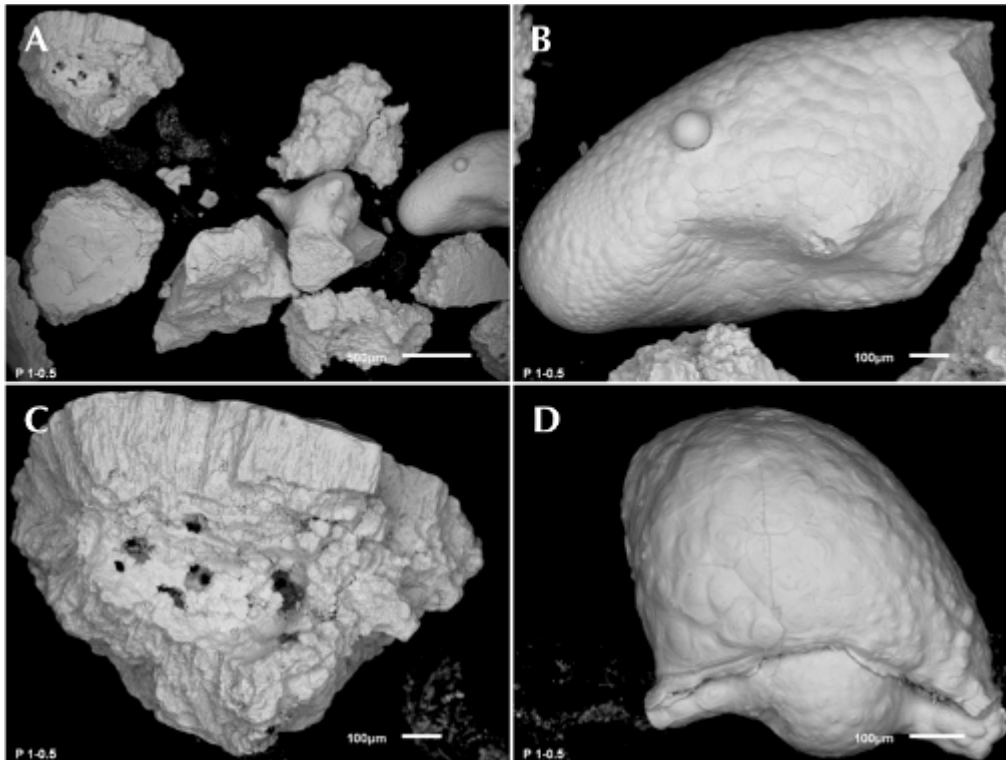
Figure 6.9 SEM micrographs of the KS2 debris 0.5-1 mm

Physical explanation of this observation can be following, a quasi-steady heat transfer is between the melt and water/steam environment. The heat is transferred from melt surface layer of certain thickness perpendicularly to the surface. This situation is known to go through Rayleigh-Benard or Benard-Marangoni instabilities [6.1]. They are often mixed up because the visual consequences on the liquid motion are similar. The Benard-Marangoni instabilities are formed due to the non-uniform gradient of surface tension of the liquid. This effect induces melt motion in the direction of from hot places (low surface tension) in radial direction to cold open surface. Colder liquid (lower surface tension) have to move to replace the hot liquid to fulfill the mass balance law (*Figure 6.10*).

The Marangoni number Ma describes the formation of the instabilities and it is defined by *Equation 6.1*. Critical Ma number for instability occurrence is usually experimentally measured.

$$Ma = \frac{d\gamma}{dT} \frac{\Delta T d}{\mu a}$$

eq. 6.1

139

where γ represents the surface tension, ΔT is the temperature difference, μ presents the dynamic viscosity and a thermal diffusivity.
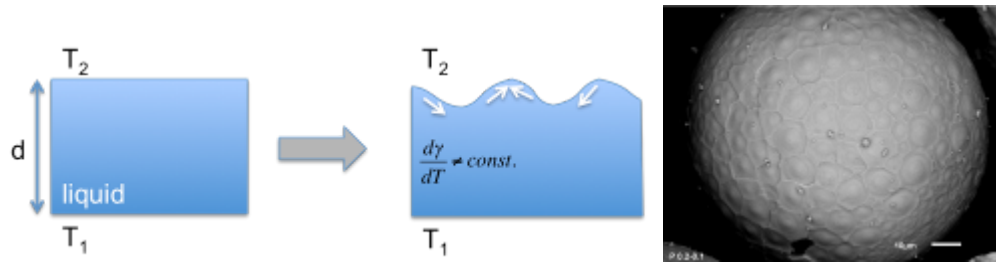
Figure 6.10 Description of the Benard-Marangoni instabilities formation - right, example of droplet surface (KS2 0.1-0.2 mm) - left

Further, SEM pictures of the KS2 powder 0.05-0.1 mm are shown in the *Figure 6.11*. In general, the particle shapes are irregular (angular) or spherical (symmetric or elongated). The surface cell (Marangoni) structure can be found as well. Detail of broken spherical particle is depicted in the *Figure 6.11d*.It shows clearly a particle with a surface that could be attributed to Marangoni effect. Photographs of the fine powder samples (< 0.02 and 0.02-0.036 mm) are presented in the *Figure 6.12*. A majority of fine powder debris looks like dust. Some spherical particles can be found as well. *Figure 6.13* illustrates the cross-section images of debris from all the sieving fractions.
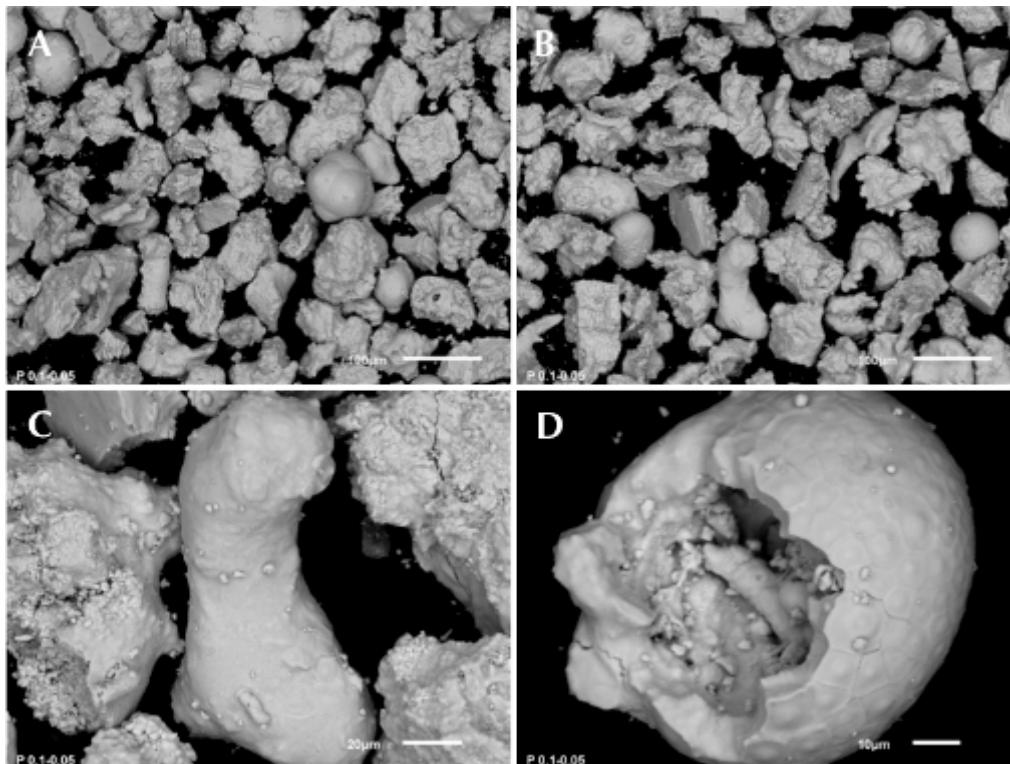
Figure 6.11 SEM investigation of the KS2 debris 0.05-0.1 mm
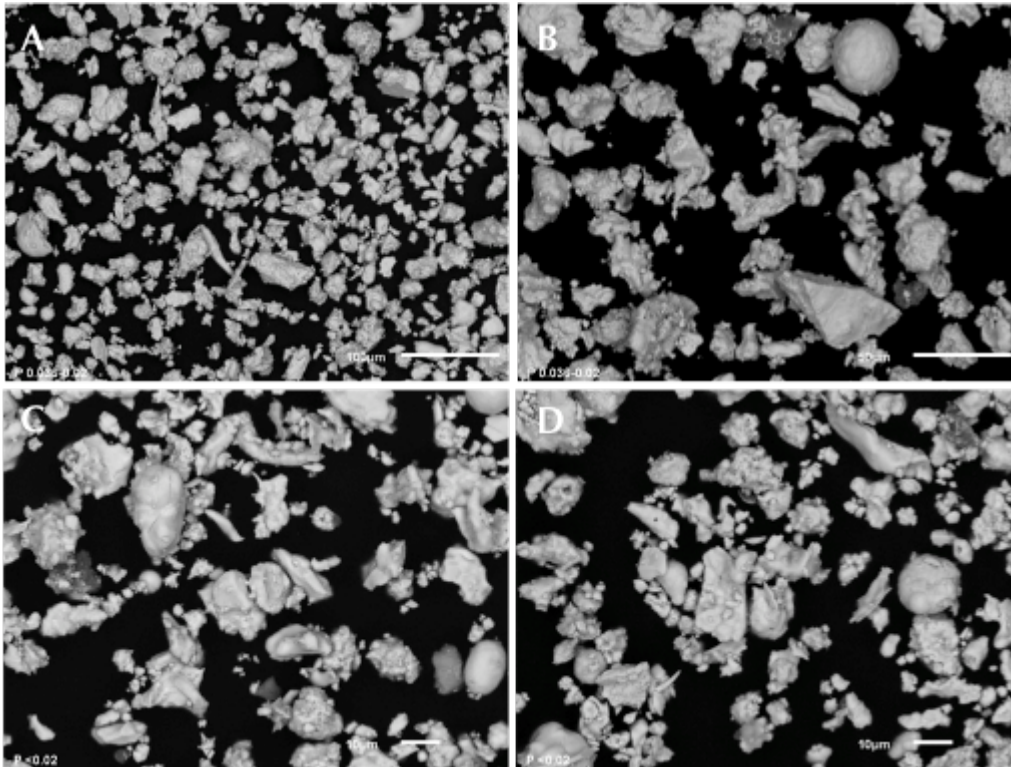
Figure 6.12 SEM micrographs of KS2 fine debris, <0.02 mm at the bottom and 0.02-0.036 at the top

Two families of debris have been identified: full debris and porous debris. They can be observed in the *Figure 6.13* for fractions 0.2-0.5 and 0.1-0.2 mm.

Detail of the particle having large internal void fraction (porosity) and particle full is given in the *Figure 6.14*. We assume that porous particles participated to the steam explosion. During the fine fragmentation the melt droplets came into close contact with water. Moreover, this morphology of internal channels and non-symmetrically irritated surface can be attributed to the Kim-Corradini mechanism of thermal fragmentation mentioned in the *Chapter 2*.

The internal porosity seems to decrease with decreasing size of the debris, while the smallest debris (< 0.02 mm) seems to be dense without any internal void.

Composition of the debris obtained by EDS analysis is shown in the *Figure 6.15*. The uranium/zirconium ratios for all sizes are depicted in the *Figure 6.16*. From this analysis, it can be noted that:

- The $UO_{2/}ZrO_2$ composition is always the same for a same class of debris,
- The $UO_{2/}ZrO_2$ composition is the same whatever the class,
- The average composition is: 67 w. UO_2 and 33 w. % ZrO_2.

Tungsten and Tin are detected. A little amount of aluminum was observed as well. No systematical tendencies in the presence of impurities were found according to the size fractions.

KS2 >1 mm

KS2 0.5-1 mm

KS2 0.2-0.5 mm

P 0.5-0.2

500μm

KS2 0.1-0.2 mm

100μm

KS2 0.05-0.1 mm

100μm

KS2 0.036-0.05 mm

KS2 0.02-0.036 mm

50μm

KS2 <0.02 mm

10μm
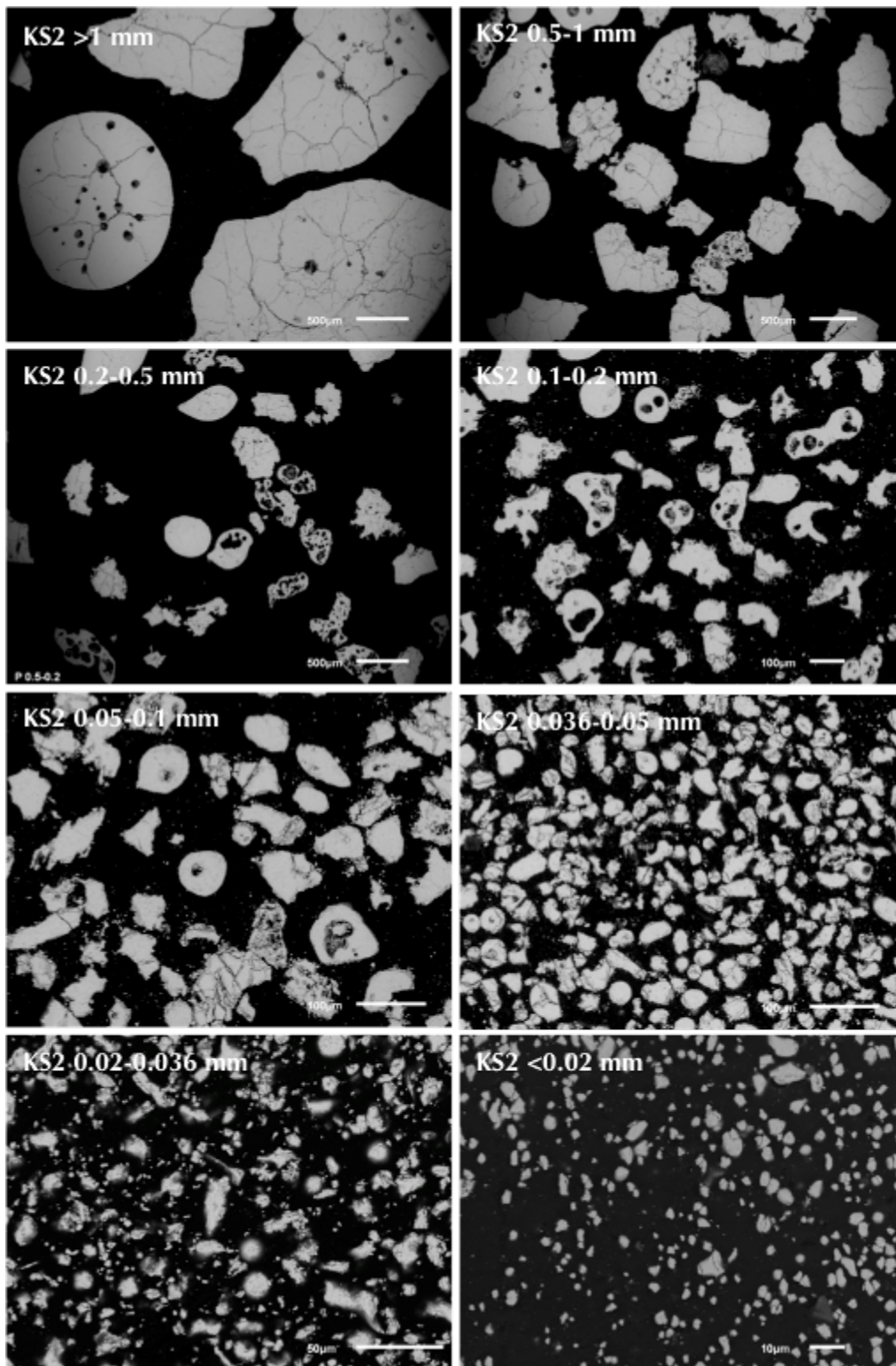
Figure 6.13 SEM images of cross-sections of debris from all sieving fractions

142
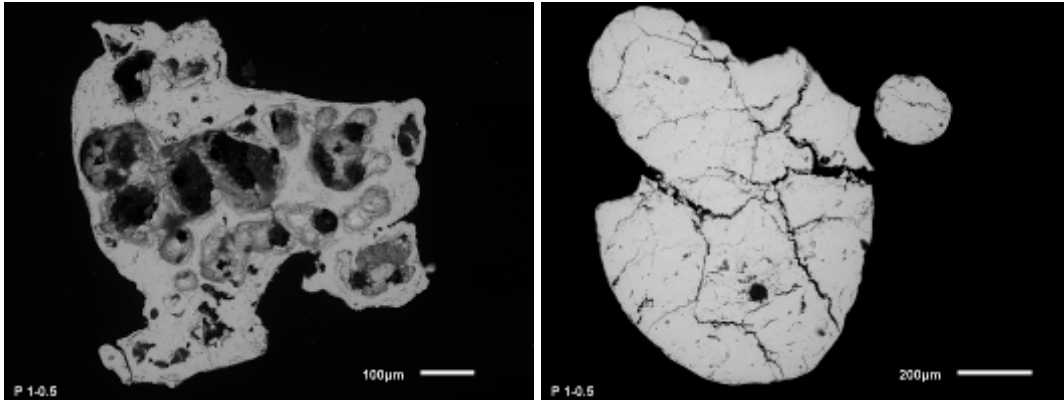
Figure 6.14 KROTS KS2 debris 0.5-1 mm, particle participation to SE - left, quenched full particle – right
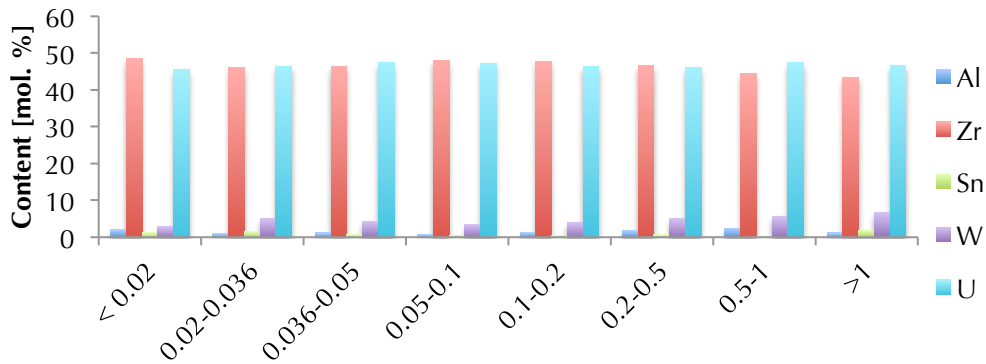
Figure 6.15 Composition of the KS2 debris by EDS, chart presents content of metals (without oxygen), size distribution in [mm]
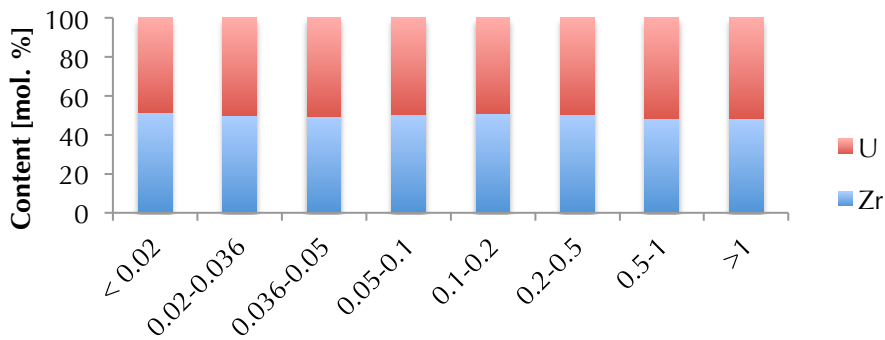
Figure 6.16 Uranium/zirconium ratio in KS2 debris (in [mm]) by EDS analysis

The analysis of the debris interior is shown in *Figure 6.17*. The melt solidified into grain (ceramic like) structure. The grain sizes are ranging from ~1 to ~10 μm. The largest grain sizes have been observed in the center of the debris, i.e. the zone of the droplet in which the slowest cooling rate occurred (*Figure 6.17*). Unfortunately, no statistical treatment was done due to the low contrast of the grain boundaries. The grain size depends indirectly on the melt quenching rate [6.2] as follows:

$$D \sim m\left(\frac{dT}{dt}\right)^{-n}$$

where D is the grain size, T is temperature, t is time and n, m are experimental coefficients.

No experimental or theoretical investigations were found for corium mixture in this direction. We can quote that the quenching rate exponentially decreases from the surface to the droplet center.
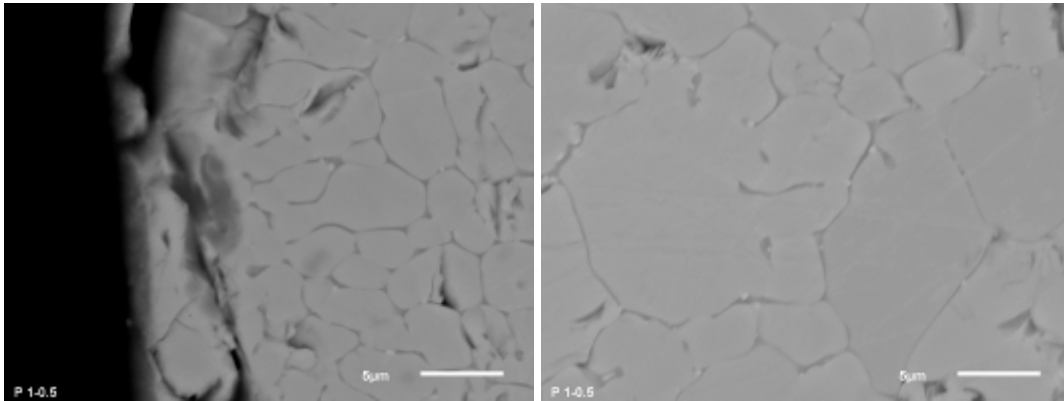
Figure 6.17 Detailed SEM picture of droplet cross-section (KS2 0.5-1 mm), surface – left, center of the droplet - right

Crucible samples

SEM/EDS analyses were performed for samples taken from the crucible. Thus, these samples didn't interact with water and present purely solidified melt in inert atmosphere.

Due to the lower cooling rate, some parts of the sample have been solidified close to the thermodynamic equilibrium and present several solid solutions. Uranium and zirconium tend to separate and uranium and zirconium rich phases are formed (*Figure 6.18*). W-UO_2-ZrO_2 eutectic mixture was observed in the sample of crucible melt. The wire like morphology of the eutectic mixture is shown in the *Figure 6.19*. Its composition obtained by EDS corresponds to 5.5 % W, 52.5 % U and 42.0 % Zr (in mol. %).
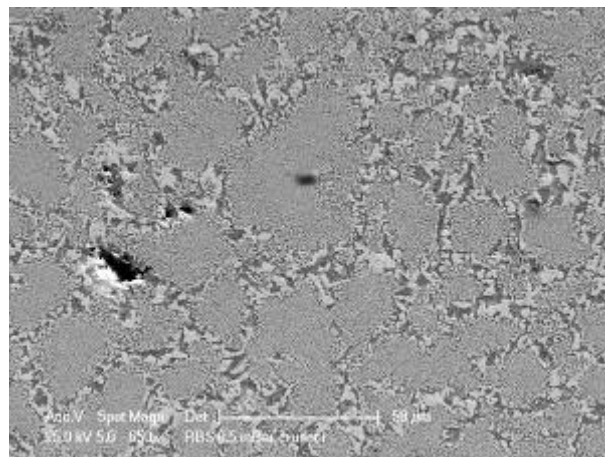
Figure 6.18 Structure of the solidified melt in the crucible
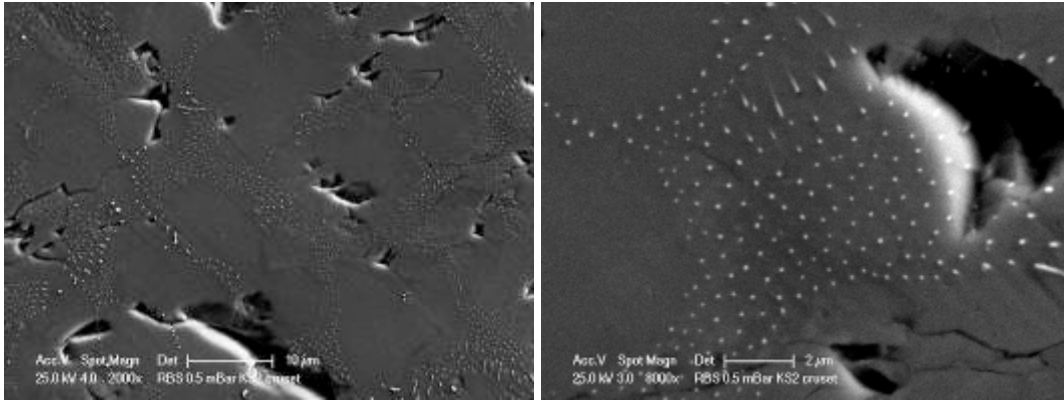
Figure 6.19 W-UO$_2$-ZrO$_2$ eutectic mixture in the KS2 crucible sample

6.4.3   KS2 image analysis

Background for the image analyses

The images of the particles cross-sections obtained by scanning electron microscopy were treated by image analyses using the ImageJ software [5.5]. We focused on the following characteristics of image analysis:

- **Circularity** – defines the relation of perimeter (P) and surface area (A). For circle it equals to 1.

$$f_{circ} = 4\pi \frac{A}{P^2}$$
eq. 6.3

- **Roundness** – defines the rotation symmetry of an object using surface are (A) and major axis (l).

$$f_{round} = \frac{4A}{\pi l^2}$$
eq. 6.4

- **Solidity** – defines the object's contour homogeneity (symmetry). It is expressed as ratio of surface area and surface area of the same object with only convex borderlines.
- **Porosity** – is defined by surface area of an object excluding internal holes (A) and by surface area including internal holes (B)

$$f_{porosity} = \frac{(B-A)}{B} \cdot 100\%$$
eq. 6.5

Several phantom pictures were used to qualify the image analysis approach and to have information about the characteristics of simple shapes. The phantom picture is shown in the *Figure 6.20* in its initial form and after image treatment. Information about the phantom objects obtained by image analysis is summarized in the *Table 6.5*. One can see the effect of the shape on circularity, roundness and solidity. Circles and rectangles has all the factors close to one, while the irregular objects tend to have values lower, even close to zero.
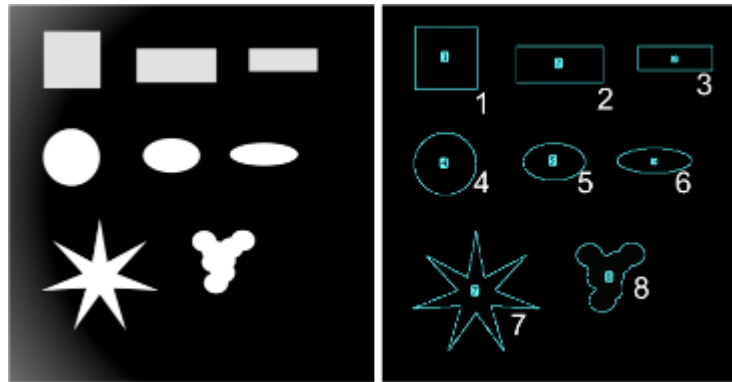
Figure 6.20 Picture of phantom shapes (left) and picture after image treatment (right)

Table 6.5 Characteristics of the phantom shapes by image analysis

Number	Area [pixels^2]	Circularity	Roundness	Solidity
1	10201	0.795	1	1
2	8460	0.666	0.426	1
3	4840	0.595	0.331	1
4	7976	0.906	0.999	0.984
5	4779	0.828	0.598	0.98
6	3829	0.607	0.333	0.975
7	9734	0.095	0.972	0.331
8	6847	0.482	0.784	0.791

According to the approach previously developed about the different families of debris _i.e. having participated or not having participated to steam explosion, it is possible to propose image analyses criterions to identify these 2 families of debris. Particles as measured by SEM and after image treatment are shown in the *Figure 6.21*. The circularity, roundness, porosity and solidity were used for description. The results are on view in the *Table 6.6*.
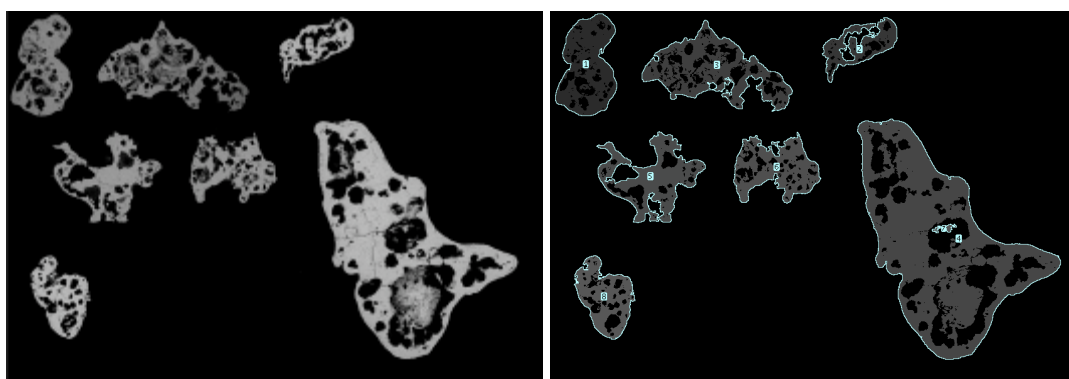
Figure 6.21 Debris (KS2 0.5-1 mm) participating to the steam explosion (left) and after image analysis (right)

Property	Average	Average deviation
Circularity	0.29	0.15
Roundness	0.57	0.1
Solidity	0.76	0.08
Porosity	21.84%	4.13%

We can quote that the particle participating to the steam explosion has notably asymmetrical shape with parts having concave contours. In average the porosity of the melt drop increase to almost 22 % by participation to the steam explosion.

All the sieving fractions were analyzed by the image analysis using the same procedure. Average image analyses characteristics are provided for all analyzed debris factions: circularity, roundness, solidity, and porosity.

Having above-mentioned results in mind a conservative borders were chosen to quantify particles of certain properties. The round (spherical particles) should have circularity and roundness higher than 0.6 at once.

Two independent criteria chosen for particles participating to SE, both based on the average characteristics of SE debris from *Table 6.6*:

First, the circularity should be lower than 0.29.

Then, the solidity should be lower than 0.76.

We have not studied the porosity (one central void) of particles that did not participate to the steam explosion. Thus we cannot establish a simple rule for the fraction of particles participating to SE using average porosity and porosity of SE particles. General scheme of the procedure is shown in the *Figure 6.22*.
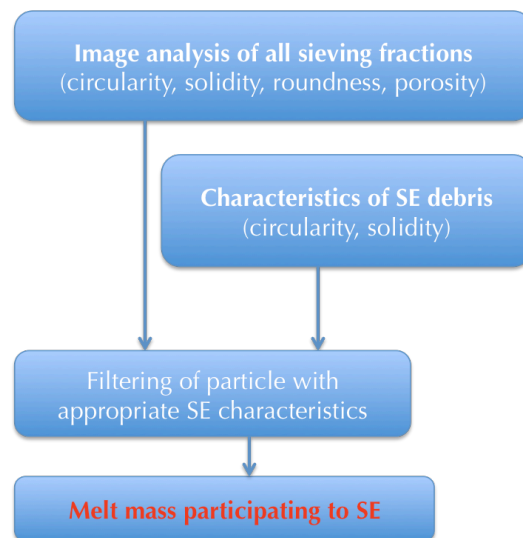
Figure 6.22 Estimation of the melt mass participation to SE by image analysis

Image analysis of KS2 debris

Statistical set of 3887 particles of KS2 debris was treated by image analysis. Firstly, the distributions of circularity and roundness are depicted in the *Figure 6.23*. Shift of the circularity distribution peak can be seen. The peak of the debris under 0.02 mm is around 0.8. This peak vanishes for fraction 0.02-0.036 mm and the circularity is

147

uniformly distributed. Small maximum is formed around 0.2 for the fraction 0.036-0.05 mm. This peak culminates for fractions 0.05-0.1 and 0.1-0.2 mm. For larger debris this maximum is shifted to higher circularity and disintegrated. Similar effect can be found for roundness, but it is not as intensive as for circularity.

This behavior corresponds to previous observations from the scanning electron microscopy. Fine debris presents grain like morphology having higher circularity and roundness. The shape irregularities are most developed for fractions from 0.05 to 0.2 mm.
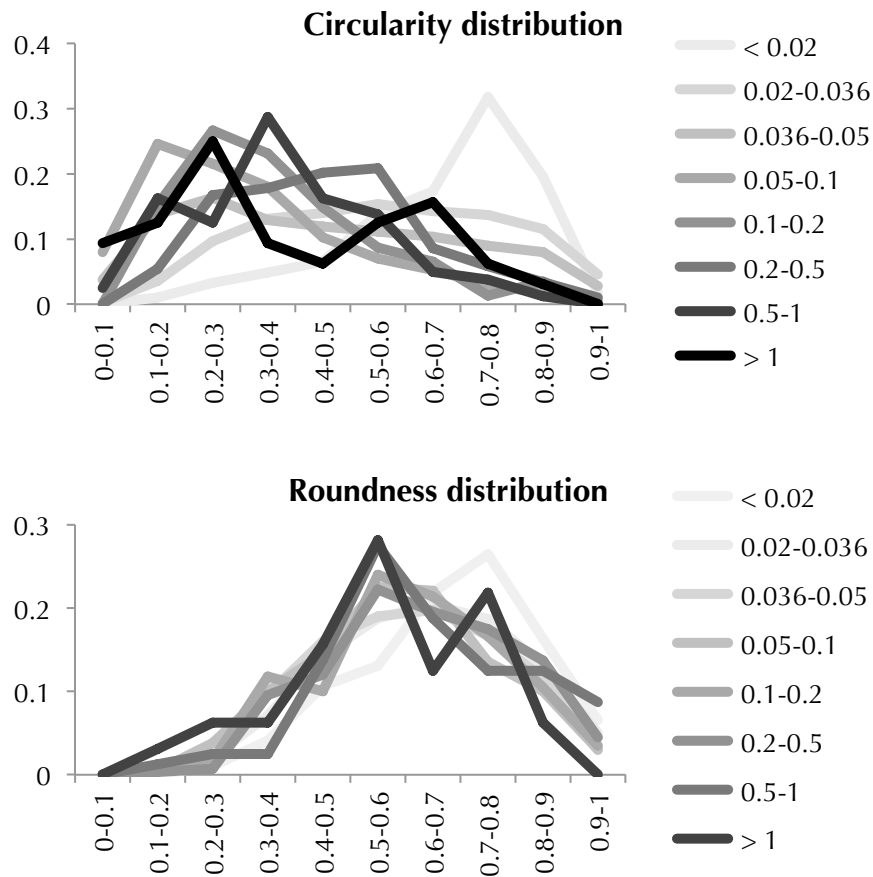
Figure 6.23 Circularity and roundness distribution for KS2 debris [mm]

More can be seen from the average values of circularity, roundness and solidity for each sieving fraction (*Figure 6.24*). The circularity reaches minimum for the fractions 0.05-0.1 and 0.1-0.2 mm. Similarly, the roundness has a local minimum at these fractions, but the difference is not significant. A deviation was obtained for roundness of debris larger than 1 mm, which is low. All mentioned above is confirmed by average solidity. The average solidity is lowest for the sieving fraction 0.05-0.1 mm.

The average debris porosity for each faction is given in the *Figure 6.25*. Two peak values correspond to the sieving fraction 0.05-0.1 mm, which contains 6.0 % of void, and 0.5-1 mm containing 4.9 % of void. The average internal porosity of the KS2 debris is 3.4 %.
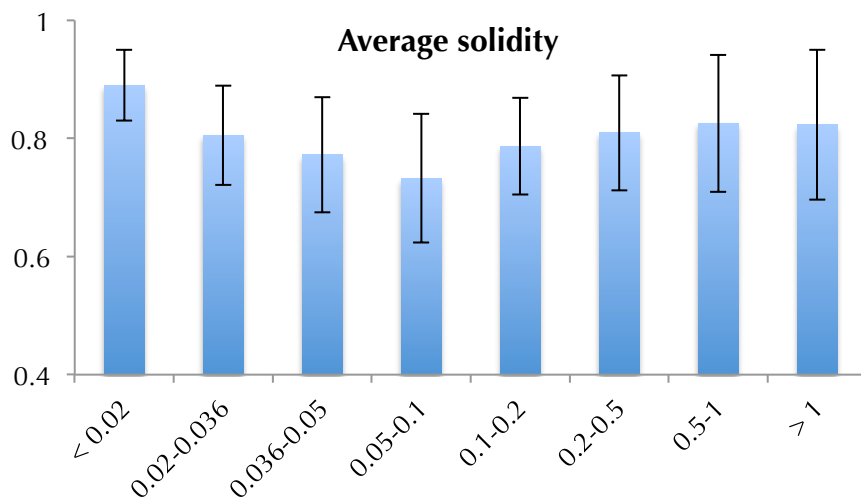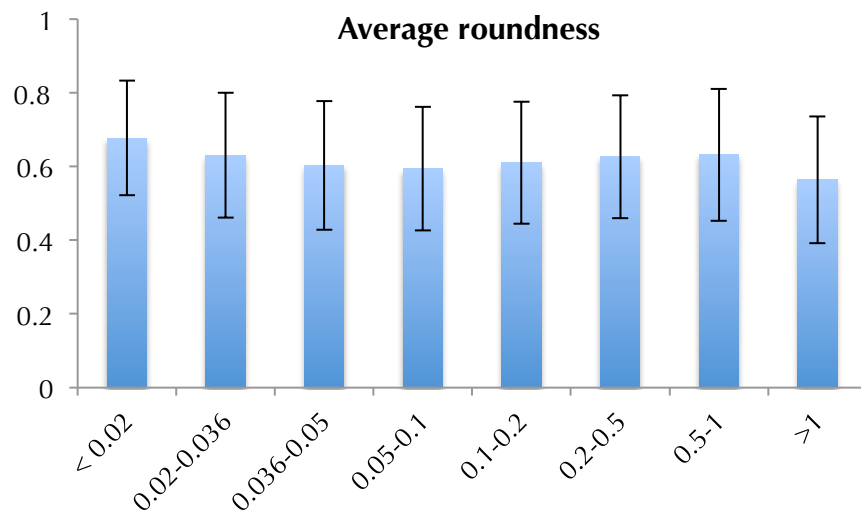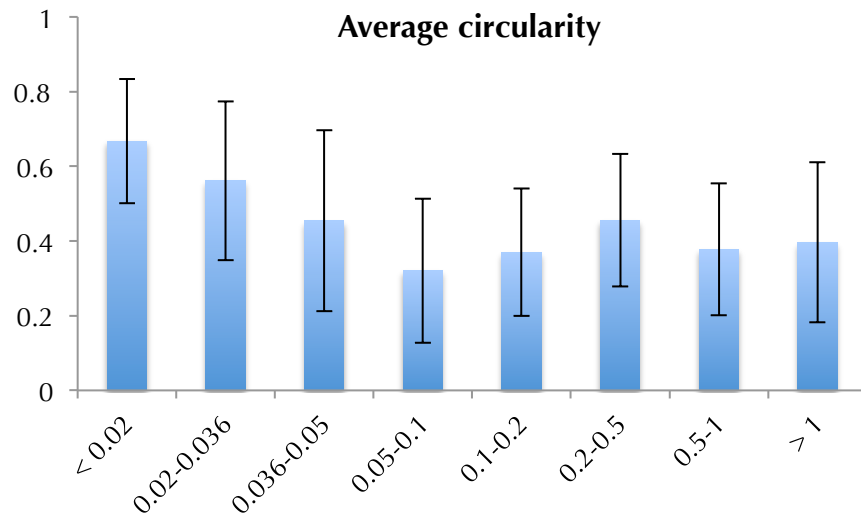
Figure 6.24 Average characteristics of KS2 debris by image analysis, size distribution in [mm]

149
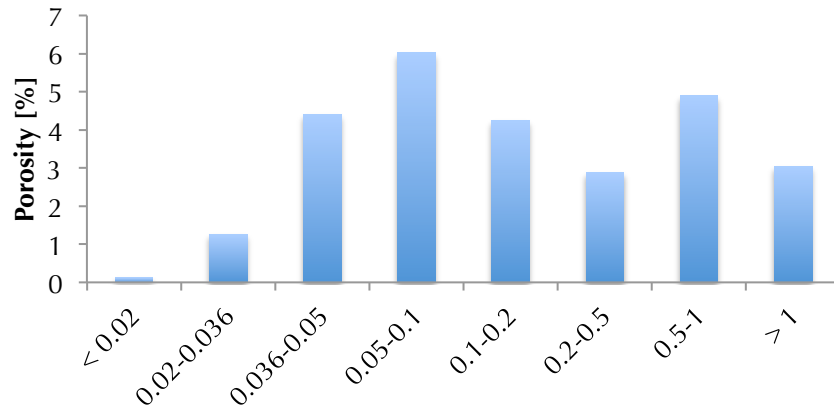
Figure 6.25 Average porosity of the KS2 sieving fractions (in [mm])

Droplet participation to the steam explosion was studied by above-mentioned criteria. All the results, summarized in the *Figure 6.26*, indicate that significant part of the debris from 0.036 to 0.5 mm participated to the steam explosion. If we average the results of the two mentioned criteria, we receive general values for the participation to the steam explosion (*Table 6.7*).

Concerning the sieving fraction distribution and masses, the amount of melt participated to SE is 1352 g, which presents 34.3 w. % of delivered melt.
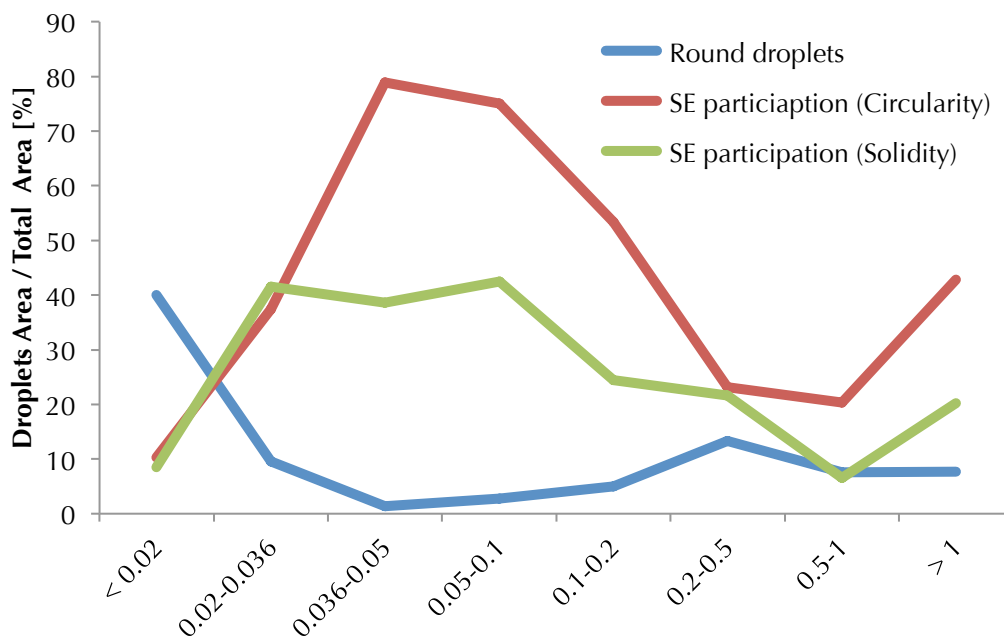
Figure 6.26 Particles participating to the steam explosion and spherical droplets in the KS2 sieving fractions (in [mm])

Table 6.7 KS2 melt participation to the steam explosion

KS2 debris [mm]	SE participation [wt. %]	Mass [g]	Mass SE [g]	
< 0.02	9.4	101.9	9.6	
0.02-0.036	39.4	304.7	120.2	
0.036-0.05	58.8	351.6	206.6	
0.05-0.1	58.8	608.8	357.9	
0.1-0.2	38.9	558.2	217.0	
0.2-0.5	22.4	741.9	165.9	
0.5-1	13.4	709.1	95.3	
> 1	31.5	570.6	180.0	
	Sum	**3946.8**	**1352.5**	**34.3 w.%**

6.4.4   X-ray powder diffraction of KS2 debris

The K2 debris was characterized by conventional X-ray powder diffraction. Overview for all the debris sieving fractions is given in the *Figure 6.27*. It was found that the melt solidifies into $U_xZr_{1-x}O_{2+y}$ solid solution having face-centered cubic crystal structure. The differences among the sieving fractions are detectable. However, slight shifts of the peak positions can be observed. This is more visible for high angle diffractions, for example patterns of planes (331) and (042). Shift of the diffraction to higher value of two theta degrees corresponds to smaller elementary cell. According to the findings mentioned in the *chapter 3,* the size of the cell is decreasing with increasing content of zirconium in the solution or increasing oxygen in over-stoichiometry. The face-centered cubic phase has only one lattice parameter. We used the whole-pattern pattern fitting method WPPF (Pawley method, Diffrac-Plus Topas, Bruker AXS, Germany, version 4.2) based on the Rietveld pattern refinement to obtain this lattice parameter and to calculate the oxygen over-stoichiometry. The uranium and zirconium contents used for these calculations were obtained from the EDS analyses.
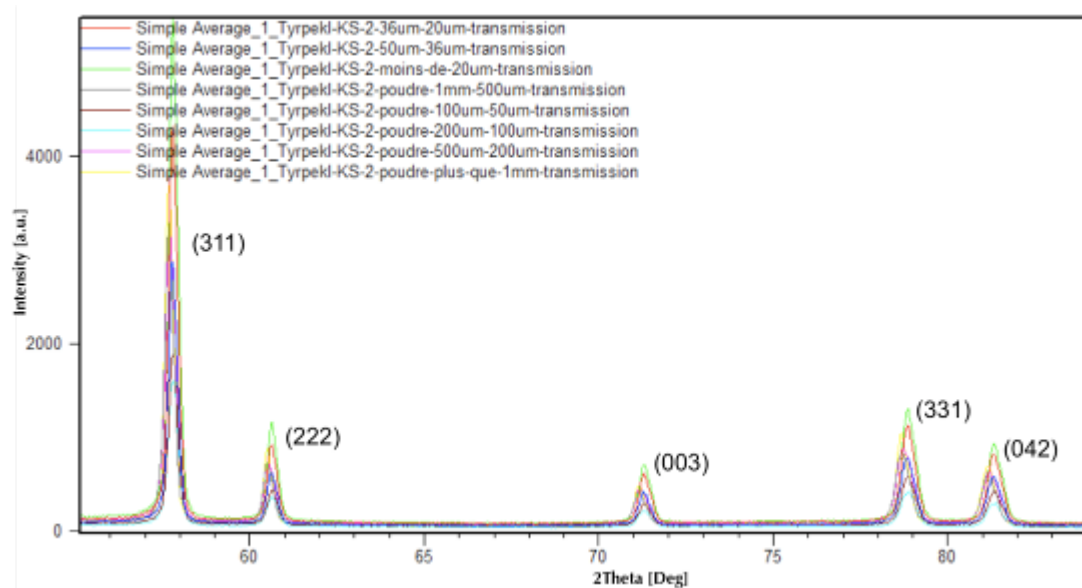
Figure 6.27 X-ray powder patterns of the KS2 debris

151

Example of the WPPF fit for KS2 debris 0.1-0.2 mm by Fm-3m space group (face-centered cubic) is shown in the *Figure 6.28*. The calculated pattern perfectly matches the measured data. The elementary cell parameters calculated for all the sieving fractions are summarized in the *Table 6.8*. This table contains also the calculated oxygen over-stoichiometry of the $U_xZ_{1-x}O_{2+y}$ solid solution expressed by y (*Figure 6.29*). Surprisingly, the oxygen over-stoichiometry is important for particles marked by the image analysis as those participating to SE. Obviously, closer water-melt contact during the fragmentation leads to deeper chemical reaction. It is considered that the melt oxygen stoichiometry is at equilibrium before contact with water/steam, thus y equals to zero. Thus, the amount of hydrogen generated by the melt – water reaction was calculated and the results are shown in the *Table 6.8* as well.
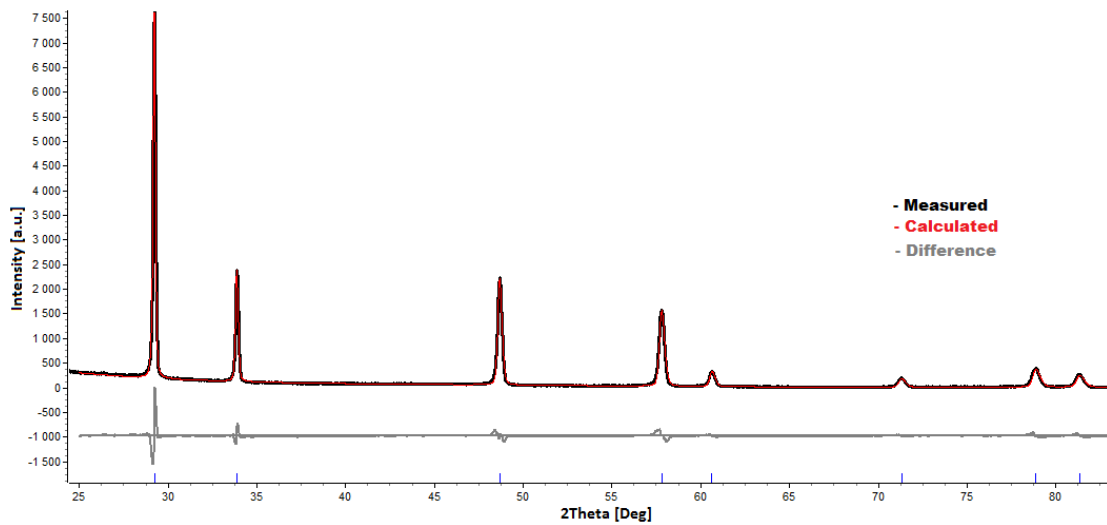
Figure 6.28 WPPF fit of the X-ray powder pattern (KS2 debris 0.1-0.2 mm)
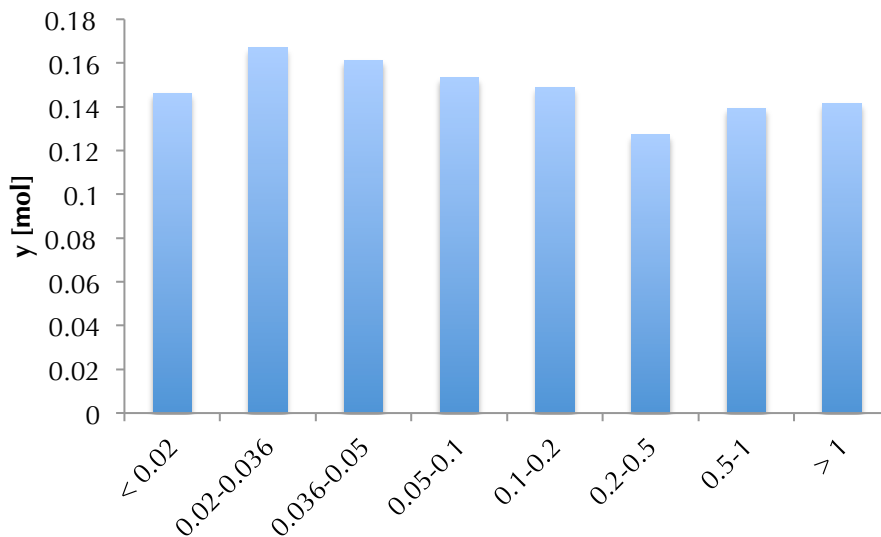
Figure 6.29 KS2 debris oxygen over-stoichiometry, expressed as y from $U_xZr_{1-x}O_{2+y}$, sieving fractions in [mm]

152

Table 6.8 KS2 debris X-ray pattern analysis, oxygen over-stoichiometry y of $U_xZr_{1-x}O_{2+y}$ solid solution and hydrogen production

KS2 debris [mm]	a [Å]	y [mol]	Hydrogen [mol]	Hydrogen [g]
< 0.02	5.285	0.146	0.076	0.153
0.02-0.036	5.286	0.167	0.255	0.514
0.036-0.05	5.288	0.161	0.284	0.572
0.05-0.1	5.287	0.153	0.470	0.948
0.1-0.2	5.287	0.149	0.419	0.845
0.2-0.5	5.293	0.127	0.476	0.959
0.5-1	5.296	0.139	0.491	0.990
> 1	5.296	0.141	0.400	0.807
		Sum	**2.871**	**5.788**

The total amount of hydrogen produced by melt-water chemical reaction is almost 5.8 g. This value cannot be taken as final, because hydrogen is generated also by water thermal decomposition (T > 2000 K). Amount of hydrogen produced by water thermal decomposition cannot be obtained as easily as in the case of melt-water chemical reaction, because the kinetics of this process is not well described.

Crucible samples

The X-ray powder pattern of the crucible sample is shown in the *Figure 6.30*. The phase composition observed is due to cooling rates close to thermodynamic equilibrium. Compared to the debris that interacted with water, the melt in the crucible has more time for reorganization and diffusion at the solid state. These results confirm the observation obtained by SEM/EDS. The powder pattern can be fitted by two face-centered cubic (a = 5.173 and 5.333 Å) and two tetragonal (a = 4.998 c = 4.909 Å and a = 5.421 c = 5.444 Å) phases.
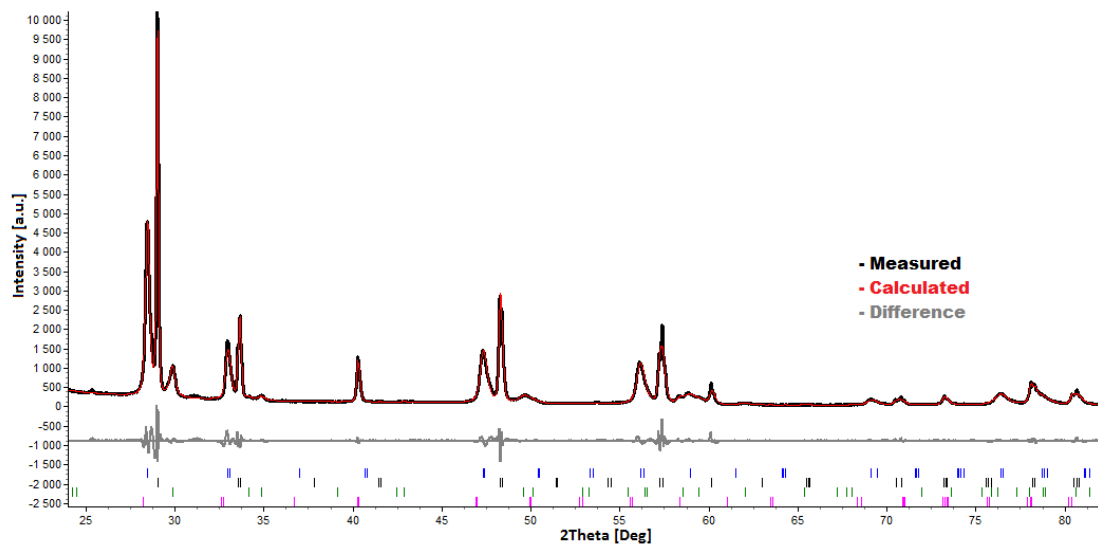
Figure 6.30 X-ray powder pattern of the KS2 crucible sample with WPPF analysis

Reduction experiments were carried out using KS2 crucible and KS2 0.02-0.036 mm debris. The power samples were introduced into a furnace and annealed for 4 hours at 800 °C under reductive atmosphere (7.5 % H$_2$ and 92.5 % Ar). Detail of the peak shift caused by reduction of oxygen over-stoichiometry is given in the *Figure 6.31* for both samples treated by the same procedure. The peak position shift is obvious for KS2 0.02-0.036 mm, but no significant difference was obtained for the sample coming from the crucible. It has been shown that the melt released from the furnace presents equilibrium stoichiometry and therefore the oxygen over-stoichiometry limits to zero.
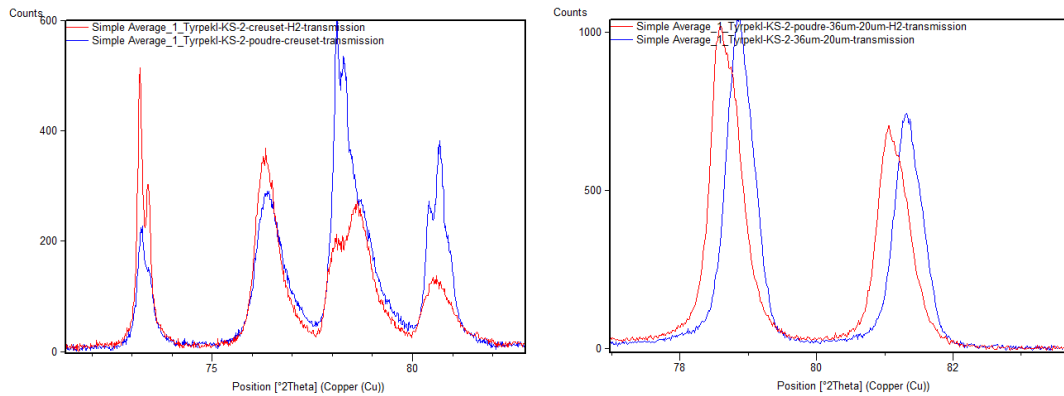
Figure 6.31 X-ray powder pattern of the KS2 crucible sample (left) and KS2 0.02-0.036 (right), reduced samples by hydrogen are in red and non-reduced samples are in blue

6.4.5 ICP/MS analyses of KS2 debris

The KS2 debris was chemically analyzed by the Inductively Coupled Plasma Mass Spectrometry (ICP/MS) as a support and confirmation of the EDS analyses. For each sieving fraction 100 mg were taken and dissolved in two periods. At first, the powder was suspended in a mixture of HNO$_3$ and HCl. The next step included dissolution of the residue in a mixture of HNO$_3$ and HF.

The results are summarized in the *Table 6.9*. The debris composition obtained by ICP/MS confirms the ones obtained by EDS analysis and give overall composition of the debris. It was confirmed that the debris is slightly polluted by tungsten and tin. The tin contamination reaching maximal value 0.38 w. % can be neglected. Debris contains up to 3.28 w. % of tungsten.

Table 6.9 ICP/MS analyses of the KS2 debris, size fractions in [mm]

		Content [w.%]			Content [w.%]
	Al	< 0.1		Al	< 0.1
	Sn	0.36		Sn	0.14
KS2 < 0.02 mm	W	3.38	**KS2 0.1-0.2**	W	2.67
	UO_2	66.26		UO_2	66.80
	ZrO_2	29.90		ZrO_2	30.33
	Al	< 0.1		Al	< 0.1
	Sn	0.23		Sn	0.12
KS2 0.02-0.036	W	3.02	**KS2 0.2-0.5**	W	3.29
	UO_2	66.49		UO_2	66.65
	ZrO_2	30.21		ZrO_2	29.90
	Al	< 0.1		Al	< 0.1
	Sn	0.17		Sn	0.38
KS2 0.036-0.05	W	3.25	**KS2 0.5-1**	W	3.28
	UO_2	65.81		UO_2	66.53
	ZrO_2	30.72		ZrO_2	29.78
	Al	< 0.1		Al	< 0.1
	Sn	0.11		Sn	< 0,05
KS2 0.05-0.1	W	2.41	**KS2 > 1 mm**	W	3.38
	UO_2	67.09		UO_2	66.85
	ZrO_2	30.35		ZrO_2	29.67

6.4.6   Conclusion

It was shown that the KROTOS KS2 experiment provided externally triggered steam explosion. Melt front position history was described, the jet release velocity reached 20m.s^{-1}.

The steam explosion efficiency calculated according to the classical approach described in *Chapter 2*, is about 0.08 %.

The released melt present $U_{1-x}Zr_xO_2$ solution with equilibrium oxygen stoichiometry. During the fragmentation the melt react with water/steam producing hydrogen and oxygen rich melt/debris.

It has been possible to distinguish two families of debris: those having participating to steam explosion and those, which have not. Porous and irregular particles were assumed to participate to the steam explosion, while full particles (round or angular) were attributed to quenching . The melt solidifies during FCI into face-

centered cubic phase. Low pollution was observed, mainly by tungsten coming from the crucible.

Cellular structure was found on the debris surface exposed to water. This phenomenon was attributed to the formation of Marangoni-Benard instabilities. The droplet interior is formed by ceramic like grains. The composition is homogenous and in average corresponds to 67 w. % of UO_2 and 33 wt.% ZrO_2.

Droplet participation to the steam explosion was studied by means of image analysis. In general, 34.3 w. % of the melt participated to the steam explosion.

The formation of hydrogen was described by chemical reaction of melt and water/steam. About 5.8 g of hydrogen was produced by this reaction.

6.5 References

6.1   http://hmf.enseeiht.fr/travaux/CD0001/travaux/optmfn/hi/01pa/
         hyb72/bm/bm.htm#part2
6.2.   M. C. Flemings: Solidification Processing, McGraw-Hill Book Company Inc.,
         New York, 1974

Chapter 7. KROTOS KS3 and KS4 tests

7

Experimental results of the KROTOS KS3 and KS4 tests are presented in following paragraphs.

7.1 KROTOS KS3 experiment

The KS3 experiment failed during the release phase. However, this test can be taken as simple melting/solidification experiment with KS2 composition (70 w. % UO_2, 30 w. % ZrO_2).

The melt solidifies into mixture of tetragonal and face-centered cubic phases due to the cooling rate closer to thermodynamic equilibrium. The X-ray powder pattern with the WPPF fit is presented in the *Figure 7.1*. The pattern was fitted using three face-centered cubic cells (a = 5.312, 5.444 and 5.169 Å) and one tetragonal phase (a = 4.441 and c = 4.477 Å).
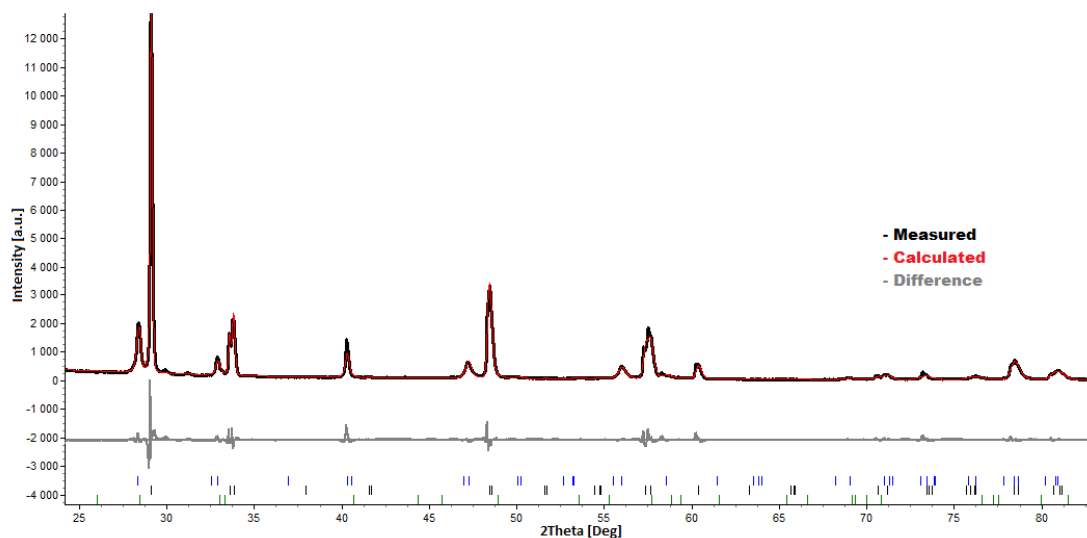
Figure 7.1 X-ray powder pattern with WPPF fit of KS3 crucible sample

An eutectic mixture of W-UO_2-ZrO_2 was observed (*Figure 7.1* left). The eutectic composition calculated from EDS data corresponds to 11.6 w. % W, 55.0 w. % UO_2 and 33.4 w. % ZrO_2, Large solidified droplets of tungsten melt were found inside the UO_2-ZrO_2 mixture (*Figure 7.2* right). In this case, we could assume the existence of two immiscible liquids (W and UO_2-ZrO_2). The composition of the tungsten phase corresponds to 57 w. % W, 28 w. % UO_2 and 15 w. % ZrO_2.
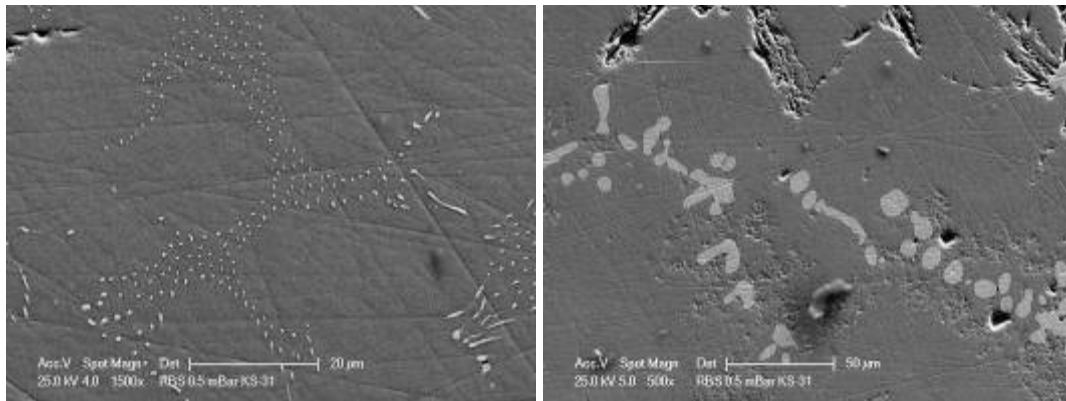
Figure 7.2 Eutectic mixture W-UO$_2$-ZrO$_2$ observed in KS3 experiment

In conclusion, it has been seen that the homogenous UO$_2$-ZrO$_2$ solution contains usually less than 1 mol. % of tungsten.

7.2 KROTOS KS4 experiment

In the KROTOS KS4 experiment 3.2 kg of corium melt (80 w. % UO$_2$ and 20 w. % ZrO$_2$) was melted and poured into water pool of 65 °C and externally triggered.

History of the melting phase is given in the *Figure 7.3*. The crucible load was stepwise heated up to 2685 °C (the actual value few second before release is 2689 °C, 2962 K), which means i.e. 60 °C over-heating above the theoretical liquidus point.
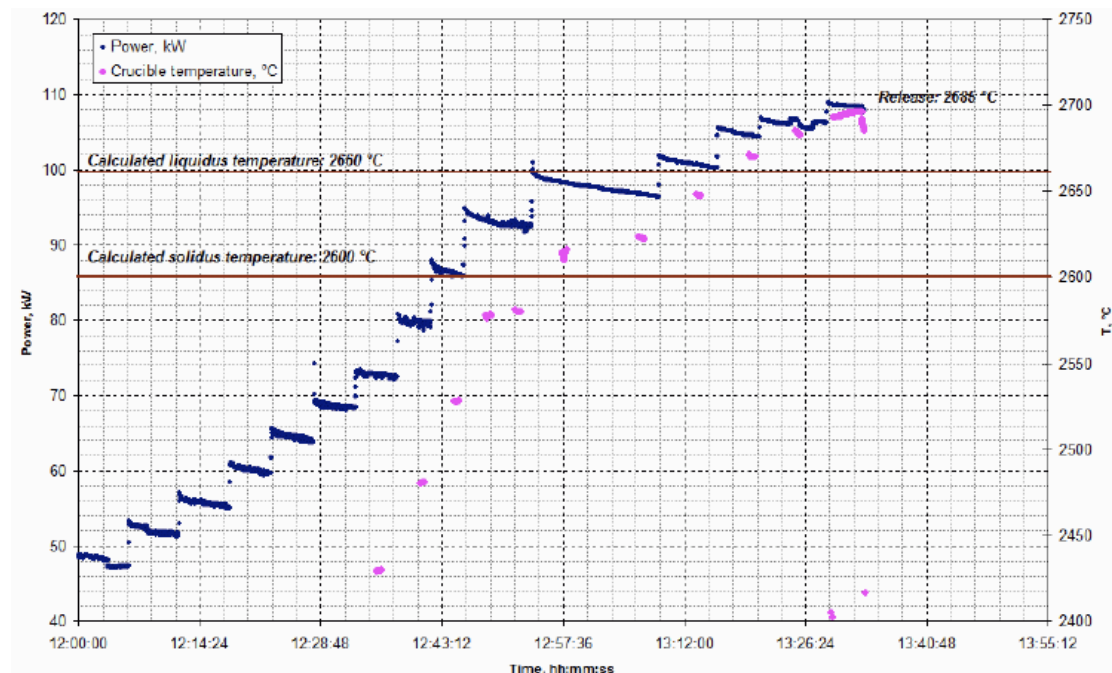
Figure 7.3 History of the melting phase in the KROTOS KS4 experiment

After the crucible impact on the puncher the melt was released and well suspended by the tin membrane. Stable and coherent melt jet was observed (*Figure 7.4*). The jet release velocity was estimated to be 2.3 m.s^{-1}.
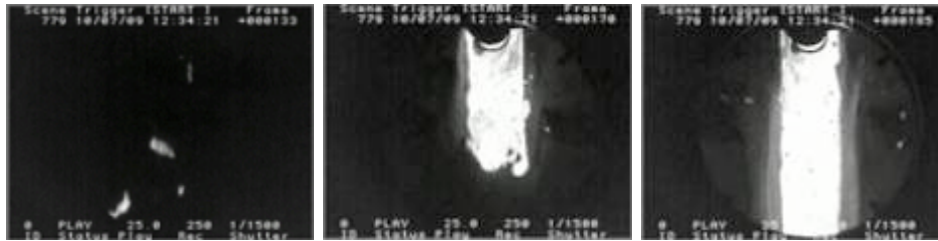
Figure 7.4 Corium release by optical camera (frame 133,166 and 185)

The jet was completely broken up at elevation ~0.7 m, while in the KS2 experiment at 0.4 m. Thus, the jet beak up length is lower for KS2 experiment. This can be explained by higher jet initial velocity in KS2 experiment.

The dynamic pressure reached the highest value among the KROTOS tests. Again we have to skip the actual values of dynamic pressure and melt front history due to the confidence restrictions of the OECD project.

Considering measured data the steam explosion efficiency was calculated. Following lines demonstrates the calculation of the final value of SE efficiency that reached 0.182 %.

$$\eta = \frac{(\int F\,dt)^2 / 2m_{water}}{m_{melt}(c_p\Delta T + H_f)} = \frac{E_{kinetic,explosion}}{E_{melt,thermal}}$$

$$\eta = \frac{(898)^2 / 2\cdot 34.5}{3.21\cdot(630\cdot 2500 + 422\cdot 10^3)}$$

$$\eta = \underline{0.182\%}$$

7.2.1 KS4 size distribution

The debris was collected after the facility dismantlement and dried for 8 hours at 150 °C. The debris size distribution performed by mechanical sieving is shown in the *Figure 7.9* and summarized in the *Table 7.1*.

The KS4 debris shows nearly monotonous size distribution. However, local maxima can be found for the fraction 0.05-0.1 mm, while lower value than expected was obtained for the fraction 0.1-0.2 mm. This situation implies an idea that a part of the ideally distributed debris in the fraction 0.1-0.2 mm were broken and transferred to the smaller range of fraction. Further, we can continue the consideration that this part could have participated to the steam explosion. Thus, it was finer fragmented and therefore deviated from the ideal (monotonous) distribution during premixing.
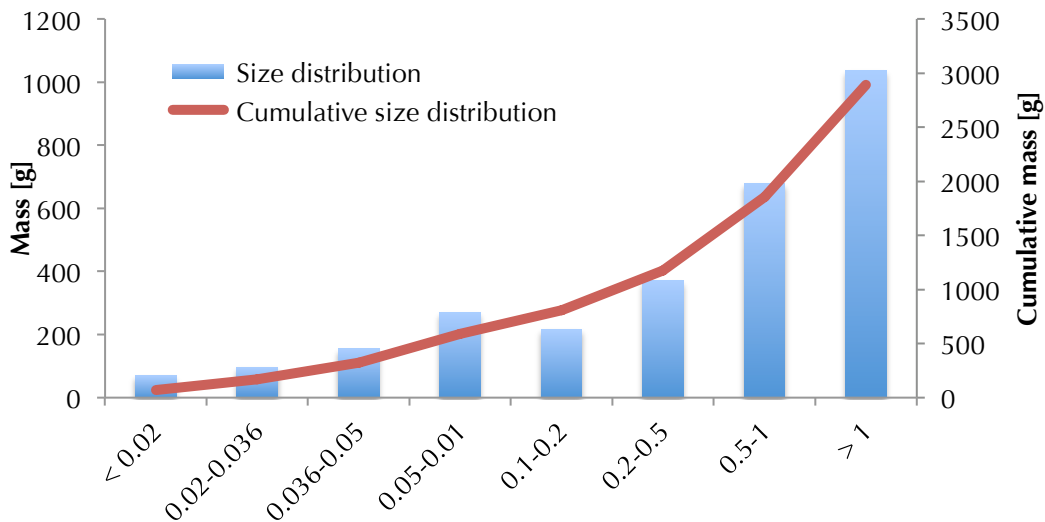
Figure 7.5 KS4 debris size distribution by mechanical sieving in [mm]

Table 7.1 Summary of the KS4 mechanical sieving

KS4 debris [mm]	Mass [g]	Cumulative mass [g]
< 0.02	70.3	70.3
0.02-0.036	96.3	166.6
0.036-0.05	154.7	321.3
0.05-0.01	269.8	591.1
0.1-0.2	215.9	807
0.2-0.5	370	1177
0.5-1	679.2	1856.2
> 1	1036.2	2892.4

7.2.2   KS4 debris SEM/EDS analyses

Scanning electron microscopy coupled with energy dispersive X-ray microanalysis was employed to characterize the debris morphology and composition. The debris was characterized in a powder form to obtain information about the nature. Particle cross-sections were prepared as well in order to describe the interior structure.

Overview of the large debris morphology is presented in the *Figure 7.6*. The debris contains round and angular particles similarly as in the case of KS2 debris. The melt surfaces exposed to water can be distinguished from the surfaces after particle solid-state fractioning. As was found also in the case of KS2 debris, the surfaces exposed to water have a cell wavy structure. Detail of such surface is given in the *Figure 7.7*. The presence of the same Benard-Marangoni instabilities for KS2 and KS4 tests, demonstrates that this kind of instability is representative of interaction between water and prototypical corium during the premixing/fragmentation stage. .

Fine powder debris morphology is shown in the *Figure 7.8*. Most of the debris has angular and irregular shape corresponding to pieces of broken particles. Presence of low fraction of spherical particles can be explained by high explosion pressure and temperature gradients. Such violent conditions can lead to significant solid particle fractioning.
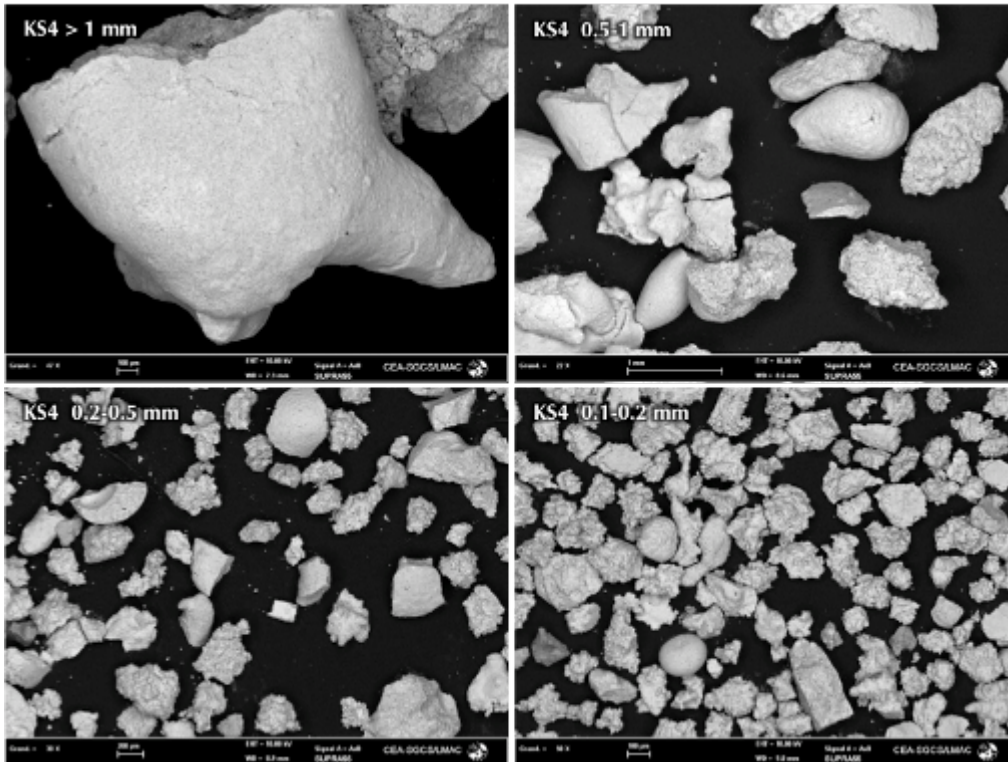
Figure 7.6 SEM micrographs of KS4 large debris
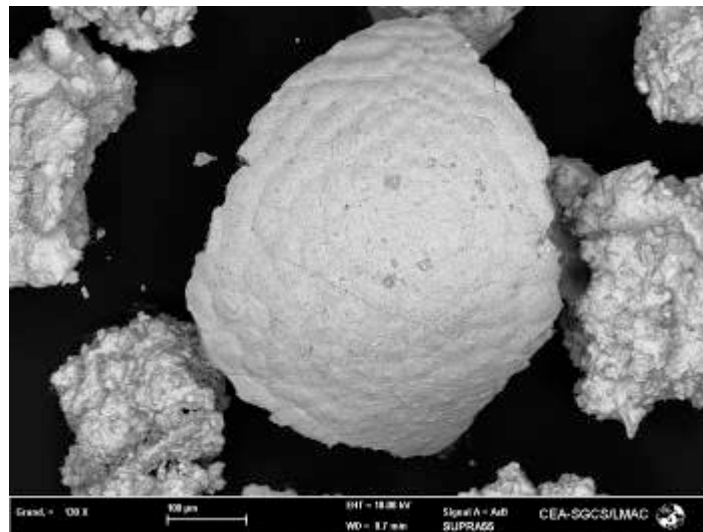
Figure 7.7 Cellular and wavy structure on the debris surface exposed to water/steam
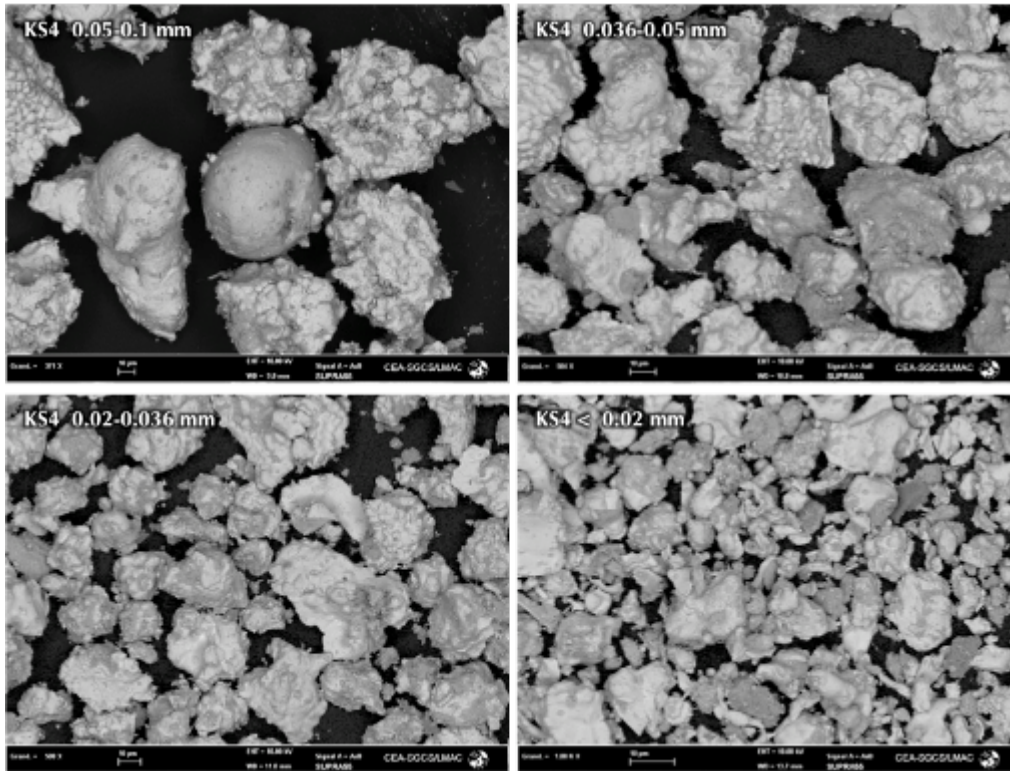
Figure 7.8 SEM pictures of fine KS4 debris

SEM investigation of the debris cross-section is given in the *Figure 7.9* for all the sieving fractions. Debris doesn't differ significantly from the KS2 test. The droplets are homogenous and no significant chemical contrast can be seen.

Similarly to KS2 two morphology types can be found: i) full and more symmetric particles; ii) Irregular and porous particles. In the case of KS4 especially fractions 0.2-0.5 and 0.1-0.2 mm have important internal porosity. This porosity has a form of rather small void bubbles compared to the droplet size. Going to smaller size fractions, the internal porosity becomes more rare.

The difference between round droplets, keeping its original shape, and their broken parts are again evident.

Figure 7.9 SEM micrographs of KS4 debris cross-sections, all sieving fractions

The debris composition is shown in the *Figure 7.10*. Increase of the tin content can be seen going down with size of the debris. The debris is polluted by about 0.9 mol.% of tin and by about 1.3 mol.% of tungsten. The uranium-zirconium ratio is shown in the next *Figure 7.11*. The uranium and zirconium are homogenously distributed in the melt. Uranium represents 59.4 mol.% and zirconium 40.4 mol.%, which corresponds to 74 w. % of UO_2 and 26 w. % ZrO_2 mixture. Similarly to KS2 the

melt and consequently the debris are depleted in UO_2. We explain this effect by possible evaporation and aerosol formation of UO_2 during the melting phase.
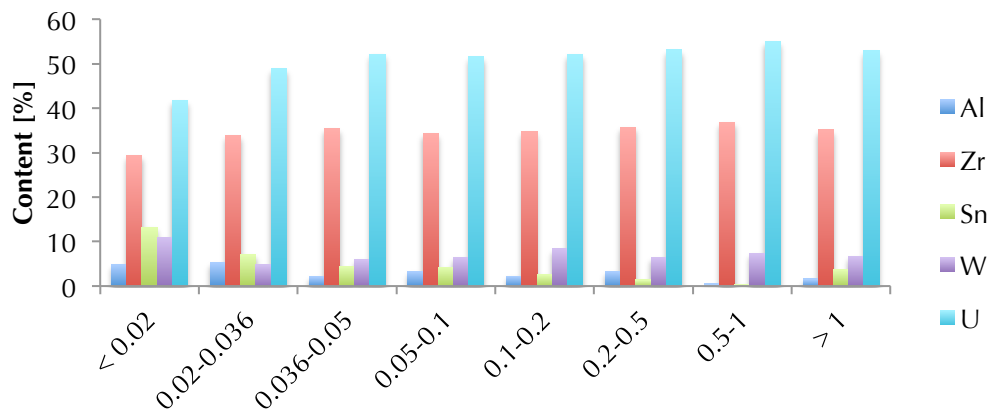
Figure 7.10 Composition of the KS4 debris fractions (in [mm]), excluding oxygen
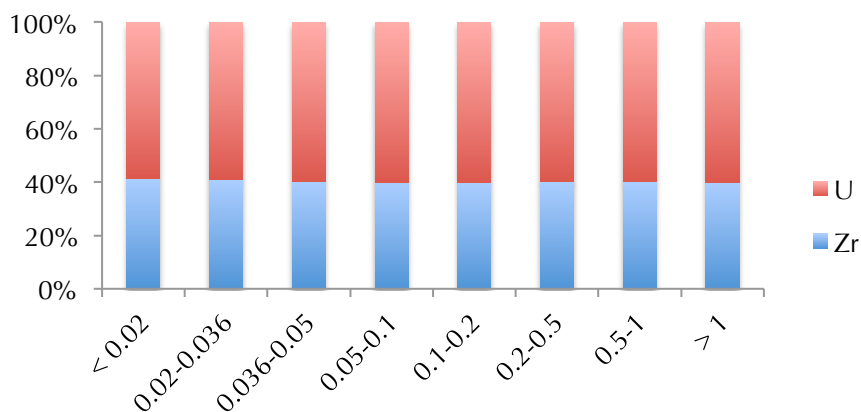
Figure 7.11 Uranium-zirconium ration for all the KS4 sieving fractions [mm]

A ceramic-like grain structure is observed inside the particle (*Figure 7.12*). The grain size increases from the droplet surface to the center. The same microstructure of the debris is observed for KS2 and KS4 experiments; it means that the cooling rate was faster on the surface of the droplet than in the center of it. A continuous crust about 5 µm on the particle surface takes place. It is composed of the U-Zr-O solid solution. The distribution of the elements is uniform for the crust. Two peaks of tungsten presence can be seen on the grain boundary.
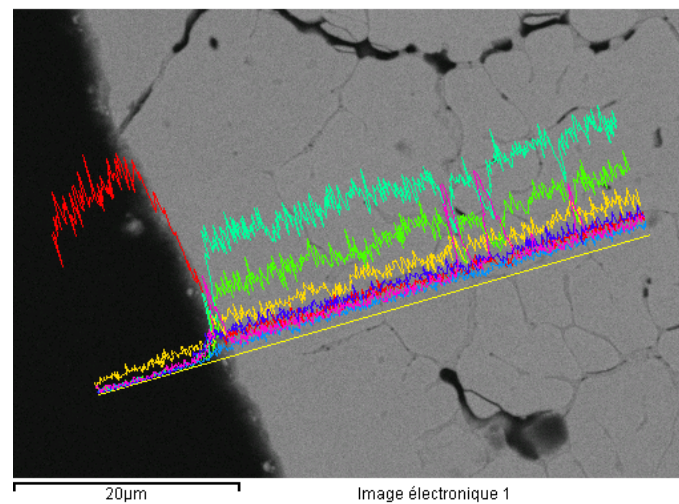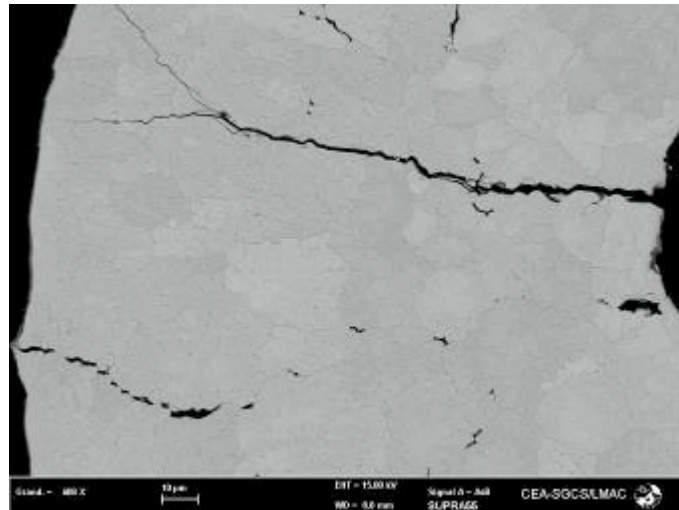
Figure 7.12 Grain structure of the particle interior (KS4 0.5-1 mm) and line scan analysis of composition (C - red, W - pink, Sn - purple, Al – blue, U - blue-green, Zr - green, O - yellow)

7.2.3   KS4 image analyses

Image analysis of selected debris (statistical set of 3748 particles) was performed in order to describe possible differences in the image characteristics of particles participating to the steam explosion. *Figure 7.13* shows KS4 debris participating to SE obtained by SEM and following image analysis. Average of the steam explosion debris characteristics are summarized in the *Table 7.2*. Later they will be used for the calculation of the melt mass participation to SE.

Circularity and roundness distribution for all the KS4 sieving fractions are depicted in the *Figure 7.14*. Concerning the circularity distribution the differences among the sieving fractions are not as clear as in the case of KS2 debris.
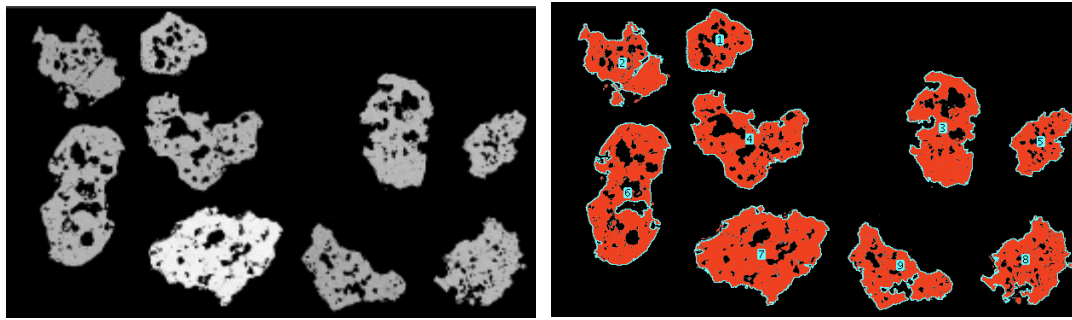
Figure 7.13 KS4 debris participating to the steam explosion (left) and figure image analysis (right)

Table 7.2 Summary of the image characteristics of KS4 steam explosion debris

Property	Average	Average deviation
Circularity	0.31	0.11
Roundness	0.63	0.09
Solidity	0.81	0.05
Porosity	17.43%	3.71%

The circularity distributions for KS4 debris fractions are more similar to each other and some tendencies are difficult to follow. For fine debris < 0.05 mm the distribution has a broad maxima around 0.5. Circularity peak value of the debris from 0.05 to 0.5 mm is shifted to lower values ~ 0.4 and for larger debris the distribution is more scattered.

The roundness distribution is very close for fine debris with maxima around 0.6. Interesting effect can be seen for the fractions above 0.5 mm. Evidently, two maxima are present, one around 0.4 and second around 0.7. It can be assumed that the peak around 0.7 corresponds to premixed and quenched droplets with rather spherical shape and the peak around 0.4 to irregular particles participating to SE.

The average values of circularity, roundness and solidity are shown in the *Figure 7.15* for all the KS4 sieving fractions. The fine debris < 0.36 mm has the highest circularity, on the other hand the actual value ~ 0.55 is rather low. Thus, we can assume that the particles are mostly powder like pieces of broken droplets. Then, the circularity has decreasing tendency to fraction 0.2-0.5 mm. The fractions from 0.05 to 0.5 mm contain then the majority of irregular particles participation to the steam explosion. The average roundness fluctuates closely around 0.6 for all the KS4 sieving fractions. Therefore, no deeper conclusions can be drawn out. The solidity follows the tendencies in circularity. Two higher values can be seen for fractions 0.02-0.036 and 0.5-1 mm, while the rest remains bellow 0.8. Large average deviations of solidity of fine < 0.02 and large > 0.5 mm debris are observed. This can be attributed to the shape non-uniformity of these sieving fractions.

Circularity distribution

Legend:
- < 0.02
- 0.02-0.036
- 0.036-0.05
- 0.05-0.1
- 0.1-0.2
- 0.2-0.5
- 0.5-1
- > 1

Roundness distribution

Legend:
- < 0.02
- 0.02-0.036
- 0.036-0.05
- 0.05-0.1
- 0.1-0.2
- 0.2-0.5
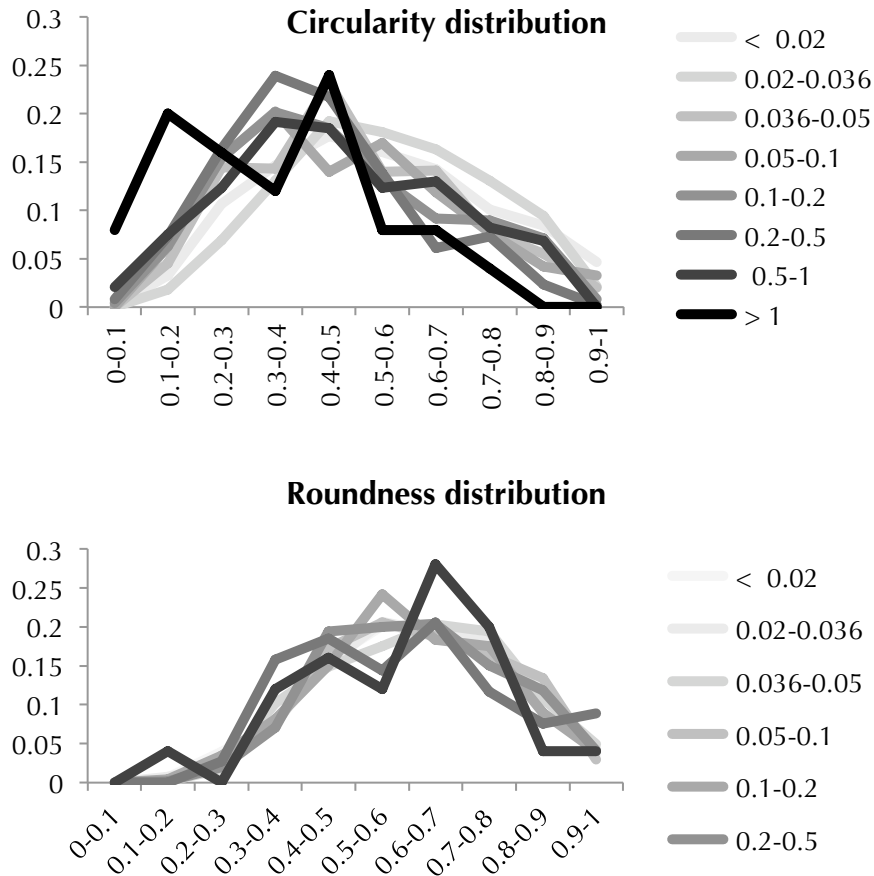
Figure 7.14 Circularity and roundness distribution of the KS4 debris size fractions (in [mm])

The average porosity of the KS4 debris equals to 3.2 %. The porosity distribution through the sieving fractions is presented in the *Figure 7.16*. It rises up with the debris size with three peak values close to 5 % for the fractions 0.05-0.1, 0.1-0.2 and > 1 mm. The average porosity and the peak value for single sieving fraction are lower than for KS2 debris. We assume that this observation is again related to more severe debris break after solidification due to more violent SE. Thus, the internal porosities are not kept during the solid droplet fractioning leading to open porosity that cannot be directly caught by this approach.

We used the average SE particle characteristic (*Table 7.2*) as border criteria (circularity and solidity) for melt participation to the steam explosion. The *Figure 7.17* shows the part of each sieving fraction participating to the steam explosion and a part of debris with spherical shape as well. All the indicators show that the debris participating to SE are between 0.05 and 0.5 mm. Majority of the round particles can be found bellow 0.05 mm and in the fraction 0.05-1 mm.

The averaged criteria for SE participation together with the sieving distribution for calculation we used for the calculation of the melt amount participating to SE. Results are summarized in the *Table 7.3*. It can be concluded that 33.5 w. % of the melt participated to the steam explosion, which is slightly lower value than for KS2. On the other hand, we believe that the results can be affected by important fractioning of the particles in solid state. Due to more violent interaction a large fraction of the droplets can be crushed in powder like particles. This effect can vanish the morphology aspects useful in the image analyses. Less violent explosion can prevent more of these aspects

resulting in enhancement of the amount of melt participating to SE compared to this case.
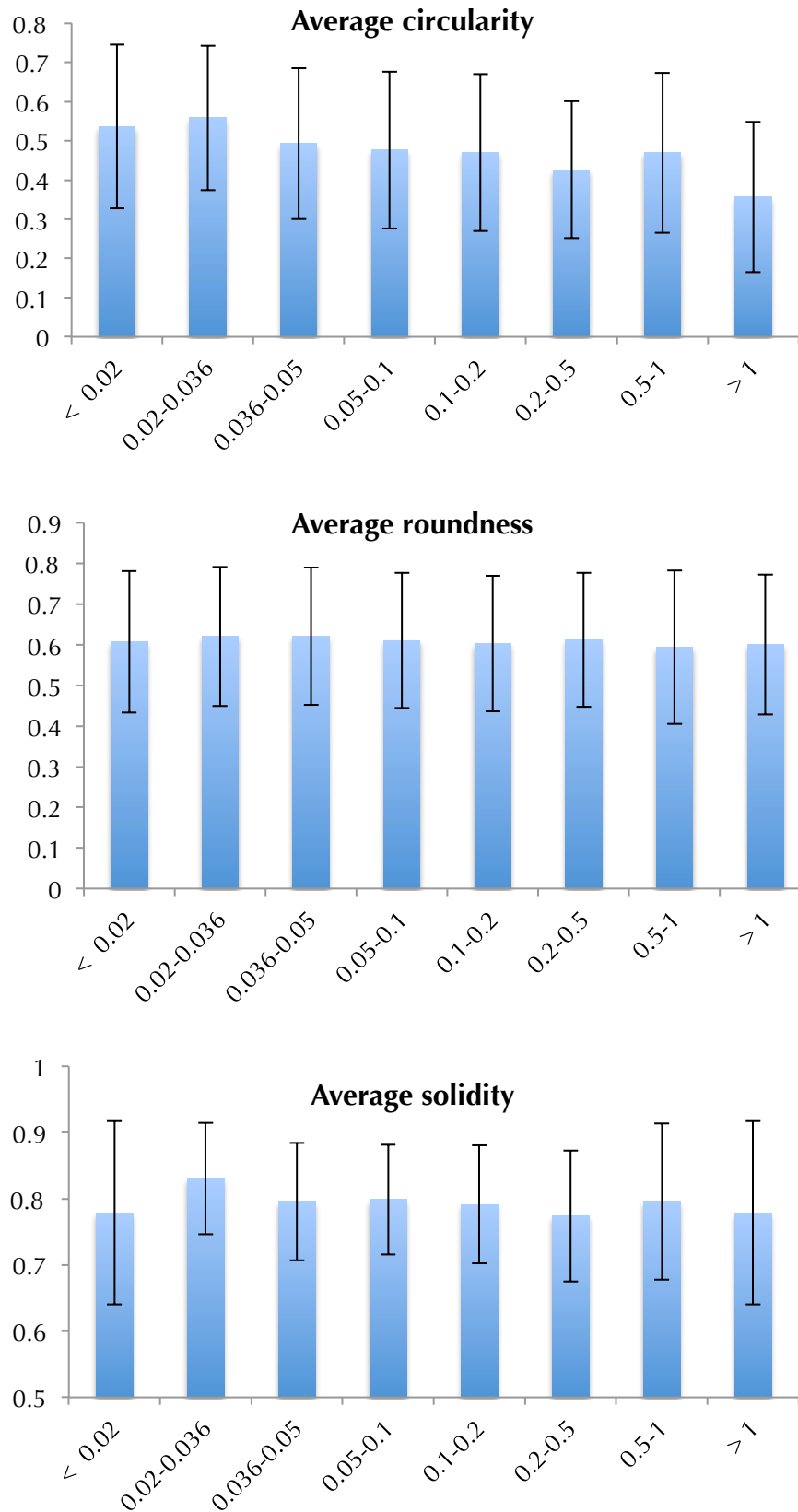
Figure 7.15 Average image characteristics of the KS4 debris fractions (in [mm])
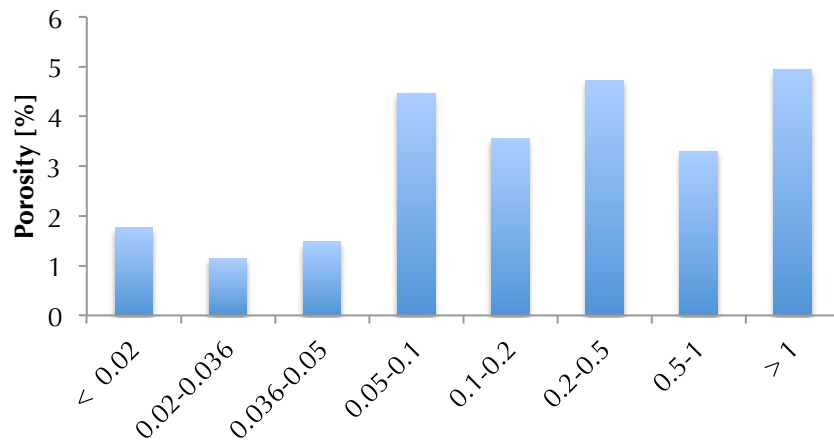
Figure 7.16 Porosity of the KS4 debris sieving fractions (in [mm]) by image analysis
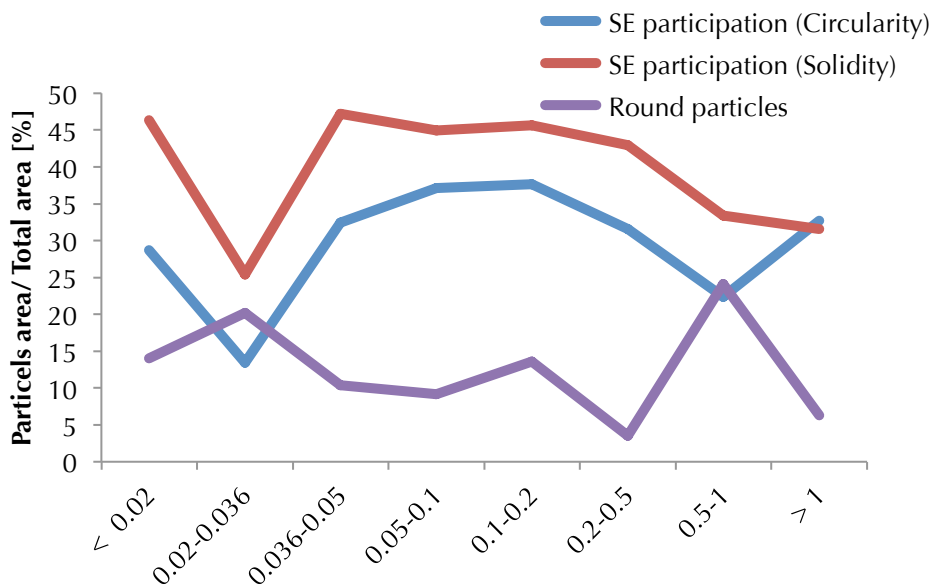
Figure 7.17 Round droplets and particles participating to the steam explosion by image analysis, sieving fractions in [mm]

Table 7.3 Summary of the KS4 debris participation to SE

KS4 debris [mm]	SE participation [%]	Mass [g]	Mass SE [g]	
< 0.02	37.5	70.3	26.4	
0.02-0.036	19.4	96.3	18.7	
0.036-0.05	39.8	154.7	61.6	
0.05-0.1	41.1	269.8	110.8	
0.1-0.2	41.6	215.9	89.9	
0.2-0.5	37.3	370.0	137.9	
0.5-1	27.9	679.2	189.3	
> 1	32.1	1036.2	333.0	
	Sum	**2892.4**	**967.7**	**33.5 w.%**

7.2.4 X-ray powder diffraction of the K4 debris

The X-ray powder patterns of all the KS4 sieving fractions are similar. Whatever the size ranges, the same UO_2-ZrO_2 solid solution face-centered cubic solution is found. However, slight shift of the peak positions can be seen especially at high two theta angles (*Figure 7.18*). The main diffraction lines correspond to the face centered cubic solution of UO_2-ZrO_2. If we take a closer look on the X-ray pattern of fine debris (KS4 < 0.02 mm in the *Figure 7.19*), we can see diffraction lines of tetragonal tin as well. For further information, move on to the tin diffraction lines intensity (*Figure 7.20*) where it can been seen that the content of tin increases for fine debris.
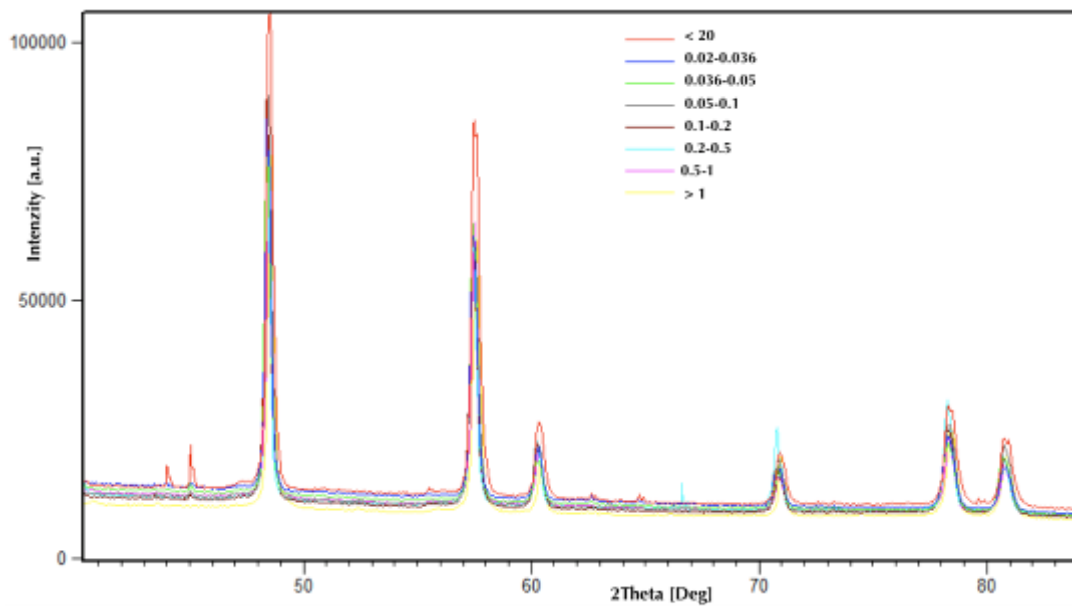
Figure 7.18 Overview of the X-ray powder patterns of the KS4 debris
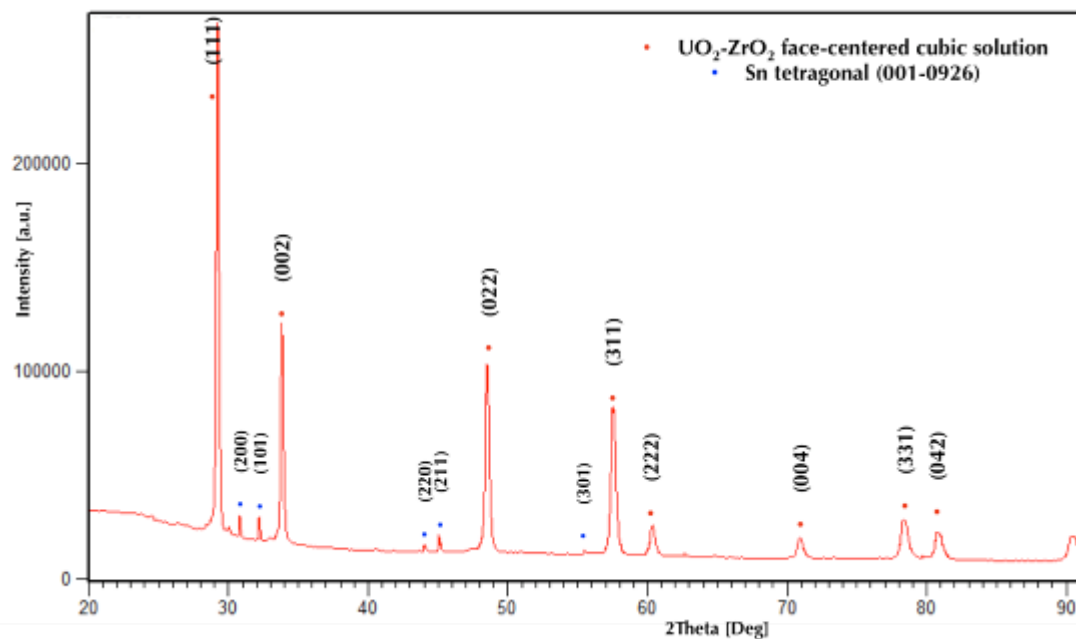
Figure 7.19 X-ray powder pattern of KS4 < 0.02 mm debris

170
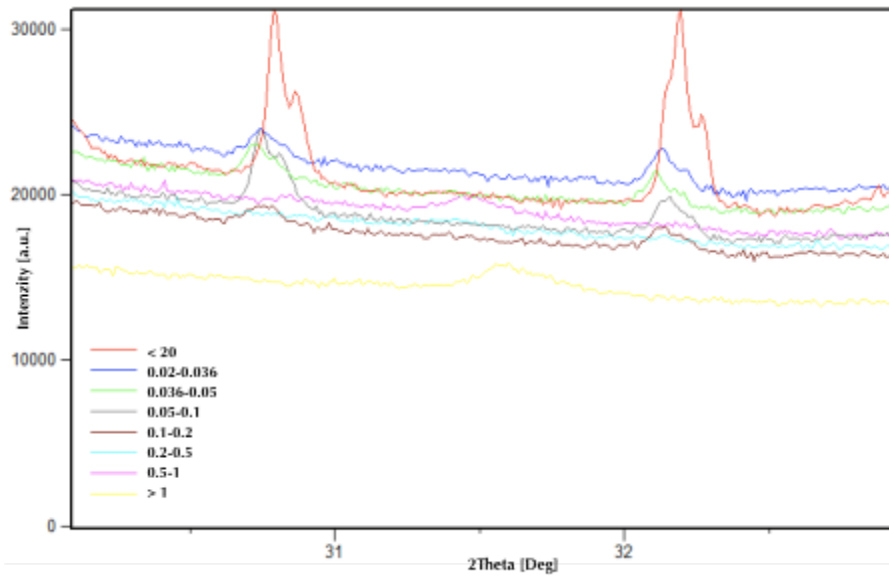
Figure 7.20 Detail of the two most intensive diffraction lines of tin for all KS4 sieving fractions

The X-ray powder patterns were treated by WPPF analysis and the oxygen over-stoichiometry y of the $U_{1-x}Zr_xO_{2+y}$ was calculated (*Figure 7.21*) for all the KS4 sieving fractions. Using this value the amount of hydrogen produced by the reaction of melt and water/steam was calculated as well. Results are summarized in the *Table 7.4*. In total 11.5 g of hydrogen was produced, which is significantly more than for KS2 test. Even if the mass of the melt in interaction with water was almost 1 kg less in the KS4 experiment, the amount of hydrogen was double. We attribute this effect to deeper interaction of the melt with water.
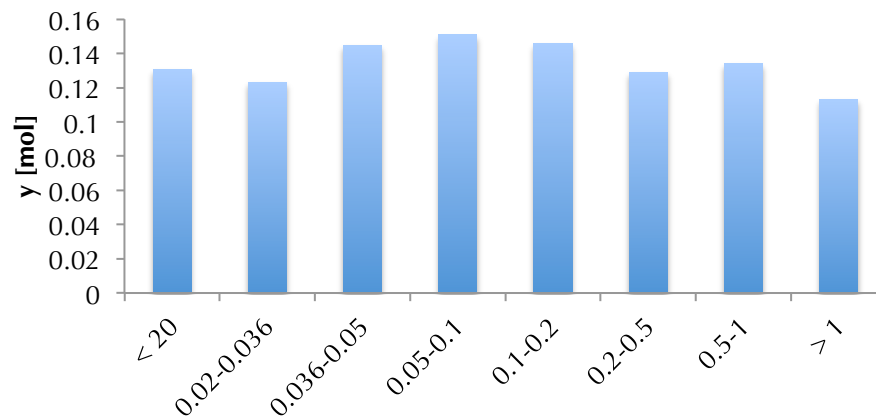
Figure 7.21 Oxygen over-stoichiometry y of the $U_{1-x}Zr_xO_{2+y}$ solid solution

Table 7.4 KS4 results of the WPPF analysis - a (cell parameter), y (oxygen over-stoichiometry) and amount of produced hydrogen

KS4 debris [mm]	a [Å]	Y [mol]	n H_2 [mol]	m H_2 [g]
< 20	5.319	0.130	0.696	1.403
0.02-0.036	5.322	0.123	0.656	1.322
0.036-0.05	5.319	0.145	0.770	1.553
0.05-0.1	5.319	0.151	0.802	1.617
0.1-0.2	5.320	0.146	0.777	1.567
0.2-0.5	5.323	0.129	0.687	1.386
0.5-1	5.322	0.134	0.714	1.439
> 1	5.327	0.113	0.602	1.213
		Sum	**5.704**	**11.498**

7.2.5 ICP/MS analysis of the KS4 debris

The ICP/MS measurements (*Table 7.5*) match the values already obtained by EDS. Low tin and tungsten pollution is observed. Tin, similarly to KS2 debris, has higher content in fine debris fractions. The content of all pollution elements don't exceed several units of percent.

7.2.6 Auger spectroscopy of KS4 droplet

A single melt droplet with spherical shape was selected by micro-manipulation and analyzed by Auger spectroscopy in order to have information about the composition of the surface layer. The analyzed droplet is depicted in the *Figure 7.22*, the excitation source was focused in the center of the droplet and the surface layer was etched by argon plasma. The *Figure 7.23* shows the U, Zr and O contents in the first 300 nm layer.

Even if the absolute values of the U, Zr and O content seem to be unreliable near the surface, the increase of the oxygen content at the droplet surface is evident. Below 100 nm from the actual surface the element ratio comes to i.e. 67 mol. % for oxygen and 33 mol. % for uranium-zirconium as is typical for $U_xZr_{1-x}O_2$.

Measured particle was selected due to its spherical shape that was conserved from the melt fragmentation during premixing. Therefore, it can be quoted that the melt/water steam reaction runs even during premixing, but just close to the interface. The hydrogen, on the other hand, is formed during the fine fragmentation as well. During participation to the steam explosion the water/steam forms internal void and porosity, thus the interaction is in volume. Consequently, more hydrogen can be formed during SE than during premixing, but the hydrogen formed during SE should be taken as a consequence of SE and not as a factor limiting its strength.

One can argue that this reaction can occur, when the debris lied in the water pool after the test. However, we suppose that elevated temperature is necessary for the reaction to be thermodynamically favorable.

Table 7.5 KS4 debris composition by ICP/MS, size fractions in [mm]

		Content [w. %]			Content [w. %]
KS4 0.02-0.036	Al	0.08	**KS4 0.2-0.5**	Al	0.15
	Sn	1.67		Sn	1.58
	W	3.61		W	3.36
	UO_2	71.1		UO_2	71.6
	ZrO_2	23.6		ZrO_2	23.3
KS4 0.036-0.05	Al	0.07	**KS4 0.5-1**	Al	0.03
	Sn	1.35		Sn	0.11
	W	3.34		W	3.57
	UO_2	71.8		UO_2	72.7
	ZrO_2	23.4		ZrO_2	23.6
KS4 0.05-0.1	Al	0.05	**KS4 > 1 mm**	Al	0.01
	Sn	0.95		Sn	0.18
	W	3.42		W	3.38
	UO_2	72.0		UO_2	73.1
	ZrO_2	23.6		ZrO_2	23.4
KS4 0.1-0.2	Al	0.07	**KS4 < 0.02 mm**	Al	0.28
	Sn	0.87		Sn	3.82
	W	3.21		W	4.58
	UO_2	72.3		UO_2	68.7
	ZrO_2	23.5		ZrO_2	22.6
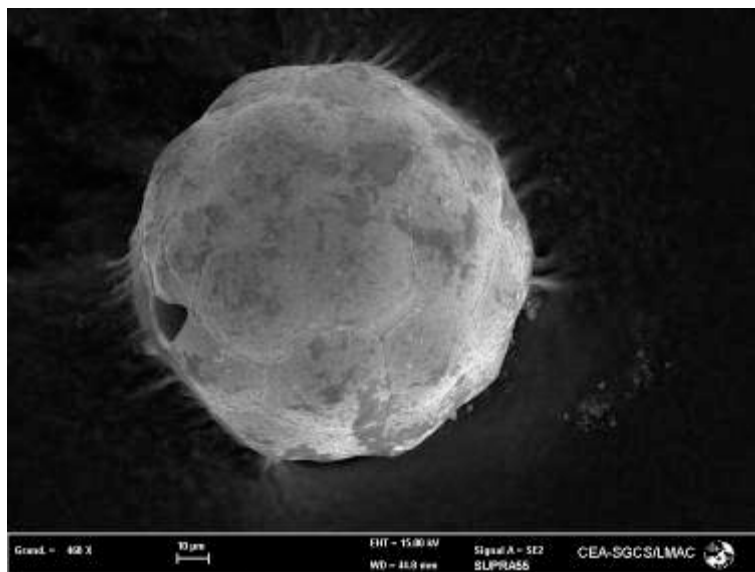
Figure 7.22 Droplet of the KS4 debris analyzed by the Auger spectroscopy
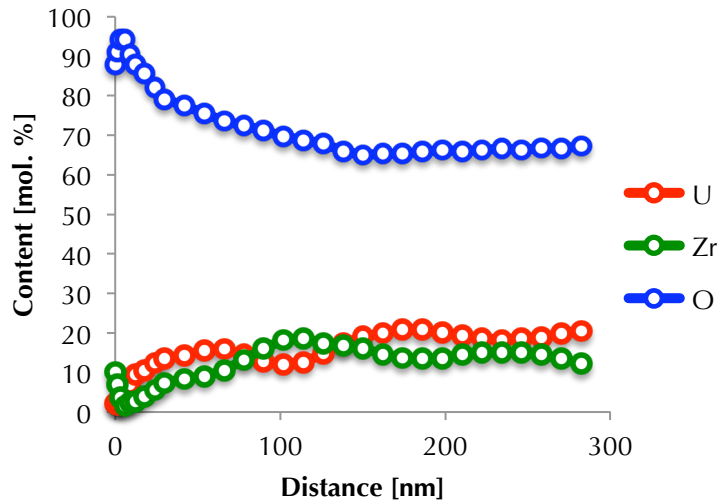
Figure 7.23 Composition (U, Zr, O) of the surface layer by Auger electron spectroscopy, KS4 spherical droplet

7.3 Conclusion

The KS3 experiment confirmed the corium melting behavior found in the KS2 experiment.

The KS4 test showed successfully triggered steam explosion reaching the highest energy conversion ratio among the KROTOS tests. The achieved SE efficiency was about 0.182%.

The FCI debris solidified into a single face-centered cubic phase – solid solution of UO_2 and ZrO_2 with average composition 76 w. % UO_2 and 24 w. % ZrO_2.

Similarly to KS2 test, two types of particles were distinguished – debris with high porosity and irregular shape identified as having participated to steam explosion and full debris angular or rounded identified as having not participated to steam explosion.

As for KS2 debris, the presence of the cellular structure due to Marangoni-Benard instabilities has been observed for the KS4 debris. These results allow us to state that during the water corium interaction, Marangoni-Benard instabilities will appear at the surface of the droplets. The particle interior presented again grain (ceramic like) structure with increasing grain size from the surface to the droplet center.

The average debris porosity reached 3.5 %. Melt fraction participating to the steam explosion was calculated to be 967.7 g, which presents 33.5 w. %. This value is a little less than for KS2, even if the explosion strength was higher. We attribute this effect to higher particle solid-state fractioning due to larger pressure peak and temperature gradients. Due to the SE violence the brittle corium solid is broken to powder like debris changing its image properties. Thus, the melt amount participating to SE can be underestimated.

11.5 g of hydrogen was formed during KS4 test by melt – water/steam chemical reaction, which is notably higher than for KS2 test, even if the melt mass is of about 1 kg less.

Chapter 8. KROTOS KS5 experiment

8

During the KS5 test 1.725 kg of sub-oxidized corium melt (80.1 w. % UO_2, 11.4 w. % ZrO_2 and 8.5 w. % Zr) was poured into water pool of 53 °C and successfully triggered. Experimental parameters were kept the same as for KS4 test.

8.1 KS5 test results

The experiment started with heating up a specially loaded crucible. The pieces of UO_2-ZrO_2-Zr mixture were place on a layer of UO_2-ZrO_2 granulate in order to prevent the crucible bottom from perforation due to the chemical ablation by sub-stoichiometric melt. The heating history is shown in the *Figure 8.1*. The melt reached 2587 °C before being released, which presents about 150 °C of over-heating.
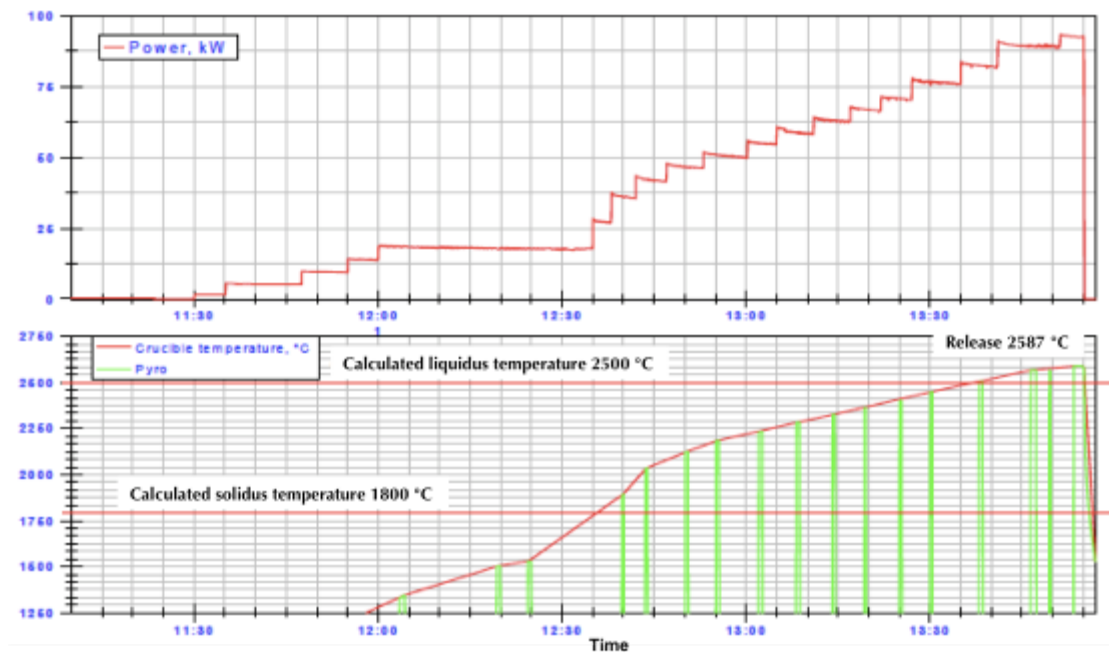
Figure 8.1 Melting history in the KS5 test

The crucible impacted of the puncher and the melt was successfully released. The tin membrane stopped the melt producing coherent and not-disturbed jet (*Figure 8.2* a to f). After the melt impacted on the water level the melt jet showed conical extension and important irritation. It can be assumed that the steam generated by the first melt – water interaction reacted very rapidly (we can say simultaneously) with the sub-oxidized melt jet affecting its characteristics.
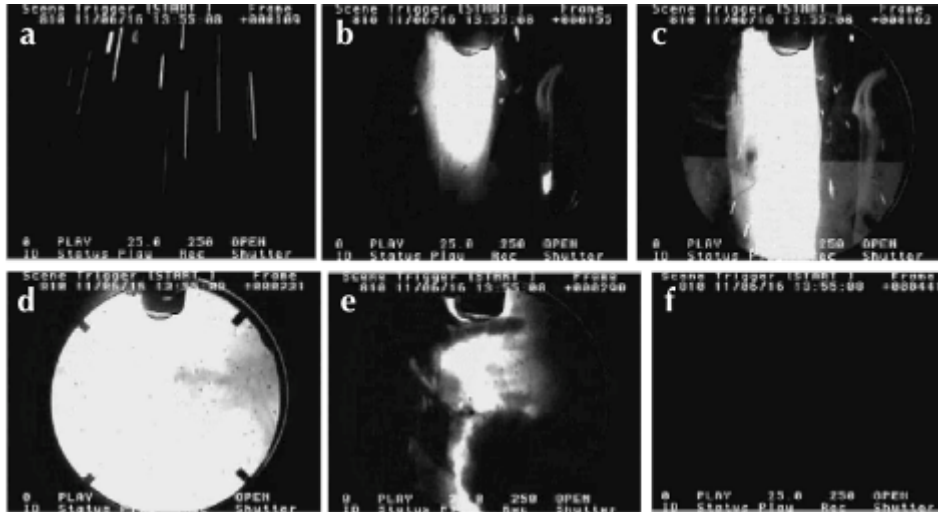
Figure 8.2 Video acquisition of the melt jet release (KS5 test) a – frame 109, b – 151, c 162, d – 231, d – 290 and e – 441

The melt felt by gravity reaching about 1.4 m.s^{-1} just before the water level. Further, the vessel pressure and melt front history should remain confident due to the OECD project restrictions.

8.1.1 KS5 size distribution

After the test the debris was collected and dried at 120 °C for 8 hours. Further, mechanical sieve was employed for debris fractioning. The final size distribution can be seen in the *Figure 8.3* and it is summarized in the *Table 8.1*. The majority of the debris is larger than 1 mm and only very few of the particles are finer. The hydrogen production probably affected significantly the fragmentation process preserving the droplets from fine fragmentation.
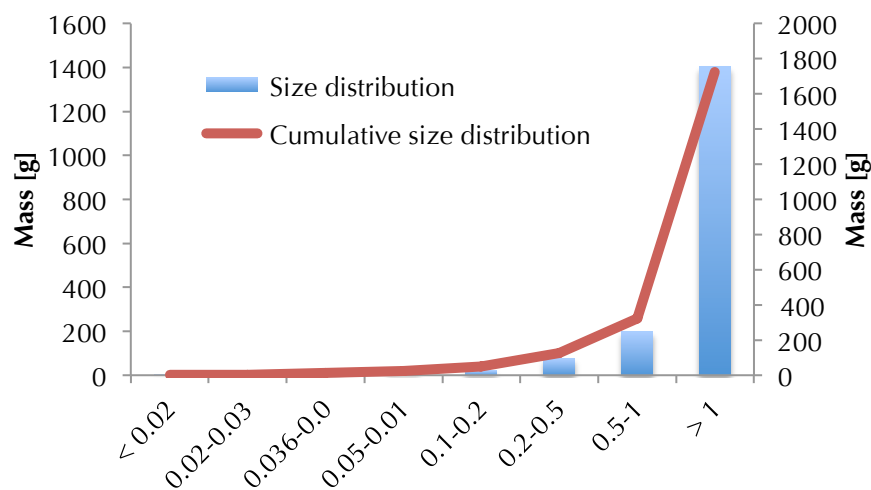
Figure 8.3 Size distribution of the KS5 debris (in [mm])

Table 8.1 Summary of the KS5 debris size distribution

KS5 debris [mm]	Mass [g]	Cumulative mass [g]
< 0.02	0.8	0.8
0.02-0.036	2.3	3.1
0.036-0.05	9.1	12.2
0.05-0.01	13.1	25.3
0.1-0.2	22.9	48.2
0.2-0.5	76.2	124.4
0.5-1	197.1	321.5
> 1	1403.5	1725

8.1.2   SEM/EDS analyses of the KS5 debris

The majority of the KS5 debris is larger than 1 mm. Due to this fact optical microscopy was used to investigate the morphology of the particles. Micrographs showing the KS5 > 1 mm debris are given in the *Figure 8.4*.
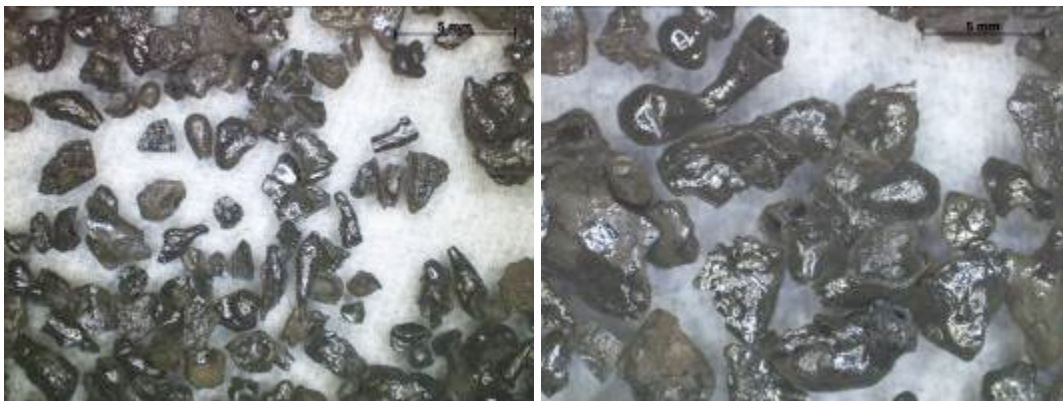
Figure 8.4 Optical microscopy pictures of the KS5 > 1 mm debris

Particles exposed to the water/steam have smooth surface with slight metallic glow pointing to the low surface roughness. Very often the particles are hollow or tube like. We assume that this structure is related to the different thermo-physical properties of the melt. A lot of these particles kept their spherical shape, which can be again attributed to the role of hydrogen or generally to non-violent interaction with water. SEM pictures of the larger debris showing their morphology are presented in the *Figure 8.5*. As common for all the KROTOS debris angular and spherical particles can be observed. The fractions from 0.1 to 1 mm contain notably more angular particles coming from broken droplets than debris larger than 1 mm.

Fine debris, shown in the *Figure 8.6*, consists mostly of powder like angular particles. Spherical droplets can be rarely found. The cell (Marangoni-Benard) structure on the surface exposed to the water/steam was not observed for KS5 debris. However, other effect never seen before was obtained on the water-exposed surfaces. *Figure 8.7* presents two droplets with surface covered by spherical rough protrusions. These globules are homogeneously distributed across the particle surface.

This specific surface morphology, i.e. globules, can be attributed to the melt – water/steam reaction. Products of the reaction produced can segregate and remain in the form of droplets on the surface.
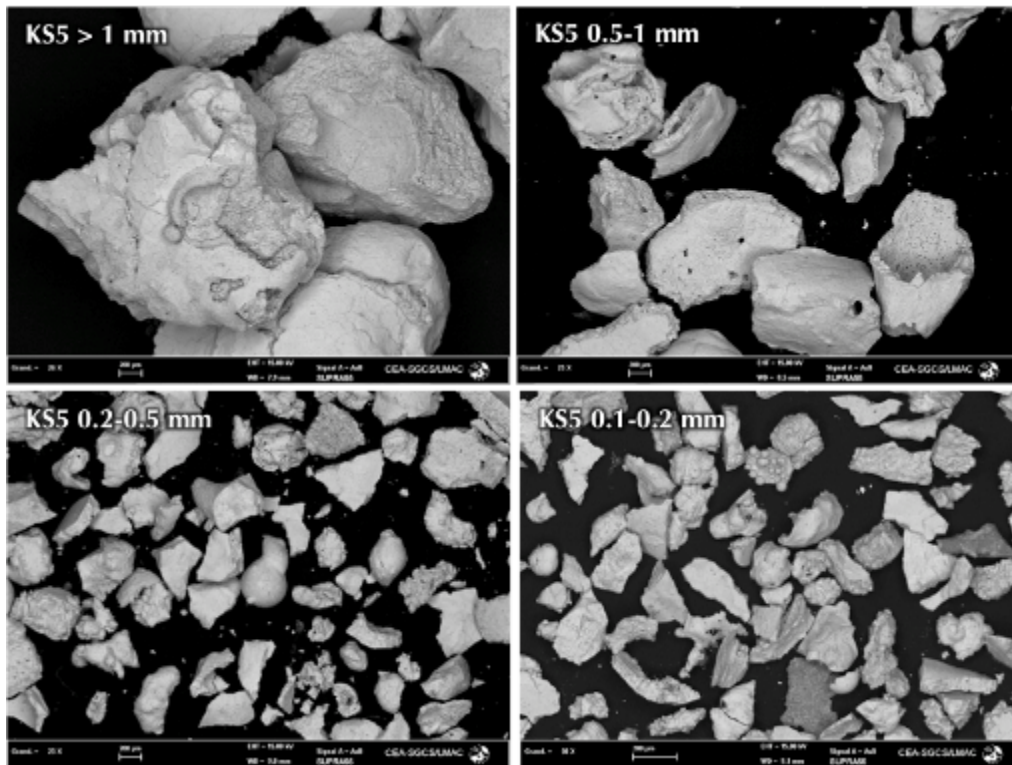
Figure 8.5 SEM investigation of the large KS5 debris fractions
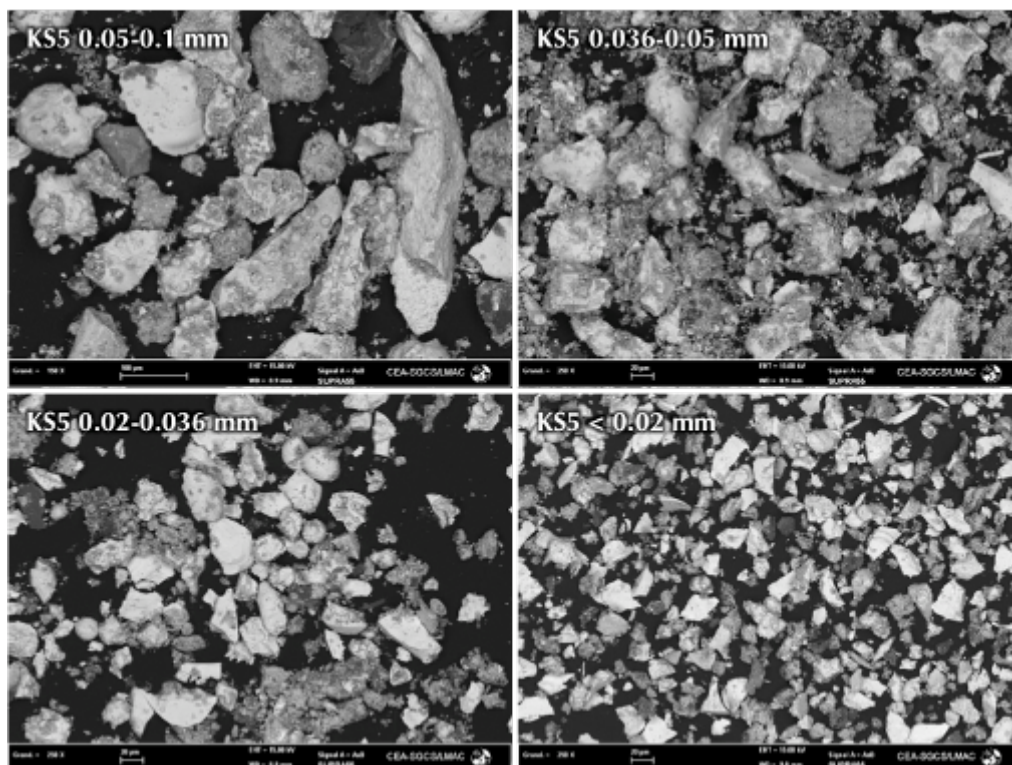
Figure 8.6 SEM micrographs of fine KS5 debris
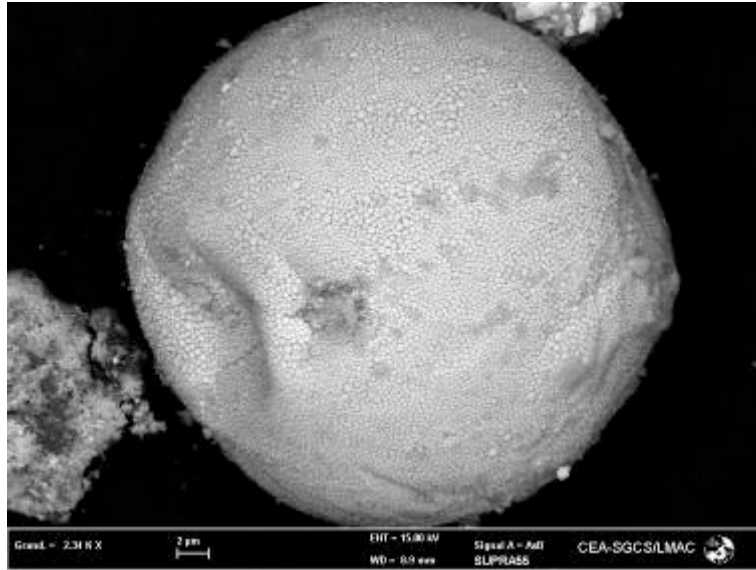
Figure 8.7 Spherical particle with rough surface, KS5 0.02-0.036 mm

Overview of the debris cross-sections is shown in the *Figure 8.8* for all the sieving fractions. The numerous well-preserved particles having large porosity or internal void are observed. Again, we can quote that the morphology could have been kept due to the hydrogen generation or generally due to non-violent interaction. The formation of one large internal void (hollow spheres) can be explained by different thermo-physical properties of the melt. Sub-oxidized corium melts have lower viscosity than fully oxidized melts. By increasing the viscosity a higher Ohnesorge number will be obtained, while changing the fragmentation mechanism for example to "bag and stamen" (see *chapter 2*) that can explain the large internal void. Internal porosity in the form of small irregular holes can be interpreted again as a result of thermal fragmentation by water entrapment inside the melt.

Debris from KS2 and KS4 show homogenous ceramic like structure. For these last two experiments, the solidification interval for UO_2-ZrO_2 mixture is small: a maximum of 50 K exists. This small interval, as seen in previous chapters, has a limited effect on solidification phenomena involved in FCI.

For melt with a large interval of solidification like for KS5 composition for which ($T_{liquidus} - T_{solidus}$) was about 700 K, different solidification processes leading to heterogeneous microstructure have been observed (*Figure 8.9*). Elemental mapping of KS5 debris > 1 mm shown in the *Figure 8.12* shows this heterogeneity. It can be assumed that during the melt cooling, UO_2-ZrO_2 phase with high liquidus temperature will solidify first followed by the metallic zirconium rich phase with a lower liquidus temperature. Taking into account this fact, the oxygen content should be lower for the zirconium rich phase. However, no such effect can be found on the oxygen map in the *Figure 8.9* and its distribution is homogenous. This can be explained only by full oxidation of metallic zirconium. Later, this observation will be confirmed by X-ray powder diffraction results. Moreover, no inclusion or grains of metallic zirconium can be found in the debris.

The average composition of the KS5 debris obtained by EDS analysis is given in the *Figure 8.10*.

Similar tendency in the tin content as for KS4 debris can be seen.
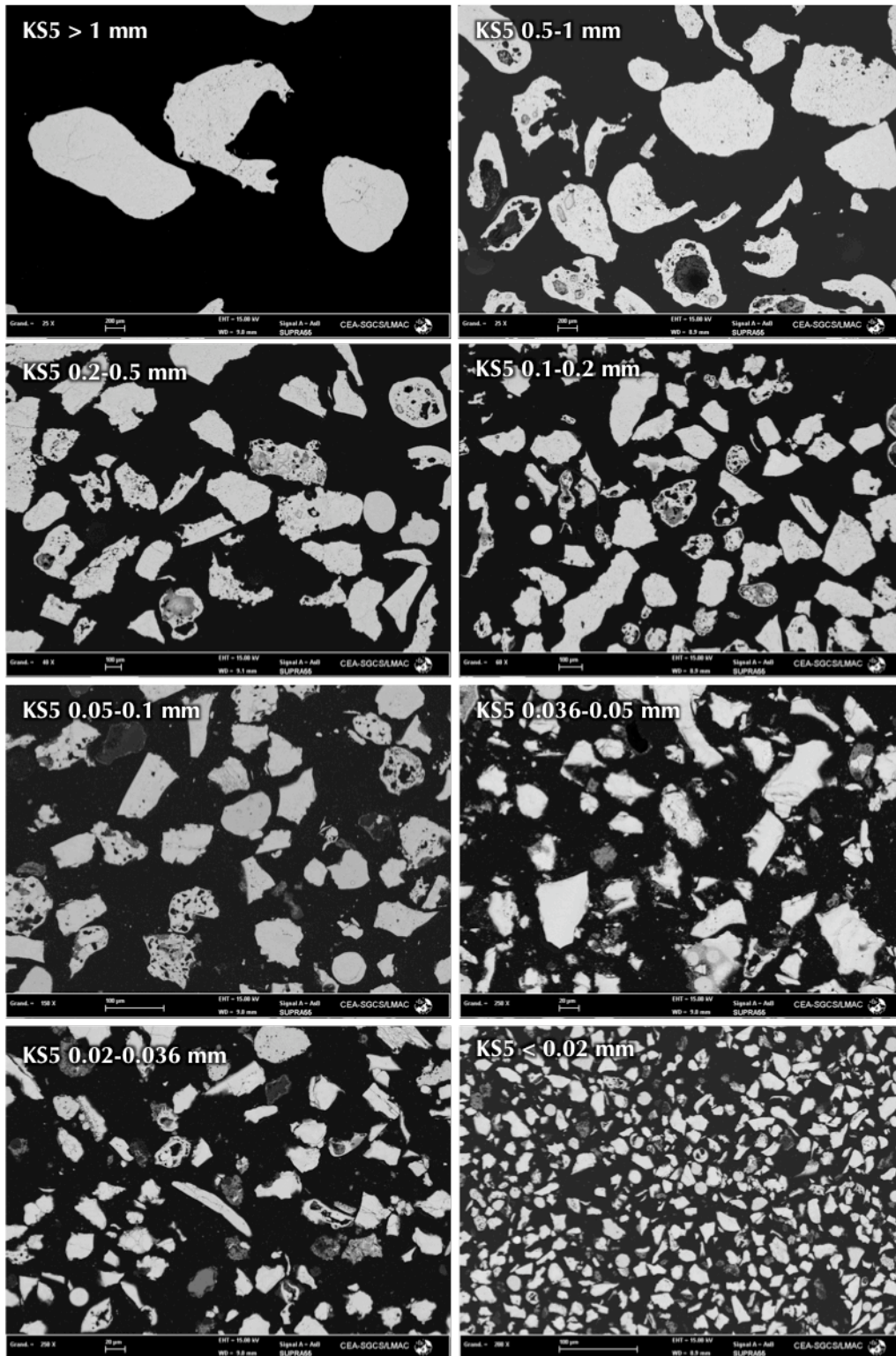
Figure 8.8 KS5 debris cross-sections by SEM

The uranium/zirconium ration (*Figure 8.11*) doesn't scatter through the sieving fractions. The average ration corresponds to 39.4 mol. % Zr and 60.4 mol. % U, which is equal to 75 w. % UO_2 and 25 w. % ZrO_2. This result matches the initial melt composition, if we consider total oxidation of metallic zirconium and calculate the UO_2-ZrO_2 ratio.
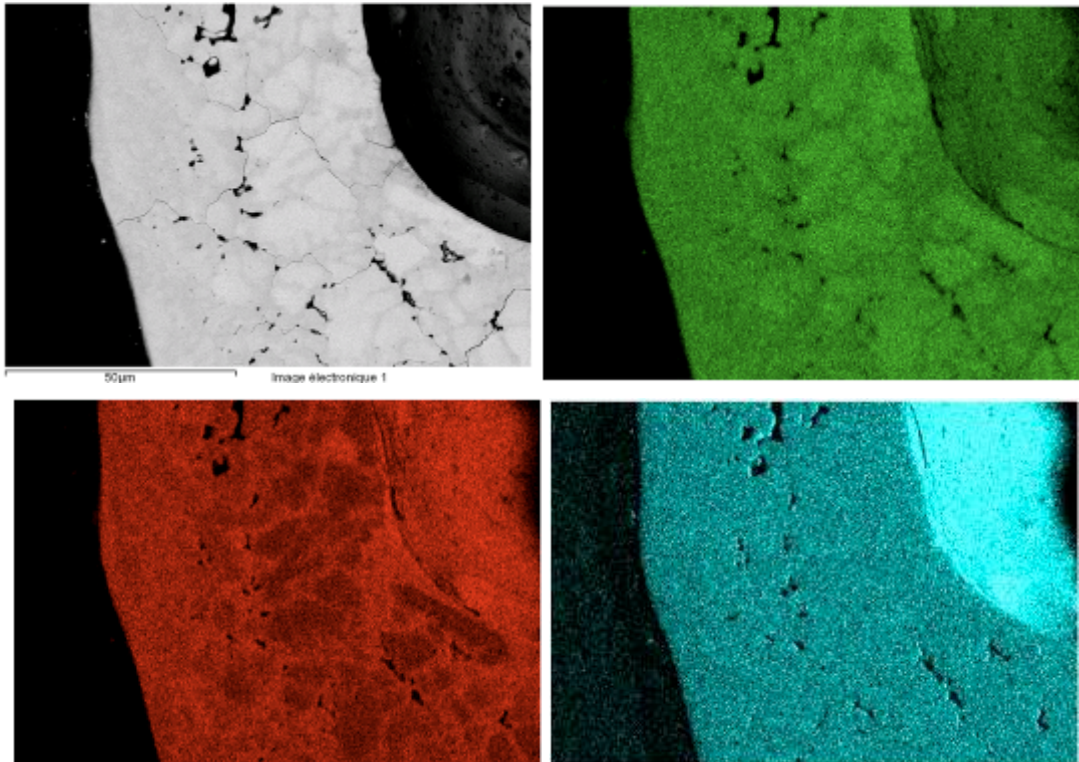
Figure 8.9 EDS mapping of the KS5 > 1 mm debris (U - green, Zr - red, O - cyan)
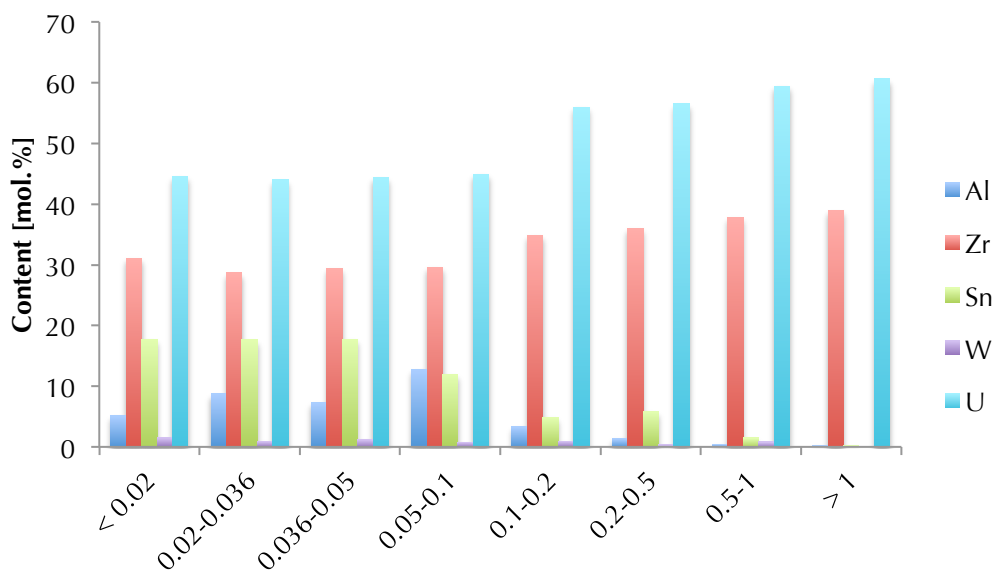
Figure 8.10 Composition of the KS5 debris by EDS analysis, size fractions in [mm]
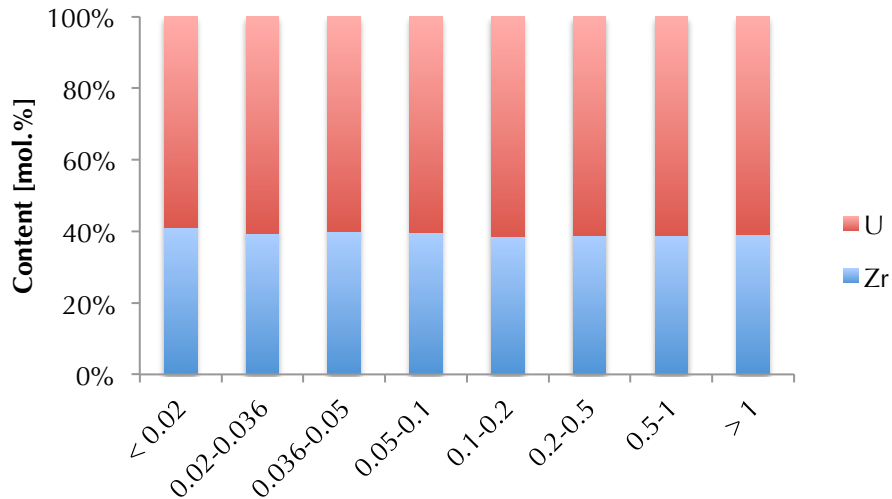
Crucible samples

Samples coming from the crucible and solidified melt near the puncher were analyzed using SEM/EDS. Similarly to KS3 crucible samples tungsten pollution in a form o two immiscible liquids was observed. *Figure 8.12* shows a EDS mapping analysis of the KS5 crucible sample. On the other side, the average tungsten content is to lowest among presented KROTOS tests (0.14 mol. %).
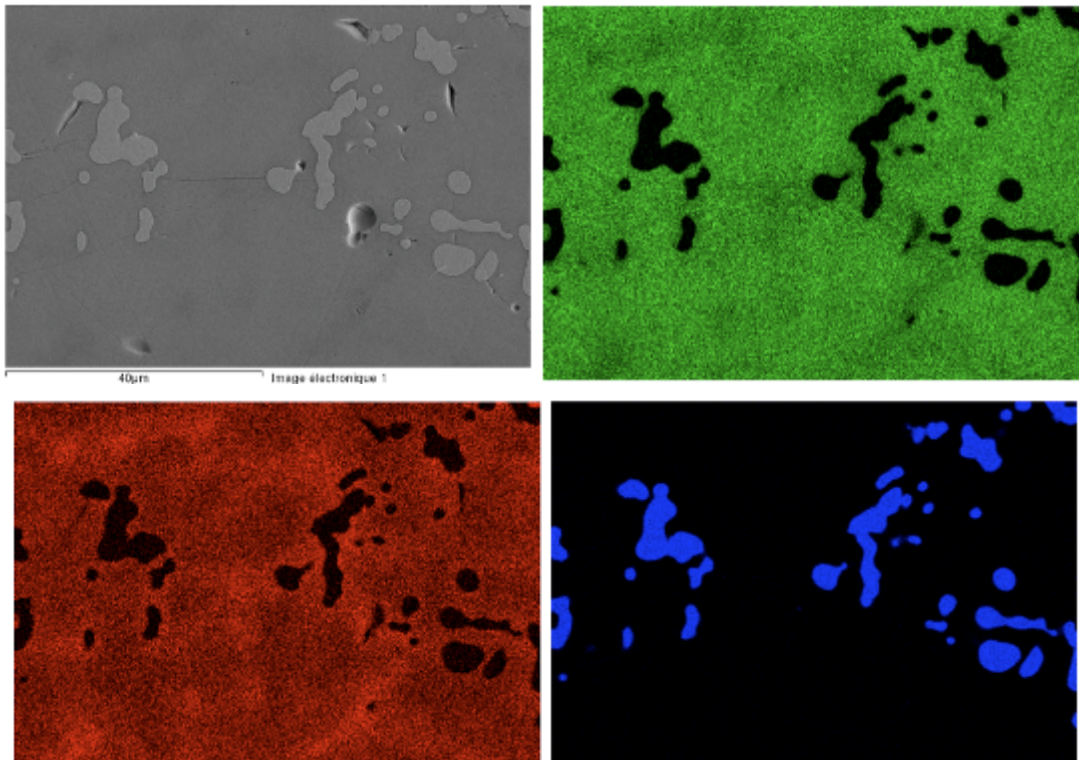
Figure 8.12 EDS mapping of the KS5 crucible sample

Moreover, footprints of metallic zirconium were found. The mixture of such composition is probably one sub-oxidized liquid phase, but at solid state the metallic zirconium precipitates from the solid solution during solidification. Example of such metallic zirconium inclusions is shown in the *Figure 8.13*.
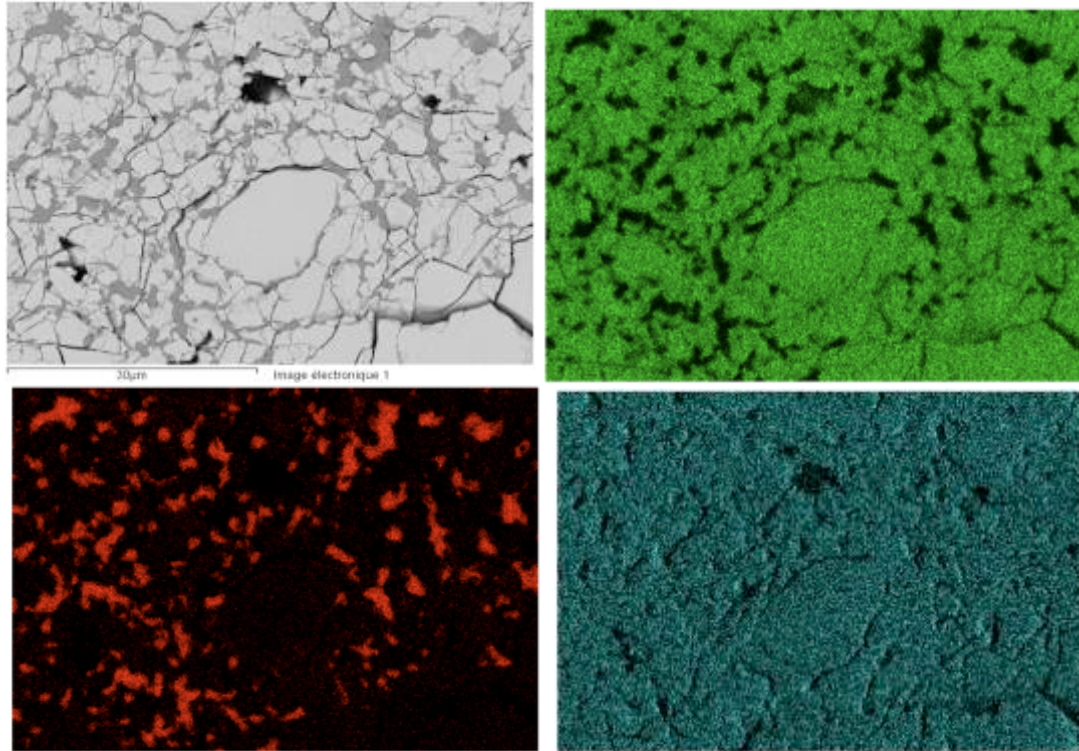
Figure 8.13 EDS mapping of the KS5 solidified melt taken near the puncher

8.1.3   KS5 image analysis

The SEM cross-section micrographs of the KS5 debris were treated by the image analysis in the same way as for previous two tests. Statistical set of 2378 particles was used through all the sieving fractions.

Average characteristics of debris participating to the steam explosion were obtained in order to establish the edge values. *Figure 8.14* shows the SE particles of the KS5 debris and their image analysis treatment. The results are summarized in the *Table 8.2*.
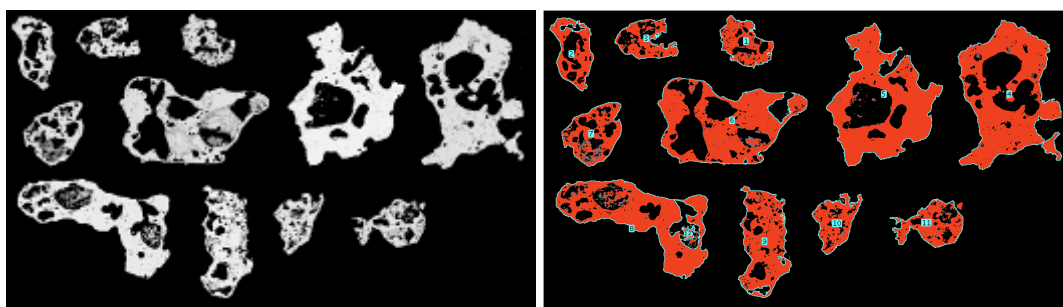
Figure 8.14 Image analysis of the KS5 debris participating to the steam explosion

Property	Average	Average deviation
Circularity	0.32	0.07
Roundness	0.62	0.10
Solidity	0.79	0.05
Porosity	29.19 %	5.55 %

To be conservative these average values of circularity and porosity are taken as a limit for particle participation to the steam explosion.

The circularity and roundness distribution and average characteristics for all the KS5 sieving fraction will follow. *Figure 8.15* presents the distribution of circularity and roundness. Interesting splitting of debris can be seen for larger sieving fractions. The circularity shows two maxima one between 0.3 and 0.4 and second between 0.6 and 0.7. This fact can be explained by two main types of the particles, one type irregular (participating to SE) and other round (quenched without SE). The local minimum of circularity around 0.5 is supported by local maximum of roundness. This maximum can be attributed to angular particles (broken droplet) that are not spherical enough to belong to spherical particles and not irregular enough to participate to SE.
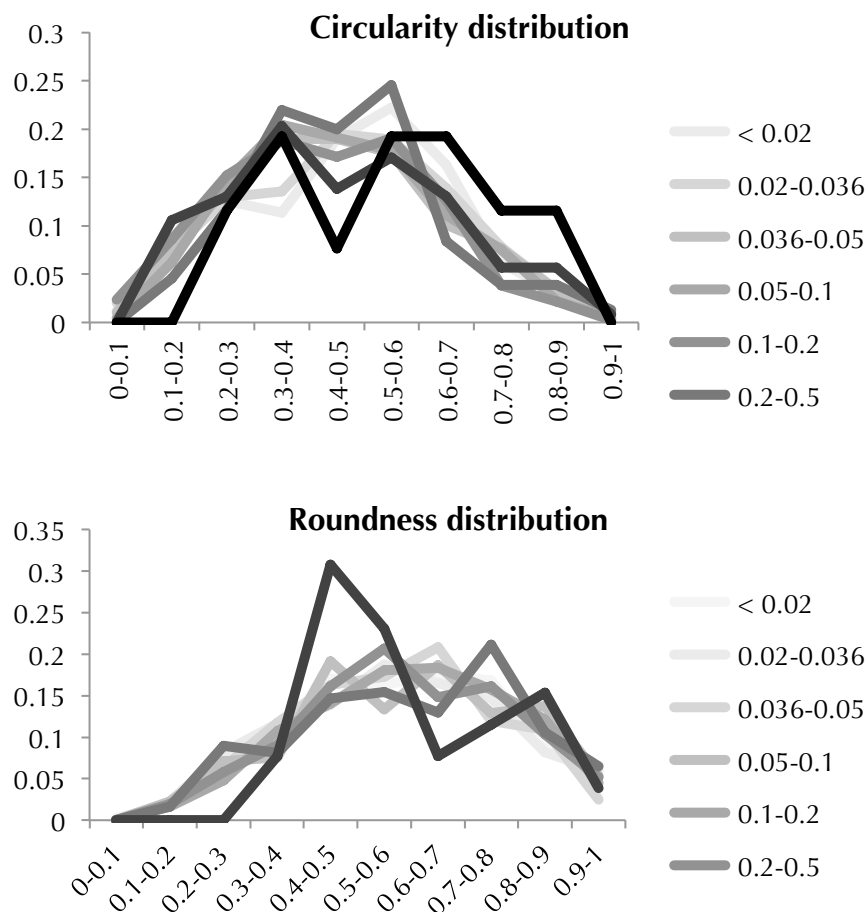
Figure 8.15 Circularity and roundness distributions for KS5 debris, size fractions in [mm]

The results of average circularity, roundness and solidity are given in the *Figure 8.16*.

Average circularity

Average roundness
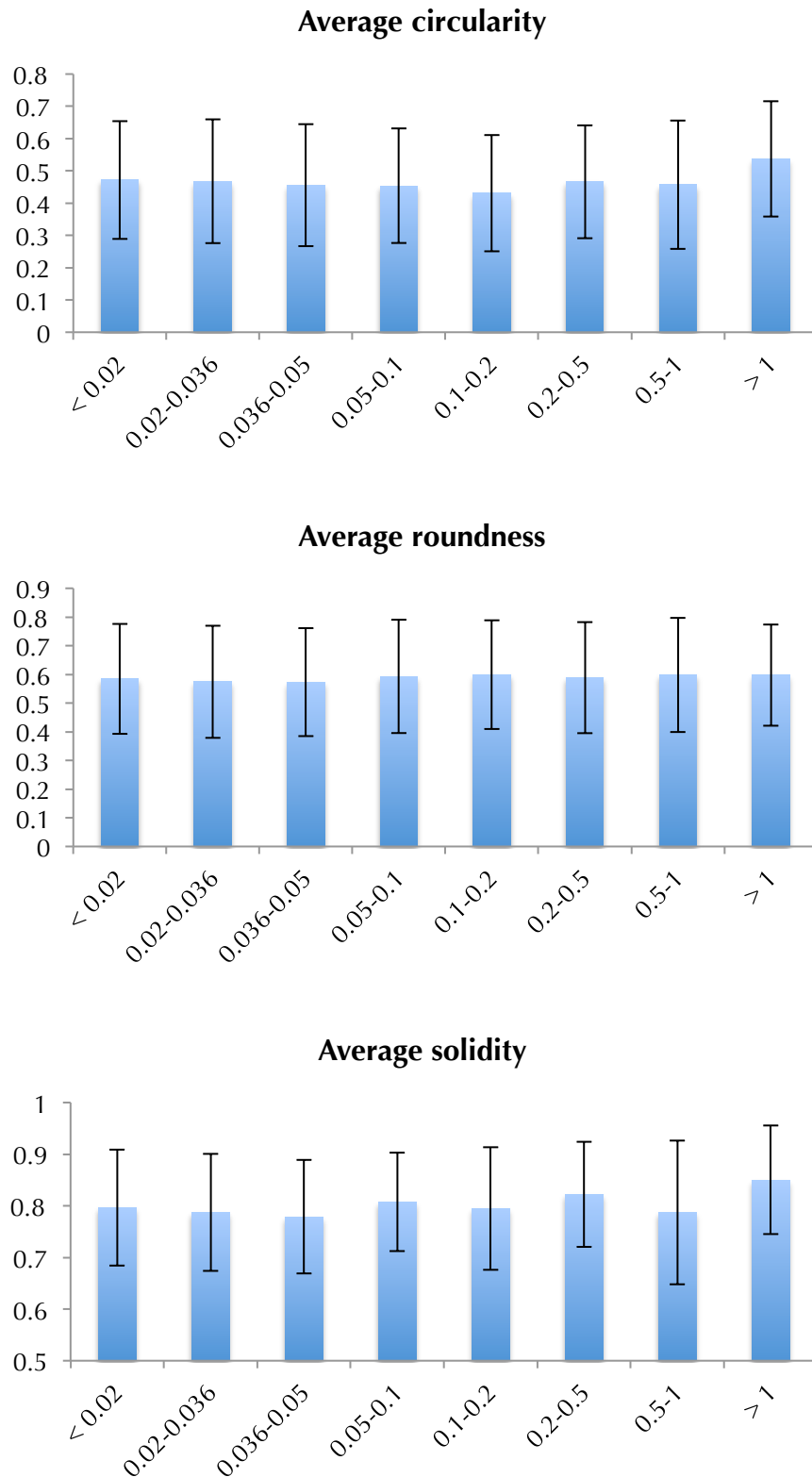
Average solidity

Figure 8.16 Average KS5 debris image characteristics, size fractions in [mm]

The most important sieving fraction for KS5 test is the larger than 1 mm. This fraction has high circularity and solidity. Thus, we can quote that the majority of the particles were quenched and not participated to the steam explosion. The lowest circularity can be found for the fraction 0.1-0.2 mm, while solidity shows local minimum for the fraction 0.036-0.05 mm. Average roundness presents constant value around 0.59 for all the sieving fractions.

Concerning debris porosity, an increase can be seen going to larger debris with maximum value 13.8 % for fraction 0.5-1 mm (*Figure 8.17*). The average debris porosity is 5.8 %, which is the highest obtained value for presented KROTOS tests. Again, the role of melt thermo-physical and hydrogen generation properties should be considered. As was found by optical microscopy investigation large particles have often one big void inside.

Figure 8.18 shows the results giving the amounts of particles participating to steam explosion for all the KS5 sieving fractions. The actual values are summarized in the *Table 8.3*. Only 16.6 w. % participated to the steam explosion in the KS5 test, this is the lowest value among the three performed KROTOS tests.
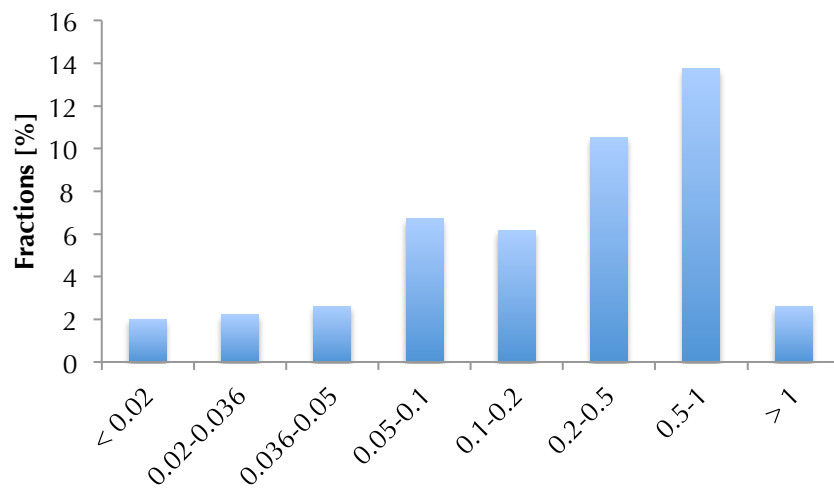
Figure 8.17 Porosity of the KS5 sieving fractions (sieving fractions in [mm])
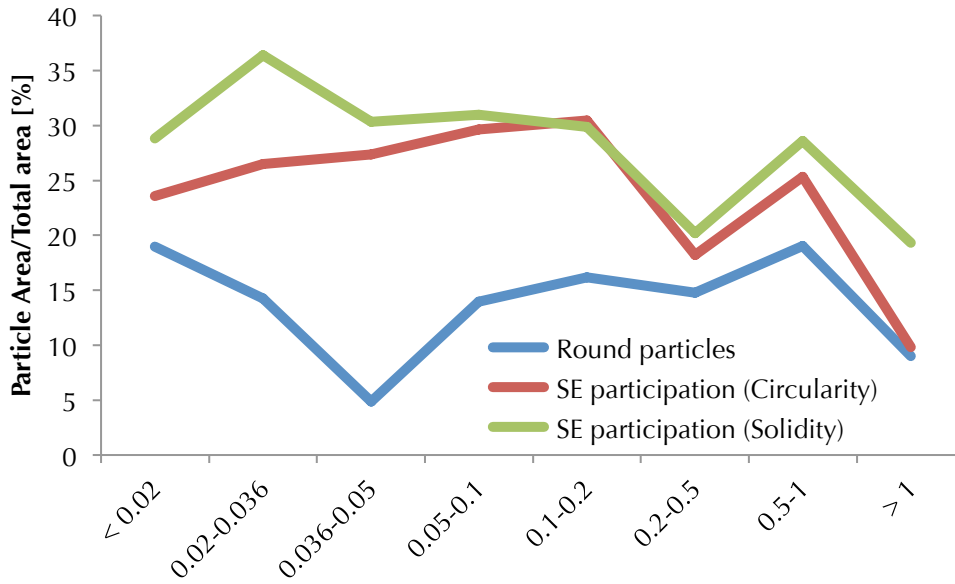
Figure 8.18 Particle participating to SE for all the KS5 sieving fractions

Table 8.3 Summary of the KS5 debris participation to the steam explosion

KS5 debris [mm]	SE participation [%]	Mass [g]	SE Mass [g]	
< 0.02	26.2	0.8	0.2	
0.02-0.036	31.4	2.3	0.7	
0.036-0.05	28.9	9.1	2.6	
0.05-0.1	30.3	13.1	4.0	
0.1-0.2	30.1	22.9	6.9	
0.2-0.5	19.2	76.2	14.6	
0.5-1	26.9	197.1	53.1	
> 1	14.5	1403.5	204.2	
	Sum	**1725.0**	**286.3**	**16.6 %**

8.1.4   X-ray powder diffraction of KS5 debris

The X-ray diffraction patterns of all the sieving fractions are presented in the *Figure 8.19*. The main lines correspond to the face-centered cubic UO_2-ZrO_2 solution. Minor phases can be observed. The *Figure 8.20* shows detailed part of the X-ray patterns. The most intensive line corresponding to a new phase never observed in previous KROTOS experiments: the tetragonal zirconium dioxide. Two main diffraction lines of tin to KS4 are also observed.
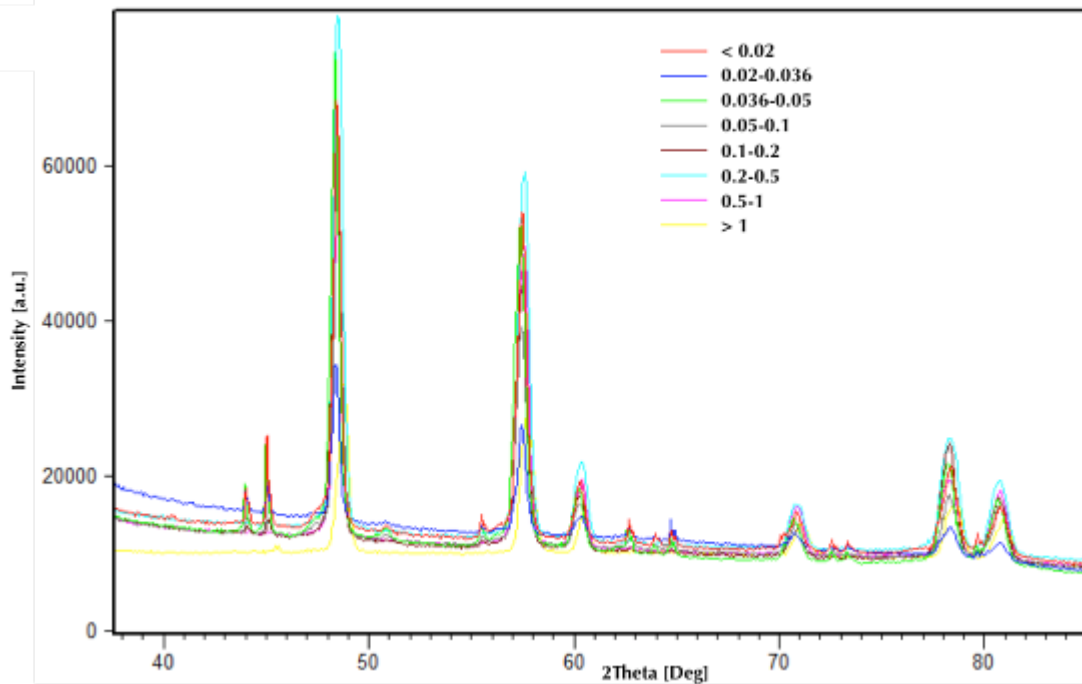
Figure 8.19 X-ray powder patterns of the KS5 debris
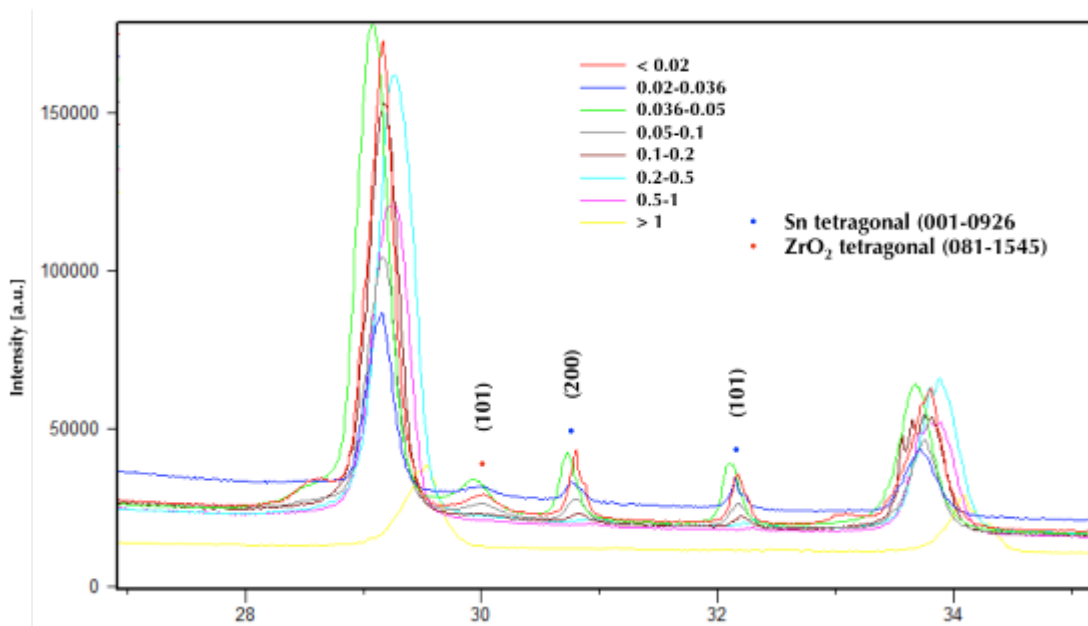
Figure 8.20 Detail of the X-ray powder patterns of KS5 debris

For the crucible sample , only one single phase has been observed: the face-centered cubic UO_2-ZrO_2. No cubic or tetragonal phases are observed (*Figure 8.21*). If the oxygen over-stoichiometry of the $U_{1-x}Zr_xO_{2+y}$ phase is calculated using the WPPF fit, the over-stoichiometry is estimated to be $y = 0.03$.

For sample near the puncher *(Figure 8.22)*, the oxygen over-stoichiometry is negative: $y = -0.01$. We can see that even if the metallic zirconium precipitates from the melt during solidification, the melt can slightly be sub-stoichiometric in oxygen.
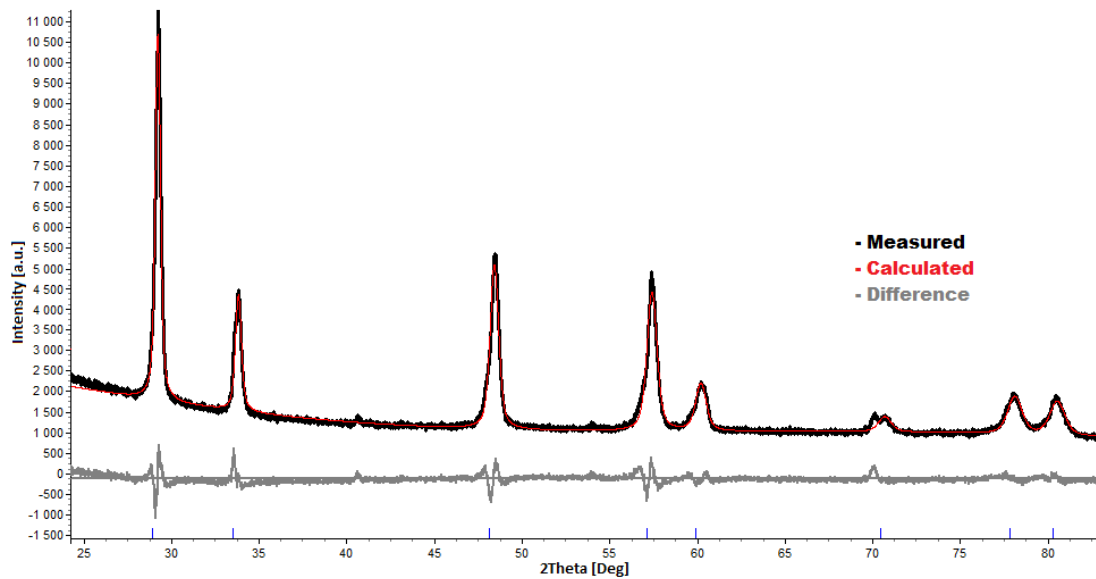
Figure 8.21 X-ray powder pattern of the KS5 crucible sample with WPPF fit
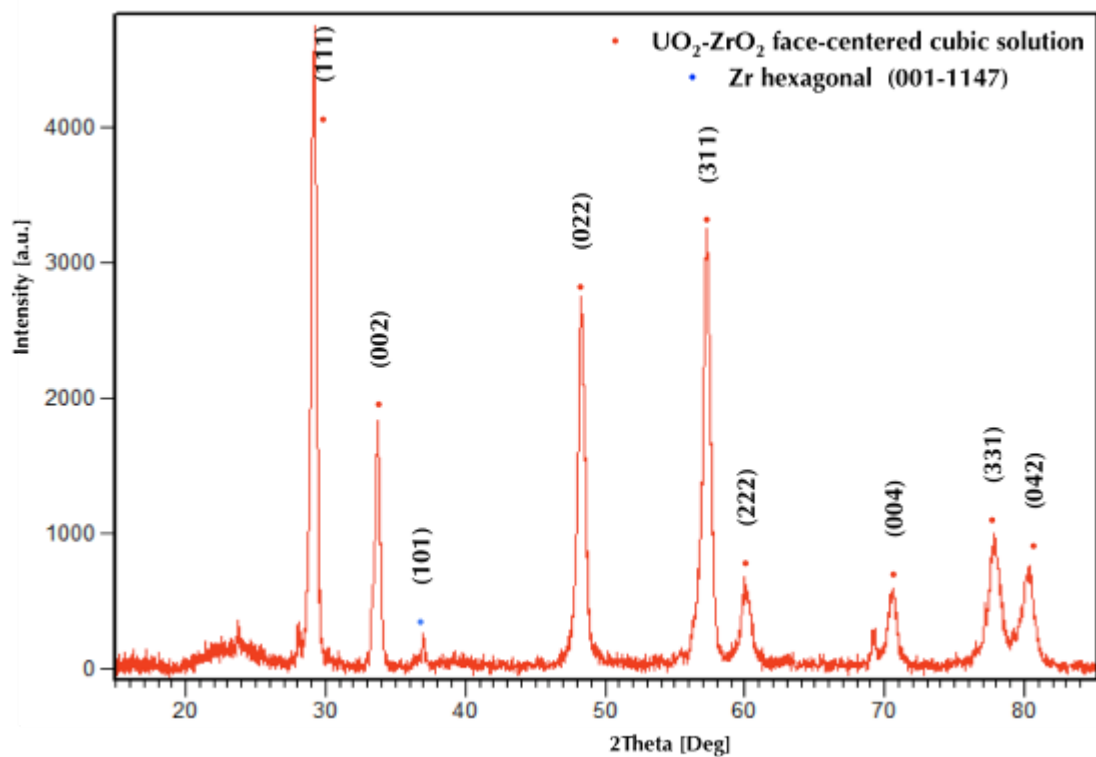
Figure 8.22 X-ray powder pattern of melt solidified near the puncher during KS5 test, the diffraction lines of UO$_2$-ZrO$_2$ mixture and the most intensive line of metallic zirconium are marked

The whole pattern profile fit was used to calculate the cell parameter of the face-centered cubic cell for all the KS5 sieving fractions. Using the cell parameter and average composition by EDS analysis the oxygen over-stoichiometry was calculated, the amount of produced hydrogen as well. Overview of the oxygen over-stoichiometry of the U$_{1-x}$Zr$_x$O$_{2+y}$ phase is presented in the *Figure 8.23*. The maximal over-stoichiometry can be found for fractions 0.05-0.1 and 0.1-0.2 mm.
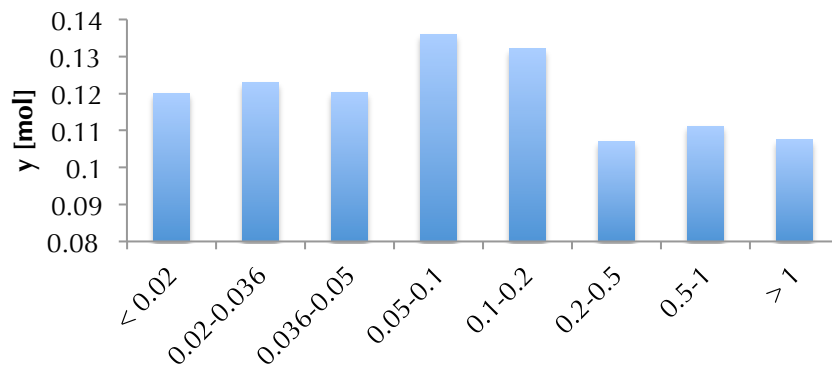
Figure 8.23 Oxygen over-stoichiometry y of the $U_{1-x}Zr_xO_{2+y}$ phase for the KS5 debris (sieving fractions in [mm])

Results of hydrogen production are summarized in the *Table 8.4*. The amount of produced hydrogen is calculated is different from previous KS2 and KS4 experiments. For KS2 and KS4 the difference between oxygen equilibrium stoichiometry and over-stoichiometry was used for calculation of the hydrogen production by melt reaction with water/steam. For the KS5 test the amount of hydrogen calculated using oxygen over-stoichiometry was increased by oxidation of 8.5 w. % of Zr in the 1725 g of delivered melt.

In total, 7.9 g of hydrogen was produced by the zirconium and UO_2-ZrO_2 mixture oxidation.

Table 8.4 KS5 results of the WPPF analysis - a (cell parameter), y (oxygen over-stoichiometry) and amount of produced hydrogen

KS5 debris [mm]	a [Å]	y [mol]	M [g]	n H_2 [mol]	M H_2 [g]
< 0.02	5.3219	0.120	0.800	0.000	0.001
0.02-0.036	5.3262	0.123	2.300	0.001	0.002
0.036-0.05	5.3255	0.120	9.100	0.004	0.008
0.05-0.1	5.3228	0.136	13.100	0.007	0.013
0.1-0.2	5.3274	0.132	22.900	0.011	0.022
0.2-0.5	5.3313	0.107	76.200	0.030	0.061
0.5-1	5.3303	0.111	197.100	0.081	0.163
> 1	5.3306	0.108	1403.500	0.559	1.127
			H_2 (Zr oxidation)	3.215	6.481
			Sum	**3.908**	**7.879**

8.1.5   ICP/MS analyses of KS5 debris

The KS5 debris sieving fractions were analyzed using ICP/MS technique in order to obtain average composition. The dissolving process was strictly the same as for previous samples. *Table 8.5* summarizes the results. The tin content is more significant than for previous tests, probably due to the lower amount of delivered melt (1.725 kg). On the other side, the tungsten pollution reaches maximally 0.58 %. The values for UO_2-ZrO_2 content agree with the EDS data and prove the melt composition and homogeneity.

8.2 Conclusion

The KS5 test provided successfully triggered FCI experiment using sub-oxidized corium melt. The mixture of UO_2-ZrO_2 and metallic Zr was melted in inert atmosphere and poured into a water pool of 53 °C.

The melt jet initially coherent and compact has instantaneously reacted with water due to the sub-stoichiometric conditions of the corium melt. Analyses of samples taken near the puncher in the release channel showed that the melt was well sub-stoichiometric during the release. For this experiment a limited steam explosion has been observed.

The majority of the debris was larger than 1 mm, which points to low melt fragmentation and limited water-melt contact. This was probably caused by the significant hydrogen production during premixing as a result of zirconium oxidation.

For the first time the effect of large solidification interval was observed. In previous tests the solidification interval of UO_2-ZrO_2 mixture was too small to have an effect on the melt solidification at FCI conditions. For KS5 the solidification interval of about 700 K brought about that two phases (UO_2-ZrO_2 rich and ZrO_2 rich) were found. It seems that the zirconium with lower $T_{liquidus}$ has been segregated to the grain boundaries of the UO_2-ZrO_2 grains with higher $T_{liquidus}$. The remaining "metallic" zirconium phases have been then oxidized. The debris composition matched the values 75 w. % UO_2 and 25 w. % ZrO_2, if the total Zr oxidation is considered.

The KS5 debris had the highest porosity among the presented KROTOS tests, in average 5.8 %. The droplets often had one large void differently to KS2 and KS4 debris. This behavior is attributed to different thermo-physical properties of the melt, especially the viscosity.

286.3 g of the melt (16.6 w. %) has been identified as possibly participating to the steam explosion. This value is the lowest for presented KROTOS test and agrees with the nonviolence of the interaction.

During the KS5 test 7.8 g of hydrogen was produced by the melt – water/steam reaction. It should be noted that significant part of the hydrogen was formed during premixing by zirconium oxidation and not by the water melt contact during SE.

Table 8.5 KS5 debris composition by ICP/MS, sieving fractions in [mm]

		Content [w. %]			Content [w. %]
KS5 < 0.02	Al	0.51	**KS5 0.1-0.2**	Al	0.05
	Sn	7.68		Sn	2.35
	W	0.58		W	0.14
	UO_2	68.81		UO_2	74.00
	ZrO_2	22.42		ZrO_2	23.46
KS5 0.02-0.036	Al	0.66	**KS5 0.2-0.5**	Al	< 0,05
	Sn	6.47		Sn	0.97
	W	0.38		W	< 0,05
	UO_2	70.11		UO_2	75.31
	ZrO_2	22.38		ZrO_2	23.67
KS5 0.036-0.05	Al	0.75	**KS5 0.5-1**	Al	< 0,05
	Sn	7.86		Sn	0.82
	W	0.34		W	< 0,05
	UO_2	68.55		UO_2	75.31
	ZrO_2	22.49		ZrO_2	23.86
KS5 0.05-0.1	Al	0.30	**KS5 > 1**	Al	< 0,05
	Sn	3.90		Sn	0.53
	W	0.25		W	< 0,05
	UO_2	72.42		UO_2	75.66
	ZrO_2	23.13		ZrO_2	23.80

Chapter 9. Conclusions and perspectives

9

In this chapter the final conclusions will be given. They will be divided into three main streams according to the analyses written in this thesis: i) Phenomenological ii) Chemical and iii) Physical aspects. Main focus will be given to describe the phenomena in a way to better understand the phenomenological aspects of Fuel Coolant Interaction.

9.1 Phenomenological aspects

9.1.1 Debris size criterion

For the FCI debris analysis, the mechanical sieving has been mainly used to describe the size distribution. It was shown that the particles are often fractionized at solid state because of the mechanical propertie. Droplets can be sintered (merged) together especially for large debris (PREMIX and ECO reults). The sieving distribution shows then misleading information about the debris diameter during premixing or after steam explosion.

Up to now, it has been considered that the following debris parameters are of first importance for steam explosion:

- Sauter diameter, defined by volume/surface area ratio.
- An arbitrary criterion for the value of this Sauter diameter: for example some users take 100 µm without any justification.

Using only particle size for FCI consideration or as a criterion for participation to SE is unappropriate.

For metals the situation is slightly different. The mechanical properties of metals predestinate the stability of solidified drops and the solid-state fractioning can be excluded.

9.1.2 Debris shape

FCI debris division of debris according to the morphology was established. For prototypic corium experiments, two main groups have been identified:

- ***Particles participating to the steam explosion*** –These particles have irregular shape with low circularity, roundness and solidity. The particles are porous, while

the porosity is in the form of rather small voids, channels or open porosity. Partly these particles can be broken after solidification to powder like debris.

- **Particles not participating to the steam explosion** – These particles can have various morphologies. At first, the melt can keep the shape formed during premixing – full round spherical particle or droplet with one internal void. These particles can be broken after solidification to angular rock like debris.

For metallic debris, the situation is quite different. As shown for MISTEE debris, the particles participating to SE have irregular shapes. We cannot speak about porosity of this debris because it is always open. This channels or voids are crated during thermal fragmentation of the droplet. This brings us to the mechanism of fine fragmentation.

9.1.3   Fine fragmentation mechanism

Among all thermal fragmentation mechanisms proposed in the past we should support the Kim-Corradini mechanism describing the fine fragmentation as entrapment of large instabilities on the water/steam interface under the melt surface. In other words, during the impact of water on the melt drop surface the water gets inside the melt and destroy the droplet integrity by further processes (vaporization, expansion, temperature gradients). The morphology of the SE particles (for both oxide or metallic melts) according to presented observations goes in this direction

9.1.4   State of the matter

Generally during FCI, the melt is coarsely fragmented during the premixing. The drops solidify according to the conditions, in which they are present (water/void around, temperature, their size). Three possible situations can be considered: i) totally liquid droplet; ii) totally solid droplet; iii) droplet with solid crust.

It can be agreed that totally liquid particle is the most favorable for thermal fragmentation. On the contrary, totally solid particle cannot participate to SE, however it should be taken in to account as a heat source for void built up.

The third case needs deeper considerations and is very questionable. The FCI community uses a crust growth model and attributes the ability to participate to SE to its mechanical properties and thickness. Considering the KROTOS debris just a very thin crust (5 microns) without well-defined grains was observed. The grain size increase to the droplet center, thus the quenching rate decreases. However, the difference in the grain size and morphology is not different, thus the droplets solidify homogenously and no significant stable curst was observed.

For KS2 and KS4 tests, the small solidification interval or pseudo-binary eutectic composition had no effect on the solidification.

The situation is different, when the melt has large solidification interval. The large solidification interval in the case of KS5 test can have an effect on the stability of the surface layer (or let say "crust").

9.1.5   Steam explosion efficiency

If we look at the definition of the SE efficiency, one question arises. The efficiency is defined using the amount of melt and amount of water in interaction when

the triggering is starting. As was observed by the image analysis of the debris not all the melt is participating to the steam explosion. Some fraction of the melt can be quenched through nonviolent steaming. Is it correct then to calculate the steam explosion efficiency using the whole melt mass? The same question can be asked for water. Some part of the water can be considered as a bulk was not participating to the rapid pressure increase.

The first question can be more expanded using results of KS2 and KS4 image analyses. In the KS2 melt the mass participated to SE was 34.3 w. % and in the KS4 test 33.5 w. %. *Table 9.1* shows how the SE efficiency changes, if we consider just the part of the melt participating to SE.

Table 9.1 SE efficiency- classical and recalculated for melt mass participating to the steam explosion

	SE efficiency (classical) [%]	SE efficiency (SE participation) [%]
KS2	0.0827	0.241
KS4	0.182	0.543

We feel that still open issue lies in the prediction of the melt mass participating to the steam explosion. Image analysis can give post-test rough estimation of the melt fraction, but nothing can be said about the conditions that led to this final state. The direct indicators localization of triggering in the water pool, void distribution, water temperature and pressure that affect the melt fraction, which is solid or liquid cannot be specified by this approach.

9.2   Chemical aspects

9.2.1   Eutectic versus non-eutectic corium mixture

As reviewed in *Chapter 3* the TROI team pointed out that the explosivity and SE efficiency is higher for eutectic corium 70 w. % UO_2 and 30 w. % ZrO_2 (70-30). According to presented analyses we should summarize following observations:

* The 70-30 corium presents only a pseudo-binary eutectic mixture. The X-ray powder diffraction analyses showed that the oxygen content is not constant for this solution. Further the thermodynamic calculation concluded that the oxygen stoichiometry has important influence on the solidus and liquidus lines. Therefore, having 70-30 pseudo-binary composition doesn't assure the real ternary eutectic composition especially in steam atmosphere.
* KS4 test with non-eutectic composition reached the highest SE efficiency among all performed KROTOS tests
* The droplet solidification and grain structure was the same for KS2 and KS4 test. The difference in the size of the solidification interval is so small that during such event as FCI it has no effect on the melt solidification.

The KS5 test describes another situation. The solidification interval is large enough to have visible effect on the melt solidification (consequent precipitation of species according to the liquidus temperature). However, influence of this

phenomenon of the general FCI was probably hidden by the effect of hydrogen production.

9.2.2   Melt – water/steam chemical reaction

The thermodynamic calculation provided the possible chemical reaction between the FCI melts and water/steam.

The aluminum oxide forms with water hydroxides and oxo-hydroxides, which have significantly lower melting point than the initial melt. The finest ECO debris contained 11.4 w. % of chemically bonded water molecules. Melt of such composition have totally different thermo-physical properties. Even the solidification behavior of aluminum oxide differs from prototypic corium melts. During SE alumina forms crystal phases out of thermodynamic equilibrium. Moreover, it doesn't form oxygen over-stoichiometric phases.

Concerning metallic melts the question lies in the kinetics of the reaction with steam. Such kinetic models are beyond scope of this thesis. However, we can conclude that this reaction affects the whole FCI process. KS5 test showed that metallic zirconium is immediately oxidized by water producing large amounts of hydrogen. PREMIX and ECO tests said that iron was partly oxidized to Fe^{2+} and formed spinel mixed oxide with aluminum. On the other side, tin is oxidized only on the surface with low reaction yield. Hydrogen production by this reaction is very important during premixing, because at this stage it can affect the SE progress. Zirconium oxide is chemically inert in these conditions and doesn't react with water.

The prototypic corium mixtures (UO_2-ZrO_2) can react with water/steam producing oxygen over-stoichiometric phases. This effect becomes more visible with UO_2 content. Uranium's ability to increase oxidation state is responsible for this effect. The oxygen over-stoichiometric content affects the solidus and liquidus lines of the mixture and is again related to the hydrogen production.

9.2.3   Hydrogen production

Hydrogen as a non-condensable gas plays an important role in the FCI progression and explosion efficiency. It was noted that hydrogen comes from two sources during FCI. Firstly, hydrogen is a product of water thermolysis at very high temperature (>2000 K). Secondly, hydrogen is product of melt – water/steam reaction.

It is necessary to distinguish hydrogen formed during premixing and hydrogen formed during thermal fragmentation, when the interaction of melt and water are more intensive. If the melt contains compound easily oxidized as in the KS5 test, the FCI can have less violent progression due to the hydrogen effect. Large amount of hydrogen can be formed as a consequence of intensive SE as was found in KS4. *Table 9.2* gives an impression of mass of hydrogen formed per one kg of delivered melt.

Table 9.2 Hydrogen production per kg of delivered melt

	Mas of H_2 [g] per mass [kg] of delivered melt
KS2	1.46
KS4	3.98
KS5	4.58

As we can see from the calculated amounts, concerning classical melt composition (UO_2-ZrO_2) the amount of hydrogen is almost three times higher for KS4 than for KS2 test. This hydrogen was formed as a consequence of steam explosion, particularly due to more intensive melt – water/steam interaction. Minor role has also higher content of UO_2 in the KS4 melt, but we believe that SE strength has more important effect than increase of UO_2 content about 10 w. %.

9.3   Physical aspects

9.3.1   Classical thermo-physical properties

The FCI research community commonly agrees on the role of classical physical properties of melts and water on the SE efficiency

Concerning melt properties we can quote:

- ***Solidus and liquidus point, or generally melting point*** – higher temperature leads to higher radiation and increase of the steam film stability
- ***Density*** – higher density leads to deeper fragmentation during premixing and therefore to smaller droplets. Smaller size leads to large interface are and faster solidification
- ***Thermal conductivity*** – Low thermal conductivity leads to the faster crust formation

For water we can postulate:

- ***Sub-cooling*** – Low sub-cooling makes the steam film more stable, larger and homogenously distributed across the melt droplet surface

In the frame of presented thesis no special efforts were done in this direction, where the general agreement exists. But we gave important attention to the melt radiation and radiation heat transfer, which have been still questioned.

9.3.2   Thermal radiation

We showed that the so-called "material effect" can be also found from the viewpoint of radiation heat transfer from the melt to the water/steam.
Prototypic corium mixtures containing high amount of UO_2 are powerful radiation bodies with constant spectral properties in the near-infrared region. At temperature typical for FCI this spectral region is of the most importance, because the melt release large amount of energy by radiation in this range and of course water absorbs this energy. Water has three significant absorption lines and the most intensive at 3 μm. By chance, at this wavelength the radiation intensity of aluminum oxide decreases rapidly with decreasing temperature. According to our calculations the radiation energy captured in the water just after 1 mm layer of steam layer is almost four times higher for UO_2 at 2800 K than for alumina melt at 2100 K.
This radiation heat transfer is important due to the kinetics of the void fraction (steam) generation in the premixture, but also for the steam film stability.

9.4 Perspectives

Concerning the effect of the solidification interval on FCI phenomena, it has not been possible to conclude on fully-oxide composition. The KROTOS KS6 test should answer partially to this point.

In the frame of this thesis, the importance of sub-cooling effect of the melt has been partially resolved for prototypical corium (UO_2-ZrO_2) composition: no metastable phase for the steam exploded debris have been found in contrary to experiment using simulant materials like alumina. Nevertheless, for the other kinds of corium composition, this point has not been solved, for example, oxide corium composition with large solidification interval.

Data and analyses provided in the current thesis describe the post-test situation. The results can be applied on the experiment considerations and calculations. However, next step should be to analyze in deep the conditions, which lead to such post-test situation. For example, what is the exact reason, why only about 30 w. % participates to the steam explosion? Is it due to the melt freezing, void distribution, increased steam film stability or the nature of the material?

The post-test debris analyses of alumina experiences could be very useful for the understanding of main FCI phenomena (analyses of pure alumina experiences).

During the material characterization of the prototypic corium debris we faced a lack of corium sample for standardization of analytical techniques (SEM, XRD).

At Nuclear Research Institute Rez plc, we launched a project of corium standard preparation in the COMETA facility.

The COMETA facility uses cold crucible induction heating to reach temperature above 3000 K. We performed two melting/solidification experiments using corium mixtures: i) 80 w. % UO_2 and 20 w. % ZrO_2; ii) 50 w. % UO_2 and 50 w. % ZrO_2. Example of analysis of sample rapidly quenched on a cooper bar can be found in the *Figure 9.1*.

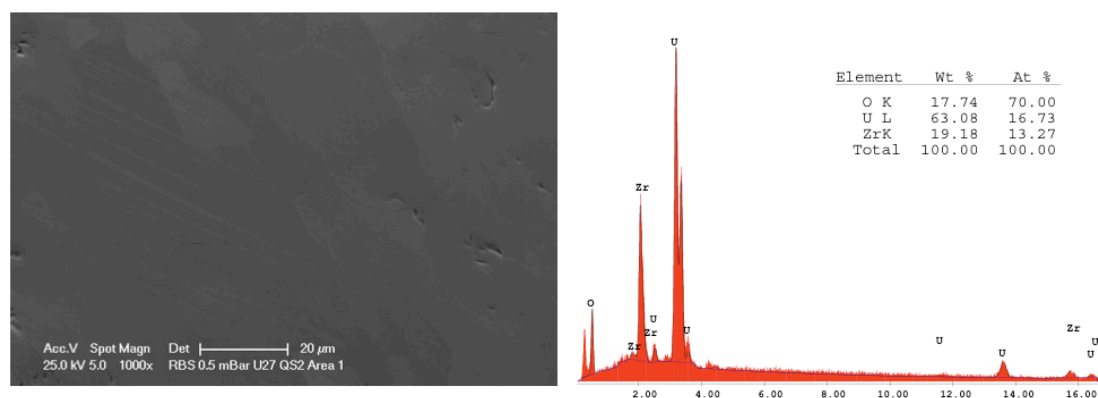| Element	Wt %	At %
O K	17.74	70.00
U L	63.08	16.73
ZrK	19.18	13.27
Total	100.00	100.00

Figure 9.1 SEM micrograph and EDS analysis of the corium standard sample

Appendix A.

FARO facility description
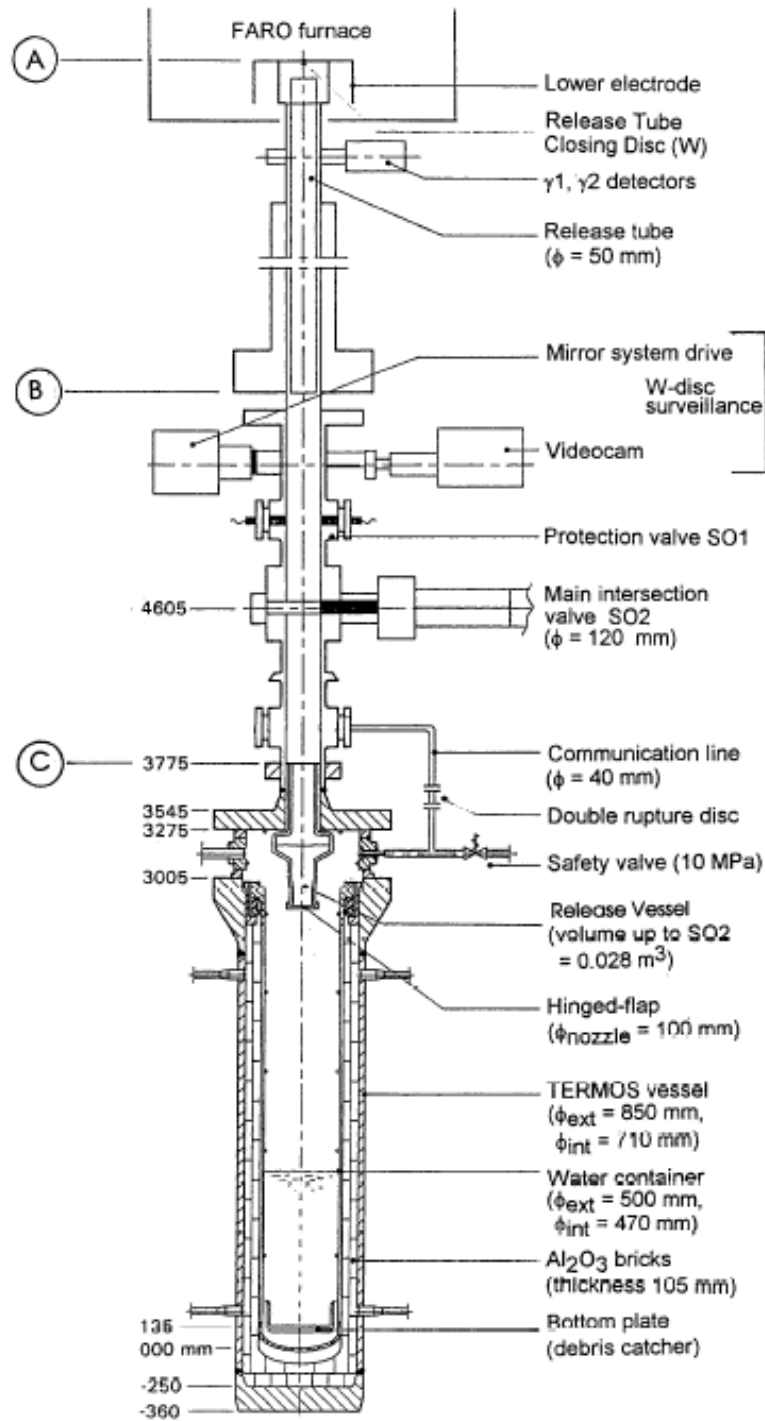
Scheme of the FARO facility test section
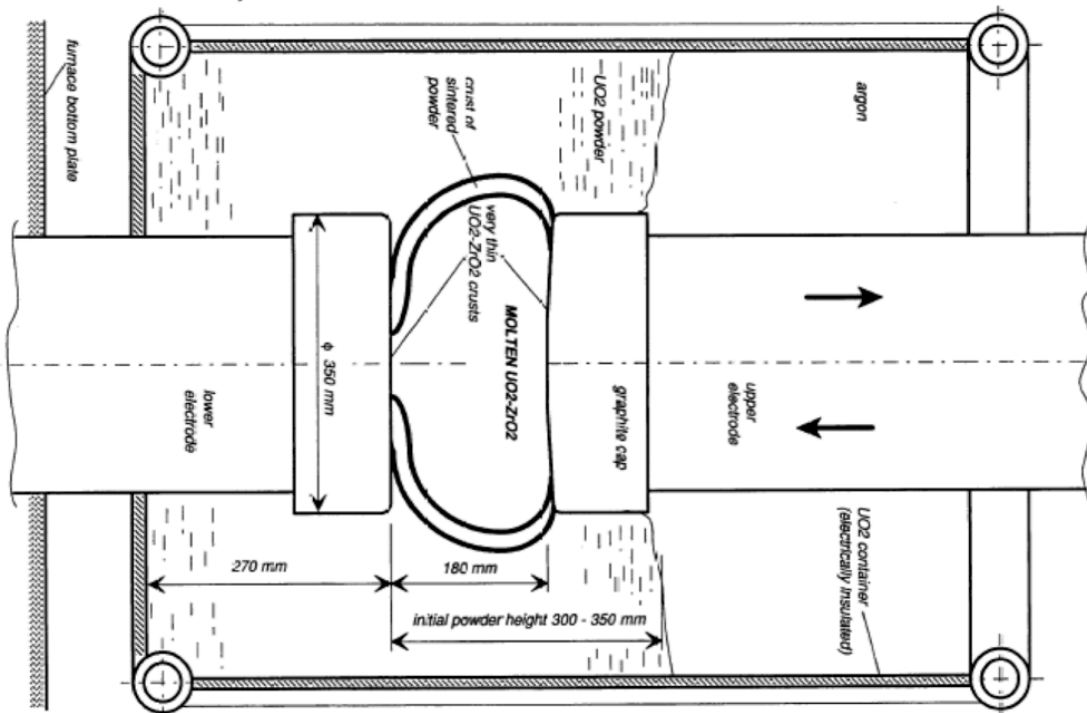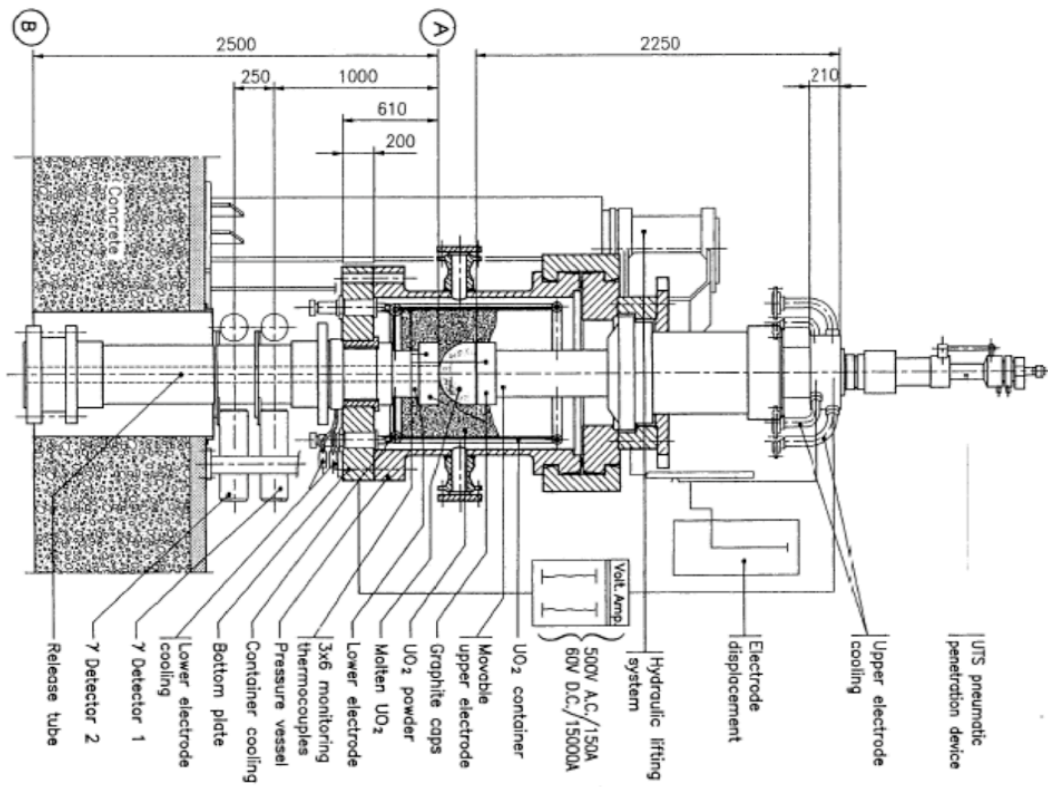
Description of the FARO furnace and detail of the melting zone

Summary of the FARO experiments

FARO	L-06	L-08	L-11	L-14	L-19	L-20	L-24	L-27	L-28	L-29	L-31	L-33
Material	UO_2/ZrO_2 80/20	UO_2/ZrO_2 80/20	$UO_2/ZrO_2/Zr$ 76,2/19,2/4,6	UO_2/ZrO_2 80/20	UO_2/ZrO_2 80/20	UO_2/ZrO_2 80/20	UO_2/ZrO_2 80/20	UO_2/ZrO_2 80/20	UO_2/ZrO_2 80/20	UO_2/ZrO_2 80/20	UO_2/ZrO_2 80/20	UO_2/ZrO_2 80/20
Melt temperature (K)	2923	3023	2800	3073	3073	3173	3023	3023	3052	-	2988	3070
Jet diameter (cm)	10	10	10	10	10	10	9,4	9,4	5	-	5	5
Flow rate (kg/s)	0,28	119	-	-	-	-	-	-	-	-	-	-
Melt amount in FCI (kg)	18	44	151	125	157	96	177,1	128,7	174,9	39	92	100
Water temperature (K)	539 (503 bottom plate)	536 (528 bottom plate)	535	537	536	486	425	424	424	-	291	274
Water mass (kg)	120	255	600	623	330	660	719	536	517	-	481	531
Water height (cm)	87	100	200	205	110	197	202	147	144	-	145	162
Steam Explosion	NO	NO	NO	NO	NO	NO	?	NO	NO	-	NO	YES
Trigger	NO	NO	NO	NO	NO	NO	NO	NO	NO	-	NO	YES
Fulet to coolant mass ratio	0,15	0,17	0,25	0,2	0,48	0,15	0,25	0,29	0,33	-	0,19	0,19
Pressure during FCI (Mpa)	5,4	6,1	4,9	5,1	5,0	2,04	0,51	0,49	0,51	0,2	0,22	41
Mean size of fragments (mm)	4,5	3,8	3,5	4,8	3,7	4,4	?	-	-	-	3,6	-
NOTES	cake 6 kg	cake 14 kg	No debris cake in the catcher-melt was breaked up maybe in the vapor - Zr H2O reaction	reproduction of L-11 without metalic Zr, melt cake 20 kg	50% of total mass formed a cake, i.e. 0,2 kg of hydrogen was produced	1/4 of total mass formed a cake, i.e. 0,2kg of hydrogen	Special debris characterization, i.e. 0,3kg of hydrogen	26 kg of cake, no debris size analysis	No debris data, i.e. 0,2 kg of hydrogen	No complete information	No cake, main diameter - 3 mm top, 3,4 middle, 5,2 bottom, hydrogen 0,05kg	no debris analysis, but fine particles

Appendix B.

TROI facility description

Two setups of the TROI facility

Summary of the TROI experiments

TROI	1	2	3	4	5	9	10	11	12	13	14
Material	ZrO_2/Zr 99/1	ZrO_2/Zr 99/1	ZrO_2/Zr 99/1	ZrO_2/Zr 99/1	ZrO_2/Zr 98,5/1,5	UO_2/ZrO_2 70/30	UO_2/ZrO_2 70/30	UO_2/ZrO_2 70/30	UO_2/ZrO_2 70/30	UO_2/ZrO_2 70/30	UO_2/ZrO_2 70/30
Melt temperature (K)	>3373	>3373	>3373	>3373	3373	3200	3800	>3800	3800	2600	3000
Melt amount in FCI (kg)	5	5,5	4,88	4,2	2,9	4,3	8,7	9,2	8,4	7,7	6,5
Water temperature (K)	365	365	323	292	337	296	298	296	293	292	285
Water mass (kg)	283	283	283	283	283	-	-	-	-	-	-
Water height (cm)	67	67	67	67	67	90	67	67	67	67	67
Steam Explosion	+/-	NO	NO	YES	YES	NO	YES	NO	YES	YES	YES
Trigger	-	-	-	-	-	-	-	-	-	-	-
Initial pressure (Mpa)	0,1	0,1	0,1	0,1	0,1	0,1	0,117	0,111	0,11	0,108	0,105
Comments # 1	variing melt jet diamter: 2,8 - 6 cm					plug/puncher - 8,0/6,5 cm					
Comments # 2					double peak explosion	dyn. pressure - no data					Two pyrometers : difference of melt T cca 800K
Coments # 3					test section broken	mixture was not fully melted	H_2 1502 ppm	H_2 18 ppm	H_2 1239 ppm	H_2 165 ppm	

TROI	17	18	23	29	32	34	35	36	37	38	39	40
Material	UO_2/ZrO_2 70/30	UO_2/ZrO_2 78/22	UO_2/ZrO_2 78/22	UO_2/ZrO_2 50/50	UO_2/ZrO_2 87/13	UO_2/ZrO_2 70/30	UO_2/ZrO_2 70/30	UO_2/ZrO_2 70/30	UO_2/ZrO_2 78/22	UO_2/ZrO_2 78/22	UO_2/ZrO_2 78/22	UO_2/ZrO_2 70/30
Melt temperature (K)						~3000	~3000	~3000	~3000	~3000	~3000	~3000
Melt amount in FCI (kg)		9,1		11,5		10,5	8	5,3	8,1	5,3	3,4	11,1
Water temperature (K)						341	334	305	313	288	285	287
Water mass (kg)						189	367	269	269	92	92	92
Water height (cm)						67	130	95	95	130	130	130
Steam Explosion	NO		NO	NO		YES	YES	YES	YES	NO	NO	NO
Trigger	-	-	-	-	-	YES	YES	YES	YES	-	-	-
Initial pressure (Mpa)							0,110		0,104	0,105	0,106	0,312
Comments # 1												
Comments # 2						Mishandling during debris measurements						
Coments # 3	H_2 789 ppm		H_2 438 ppm	H_2 619 ppm	H_2 1010 ppm		H_2 14200 ppm					

TROI	49	50	51	52
Material	$UO_2/ZrO_2/Zr/Fe$ 62,3/15/11,7/11	$UO_2/ZrO_2/Zr/Fe$ 59,5/18/11,9/10,6	$UO_2/ZrO_2/Zr/Fe$ 60,5/16,7/12,1/10,7	$UO_2/ZrO_2/Zr/Fe$ 61/16/12/11
Melt temperature (K)	2730 (3360)		2695 (3420)	2650
Melt amount in FCI (kg)	15,96	14,46	6,3 (14,2 load)	8,6 (14,1 load)
Water temperature (K)			294	285
Water mass (kg)			367	367
Water height (cm)			130	130
Steam Explosion	-	-	YES	+/-
Trigger	-	-		
Initial pressure (Mpa)	-	-	0,115	0,116
Comments # 1	apparatus test section changed			
Comments # 2	metal added phase separation		metal added + steam expl.	
Coments # 3	two articles – two temperatures, compositions		two articles – two temperatures, compositions	melt delivery not controled

Appendix C.

Summary of the KROSTOS tests

| KROTOS	26	27	28	29	30	32	33	35	36	37	38	40	41
Material	Al_2O_3	Al_2O_3	Al_2O_3	Al_2O_3	Al_2O_3	UO_2/ZrO_2 80,8/19,2	UO_2/ZrO_2 81,2/18,8	UO_2/ZrO_2 79/21	UO_2/ZrO_2 79/21	UO_2/ZrO_2 80/20	Al_2O_3	Al_2O_3	Al_2O_3
Melt temperature (K)	2573	2623	2673	2573	2573	3063	3063	3023	3025	3018	2665	3073	3073
Jet diameter (cm)	3	3	3	3	3	3	3	3	3	3	3	3	3
Melt amount in FCI (kg)	1,43	1,43	1,44	1,53	1,52	3,03	3,17	3,1	3,02	3,22	1,53	1,47	1,43
Water temperature (K)	333	361	360	293	293	351	298	363	294	296	294	290	368
Water mass (kg)	7,2	7,2	7,2	7,65	7,45	7,1	7,7	7,7	7,7	34,2	34	34,7	33,4
Water height (cm)	112	112	112	108	108	108	108	108	108	111	111	111	111
Steam Explosion	YES	NO	YES	YES	YES	NO	NO	NO	NO	NO	YES	YES	NO
Trigger	YES	NO	YES	NO	NO	NO	NO	YES	YES	YES	YES	NO	NO
Trigger pressure (Mpa)	11,2	-	8,5	-	-	-	-	?	13	13	?	-	-
Fulet to coolant mass ratio	0,2	0,2	0,2	0,2	0,2	0,43	0,41	0,4	0,39	0,09	0,045	0,04	0,04
Pressure during FCI (Mpa)	0,1	0,1	0,1	0,1	0,1	0,1	0,1	0,1	0,1	0,1	0,1	0,1	0,1
Mean size of fragments (mm)											0,16	0,7	
NOTES	damage	0,45 kg cake 0,3 kg out of test vessel	damage	fine fragmentation	fine fragmentation, higher melt release speed					new 200 mm inner diameter water pool (95 mm before)	spontaneous SE before trigger		small cake, coarse debris

KROTOS	42	43	44	45	46	47	48	49	50	51	52	53
Material	Al_2O_3	Al_2O_3	Al_2O_3	UO_2/ZrO_2 80/20	UO_2/ZrO_2 80/20	UO_2/ZrO_2 80/20	Damage to the KROTOS Furnace	Al_2O_3	Al_2O_3	Al_2O_3	UO_2/ZrO_2 80/20	UO_2/ZrO_2 80/20
Melt temperature (K)	2465	2625	2673	3106	3086	3023		2688	2473	2748	3133	3129
Jet diameter (cm)	3	3	3	3	3	3		3	3	3	3	3
Melt amount in FCI (kg)	1,54	1,5	1,5	3,09	5 (5,1 releas	3 (5,1 releas		1,47	1,7	1,79	2,62	3,6
Water temperature (K)	293	295	363	369	290	291		294	360	368	290	290
Water mass (kg)	34,6	34,6	32,9	36,3	34,1	34,1		34	33,7	33,5	34,1	34,1
Water height (cm)	111	111	111	114	111	111		111	111	111	111	111
Steam Explosion	YES	YES	YES	NO	NO	NO (YES)		YES	NO	NO	NO (YES)	NO (YES)
Trigger	NO	NO	YES	YES	YES	YES		NO	NO	NO	YES	YES
Trigger pressure (Mpa)	-	-	?	14,5	15,5	15		-	-	-	14,5	15,2
Fulet to coolant mass ratio	0,04	0,04	0,05	0,09	0,15	0,15		0,04	0,05	0,05	0,08	0,11
Pressure during FCI (Mpa)	0,1	0,2	0,1	0,1	0,1	0,1		0,37	0,1	0,1	0,2	0,36
Mean size of fragments (mm)	0,2	0,4	0,11	1,7	0,5			0,17	15		1	
NOTES	presure expl. Peak only 56 Mpa, low melt overheating	double initial pressure, damage, but pressure peaks similar, lower steaming			pressure sipkes 20 Mpa	pressure sipkes 16 Mpa		SE 127 Mpa	No cake	Cake formed	20 Mpa propagation	

KROTOS		54	56	57	58	63
Material			UO_2/ZrO_2 80/20	Al_2O_3	UO_2/ZrO_2 80/20	UO_2/ZrO_2 80/20
Melt temperature (K)			3033	2670	3077	3133
Jet diameter (cm)			3	3	3	3
Melt amount in FCI (kg)	K R O T O S		4,02	1,41	3,6	2
Water temperature (K)			290	290	289	295
Water mass (kg)			35,1	36,6	30,9	29,6
Water height (cm)			97	110	91	94,5
Steam Explosion	F u r n a c e		NO	NO	YES	YES
Trigger			NO	NO	YES	YES
Trigger pressure (Mpa)			-	-	15	14,3
Fulet to coolant mass ratio			0,11	0,04	0,12	0,07
Pressure during FCI (Mpa)	d a m a g e		0,37	0,1	0,37	0,21
Mean size of fragments (mm)			1,4		0,177	0,3
NOTES			camera visualization	Cake formed, camera visualization	mild SE	slow melt delivery, 2g of hydrogen

Appendix D.

MISTEE facility description
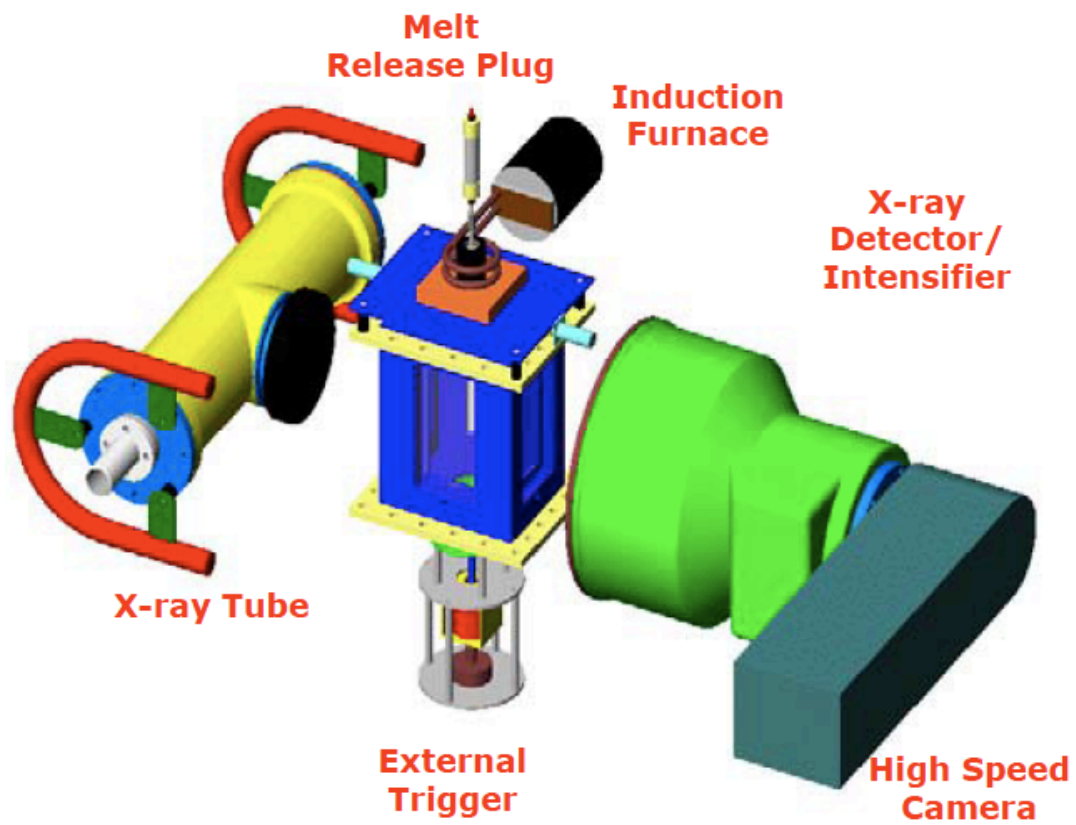
Appendix E.

MATLAB source for the radiation heat transfer model

```
clear all, close all, clc
k=1.3806505e-23; c=299792458; h=6.6260693e-34; mu=1.66053886e-27;

lambda=1e-6*(0.2:2.5e-2:100); % wavelength range [m]
nu=c*lambda.^-1; % [Hz]
dnu=diff(nu);

m=length(nu); % number of points

%--------------------------
% BB radiation (dI/d nu):
T=1600;  % [K]
B= @(nu) 2*h*c^-2*nu.^3 .*(exp(h/k/T*nu)-1).^-1;

%--------------------------
% SPECRAL EMISSIVITY eps

%UO2
%eps=0.85*ones(size(nu));

%Al2O3 (1600K!)
al=dlmread('spectral_emissivty_file.txt'); al(:,1)=c*(1e-
6*al(:,1)).^-1; eps=interp1(al(:,1),al(:,2),nu);

%plot(lambda,eps)
%break

% Emission of the material:
I0=eps.*B(nu);

%---------------------------
% ABSORPTION IN WATER
Nw=1000/(18.01528*mu); % particle density of liquid water [m-3]

% vapor
pv=200e3; % pressure [Pa]
Tv=500; % vapor temperature [K]
Nv=pv/(k*Tv);


a=dlmread('water_spectral_absoprtion.txt'); % G. M. Hale and M. R.
Querry. Optical Constants of Water in the 200-nm to 200-µm Wavelength
Region, Appl. Opt. 12, 555-563 (1973) doi:10.1364/AO.12.000555

sigma=interp1(c*(1e-6*a(:,1)).^-1 , 1e+6 * 4*pi/Nw* a(:,3) ./
a(:,1)),nu);


% layer of vapor:

D=10e-4; % thickness of vapor [m]
%D=0;
```

```matlab
% vapor/water interface
I1r=I0.*exp(-Nv*D*sigma); % Intensity on the right-hand side of the
vapor/water interface

nw=interp1(c*(1e-6*a(:,1)).^-1,a(:,2),nu);
R=((nw-1)./(1+nw)).^2;
%R=0;
I1l=(1-R).*I1r;



x=linspace(0,1e-4,1e2); % distance from the water surface [m]
n=length(x);

for i=1:n
    I(i,:)=I1l.*exp(-x(i)*Nw*sigma);
    sigmaI=sigma.*I(i,:);
    dE(i)=sum(-Nw*0.5*(sigmaI(2:m)+sigmaI(1:m-1)).*dnu);
end

figure(1)
subplot(2,1,1)
semilogx(1e6*lambda,I1l./I0, 1e6*lambda, 1/max(B(nu))*B(nu),
1e6*lambda, 1/max(B(nu))*I1l)
xlabel('\lambda [\mum]')
subplot(2,1,2)
semilogy(1e3*x,dE)
xlabel('x [mm]'), ylabel('dE/dt [J s^{-1} m^{-3}]')

%dlmwrite('results.txt',dE);
```

Appendix F.

Characterization techniques

Electron microscopy analyses were done using scanning electron microscope Philips XL 30 CP in a low vacuum system (0.5 mbar). Images and analyses were obtained by Robinson back-scattered electrons detector and energy dispersive EDAX Ametek detector. The SEM/EDS type Zeiss supra 55 /Oxford Xmax was used as well.

X-ray powder patterns (XRD) were collected using a PANalytical X´Pert PRO diffractometer (and Bruker D8) equipped with a conventional X-ray tube (CoKα 40 kV, 30 mA, a line focus) in reflection Bragg-Brentano geometry. A divergence slit of 1°, an anti-scatter slit of 2°, a mask of 15 mm and a Soller slit of 0.04 rad were used in the primary beam. A fast linear position sensitive detector X'Celerator with an anti-scatter shield, a Soller slit of 0.04 rad and Fe beta-filter were used in the diffracted beam. Qualitative analysis was performed with HighScorePlus software package (PANalytical, the Netherlands, version 3.0), Diffrac-Plus software package (Bruker AXS, Germany, version 8.0) and JCPDS PDF-2 database [1]. For Whole-Pattern Profile Fitting (WPPF) we used Diffrac-Plus Topas (Bruker AXS, Germany, version 4.2) using the Pawley method.

The IR spectra were recorded on Nicolet NEXUS 670 FT- Infrared Spectrometer

The TGA/MS analyses were performed using NETZSCH STA 409 MS and SETARAM SetsysEvolution –16MS.

The ICP/MS data were collected using Thermo electron pq excel equipment.

The Auger spectra were recorded using apparatus VG Microlab 310F.

1. JCPDS PDF-2 database, International Centre for Diffraction Data, Newtown Square, PA, U.S.A. release 54, 2004